

Mechanistic Understanding of Co-crystal solubility and dissolution by using a combination of Experimental and Molecular Modelling Techniques

PREYANTHINY KIRUBAKARAN
DE MONTFORT UNIVERSITY

In partial fulfilments of the requirements for the degree of

PhD in Co-crystallisation

Submitted to: **De Montfort University, Doctoral College**

Health and Life Sciences Faculty

Supervisor: Professor Mingzhong Li

Second supervisor: Dr Richard Cross

Version: Final

Date: 14/01/2021



Contents

Contents	1
Declaration	5
Acknowledgements.....	6
Publications.....	7
Journal publications	7
Awards	7
Conference poster presentations.....	7
Conference oral presentations.....	8
Abstract.....	9
List of figures.....	10
List of equations	14
Chapter 1: Introduction.....	17
1.1 Research Background	17
1.2 Research aims and objectives.....	19
1.3 Thesis structure	20
Chapter 2 – Literature review.....	22
2.1 Chapter review.....	22
2.2 Biopharmaceutics classification system (BCS).....	22
2.3 Enhancing dissolution for poorly water-soluble drugs	24
2.3.1 Particle size reduction	24
2.3.2 Supercritical Fluid (SCF) Process.....	25
2.3.3 Cyclodextrin complexation.....	25
2.3.4 Solid dispersion	26
2.3.5 High pressure homogenisation	27
2.3.6 Pharmaceutical co-crystals.....	27
2.4 Pharmaceutical co-crystals	28
2.4.1 Co-crystal design mechanism.....	28
2.4.2 Co-crystal formation methods	30
2.4.3 Properties	36
2.4.4 Characterisation techniques.....	40
2.5 Pharmaceutical co-crystal Formulation and Development.....	40
2.5.1 Solution mediated phase transformation.....	40

2.5.2	Precipitation inhibitors	42
2.5.3	Spring and Parachute model.....	42
2.6	Flufenamic acid CO, Carbamazepine CO, and their cofomers.....	43
2.6.1	Flufenamic acid drug introduction.....	43
2.6.2	Flufenamic acid co-crystals synthesis.....	44
2.6.3	Carbamazepine drug introduction.....	45
2.6.4	Carbamazepine co-crystals synthesis	46
2.6.5	Pharmaceutical co-formers Nicotinamide and Theophylline	46
2.7	Introduction to polymers	48
2.7.1	Polyethylene glycol 400.....	48
2.7.2	Polyvinyl Pyrrolidone K30	49
2.7.3	Plasdone S630 (PVP-VA).....	49
2.8	Molecular modelling and molecular dynamics	50
2.8.1	Forcefields	51
2.8.2	Geometry optimization.....	56
2.8.3	Dynamics theory.....	58
2.9	Chapter conclusion.....	62
Chapter 3	– Materials and Methods	63
3.1	Chapter overview.....	63
3.2	Materials.....	63
3.3	Methods	64
3.3.1	Preparation and synthesis	64
3.3.2	Analytical techniques.....	66
3.3.3	Calculating molecular dynamic properties.....	75
3.4	Chapter conclusion.....	79
Chapter 4	– Characterisation of Samples	80
4.1	Chapter Overview.....	80
4.2	Materials and Methods	80
4.3	Results - Characterisation of cocrystals.....	81
4.3.1	ATR-FTIR	81
4.3.2	Differential Scanning Calorimetry	84
4.3.3	X-Ray powder diffraction.....	87
4.4	Chapter Conclusion.....	89
Chapter 5	– Investigating the effects of polymers on single crystals using experimental methods	90
5.1	Chapter overview.....	90

5.2 Materials and Methods	90
5.2.1 Materials	90
5.2.2 Powder FFA and CBZ Co-crystals Preparation.....	90
5.2.2 Experimental methods.....	91
5.3 Results	94
5.3.1 AFM results	94
5.3.2 SEM experiments	95
5.3.3 Raman experiments.....	96
5.4 Discussion	97
5.5 Chapter conclusion.....	99
Chapter 6 - Investigating the influence of polymers on co-crystal dissolution using Molecular Modelling Techniques	100
6.1 Chapter overview.....	100
6.2 Molecular modelling methods.....	100
6.2.1 Single co-crystal morphology prediction and face indexing.....	100
6.2.1 Building of polymer using polymer builder.....	101
6.2.2 Building of crystal surface	103
6.2.3 Building polymer and crystal surface together.....	103
6.3 Results	105
6.3.1 Morphology prediction and face indices of co-crystals.....	105
6.3.2 Using MD simulation to identify the effect of polymers on co-crystal dissolution.....	107
6.4 Discussion	116
6.5 Chapter Conclusion.....	117
Chapter 7 - Influence of polymers on the diffusion coefficient of drug molecules using NMR techniques.....	118
7.1 Chapter overview.....	118
7.2 Materials and methods	118
7.2.1 Powder FFA and CBZ Co-crystals Preparation.....	118
7.2.2 NMR and DOSY Measurements.....	119
7.3 Results	120
7.3.1 ¹ H NMR Analysis of Binary Components	122
7.3.2 ¹ H NMR Analysis of Ternary Components	132
7.3.3 Diffusion coefficient.....	143
7.4 Discussion	153
7.5 Chapter conclusion.....	155

Chapter 8 – Investigating the influence of polymers on drug molecules in solution using Molecular Modelling Techniques.....	156
8.1 Chapter overview.....	156
8.2 Methods	157
8.2.1 Construction of simulation model.....	157
8.2.2 Dynamics simulations.....	158
8.2.3 Calculating properties.....	159
8.3 Results	160
8.3.1 Calculating the energy of API molecules.....	160
8.3.2 Calculating the kinetic properties of API molecules.....	163
8.4 Discussion	169
8.5 Chapter conclusion.....	170
Chapter 9 – Conclusion and future work.....	171
9.1 Conclusion.....	171
9.2 Future work.....	172
References.....	173
Appendix.....	200
A1 ATR-FTIR	200
A2 Atomic force microscopy.....	202
A3 Scanning electron microscope.....	203
A4 MD Simulations.....	204
A5 NMR Spectra	207
A6 DOSY Spectra	219
A7 Molecular dynamic simulations	239

Declaration

I declare that the work described in this thesis is original and was undertaken by myself for the Doctor of Philosophy degree, at the Doctoral college, Faculty of Health and Life Sciences, De Montfort University, Leicester, United Kingdom.

No part of the material described in this thesis has been submitted for the award of any other degree or qualification in this or any other university or college for advanced education.

Preyanthiny Kirubakaran

Acknowledgements

I would like to express my special appreciation and thanks to my Supervisor Professor Mingzhong Li. You have been a tremendous mentor for me and have supported me to the best of your ability. I would like to thank you for encouraging my research and for allowing me to grow as a research scientist.

Secondly, I wish to extend my thanks to my second supervisor Dr Richard Cross for his support with my PhD research and with the AFM equipment. I would like to thank all technicians in faculty of Health and Life Science for their technical support and professional advice for my research.

A special thanks to my family. Words cannot express how grateful I am for all of the sacrifices that you've made for me on my behalf. Thank you for funding my PhD and for helping me achieve my goals. Your constant support and prayers for me was what sustained me thus far and pushed me beyond my limits. I would also like to thank all my colleagues and friends, especially Dr Minshan Guo and Dr Manreet Kaur for supporting me through difficult times and in writing and encouraging me to strive towards my goal.

Publications

Journal publications

Preyanthiny Kirubakaran, Ke Wang, Ian Rosbottom, Richard Barrie Michael Cross, and Mingzhong Li, 'Understanding the effects of a polymer on the surface dissolution of Pharmaceutical Co-crystals using combined experimental and molecular dynamics simulation approaches', *Molecular Pharmaceutics*, 2020, 17, 2, 517-529. Impact factor = 4.57.

Awards

June 2017 – Winner of the 48th annual British Association of Crystal Growth conference poster competition.

The British Association for Crystal Growth was created in 1969 with the aim of bringing together researchers having an interest in crystal growth. The Association has held an annual conference each year since 1970. Every year many high-profile speakers are invited to give talks during the meeting. Representatives from all the major world-wide pharmaceutical companies have also been at this meeting to provide important networking potential which undoubtedly reinforces the high quality and interdisciplinary perspective of engineering research in the UK.

Conference poster presentations

- 1) 'Mechanistic understanding of co-crystal solubility and dissolution', University of Manchester, BACG 2017.
- 2) 'Mechanistic understanding of co-crystal solubility and dissolution', HLS poster competition, De Montfort University, 2017.
- 3) 'Use of Atomic force microscopy and molecular simulations to understand co-crystal solubility and dissolution', University of Limerick, BACG 2018.
- 4) 'Co-crystals: A way of improving the properties of medicines', HLS poster competition, De Montfort University, 2018.

- 5) 'A quality by design approach to understanding co-crystal solubility and dissolution', QBD symposium, De Montfort University, 2018.
- 6) 'Co-crystals: A way of improving the properties of medicines', QBD symposium, De Montfort University, 2019.
- 7) 'Understanding the effects of a polymer on the surface dissolution of Pharmaceutical Co-crystals using combined experimental and molecular dynamics simulation approaches', Royal college of Obstetricians and Gynaecologists, BACG 2019.
- 8) 'Co-crystals: A way of improving the properties of medicines', HLS poster competition, De Montfort University, 2019.
- 9) 'Use of NMR to investigate the component interactions in pharmaceutical co-crystal formulations', P.Kirubakaran, M.Kaur, M.Guo, HLS, De Montfort University, 2019.

Conference oral presentations

- 1) 'Mechanistic understanding of co-crystal solubility and dissolution', HLS student conference, De Montfort University, 2017.

Abstract

The purpose of this study is to improve the solubility, dissolution rate and permeability of poorly water-soluble drugs by understanding the mechanism of dissolution at molecular level of Flufenamic acid and Carbamazepine co-crystals in the presence of polymers. This study has been separated into four sections: (1) Formation of pharmaceutical co-crystals: Three pharmaceutical co-crystals of poorly water soluble active pharmaceutical ingredient (API) of Flufenamic acid (FFA) and Carbamazepine (CBZ) were synthesized, including 1:1 Flufenamic acid-theophylline co-crystal (FFA-TP CO), 1:1 Flufenamic acid-nicotinamide co-crystal (FFA-NIC CO) and 1:1 Carbamazepine-nicotinamide co-crystal (CBZ-NIC CO). The results of Fourier Transform Infrared spectroscopy (FTIR), Differential scanning calorimetry (DSC) and X-ray Powder Diffraction (XRPD) confirmed the formation of co-crystals. (2) The effect of polymers on the surface dissolution of co-crystals: The influence of three polymers (polyethylene glycol (PEG), polyvinylpyrrolidone (PVP), and a copolymer of N-vinyl-2-pyrrolidone (60%) and vinyl acetate (40%) (PVP-VA)) on the surfaces of FFA-TP CO, FFA-NIC CO and CBZ-NIC CO was studied using Atomic force Microscopy (AFM), Scanning electron microscopy (SEM) and Raman spectroscopy. It was found that the co-crystals have different dissolution mechanisms, and that addition of polymers can alter the dissolution properties of co-crystals by interacting with the crystal faces. (3) The molecular interactions between the drugs, co-formers and polymers were investigated using Nuclear Magnetic Resonance (NMR) and Diffusion Ordered Spectroscopy (DOSY). It was found that the type of a polymer, its concentration, and the interaction of the polymer with a co-former in solution will significantly affect the FFA and CBZ co-crystals (4). Molecular modelling of free drug molecules with co-formers and polymers in the presence of water molecules: Results indicate bulk precipitation could be occurring for FFA molecules in solution and that PVP-VA was an effective precipitation inhibitor for all three co-crystals studied in solution. Overall, PVP was an effective polymer for surface precipitation inhibitor and PVP-VA was the most effective inhibitor for precipitation in solution.

List of figures

Figure 1 - Biopharmaceutics classification system	23
Figure 2 - examples of homosynthons and heterosynthons.....	29
Figure 3 - Stages of designing a co-crystal.....	29
Figure 4 - The different methods used for creating pharmaceutical co-crystals	31
Figure 5 - Schematic representation of isothermal ternary phase diagram	32
Figure 6 - Spring and parachute model	43
Figure 7 - Structure of Flufenamic acid.....	44
Figure 8 - (a) below shows the bonding between FFA-TP CO. Figure (b) shows the packing interactions of the FFA molecules in the FFA crystal.	45
Figure 9 - Structure of Carbamazepine	46
Figure 10 - Structure of Nicotinamide	47
Figure 11 - Structure of Theophylline.....	47
Figure 12 - Structure of PEG	48
Figure 13 - Structure of PVP	49
Figure 14 - Structure of PVPVA.....	50
Figure 15 - Line search optimiser	57
Figure 16 - EnSpectr R532 Raman Spectrometry and the Raman effect	70
Figure 17 - AFM and Imaging Modes	72
Figure 18 - ATR-FTIR spectra of FFA-TP	81
Figure 19 - ATR-FTIR spectra of FFA-NIC	82
Figure 20 - ATR-FTIR spectra of CBZ-NIC.....	83
Figure 21 - DSC spectra of FFA-TP	84
Figure 22 - DSC spectra of FFA-NIC	85
Figure 23 - DSC spectra of CBZ-NIC.....	86
Figure 24 - XRPD spectra of FFA-TP	87
Figure 25 - XRPD spectra of FFA-NIC	88
Figure 26 - XRPD spectra of CBZ-NIC.....	89
Figure 27 - Peak to valley height measurement.....	92
Figure 28 - Raman spectroscopy results of the co-crystal surfaces before and after etching experiments.....	96
Figure 29 - Illustration of molecular dynamic procedure	104
Figure 30 - 2D DOSY spectra of FFA and PEG in CDCl ₃	151
Figure 31 - Simulation box containing FFA and water molecules after geometry optimisation.	157

List of tables

Table 1 - List of materials used in this study.....	63
Table 2 - DSC onset and peak values of FFA-TP.....	84
Table 3 – DSC onset and peak values of FFA-NIC	85
Table 4 - DSC onset and peak values of FFA-NIC.....	86
Table 5 - Predetermined time intervals of dissolution studies.....	91
Table 6 - AFM etching results of FFA-TP, FFA-NIC and CBZ-NIC co-crystal surfaces	94
Table 7 - SEM etching results of FFA-TP, FFA-NIC and CBZ-NIC co-crystal surfaces	95
Table 8 - Structure of polymers built using the polymer builder.....	102
Table 9 - The molecular structures, weights, and no. of monomers of co-crystals and polymers	102
Table 10 - Simulation box details on FFA-TP, FFA-NIC and CBZ-NIC.....	103
Table 11 - Predicted morphologies, surface and XRD comparison of single co- crystals.....	106
Table 12 - Snapshots of polymers on FFA-TP surfaces at 298k at 0, 10, 30, 60, 100 and 150ps.....	108
Table 13 - Snapshots of polymers on FFA-NIC surfaces at 298k at 0, 10, 30, 60, 100 and 150ps.....	110
Table 14 - Snapshots of polymers on CBZ-NIC surfaces at 298k at 0, 10, 30, 60, 100 and 150ps.....	112
Table 15 - Summary of polymer stabilisation time	113
Table 16 - Conformation of polymers on co-crystal surfaces at equilibrium at 298K and 200ps.....	113
Table 17 - Binding energy, hydrogen bonding, van der Waals and electrostatic attractions on co-crystal surfaces	114
Table 18 - Mean square displacement of a polymer on the crystal surface at equilibrium	115
Table 19 - Drug and structure with proton identification	120
Table 20 - Peak position and proton identification of the drugs.....	122
Table 21 - Singular and binary component NMR analysis of FFA, TP and NIC with 0.3mg/ml PEG, PVP or PVP-VA.....	123

Table 22 - Singular and binary component NMR analysis of CBZ and NIC with 0.3mg/ml PEG, PVP or PVP-VA.....	124
Table 23 - Singular and binary component NMR analysis of FFA, TP and NIC with 0.5mg/ml PEG, PVP or PVP-VA.....	125
Table 24 - Singular and binary component NMR analysis of CBZ and NIC with 0.5mg/ml PEG, PVP or PVP-VA.....	126
Table 25 - Singular and binary component NMR analysis of FFA, TP and NIC with 1mg/ml PEG, PVP or PVP-VA.....	126
Table 26 - Singular and binary component NMR analysis of CBZ and NIC with 1mg/ml PEG, PVP or PVP-VA.....	127
Table 27 - Summary of the peak shift differences in singular and binary components	129
Table 28 - Binary and ternary component NMR analysis of 1:1 FFA-TP and FFA-NIC with 0.3mg/ml PEG, PVP or PVP-VA.....	132
Table 29 - Binary and ternary component NMR analysis of 1:1 CBZ-NIC with 0.3mg/ml PEG, PVP or PVP-VA.....	134
Table 30 - Binary and ternary component NMR analysis of 1:1 FFA-TP and 1:1 FFA-NIC with 0.5mg/ml PEG, PVP or PVP-VA.....	134
Table 31 - Binary and ternary component NMR analysis of CBZ-NIC with 0.5mg/ml PEG, PVP or PVP-VA	136
Table 32 - Binary and ternary component NMR analysis of 1:1 FFA-TP and 1:1 FFA-NIC with 1mg/ml PEG, PVP or PVP-VA.....	136
Table 33 - Binary and ternary component NMR analysis of 1:1 CBZ-NIC with 1mg/ml PEG, PVP or PVP-VA.....	138
Table 34 - Summary of peak shift differences of binary and ternary components....	139
Table 35 – Singular, binary, and ternary components FFA-TP, FFA-NIC and CBZ-NIC with 0.3mg/ml PEG, PVP or PVP-VA.....	143
Table 36 - Singular, binary, and ternary components FFA-TP, FFA-NIC and CBZ-NIC with 0.5mg/ml and 1mg/ml PEG, PVP or PVP-VA.....	146
Table 37 - Summary of Diffusion coefficient corresponding to the H _j peak of FFA ..	149
Table 38 - Summary of Diffusion coefficient corresponding to the H _a peak of CBZ	150
Table 39 - Simulation of FFA-NIC, PEG and Water at 0, 10, 20, 30 and 50ps	158
Table 40 - Total energy, van der Waals and electrostatic interactions of API at the start of the production run in the presence of PEG, PVP and PVP-VA.....	161

Table 41 - Total energy, van der Waals and electrostatic interactions of API at the end of the production run in the presence of PEG, PVP and PVP-VA.....	161
Table 42 - Summary of total energy, van der Waals and electrostatic interactions of API at the end of the production run in the presence of PEG, PVP and PVP-VA	162
Table 43 - The evolution of bond lengths of FFA molecules at various time intervals in a 50ps production run.....	164
Table 44 - Length evolution and length distribution of APIs with/without polymers over a 50ps production run.....	166
Table 45 - Mean square displacement and radial distribution functions of API molecules.	167

List of equations

Equation 1 - Total potential energy	53
Equation 2 - Valence cross terms.....	53
Equation 3 - Non-bond interactions.....	53
Equation 4 - COMPASS analytical expression.....	54
Equation 5 - Newton's equation of motion.....	58
Equation 6 - The Verlet velocity algorithm.....	59
Equation 7 - NVT Ensemble	60
Equation 8 - Nosé-Hoover dynamics	60
Equation 9 - NVE Ensemble.....	61
Equation 10 - Bragg's Law.....	68
Equation 11 - NMR chemical shift	74
Equation 12 - Diffusion coefficient by Wilke and Chang	75
Equation 13 - Binding energy	76
Equation 14 - Electrostatic interaction	76
Equation 15 - Van der Waals interactions	77
Equation 16 - Hydrogen bond	77
Equation 17 -Radial distribution function.....	78
Equation 18 - Mean square displacement.....	79
Equation 19 - Surface Roughness (Ra).....	92

Abbreviations

¹ H NMR	One Dimensional Proton Nuclear Magnetic Resonance
AFM	Atomic Force Microscopy
API	Active Pharmaceutical Ingredient
ATR-FTIR	Attenuated Total Reflectance-Fourier Transform Infrared Spectroscopy
BCS	Biopharmaceutics classification system
BFDH	Bravais-Friedel-Donnay-Harker
CBZ	Carbamazepine
CBZ-NIC	Carbamazepine - Nicotinamide
CCF	Co-crystal co-former
CCX	Celecoxib
CD	Cyclodextrin
CDCl ₃	Deuterated chloroform
CMC	Critical micelle concentration
CSD	Cambridge structural database
CUR	Curcumin
DOSY	Diffusion ordered spectroscopy
DPP	Dissolution performance parameter
FDA	Food and drug administration
FFA	Flufenamic acid
FFA I	Flufenamic acid form I
FFA III	Flufenamic acid form III
FFA-NIC CO	Flufenamic acid – nicotinamide co-crystal
FFA-TP CO	Flufenamic acid – theophylline co-crystal
FTIR	Fourier Transform Infrared Spectroscopy
GI	Gastrointestinal
GO	Geometry optimized
HPH	High pressure homogenization
HPMC	Hydroxypropyl methylcellulose
IND-SAC	Indomethacin-saccharin
MD	Molecular dynamics

MSD	Mean square displacement
NIC	Nicotinamide
NPH	Constant number of molecules, pressure and enthalpy
NPT	Constant number of molecules, pressure and temperature
NVE	Constant number of molecules, volume and energy
NVT	Constant number of molecules, volume and temperature
PEG	Polyethylene glycol
PFGSE	Pulsed field gradient spin echo
PVP	Polyvinylpyrrolidone
PVP-VA	Copolymer of N-Vinyl-2-Pyrrolidone (60%) and Vinyl Acetate (40%)
RDF	Radial distribution function
RESS	Rapid expansion of supercritical solutions
SCF	Supercritical fluid
SD	Solid dispersion
SEM	Scanning electron microscope
SLS	Sodium Lauryl Sulphate
SMPT	Solution Mediated Phase Transformation
SSNMR	Solid state nuclear magnetic resonance spectroscopy
TP	Theophylline
TPD	Ternary phase diagram
TSE	Twin screw extrusion
UV	Ultraviolet
VA	Vinylacetate
vdW	van der Waals
VP	Vinylpyrrolidone
XRD	X-Ray diffraction
XRPD	X-Ray Powder Diffraction

Chapter 1: Introduction

1.1 Research Background

One of the major and common problems encountered by pharmaceutical industries are poor biopharmaceutical properties of drugs including low solubility, dissolution rate and intestinal permeability of drugs [1]–[4]. Majority of the new chemical entities developed in the pharmaceutical industries, 40% of existing drug products and up to 90% of new chemical entities, are insoluble in water. Poorly water soluble drugs lead to slow drug absorption and therefore inadequate and variable bioavailability [5]–[7]. Poorly water soluble drugs therefore require higher doses to produce a therapeutic effect [8].

A key challenge to successfully developing new medicines is to enhance the solubility and dissolution rates of poorly soluble drugs in order to increase the bioavailability [9],[7]. This therefore provides a driving force to developing new approaches to designing new chemical entities with increased bioavailability such as salt formation, solid dispersion, particle size reduction, high pressure homogenisation and complexation [10]–[12]. Pharmaceutical co-crystals have been recognised as an alternative approach to provide new stable forms of drugs [3], [13]. As well as increased solubility and bioavailability, pharmaceutical co-crystals also provide various advantages such as improved stability, flowability and compressibility due to the different crystal structure of the co-crystals [8]. An exponential increase has been seen in the past decade on research in co-crystal structure and applications which is evident in the number of co-crystal structures deposited in the Cambridge Structural Database and co-crystal related patent applications [14].

A key limitation to this alternative approach however, is that a stable form of the drug is recrystallized during the dissolution of the co-crystals [7]. This leads to the loss of newly improved drug properties. To inhibit the recrystallization of the drug in aqueous solution, the effects of various polymers of different concentrations on the phase transformations and release profiles of co-crystals has been studied and has proven to be effective [4], [10], [11], [15]–[19]. Currently, only a small amount of study has been contributed into researching co-crystals and even less research into studying the interaction of polymers with co-crystals at molecular level using a combination of experimental and molecular dynamic methods.

This study probes into details of the molecular interactions of polymers of Polyethylene glycol (PEG), Polyvinyl pyrrolidone (PVP) and polyvinyl pyrrolidone-vinyl acetate (PVP-VA), on the co-crystals of Flufenamic acid-Theophylline (FFA-TP), Flufenamic acid-Nicotinamide (FFA-NIC) of Carbamazepine-Nicotinamide (CBZ-NIC) during surface dissolution and in solution. Atomic force microscope and scanning electron microscope were used to compare the etching patterns of different polymers followed by molecular dynamic methods used to calculate van der Waals and electrostatic interactions. Nuclear Magnetic Resonance (NMR) and Diffusion Ordered Spectroscopy (DOSY) was used to calculate the diffusion coefficient of each of the different combinations of co-crystals with polymers.

1.2 Research aims and objectives

The aim of this study is to investigate the effect of various polymers on the dissolution and phase transformation of single co-crystals of Flufenamic acid and Carbamazepine. Interactions of polymers on the surfaces of crystals will be studied at molecular level by a combination method of non-contact AFM, SEM, Raman and molecular modelling techniques. Interactions of drug molecule, co-former and polymer in solution will be studied by using both Nuclear Magnetic Resonance (i.e., ^1H NMR and DOSY) and molecular modelling methods.

Objective 1: Review of pharmaceutical co-crystals definition, synthesis methods and characterization techniques. Review of molecular modelling and exploring the advantages and disadvantages of this technique.

Objective 2: Synthesis of crystals, co-crystals, and single co-crystals of Flufenamic acid I (FFA), 1:1 Flufenamic acid-nicotinamide co-crystal (FFA-NIC CO), 1:1 Flufenamic acid-theophylline co-crystal (FFA-TP CO), Carbamazepine III (CBZ), 1:1 Carbamazepine-Nicotinamide (CBZ-NIC). Characterize these samples by using FTIR, DSC and XRPD.

Objective 3: Use of non-contact Atomic force microscopy (AFM), Raman spectroscopy and Scanning electron microscope (SEM) to investigate the influence of polymers on the surface of single co-crystals in solution in the absence or presence of polymers.

Objective 4: Understand the dissolution mechanisms and interactions of co-crystals in solution in the absence and presence of pre-dissolved polymers at molecular level by using molecular modelling techniques.

Objective 5: Apply one dimensional proton nuclear magnetic resonance (^1H NMR) and Diffusion ordered spectroscopy (DOSY) to study the interaction between API, co-formers, and polymers in solution. Molecular modelling techniques will also be used to explore further the interactions between the different components in the system.

1.3 Thesis structure

This thesis will be presented in 9 chapters as follows:

Chapter 1 will include a brief research background to the topic, research aims and objectives and the structure of the thesis.

Chapter 2 will explore the biopharmaceutical classification system, methods for enhancing dissolution of poorly water-soluble drugs, crystallisation, single co-crystals, Flufenamic acid co-crystals, Carbamazepine co-crystals, molecular modelling and molecular dynamics and the chapter conclusion.

Chapter 3 will present the materials and methods used, preparation and synthesis for both experimental and computational methods and chapter conclusion.

Chapter 4 will contain samples characterisation of all pure drugs, co-crystals and single co-crystals by use of ATR-FTIR, DSC and XRD followed by the chapter conclusion.

Chapter 5 will explore the surface dissolution of single co-crystals in the presence/absence of polymers in solution by the use of non-contact AFM, Raman spectroscopy and SEM to detect any surface change. The polymers that will be used in this study are PEG, PVP and PVP-VA. Recrystallisation on the surfaces will be discussed here followed by the chapter conclusion.

Chapter 6 will look at interaction of polymers on surfaces of single co-crystals by using computational methods. Cambridge structural database (CSD) will be used to predict morphology of the single co-crystals in order to gather information on the face index. Forcite module in Materials studio will be used to build the surface and the polymer system followed by running molecular dynamics in order to investigate the interactions between the different polymer and crystal surfaces. The interaction energies and mean square displacement will be calculated and discussed followed by the chapter conclusion.

Chapter 7 will explore the interactions of drug-drug, drug-polymer and co-former-polymer in solution by investigating the chemical shifts of the characteristic peaks in the presence of polymers using NMR spectroscopy. Diffusion coefficient of the drug, co-former and polymer molecules will also be calculated using DOSY.

Chapter 8 will explore the interactions of free drug molecules, co-former molecules, and monomers in the presence of water molecules using molecular modelling techniques. Amorphous cell module in materials studio will be used to construct the system and Forcite will be used to run molecular dynamics. The interaction energies, length evolution and distribution, mean square displacement and radial distribution function will be calculated and discussed followed by the chapter conclusion.

Chapter 9 will present the conclusions of this study followed by future studies.

Appendix will present the additional and supplementary information related to each of the chapters.

Chapter 2 – Literature review

2.1 Chapter review

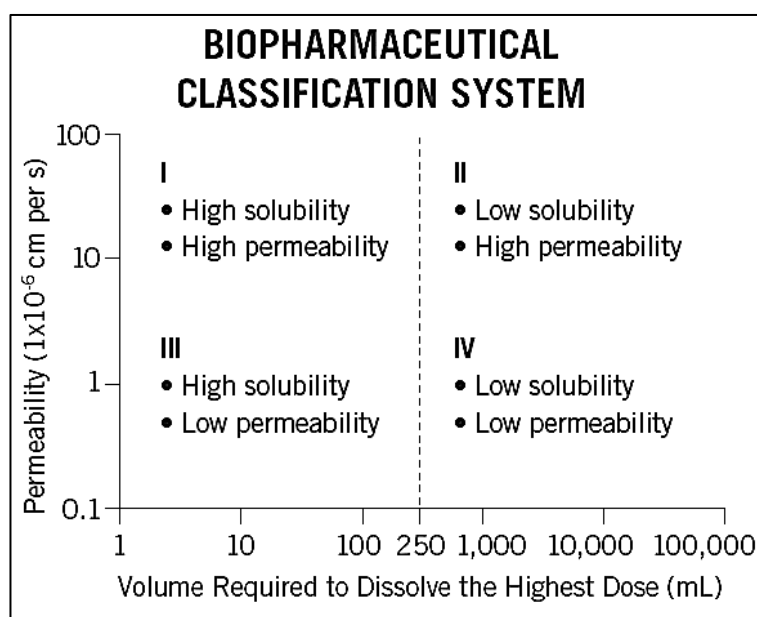
In this chapter, an introduction of the current approaches for improving the bioavailability of poorly water-soluble drugs are explored. This is followed by a comprehensive introduction and understanding of pharmaceutical co-crystals including co-crystals definition, co-crystals design mechanisms, co-crystals formulation methods and physicochemical properties and characterisation techniques. Following that, the problems encountered by co-crystals during the formulation phase are discussed such as solution mediated phase transformation and ways to overcome this challenge. The basic information about the materials used in this study is introduced, including FFA, NIC, TP, FFA-TP, FFA-NIC, CBZ, CBZ-NIC, PEG, PVP and PVP-VA. Finally, the molecular modelling and molecular dynamics are explored such as forcefields, geometry optimisation, dynamics and calculated properties.

2.2 Biopharmaceutics classification system (BCS)

Biopharmaceutical classification system (BCS) introduced into the Food and Drug Administration (FDA) has provided a mechanistic framework into differentiating drug absorption in terms of solubility and permeability [20]–[23]. All Active pharmaceutical ingredients (APIs) are classified using this framework during drug development, and helps in identifying the drugs that should not be clinically tested unless formulation strategies are put into place to enhance the solubility and permeability [24], [25]. This makes BCS a fundamental system in the development of oral drug products. If the highest strength of a drug is soluble in 250ml or less aqueous media over 1 – 7.5 pH, the drug is considered highly soluble [26]. Otherwise, the drug is considered poorly soluble.

The different classifications of drugs in BCS, along with their solubility, permeability and absorption pattern are given in the figure below.

Figure 1 - Biopharmaceutics classification system



The high permeability and high solubility of Class 1 compounds allows high concentrations of the drug in the gut to saturate both efflux and uptake transporters. In-vitro-in-vivo correlation is expected if the dissolution rate is faster than the gastric emptying rate [26]. Dissolution and bioavailability of the drug are not rate limited. Class 2 drugs are likely to have the bioavailability to be dissolution rate limited. This therefore makes the class 2 drugs the focus for solubility enhancement studies due to their high permeability and consequently several approaches have been developed [20], [27]. For class 3 drugs, the bioavailability is permeability rate limited, therefore, in order to improve permeability, absorption enhancers are added in the formulation of the drug products [23], [26]. For class 4 drugs, bioavailability is limited by both dissolution and permeability. Enhancing solubility and dissolution alone might not help improve bioavailability. Poor solubility of these compounds can be overcome by new approaches to drug development which will be discussed in the next chapter along with solubility enhancers such as polymers and surfactants.

2.3 Enhancing dissolution for poorly water-soluble drugs

Factors such as first-pass metabolism, chemical stability, transport, solubility, and dissolution can limit the oral bioavailability of drugs in the body [28]. This can be overcome by chemically modifying the molecule to improve its bioavailability. However, this approach can result in significant alterations to the biological interactions of that molecule [29]. Therefore, modifying the bioavailability of a molecule is an attractive alternative but have only been slightly successful. Compounds with poor solubility are eliminated from the GI tract before they can fully dissolve and be absorbed into the blood stream [30], [31]. This results in low and irregular bioavailability and poor dose proportionality. Some of the methods for enhancing the solubility of poorly soluble molecules are mentioned below.

2.3.1 Particle size reduction

Particle size reduction is a promising approach to improve the invitro-dissolution of insoluble drugs [28], [32], [33]. When the surface area of particles is increased, this in turn increases a drug's dissolution rate. Reducing the size of the particles therefore, is a method of increasing the bioavailability of drugs as the surface area is increased and the thickness of the diffusion layer is decreased [31]. Mechanical techniques to decrease the particle size of solids are classified in three categories: dry-milling, wet-milling, and high-pressure homogenization. Particles that need to be produced in the submicron (nano) range are produced by using techniques such as wet-media milling, piston-gap homogenization, and micro-fluidisation [34].

Jinno *et al.* studied the effect of particle size reduction on dissolution and oral absorption of a poorly water-soluble drug, cilostazol, in beagle dogs. Using hammer-milled, jet-milled and nanocrystal spray drying techniques, three different suspensions of different particle sizes were prepared. Their research showed an increase in dissolution rate and bioavailability with a reduction of particle size [32].

The most current research on particle size reduction has focused on a combination of two techniques, bottom-up and top-down [35]–[37]. The first process, bottom-up, produces drug nanocrystals by precipitating dissolved molecules. The second process, top-down, involves particle size reduction [38]. This combinative method was developed to improve the particle size reduction effectiveness of the standard techniques.

2.3.2 Supercritical Fluid (SCF) Process

SFC is a novel nanosizing and solubilisation technology for the reduction of particle size. Supercritical fluids are fluids whose temperature and pressure are greater than its critical temperature and critical pressure [39]–[42]. This asset allows the fluid to have the properties of both a liquid and a gas. At near-critical temperatures, SCFs are highly compressible and so can be used to pressurise a reactor containing drugs and polymeric excipients [41]. Once the drug particles are solubilised within the SCF, they are then recrystallised as smaller particles which improves the solubility and bioavailability. Carbon dioxide is the most widely used medium due to its low values of critical temperature (31.0°C), pressure (72.8 atm) and environmental pollution [40]–[42].

SCF processes have been successfully applied for dissolution enhancement of Carbamazepine and Indomethacin. Moneghini applied SCF for the processing of Carbamazepine–PEG 4000 solid dispersions and Gong applied SCF for the formation and characterization of porous Indomethacin-PVP Co-precipitates [43], [44]. Kazarian researched the applications of supercritical fluids for polymer processing and found supercritical carbon dioxide to swell and plasticize polymers, which is crucial to the impregnation, extraction, and modification of polymeric materials. This in turn reduced the viscosity and facilitated the processing of polymers due to lower shear stresses [42].

2.3.3 Cyclodextrin complexation

Cyclodextrins (CDs), are a group of oligosaccharides which are formed by glucose units binding together in a ring. Cyclodextrins can potentially increase the oral absorption of poorly water-soluble API by forming inclusion complexes [28], [45]–[47].

Cyclodextrins can form complexes with drug molecules and improve their physicochemical properties without changing their structure. Cyclodextrins have a hydrophobic cavity interior with a hydrophilic exterior surface and they act as true carriers by dissolving and delivering hydrophobic drug molecules through the aqueous exterior of lipophilic biological membrane barriers [45]. Examples of such tablet formation include Cephalosporin, Chlordiazepoxide and Omeprazol [48].

Various research has taken place in order to understand the complexes, mechanisms and its properties to improve the solubility of insoluble drugs.

Wang applied cyclodextrin complexations to enhance stability and non-invasive pulmonary delivery of Resveratrol, a drug used for lung cancer treatment. Stability studies at pH 7.4 and in plasma indicated significant improvement in RES stability after complexation, with a much longer half-life [49].

2.3.4 Solid dispersion

Among the methods to improve bioavailability, solid dispersion (SD) is one of the most potent and successful methods. A solid dispersion is a drug–polymer two-component system consisting of a hydrophilic matrix containing a hydrophobic drug. In solution, polymeric micelles are nanoscopic (>100 nm) structures that form, above a certain concentration named the critical micelle concentration (CMC) [50]–[52]. They are formed when amphiphilic block copolymers composed of hydrophilic and hydrophobic chains self-assemble in water [51]. This results in enhanced surface area, leading to higher drug solubility and dissolution rate and therefore enhanced drug bioavailability. Enormous studies have shown that solid dispersion can enhance the drug release rate [2], [5], [53], [54].

Onoue *et al.* designed efficacious formulations of curcumin, including nanocrystal solid dispersion (CSD-Cur), amorphous solid dispersion (ASD-Cur), and nanoemulsion (NE-Cur), to improve the physicochemical and pharmacokinetic properties. Their research showed significant improvement in pharmacokinetic behaviour in the newly developed formulations. ASD-Cur, CSD-Cur and NE-Cur showed a 12 fold, 16 fold and 9 fold increase of oral bioavailability respectively [55].

Yan *et al.* prepared novel valsartan-loaded solid dispersions with water, hydroxypropyl methylcellulose (HPMC) and sodium lauryl sulphate (SLS). The drug-loaded solid dispersion composed of valsartan/HPMC/SLS improved the drug solubility by 43 folds [56].

2.3.5 High pressure homogenisation

High pressure homogenization (HPH), is a technique widely used for the preparation of nano-suspensions of drugs that are poorly soluble in water [34], [36], [38]. HPH has been known to improve the solubility of poorly soluble drugs such as budesonide and omeprazole by effectively reducing the size to the nano-size range [31]. The poorly soluble drug is first dispersed in a suitable fluid, followed by being forced under pressure through a nano-sized hole (0.1-2mm) of a high-pressure homogeniser [57]. The suspension is passed through with a high velocity which follows a sudden pressure drop and turbulent flow conditions which reduces the size of the particles into fragments via collision [38]. The size of particles can be reduced from approximately 30 μ m to 5 μ m [58]. Depending on the instrument available, the operating pressure for HPH ranges from 10 to 500 MPa [59].

2.3.6 Pharmaceutical co-crystals

Co-crystals are supramolecular systems in which one component is a poorly soluble active pharmaceutical ingredient (API) and the second component (co-former) is a readily soluble compound fully digested in the body and involved in enzymatic reactions. Co-formers are readily soluble substances which are recommended for use in the food and pharmaceutical industries [60].

Pharmaceutical Co-crystals have attracted a lot of interest in recent years as a potential method to improve the bioavailability of low soluble drugs by forming intermolecular interaction between the API and highly soluble co-formers by the formation of hydrogen bonding, $\pi \cdots \pi$ stacking interactions and van der Waals forces [3], [13], [61]. Co-crystals address the problems of poorly water soluble drugs by improving the dissolution and bioavailability rates [3], [13]. They are of an interest to the pharmaceutical industries due to their offering of a diverse range of solid-state forms for APIs that lack ionisable functional groups [61]. The crystals contain two or more molecules arranged in order, to create a new crystal that is superior to the parent molecule. The co-crystals differ from traditional solid-state API as the co-crystals are formed between a drug molecule and co-crystal former known as a co-former and are arranged in a crystal lattice. The components in a co-crystal are in a neutral state and interact via non-ionic interactions. A single co-crystal is a solid in which the crystal lattice of the entire sample is continuous and

unbroken to the edges of the sample and contains no grain boundaries. Formation of API as co-crystals greatly improves the bioavailability, stability and manufacturing properties when compared to the parent crystalline drug of the same form [8].

A wide range of co-formers are available to form co-crystals using APIs with low solubility in order to improve or maintain the solubility as compared to the parent drug [8]. Co-crystals with low solubility are not desirable for BSC II drugs as they require an improvement in the solubility and bioavailability. Co-crystals with a high solubility are also not desirable as they undergo a phenomena called solution mediated phase transformation [3]. Desirable cocrystals should have adequate solubility with a high bioavailability.

Currently research in co-crystallisation is focussed on co-former selection. Very limited work has been carried out to identify a co-former that can form co-crystal with the desired in vivo and in vitro properties. The co-former selection rule that has been followed is that the solubility of the co-former should be approximately 10 times higher than the API.

2.4 Pharmaceutical co-crystals

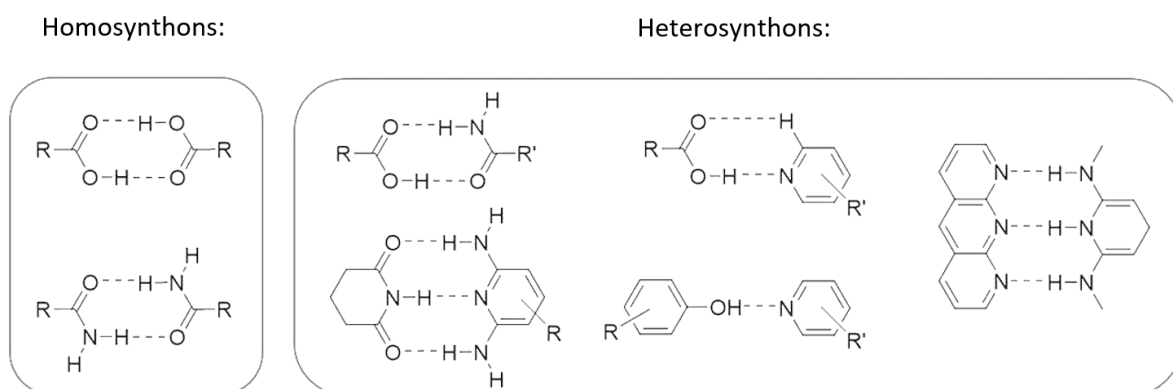
2.4.1 Co-crystal design mechanism

Co-crystal screening is a crucial part of the overall process of investigating multicomponent structures. The compound of interest needs to be screened against a variety of co-crystal formers in order to discover new co-crystals which will then be characterised [14], [62]. The design of co-crystals involve the construction of solid crystals with acceptable physical properties with respect to supramolecular structure assemblies [63].

The synthesis of new co-crystals is mostly affected by the nature of solvent and the reactants. For example, the presence of functional groups, the solubility of reactants in the solvent and the experimental conditions such as the stoichiometric ratio of the co-former and API, temperature, stirring and pH [14], [64], [65]. The bioavailability and chemical stability of co-crystals are dependent on the non-covalent interactions in the crystal structures such as hydrogen bonding, van der Waals interactions, π - π stacking and electrostatic interactions [66], [67].

To design co-crystal systems, the rules of hydrogen bonding, supramolecular synthons, and graph sets could be used. Successful formation of hydrogen bonds between two molecules involves designing appropriate donor and acceptor moieties that will engage in the interaction. A common approach is to use supramolecular synthons, which exist as homosynthons or heterosynthons [68], [69]. Synthons are defined as 'structural units within a molecule that can be assembled using known synthetic operations' [70]. Using this strategy, hydrogen bonding between functional groups can be predicted and co-crystal structures can be proposed. Homosynthons contain identical functional groups that exhibit molecular complementarity, and they are often deemed 'self-association motifs' and heterosynthons contain non-identical functional groups, but they also exhibit molecular complementarity [71]. The figure below shows examples of synthons based on hydrogen bonds: homosynthons and heterosynthons.

Figure 2 - examples of homosynthons and heterosynthons



There are several stages for designing, formation and testing an ideal pharmaceutical co-crystal. This can be broken down into steps as shown in the diagram below.

Figure 3 - Stages of designing a co-crystal



A widely used strategy in crystal engineering is to first investigate the crystal structure of the target API and to evaluate which non-covalent interactions could

aid in the formation of new supramolecular synthons between the target API and co-former [72].

Because co-crystallisation experiments can be time consuming, computational techniques based on molecular modelling [73]–[75] molecular descriptors [76], [14], and hydrogen bond propensity [77] have been developed to steer the search for new co-crystals. These approaches have succeeded in broadening the understanding of the principles behind co-crystallisation.

2.4.1.1 Co-former selection

Co-former selection is a crucial step in the design of pharmaceutical co-crystals as the different physicochemical properties of selected co-formers play a part in the in-vivo properties of the produced co-crystals. The Cambridge Structure Database (CSD) and “supramolecular synthon approach” was applied to effectively screen suitable co-formers for co-crystal development [78]. Although the design strategy was accelerated by using both these approaches, prediction of the physicochemical properties of the resulting co-crystals remained challenging [79].

Much research has gone into selection of suitable co-formers for improved co-crystals [80]–[82]. Tomaszewska studied the importance of in-vivo conditions and the type of co-former for Carbamazepine saccharin (CBZ-SAC) and Carbamazepine-nicotinamide (CBZ-NIC) and concluded that the characteristics of the co-former define a critical variable for dissolution of pharmaceutical co-crystals with important implications for their in vivo performance [83].

2.4.2 Co-crystal formation methods

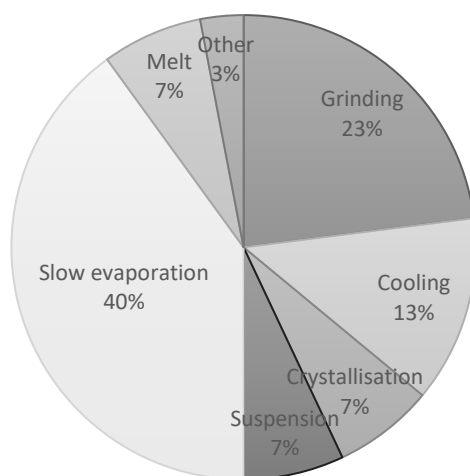
A wide range of successful co-crystal preparation methods have been documented over the years such as solvent evaporation [54], [84], solid state grinding [85], solution crystallization [86],[87], slurry conversion [14], melt crystallization [88], hot melt extrusion [16], and spray crystallization [89]; with slow evaporation from solution being the most common technique [60].

For the solvent-based methods, the selection of the solvent is crucial since a suitable solvent alter the intermolecular interactions and potentially lead to better crystallisation results. Other methods may also have limitations [90], such as:

- Thermal methods that require melting needs high temperatures and can affect the stability of heat-sensitive compounds.
- Mechanical methods, such as grinding can produce amorphous materials, limiting their effectiveness if a suitable solvent is not used.
- Methods based on precipitation from solution require continuous and precise control of the supersaturation level of the components' concentration. The use of a solvent is also not environmentally friendly.

Figure 4 - The different methods used for creating pharmaceutical co-crystals

Design of Pharmaceutical co-crystals



2.4.2.1 Solution based methods

The most conventional method used for crystal formation is the use of suitable solution with proper degree of supersaturation. The supersaturation of a solution is the driving force for crystallization. There are two concentrations to consider within the co-crystal system: the API concentration and the conformer concentration. These concentrations in relation to the co-crystal solubility is what dictates the supersaturation for co-crystallisation [14], [91].

Eutectic points offer an experimentally accessible method to assess co-crystal solubility and stability regardless of the solubility relationship between co-crystal and drug. A co-crystal eutectic point is a point where two solids, API and conformer, and a solution coexist in equilibrium [81].

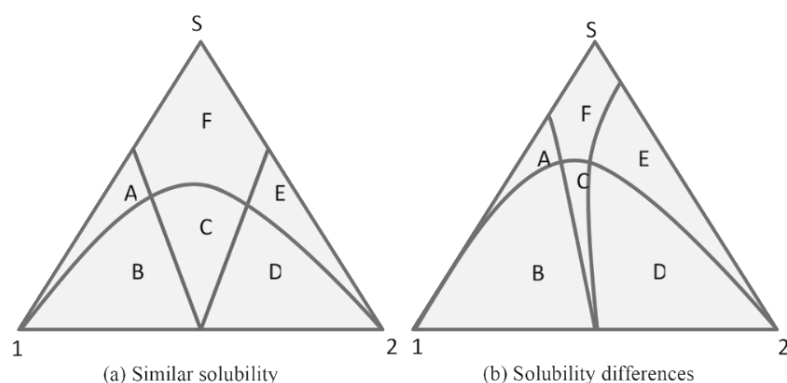
Eutectic points will exist for the system where at one fixed solution concentration:

- (i) The co-crystal and the target molecule are stable.
- (ii) Mixture of the co-crystal and conformer are present.

The eutectic point represents the solution minima; if the solvent content is low, solubility will be high. The co-crystal will only be stable at concentrations that lie between the eutectic points. Knowledge of this concentration range is key to designing a successful solution co-crystallisation process. Operation outside of this range can fail to yield a co-crystal or can yield a mixture in the solid phase such as co-crystal and co-former [92].

The behaviour of a mixture of two crystalline compounds and a solvent can be visualized and explained by using ternary phase diagram [87]. The ternary phase diagram (TPD) shown below represents the solubility of a co-crystal system in each given solvent at a fixed temperature and pressure.

Figure 5 - Schematic representation of isothermal ternary phase diagram



(a) Similar solubilities between API and co-former (1 and 2) in solvent S and (b) different solubilities of 1 and 2 in S [14].

When A and B form a compound AB of stoichiometry 1:1, the ideal solubility of AB is represented by C in the TPD. The TPD contains six regions: (A) $A_{\text{cocystal}} + \text{solution}$,

solid A is in equilibrium with solution; (B) $A_{\text{cocrystal}} + AB_{\text{cocrystal}} + \text{solution}$, solid A and AB (cocrystal) are in equilibrium with solution; (C) $AB_{\text{cocrystal}} + \text{solution}$, solid AB is in equilibrium with solution; (D) $B_{\text{cocrystal}} + AB_{\text{cocrystal}} + \text{solution}$, solid B and AB are in equilibrium with solution; (E) $B_{\text{cocrystal}} + \text{solution}$, solid B is in equilibrium with solution; (F) Solution (A+B+AB), A or B and AB are completely dissolved in the solvent [93].

In Figure 6 (a) the solubility of A and B are similar in solvent and therefore solution crystallization with equimolar reactants will result in a 1:1 AB co-crystal by solvent evaporation. Components with non-equivalent solubility in solvent in shown in figure 6(b) where the resulting co-crystal formed by solvent evaporation may lead to producing the pure starting crystalline materials, or mixture of co-crystals and co-formers [94].

Evaporative crystallization

The most common method of solution crystallisation is evaporative crystallisation. This method involves the nucleation and growth of a co-crystal from a solution consisting of both co-formers and API in a solvent [64]. The supersaturation of the solution is provided by the removal of the solvent from the solution via evaporation. A slow rate of evaporation is usually desired to form a smaller number of larger crystals as opposed to a high number of smaller crystals. Once the crystals are formed, they are harvested and dried [95].

The biggest challenge to evaporative crystallisation is the reproducibility and homogeneity which can prove difficulties due to a lack of control over crystallisation conditions such as nucleation and growth [66].

Cooling crystallisation

Cooling crystallisation has drawn a lot of attention due to its potential for large scale co-crystal production [79]. In cooling crystallisation, the temperature of the crystallisation system is varied by firstly heating the mixture containing drug, co-former and solvent to high temperatures, followed by the cooling down step. Co-crystals will precipitate when solution becomes supersaturated as the temperature drops down. Cooling crystallisation is the preferred choice currently for industrial crystallisation of pharmaceuticals as it can provide more control over the production of co-crystals [66].

Fucke screened piroxicam against 20 different co-formers and found that the cooling experiments - fast and slow – resulted in 39 crystalline products of which 21 could be identified as co-crystals [96].

The co-crystal formation rate of Theophylline-benzoic acid by monitoring it using on-line Raman spectroscopy was investigated by Yaohui Huang. The nucleation time, nucleation temperature and cooling ending point can be gained from results of on-line Raman monitoring [97].

2.4.2.2 Solid state formation methods

Solid state formation of pharmaceutical co-crystals has attracted great interest due to the advantages provided by these processes. They are synthesised in the absence of solvents or by using very small amounts, have excellent purity and quality and provide a high throughput with fast processing times [64].

The grinding methods

Solid state grinding is an alternative synthetic method to solution-based co-crystallization process. The reduction of particle size is carried out in the mixture which in turn increases the covalent reactivity [63], [64], [98].

Solvent drop grinding involves grinding two materials together i.e., solid-state grinding with incorporation of small quantity of solvent. The solvent used will act as catalyst. Fucke compared three different methods: crystallisation from the melt, from solution and solvent-drop grinding for the co-crystal formation of piroxicam with 20 different co-crystals and found that solvent-drop grinding showed the highest absolute number of experiments resulting in co-crystals [96].

Hot melt extrusion

Hot melt extrusion is a manufacturing process which has significant potential in continuous pharmaceutical manufacturing process [99]. Hot melt extrusion involves the formation of co-crystals by use of highly efficient mixing and improved surface contacts of materials. Solvent drop extrusion technique can also be used to

optimize and make the process more flexible as well as aid in carrying out the process in lower temperatures.

Liu investigated the chemical stability of CBZ-NIC co-crystals and found that preparation of CBZ-NIC CO by hotmelt extrusion significantly depresses the processing temperature (190°C to 160°C) and thus minimises the thermal degradation of the heat-sensitive drug [100].

2.4.2.3 Other methods

Alhalaweh and Velega studied the formation of Co-crystals from stoichiometric solutions of incongruently saturating systems of 6 different co-crystals by spray drying and found that pure co-crystals were formed in comparison to solvent evaporation [101]. Ober and Gupta formed co-crystals of Itraconazole-succinic acid by gas antisolvent crystallisation method and found that the co-crystals remained stable for up to 4 weeks against thermal stress [102].

Chow formed co-crystals of Ibuprofen and Flurbiprofen with Nicotinamide through rapid solvent removal using rotary evaporation and found that co-crystallisation with nicotinamide can simultaneously improve tableting behavior, hygroscopicity, and dissolution performance of ibuprofen and flurbiprofen [62].

Müllers investigated the formation and micro-ionisation of ibuprofen-nicotinamide co-crystals by rapid expansion of supercritical solutions (RESS) using CO₂ and found that the surface area of the co-crystals increased by a tenfold in comparison to co-crystals formed by the slow evaporation method. This in turn decreased the mean evaporation time. RESS offers an advantage of combining micro-ionisation and co-crystallisation for drugs with dissolution limited bioavailability [84].

Daurio investigated the application of twin-screw extrusion (TSE) as a scalable and green process for the manufacture of co-crystals of Caffeine-Oxalic acid, Nicotinamide-trans cinnamic acid, Carbamazepine-Saccharin, and Theophylline-Citric acid. TSE resulted in being an effective method to make co-crystals for all four systems studied [103].

Many techniques as mentioned above are capable of producing co-crystals. However, a challenge remains in the control of the nucleation, crystallisation and the phase evolution of the co-crystals [104], [105]. Although many technological improvements have been made, the underlying mechanisms of co-crystal formation

is still not fully understood [102]. Therefore, many efforts have been put into understanding the underlying mechanism of these techniques. Techniques that probe a reacting system in situ are preferred and remain experimentally challenging.

Mandala reported a solid-state in situ NMR study of the spontaneous formation of a co-crystal between the API caffeine and co-former malonic acid. The study found that during the reaction, the technique provided subtle clues to the mode of mass transfer that underlies co-crystal formation [106].

2.4.3 Properties

Salt formation is currently one of the primary solid-state approaches used to modify the physical properties of APIs. However, a major limitation is that the API must possess a suitable site for ionisation. In comparison, co-crystals consist of an API which regardless of acidic, basic, or ionizable groups, could potentially be co-crystallised [65].

It is crucial to investigate the physical and chemical properties of a co-crystal to determine whether it can be developed into a marketed dosage form. Properties such as crystallinity, melting point, solubility, stability and dissolution of a co-crystal needs to be studied at the early stages of development [65]. Changing the properties can improve the stability and efficacy of a dosage form while maintaining its pharmacological activities [107]. Currently, there are over 100 studies of co-crystals that have exhibited improved solubility and/or dissolution rates with improved physical and chemical stability [108]–[110].

The main properties of pharmaceutical co-crystals are as follows:

2.4.3.1 *Melting point*

The melting point of a compound is generally used as a method of characterization or purity identification and are used to evaluate the energy of a crystal lattice [111]. It is hypothesized that by co-crystallizing an API of interest with a co-former with a similar melting point, can fine tune the melting point and aqueous solubility of the API [79]. Extensive research has been carried out to investigate if the melting point of a co-

crystal changes with respect to the individual components and whether the melting points can be estimated and regulated within a co-crystal system [62] [112].

Liu used melting method and hot melt extrusion to depress the processing temperature of Carbamazepine-nicotinamide (CBZ-NIC) co-crystals in solid dispersions and thus minimizing the thermal degradation of the heat sensitive Carbamazepine. It was found that chemically stable amorphous solid dispersions were prepared which had a significant increase in the dissolution rate [100]. Nechipadappu studied the thermal analysis of Flufenamic acid with 2-chloro-4-nitrobenzoic acid (CNB) and ethenzamide (ETZ) using DSC and found that melting peak temperature for the co-crystals FFA-CNB and FFA-ETZ was found at 143.93°C and 97.28°C, respectively. It was observed that FFA-CNB co-crystal melts exactly in-between the melting point of its constituent starting materials, whereas FFA-ETZ co-crystal melts at low temperature compared to its starting materials. This was due to the loose crystal packing of FFA-ETZ co-crystal when compared to FFA-CNB co-crystal [113].

2.4.3.2 Stability

Stability is a heavily studied parameter during the development of new chemical entities. Depending on the structure and the characteristics of a molecule, different types of stability tests need to be carried out. Chemical and physical stability are usually studied at accelerated stability conditions to determine developability and shelf life [65]. It is also critical to determine the stability of co-crystals in solution as precipitation could occur of the parent drug in a process known as solution mediated phase transformation.

Common stability tests include relative humidity tests [114], thermal stress tests [115], chemical stability [116] and thermal stability [117].

Trask subjected theophylline co-crystals to relative humidity challenges in order to assess their stability in comparison to crystalline theophylline anhydrate, and caffeine co-crystals. The study showed none of the co-crystals converted into a hydrated co-crystal upon storage at high relative humidity [118].

Tsutsumi studied Miconazole salts and co-crystals to improve the physicochemical properties of miconazole. Stability tests of preliminary formulations prepared with each crystal form indicated that maleate (salt) and hemifumarate (co-crystal) were unstable at 80 °C and generated a specific degraded product, i.e., a Michael addition, between miconazole and the acids [117].

2.4.3.3 Mechanical properties

Study of the mechanical properties of drugs are important for bulk powder compaction and tableting. Compaction includes compression (volume reduction and particle rearrangement) and consolidation (interparticle bond formation) [119].

The mechanical deformation mechanisms of solid materials are elastic, plastic, viscoelastic, and fragmentation [120]. The elasticity of a material is the ability to undergo reversible deformation under an externally applied stress. Upon removal of the stress, the material should exhibit no residual deformation. Plastic deformation on the other hand, is permanent and irreversible [121]. In order to produce stable, intact tablets, it is crucial to study the mechanical properties of the co-crystals. The relationship between crystal structure and mechanical properties have been investigated thoroughly.

Chattoraj studied the Origin of Deteriorated Crystal Plasticity and Compaction Properties of a 1:1 co-crystal between Piroxicam and Saccharin and found that the 1:1 co-crystal between piroxicam and saccharin exhibits significantly deteriorated powder compaction properties compared to both the co-formers [122].

Ahmed studied the relationship between mechanical properties and crystal structure in co-crystals and salt of paracetamol and reported that it was possible to explain the improved mechanical properties of powders based on the crystal structure [123].

Hiendrawan studied the physicochemical and mechanical properties of paracetamol co-crystal with 5-nitroisophthalic acid and reported that the co-crystal displayed superior tableting performance in comparison to the API alone [124].

2.4.3.4 Solubility

Co-crystallisation can dramatically change the properties of API, particularly the increased solubility and dissolution rate of the API [8], [120], [125]. The overall effect of a co-former on the co-crystal solubility is dependent on the solvation energy of the components and the co-crystal lattice energy. A highly soluble co-former can form strong solvent-solution interactions and can promote co-crystal dissolution, which then drives the supersaturation of the solution and increases the bioavailability of the API [126].

When studying the solubility of co-crystals, it is important to consider the equilibrium vs kinetic solubility measurements and the form changes of the API [62], [78]. Equilibrium vs kinetic solubility measurements are usually based on one measurement at one time point. Equilibrium solubility is dependent on the concentrations of the drug and co-former in solution and provides insight about the origin of the co-crystal solution phase behaviour. This information is crucial for addressing the limitations of poorly soluble drugs [127]. Kinetic solubility shows the dissolution rate of the co-crystals and indicates apparent solubility due to the instability of the co-crystal in solution [128]. Form change of an API can be revealed by taking various time point measurements to detect a decrease in concentration. This indicates the crystallisation of the less soluble form of the API, a process known as solution mediated phase transformation [65].

Ren studied the effects of pH, surfactant, ion concentration, co-former, and molecular arrangement on the solubility behavior of myricetin co-crystals and observed that kinetic solubility of myricetin co-crystals was modulated by pH and co-crystal co-former (CCF) ionization in buffer solution. The results also indicated that the solubility of MYR co-crystals was increased in a concentration dependent fashion by the surfactant or ion concentration [129].

Bethune studied the effect of co-crystal components on the pH and co-crystal solubility and found that Carbamazepine-salicylic acid and Carbamazepine-4-aminobenzoic acid revealed co-crystals of a nonionizable drug when co-crystallized with ionizable co-former achieved pH-dependent solubility [130].

2.4.3.5 Bioavailability

Using co-crystallisation to improve bioavailability of poorly water-soluble drugs have attracted a lot of interest over the years [91], [131]. Despite the current interest, a very limited number of animal bioavailability studies for co-crystal forms of APIs have been reported to date.

Jung studied the bioavailability of Indomethacin-saccharin co-crystals in beagle dogs. Results showed that the in-vitro dissolution rate of the co-crystals was higher than that of IND and the in-vivo bioavailability of the IND–SAC co-crystals in dogs was significantly higher than that of IND [132].

Smith synthesised and studied the dissolution and bioavailability of Co-crystals of Quercetin and found that the co-crystals exhibited pharmacokinetic properties that are

vastly superior to those of quercetin alone. Furthermore, the co-crystals showed an increase in bioavailability of up to 10 fold [131].

2.4.4 Characterisation techniques

Understanding the structural information and physicochemical properties of co-crystals is essential for co-crystal research and synthesis. Various techniques have been used to characterize co-crystals.

Co-crystals can be characterised using powder X-ray diffraction (XRPD), single co-crystal X-ray diffraction (SXRD), Raman spectroscopy, Infrared spectroscopy (IR) and differential scanning calorimetry (DSC) [79], [133], [134]. More information on the characterisation techniques are presented in Chapter 3.

2.5 Pharmaceutical co-crystal Formulation and Development

To successfully develop new drug candidates and acquire the desired therapeutic performance, it is essential to improve the solubility of poorly water-soluble drugs. Pharmaceutical co-crystals have been demonstrated to be an effective tool for enhancing the solubility by creating a supersaturated state of poorly water-soluble drugs [79], [128], [134], [135]. However, co-crystals in solution are not thermodynamically stable which leads to a phenomenon called solution-mediated phase transformation (SMPT) where the drug recrystallises from a metastable form to a stable form either in solution or on the surface of the dissolving solid [136]. This phenomenon can be overcome by using precipitation inhibitors [7] and the spring and parachute model [137].

2.5.1 Solution mediated phase transformation

Pharmaceutical development of drugs with thermodynamically metastable forms is usually desired due to their higher solubilities and faster dissolution rates. However, the metastable forms are undesirable in some cases because of recrystallization of the API to a more thermodynamically stable state during processing, storage, or

dissolution [138]. Recrystallisation of the drug usually occurs during the dissolution process which decreases the concentration of the drug, which then reduces the absorption rate and therapeutic effect [136].

This phenomenon has been studied extensively by our research group for Carbamazepine and Flufenamic acid. Qiao monitored the in-situ Carbamazepine-nicotinamide co-crystal intrinsic dissolution behaviour and reported that compared with CBZ III and I, the rate of intrinsic dissolution rate of CBZ–NIC co-crystal decreased slowly during dissolution. In situ solid-state characterisation was also performed which showed the change of CBZ–NIC co-crystal and polymorphs to its dihydrate form [139].

Guo studied Flufenamic acid co-crystal dissolution in the presence of a polymer in solution and reported that the dissolution mechanisms of FFA-TP CO are controlled by the defect sites of the crystal surface. Precipitation of the parent drug FFA occurred as individual crystals in the bulk fluid. On the other hand, the dissolution mechanisms of FFA-NIC CO are controlled by surface layer removal and by a surface precipitation mechanism. The parent drug FFA precipitates directly onto the surface of the dissolving co-crystals [140].

Although many researches has gone into understanding SMPT, understanding the kinetics behind the transformation remains challenging [141].

Three essential processes are involved in SMPT:

- (i) Dissolution of the metastable solid
- (ii) Nucleation of a more stable solid phase
- (iii) Growth of the stable phase

The nucleation and growth of the more stable phase often occur on the metastable phase, reducing the dissolution rate of that API [136]. The metastable solid first dissolves creating a supersaturated solution containing the thermodynamically stable solid. Supersaturation causes stable phase of the solid to nucleate and grow, often on the surface of the metastable solid [142]. This reduces the enhanced properties of the co-crystals and reduces the solubility and dissolution rates. The process of nucleation and grown depends on factors such as supersaturation, interfacial tension, and temperature of the solution [143]. Precipitation can occur either on the surface of crystals where the nucleation and growth occur on the surface molecules present in the crystal or in the bulk solution where nucleation and growth occurs between the already dissolved molecules [144].

2.5.2 Precipitation inhibitors

Extensive research on precipitation inhibitors have showed that solubility of poorly soluble drugs can be improved by the addition of polymers or surfactants [52], [54], [109], [145]. Polymers, including polyvinylpyrrolidone (PVP K30), polyvinylpyrrolidone K90 (PVP K90), polyethylene glycol (PEG 6000) and hydroxy propyl methyl cellulose (HPMC), have been reported to enhance the solubility of co-crystals [140]. Surfactants promote drug solubility by the formation of micelles of the additive and API while polymers form specific molecular interactions with the API and solution. The key factors which play a part in the inhibition effect include the hydrophobic level of additives and the ability of the polymers to form hydrogen bonding with the API [146].

Polymers inhibit nucleation by forming intermolecular interaction with the API during the embryo formation of the solute molecules and disrupt the self-assembly. Induction/nucleation time is the time span between the supersaturated solution to the formation of the first nuclei and acts as a useful method for understanding the kinetics of the nuclei formation [147]. The amount of induction time required, or nucleation is dependent on the strength of the interactions between the API and additives which is determined by hydrogen bonding and van der Waals interactions [148].

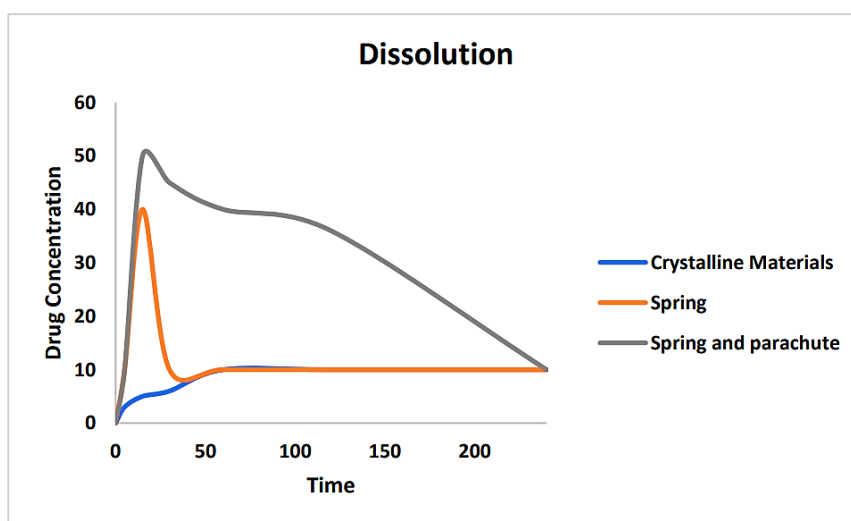
The additives inhibit crystal growth by attaching onto the growth site and act as a mechanical barrier. Additives can attach themselves in two ways: reversible physical absorption which includes van der Waals and electrostatic forces, and irreversible chemical absorption which include covalent bonding [149], [150]. The key factors that facilitate adsorption of polymers on crystal surfaces are hydrophobic interactions, electrostatic interactions, and hydrogen bonding [12], [151].

2.5.3 Spring and Parachute model

In order to improve the oral absorption of a poorly water-soluble drug, a method called 'spring and parachute' (Figure 6) has been widely used to promote and maintain the supersaturation of the API [150], [152]. The high energy form of the drug which rapidly dissolves to generate a supersaturated solution then immediately precipitates, is referred to as the 'spring'. The additives, which act as precipitation inhibitors, are referred to as the 'parachute' as they have to ability to maintain the supersaturation of the drug long enough to allow the required amount of drug absorption in the body to

increase the bioavailability [153], [137]. The figure below shows a diagram of the 'spring and parachute' model.

Figure 6 - Spring and parachute model



Liu studied the oral bioavailability of Sorafenib by Optimizing the “Spring” and “Parachute” based on molecular interaction mechanisms. It was observed that the solubility of sorafenib could be increased ~50-fold in the coexistence of poly(vinylpyrrolidone-vinyl acetate) (PVP-VA) and sodium lauryl sulphate (SLS). However, SLS impaired the ability of PVP-VA to act as an efficient “parachute” to keep the drug in solution and maintain drug supersaturation. It was concluded that despite its forceful “spring”, the formulation containing both PVP-VA and SLS showed a moderate bioavailability enhancement, due to the lack of an efficient “parachute” [154].

2.6 Flufenamic acid CO, Carbamazepine CO, and their cofomers

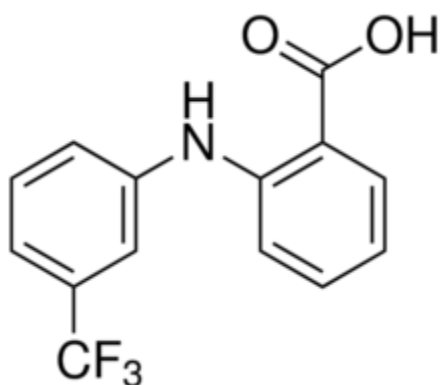
2.6.1 Flufenamic acid drug introduction

Flufenmaic acid is a nonsteroidal anti-inflammatory drug belonging to the group fenamates. It contains the functional group of N-phenylanthranilic acid which contributes to the anti-inflammatory properties [155]. FFA, together with mefenamic acid is considered as one of the most potent NSAIDs and is used for the treatment of lower back pain and can be administered orally or topically [156]. Flufenamic acids have nine polymorphs but only form I and form III are used as commercial drugs. FFA

has low solubility and high permeability and belongs to class II of the biopharmaceutical classification system.

FFA has a solubility of 0.00909g/l and permeability of $\log P = 5.25$ [157]. Research carried out by Guo in 2014 reported that the melting points of FFA form III and FFA form I was 126.5°C and 134°C respectively [146]. Form I is stable above 42°C while form III is stable at room temperature. FFA has been reported to show a potency of 16 times higher than that of aspirin and 3.2 times of Mefenamic acid [158].

Figure 7 - Structure of Flufenamic acid



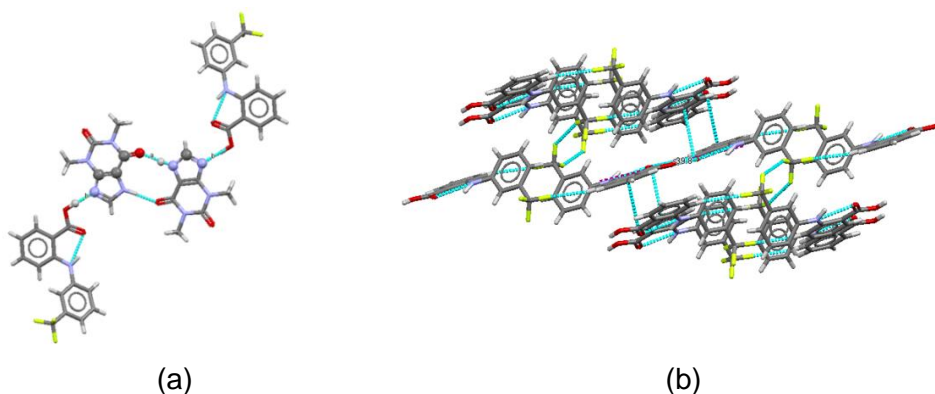
2.6.2 Flufenamic acid co-crystals synthesis

Much research have been carried out on FFA co-crystals and single co-crystals using co-formers such as Nicotinamide, 2-pyridone, Theophylline and 4-4'-bipyridine. Fabian *et al.* reported a 1 : 1 co-crystal of FFA with a pharmaceutically acceptable co-former, nicotinamide [155]. Lee described the epitaxial sublimation behaviour of a structurally related compound, mefenamic acid on the (100) faces of Flufenamic acid form I and III single co-crystals [159]. However, there is still a lot to understand about co-crystals and single co-crystals such as dissolution behaviours at molecular level. In this research, FFA-NIC and FFA-TP co-crystals and single co-crystals were synthesised in order to look at dissolution of the surface molecules at molecular level.

Delaney and Korter investigated FFA-NIC CO using terahertz spectroscopy and solid-state density functional theory and concluded that the co-crystal has better overall

binding energy, driven by increased intermolecular hydrogen bond strength and intermolecular forces [160].

Figure 8 - (a) below shows the bonding between FFA-TP CO. Figure (b) shows the packing interactions of the FFA molecules in the FFA crystal.

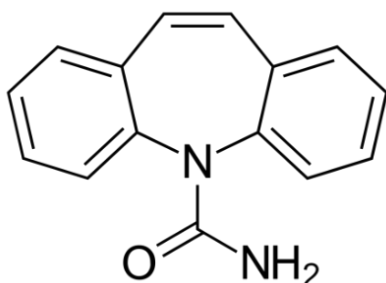


2.6.3 Carbamazepine drug introduction

Carbamazepine is an antiepileptic drug that has been in use for several decades to treat seizures and nerve pain. It was introduced for pharmaceutical use in the late 1960s [161]. In recent times, it has been approved for its anticonvulsant role in administrations in patients with epileptic problems or as a pain reliever in trigeminal neuralgia, the mechanism of action being associated with the modification of synaptic transmission [162].

CBZ was also evaluated as a possible therapeutic scheme for bipolar disorder [163], attention-deficit hyperactivity disorder [164], schizophrenia [165], and other psychiatric disorders [166], [167]. CBZ has low water solubility therefore requires a higher dose in order to produce a therapeutic effect. CBZ also exhibits complexity in its crystal forms.

Figure 9 - Structure of Carbamazepine



2.6.4 Carbamazepine co-crystals synthesis

One strategy used for the formation of CBZ co-crystals involves the breaking of the amide-amide dimer and forming a supramolecular heterosynthon between CBZ and a co-crystal former [168]. Formation of CBZ into a co-crystal has shown significant improvement in the physicochemical properties. CBZ co-crystal solubility varies greatly, demonstrating 2 to 152 times greater than the stable CBZ dihydrate [169]. Qiao investigated the dissolution and phase transformation behaviour of Carbamazepine–nicotinamide (CBZ–NIC) co-crystals using in situ techniques of UV imaging system and Raman spectroscopy, and demonstrated that the enhancement of the apparent solubility and dissolution rate has been reduced significantly due to its conversion to CBZ DH [139].

2.6.5 Pharmaceutical co-formers Nicotinamide and Theophylline

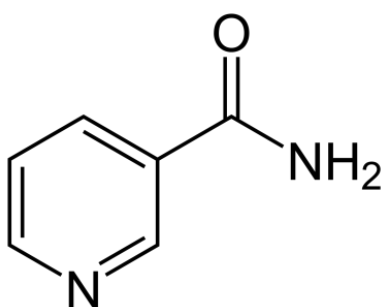
Nicotinamide (NIC) was chosen as a co-former for FFA and CBZ due to its high solubility. NIC is a suitable co-former due to its high likelihood of hydrogen bond forming between the carboxylic acid present in FFA structure and nitrogen atom belonging to NIC.

NIC is classified as a Class I drug and is often utilized in much larger doses than seen in co-crystal formation to treat high cholesterol [170]. It has four known polymorphs, I–IV, Form I is the stable and the others are metastable [171]. The melting points of Forms I, II, III and IV were 126–128°C, 112–117°C, 107–111°C and 101–103°C, respectively [172]. NIC has been utilized as a co-former for the co-crystallization of

ibuprofen [173] and 3-hydroxybenzoic acid, 4-hydroxybenzoic acid, Carbamazepine and other APIs [174], [175].

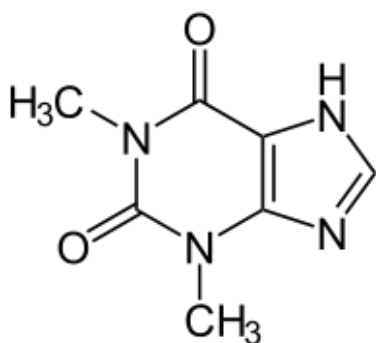
The solubility of NIC in water is about 570 mg/ml at 37°C. In his research, Rahman looked at co-crystallisation of CBZ with NIC and concluded that the pre-formulation profile of the co-crystals was similar to CBZ, except that it had an advantageous resistance to hydrate transformation [176].

Figure 10 - Structure of Nicotinamide



Theophylline was chosen as a co-former for FFA. Theophylline is a drug used for respiratory diseases, which can act as hydrogen-bond donors and hydrogen-bond acceptors [177]. In a previous research, Aitipamula investigated the physicochemical properties of FFA-TP and compared it with a reported FFA co-crystal with nicotinamide. Properties such as stability, hygroscopicity, solubility, and dissolution rate were measured and was found that FFA-TP was offered better solubility and dissolution rate [157].

Figure 11 - Structure of Theophylline



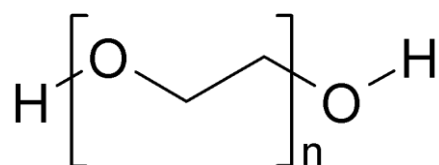
2.7 Introduction to polymers

Polymers can enhance crystallisation of co-crystals by forming ternary complexes or co-complexes between the co-crystal and polymer [11]. Polymers such as water-soluble cellulose derivatives can form complexes with FFA-TP that have different physicochemical properties than those of FFA alone [178]. When added in small amounts, water-soluble polymer agents enhance co-crystal solubilizing effect by increasing the apparent complex stability constant. The polymers, due to their direct participation in drug complexation, improve both pharmaceutical and biological properties of co-crystal complexes, independent of drug's physicochemical properties [141], [150].

2.7.1 Polyethylene glycol 400

PEG 4000 is a commonly used pharmaceutical polymer with a melting point of 50-58°C [179]. It has a high molecular weight of about 3500-4500 and its solubility in water is 50 mg/ml at 25°C [180]. PEG has been extensively used as carriers for solid dispersion [181] due to its favourable properties such as low melting point, rapid solidification rate, capability of forming solid drug solutions, low toxicity and low costs [182]. PEG is a hydrophilic polymer that can enhance the dissolution, solubility and have the ability to prevent the re-crystallization of drug by forming hydrogen bonding with the drug [163]. PEG 4000 has been studied in our research group as a potential polymer to inhibit recrystallisation of API in co-crystals. Guo investigated the influence of polymers on supersaturated Flufenamic acid co-crystal solutions and reported that the supersaturated co-crystal solutions with pre-dissolved PEG demonstrated more effective stabilization in comparison to the pure FFA in the presence of the same polymer [146].

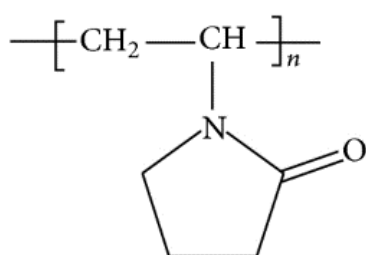
Figure 12 - Structure of PEG



2.7.2 Polyvinyl Pyrrolidone K30

Polyvinyl pyrrolidone (PVP) has good solubility in a wide variety of organic solvents therefore it is suitable for the preparation of solid dispersions by the solvent method [183], [184]. The average molecular weight of PVP K30 is 40000 with T_g at 165.03°C. PVP is widely used as an excipient in the pharmaceutical industry. It is not regarded as toxic when given orally due to its high molecular weight and inability to pass through the membrane of the GI tract [185]. PVP has also been found to stabilize the supersaturated condition of drugs by forming hydrogen bonding, such as with indoprofen [186] and BMS-488043 [187]. The functional groups =N- and C=O are likely to form hydrogen bonding with other molecules. The carbonyl group is preferred for hydrogen bonding in comparison to the nitrogen atom because the steric hindrance present in the nitrogen atom interrupts the intermolecular interactions [188]. Kothari studied the role of drug-polymer hydrogen bonding interactions on the molecular mobility and physical stability of nifedipine solid dispersions and reported that PVP was the best polymer to use in terms of drug-polymer hydrogen bonding, the structural relaxation time, and the crystallization kinetics [189].

Figure 13 - Structure of PVP

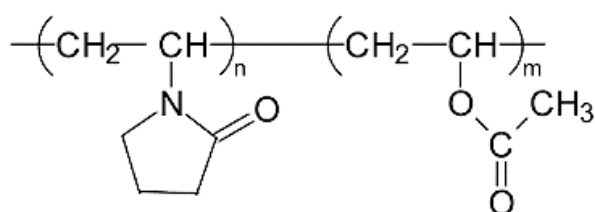


2.7.3 Plasdone S630 (PVP-VA)

PVP-VA is an amorphous copolymer of N-vinyl-2-pyrrolidone (60%) and vinyl acetate (40%) with an average molecular weight of 51000. It is a white, odourless powder and is more hydrophobic than PVP. Due to the presence of vinyl acetate groups, PVP-VA has a lower T_g 106°C compared to PVP. This makes it very soluble in water and many organic solvents. PVP-VA contains two strong hydrogen bonding acceptors of C=O of vinylpyrrolidone and C=O vinyl acetate group.

PVP-VA acts as a good binder for the direct-compression of tablets, drug granulation and for coating materials of control release drugs [190]–[192]. It is also a good stabilizer for preventing drug crystallization and many researches has reported the inhibition of crystal growth rate such as of bifonazole and nimesulide [193] in the presence of PVP-VA. Knopp investigated the influence PVP(VA) on the non-sink *in vitro* dissolution behaviour and *in vivo* performance of celecoxib (CCX) amorphous solid dispersions. Knopp reported that the hydrophilic monomer vinylpyrrolidone (VP) was responsible for the generation of CCX supersaturation whereas the hydrophobic monomer vinyl acetate (VA) was responsible for the stabilization of the supersaturated solution [194].

Figure 14 - Structure of PVPVA



2.8 Molecular modelling and molecular dynamics

Molecular modelling, a computer-based technique, can be used for deriving, representing, and manipulating the structures and reactions of molecules. Due to the advancement of computers, the development of molecular modelling has increased largely in the last couple of years. For several decades, theories have been linked with molecular modelling or quantum mechanics and this technique has been applied to understand the electronic properties and chemical reactivity [195]. Molecular modelling can be used to predict a suitable co-former to form co-crystals as well as crystal structures, bonding, and interactions between molecules. Molecular dynamics (MD) simulations are a well-established methodology capable of modelling the dynamic aspect of materials at the atomistic level. Various problems such as protein folding and drug discovery have successfully been studied using molecular dynamics [196]. However, MD simulations to investigate organic crystal structures have been relatively limited [197].

Molecular modelling has been increasingly used in crystal engineering by a number of researchers. Research have been carried out to study the impact of choice of solvent on morphology of crystals such as by Song who investigated the crystal morphology of a nitroguanidine (NQ) via molecular dynamics simulations [198]. Hammond applied grid-based molecular methods for modelling solvent-dependent crystal growth morphology for aspirin [199] and Larsen studied the dehydration of hydrates based on molecular dynamics simulations and applied this approach to the dehydration of ampicillin trihydrate [200]. Tsangarides fabricated a pH sensitive photonic crystal sensor through photochemical patterning and demonstrated computational simulations of the sensor through a finite element modelling technique to analyse its optical properties [201]. Simulations can accurately predict many important molecular motions however, these simulations are poorly suited for systems where quantum effects are important, for example, such as when transition metal atoms are involved in binding [108].

Yang studied the structural and computational insights into co-crystal interactions of antipyrine and aminophenazone and reported that density functional calculations indicated that H bond interactions in co-crystals [202]. Xiong studied the Molecular dynamic simulations on Dihydroxylammonium 5,5'-bistetrazole-1,1'-diolate - Cyclotrimethylenetrinitramine (TKX-50/RDX) co-crystal and reported that hydrogen bond and van der Waals force interactions exist in the co-crystal system and the hydrogen bonds are mainly derived from the hydrogen atom of TKX-50 with the oxygen or nitrogen atom of RDX [203].

2.8.1 Forcefields

The most important part of any simulation is the choice of forcefield which describes the approximate potential energy hypersurface on which nuclei of atoms move. Choice of forcefield will depend on the type of structure being examined [204]. This is because it is chosen for a group of systems rather than for individual structures. Forcefields are able to describe the potential energy surfaces of a group of molecules with reasonable accuracy [205]. Some forcefields aim for high accuracy for a limited set of elements, which enables excellent predictions of many molecular properties, while others aim for the widest coverage of the periodic table, with inevitably lower accuracy [206].

A given forcefield usually contains several different interaction terms describing different types of strain possible in a molecular system.

The components of a forcefield are as follows:

- A list of forcefield types
- A list of partial charges
- Forcefield-typing rules
- Functional forms for the components of the energy expression
- Parameters for the function terms

Many experimental properties such as vibrational frequencies, sublimation energies, and crystal structures can be reproduced with a forcefield [207], [208]. This is because the forcefield can reproduce relevant observables and include most of the quantum effects empirically.

The forcefields commonly used for describing molecules use a combination of internal coordinates and terms such as bond distances, bond angles and torsions and external non-bond terms such as van der Waals, electrostatic and hydrogen bond interactions [209], [210].

The properties taken into consideration to define a particular forcefield type [211], [212] are as follows:

- Element
- Type of bonds
- Number of other particles to which the given particle is bonded
- The type of particles to which the given particle is bonded
- Hybridization
- Formal Charge

Once the forcefield types have been defined for all the particles in the simulation, the Forcite parameter assignment engine can use them to locate the correct parameters for a given term in the energy expression [213].

2.8.1.1 Energy expressions

An energy expression is created when the coordinates of a structure combines with a forcefield and describes the potential energy surface of a particular structure as a function of its atomic coordinates [214]. The potential energy of a system can be

expressed as a sum of valence, cross-term, and nonbond interactions [215], [216] as shown in the equations below:

Equation 1 - Total potential energy

$$\Sigma_{total} = \Sigma_{valence} + \Sigma_{crossterm} + \Sigma_{non-bond}$$

Equation 2 - Valence cross terms

$$\Sigma_{valence} = \Sigma_{bond} + \Sigma_{angle} + \Sigma_{torsion} + \Sigma_{inversion} + \Sigma_{UB}$$

The energy of valence interactions is accounted for by *diagonal terms*, such as bond stretching, (E_{bond}), valence angle bending (E_{angle}), dihedral angle torsion ($E_{torsion}$), and inversion ($E_{inversion}$) terms, which are part of nearly all forcefields for covalent systems. van der Waals, electrostatic and hydrogen bonding account for the energy of non-bond interactions [217]. A Urey-Bradley term (E_{UB}) may be used to account for interactions between atom pairs involved in 1-3 configurations i.e atoms bonded to a common atom [218].

Equation 3 - Non-bond interactions

$$\Sigma_{non-bond} = \Sigma_{vdW} + \Sigma_{Coulomb} + \Sigma_{hbond}$$

The energy of interactions between nonbonded atoms is accounted for by van der Waals (E_{vdW}), electrostatic ($E_{Coulomb}$), and hydrogen bond (E_{hbond}) terms [219].

2.8.1.2 Forcefield types

The type of forcefield used gives an indication of the nature of the local microchemical environment of a given atom [220]. In this research the two different types of forcefield used are COMPASS and DREIDING, which are outlined below.

COMPASS

Condensed-phase optimized molecular potentials for atomistic simulation studies (COMPASS) is the first ab initio forcefield [221] that for a broad range of molecules and polymers, enables accurate and simultaneous prediction of:

- gas-phase properties such as structural, conformational, and vibrational properties
- condensed-phase properties such as the equation of state cohesive energies

It is also the first high quality forcefield to establish parameters of organic and inorganic materials [221]. Various calculation methods have been used to validate the parameters for covalent molecules including extensive molecular dynamics simulations of liquids, crystals, and polymers [222], [223]. COMPASS forcefield had a broad coverage with organic molecules, small inorganic molecules and polymers [224] and can predict various properties such as molecular structures [225], crystal structures [226], equations of state [227], vibrational frequencies [228], conformation energies [221], dipole moments [229], liquid structures [230], and cohesive energy densities [231].

The analytic expressions used to represent COMPASS forcefield [232] is shown below.

Equation 4 - COMPASS analytical expression

$$\text{Term 1} \quad E_{bond} = \sum_b \left[k_2 (b - b_0)^2 + k_3 (b - b_0)^3 + k_4 (b - b_0)^4 \right]$$

$$\text{Term 2} \quad E_{angle} = \sum_{\theta} \left[H_2 (\theta - \theta_0)^2 + H_3 (\theta - \theta_0)^3 + H_4 (\theta - \theta_0)^4 \right]$$

$$\text{Term 3} \quad E_{torsion} = \sum_{\phi} \left[V_1 \left[1 - \cos (\phi - \phi_0)^2 \right] + V_2 \left[1 - \cos (2\phi - \phi_0)^2 \right] + V_3 \left[1 - \cos (3\phi - \phi_0)^2 \right] \right]$$

$$\text{Term 4} \quad E_{oop} = \sum_{\chi} k_{\chi} \chi^2$$

$$\begin{aligned}
\text{Term 5} \quad E_{cross} &= \sum_b \sum_{b'} F_{bb'}(b - b_0)(b' - b'_0) + \sum_\theta \sum_{\theta'} F_{\theta\theta'}(\theta - \theta_0)(\theta' - \theta'_0) \\
&+ \sum_b \sum_\theta F_{b\theta}(b - b_0)(\theta - \theta_0) \\
&+ \sum_b \sum_\phi F_{b\phi}(b - b_0) \left[V_1 \cos \phi + V_2 \cos 2\phi + V_3 \cos 3\phi \right] \\
&+ \sum_{b'} \sum_\phi F_{b'\phi}(b' - b'_0) \left[V_1 \cos \phi + V_2 \cos 2\phi + V_3 \cos 3\phi \right] \\
&+ \sum_\theta \sum_\phi F_{\theta\phi}(\theta - \theta_0) \left[V_1 \cos \phi + V_2 \cos 2\phi + V_3 \cos 3\phi \right] \\
&+ \sum_\theta \sum_{\theta'} \sum_\phi k_{\phi\theta\theta'} \cos \phi (\theta - \theta_0)(\theta' - \theta'_0) \\
\text{Term 6} \quad E_{elec} &= \sum_{i,j} \frac{q_i q_j}{\epsilon r_{ij}} \\
\text{Term 7} \quad E_{lj} &= \sum_{i,j} \epsilon_{ij} \left[2 \left(\frac{r_{ij}^0}{r_{ij}} \right)^9 - 3 \left(\frac{r_{ij}^0}{r_{ij}} \right)^6 \right]
\end{aligned}$$

Where \sum_b , \sum_θ , \sum_ϕ and \sum_x , was the bond, angle, torsion, and out-of-plane angle coordinates respectively. Among the cross-coupling terms, F_{bb} was the bond-bond, $F_{b\theta}$ was the bond-angle and $F_{b\phi}$ was the bond torsion. r^0 is the vdW radii and q_i is the net partial charge of the atom.

The COMPASS forcefield consists of quartic polynomials for bond stretching (Term 1) and angle bending (Term 2) and a three-term Fourier expansion for torsions (Term 3), the out-of-plane coordinate or inversion (Term 4), crossterms (Terms 5), coulombic or Electrostatic interaction between the atomic charges (term 6) and van der Waals interactions (Term 7) [233].

DREIDING

The DREIDING forcefield is based on simple hybridization rules rather than on specific combinations of atoms. It does not generate parameters automatically in the way that other forcefields do. Instead, explicit parameters are derived by a rule-based approach [234].

DREIDING has a hydrogen bond term to describe interactions involving a hydrogen atom on very electronegative atoms such as -N or =O [235], [236]. The van der Waals interactions are described by the Lennard-Jones potential. Electrostatic interactions

are described by atomic monopoles and a distance dependent Coulombic term. Hydrogen bonding is described by an explicit Lennard-Jones 12-10 potential [234].

DREIDING forcefield allows reasonable predictions for a much larger number of structures, including those with novel combinations of elements and those for which there is little or no experimental data. The forcefield has good coverage for organic, biological and main-group inorganic molecules and can predict geometries [237], conformational energies [238], intermolecular binding energies [239] and crystal packing [240].

2.8.2 Geometry optimization

Geometry optimization generates the optimal lowest energy structure of a molecule from a high energy starting state and proceeds as a set of single point energy calculations [241]. The optimization of a structure is completed in a two-step process; Energy evaluation and conformation adjustment. GO has been used for energy minimization of molecular clusters and complexes [242], large molecules [243], periodic systems [244] and crystal structures [245].

Energy evaluation

For any given conformation it is crucial to define and evaluate an energy expression [246]. Energy expressions includes external restraining terms that may need to be defined in addition to the energy terms.

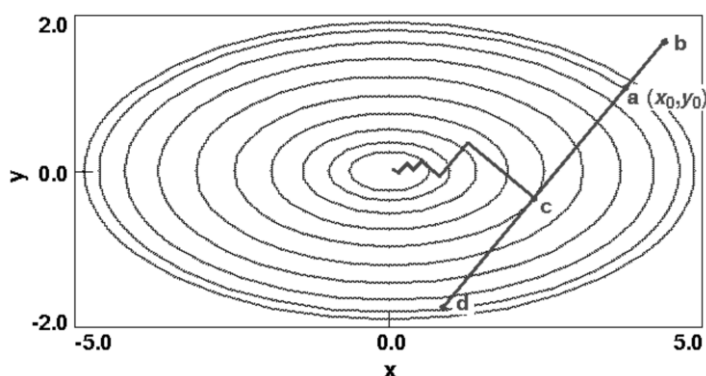
Conformation adjustment

The conformation is adjusted to reduce the value of the energy expression [247]. A minimum energy structure may be found after one adjustment or may require more iterations, depending on the size of the structure, nature of the algorithm and the form of the energy expression [248]. The effectiveness of the optimization is evaluated by both the time needed to calculate the energy expression and the number of structural iterations needed to change to the minimum [249].

2.8.2.1 Line search

The most common component of an optimizer is the 'line search' that modifies the coordinates to generate a new, lower energy structure [250]. An illustration of the line search is shown in the figure below. The derivative vector from the initial point $a(x_0, y_0)$ defines the line search direction. Line search sums the one-dimensional optimization along a direction vector determined at each iteration [251].

Figure 15 - Line search optimiser



Extensive line searches are desirable because all the energy from one direction is extracted before moving on to the next [252]. The new derivatives are always perpendicular to the previous direction which produces a successful path to the minimum for surfaces that are approximately quadratic [253]. However, line searches are time consuming in terms of the number of function calculations that must be completed. The energy must be evaluated at 3-10 points to precisely locate the one-dimensional minimum, and therefore extensive line searches are inefficient [254].

2.8.2.2 Optimization algorithm

In mathematical terms the optimization of a molecular structure can be considered as optimization in a multidimensional space. The algorithm used for optimization in this research was the steepest descent algorithm [255]. The line search direction in the steepest descent algorithm is marked along the direction of the local downhill gradient. Each line search will produce a new direction perpendicular to the previous gradient and this oscillates to the minimum [256].

The steepest descents method is often used when the gradients are large, and the configurations are far from the minimum which is usually the case for the initial relaxation for built models. Convergence is slow near the minimum as the gradient approaches zero, but the method is extremely robust [257], even for systems that are far from harmonic. Steepest descent method is most likely to generate the true low-energy structure, regardless of what the function is or where the process begins [256].

2.8.3 Dynamics theory

All equations were taken from the BIOVIA Materials studio handbook [258].

Molecular dynamics solves Newton's equation of motion which states that the time rate of change of the momentum of a body is equal in both magnitude and direction to the force imposed on it [259], [260]. Once the initial coordinates and velocities are known, the coordinates and velocities later can be determined.

Equation 5 - Newton's equation of motion

$$F_i(t) = m_i a_i(t)$$

where F_i is the force, m_i is the mass, and a_i is the acceleration of atom i [261].

2.8.3.1 Velocity verlet integrator

Molecular dynamics is generally utilized on large models. Energy evaluation therefore is time consuming and requires large computer memory. Energy conservation is also crucial to generate the correct statistical ensemble. Therefore, a good integrator for molecular simulations is required [262].

The requirements for a good integrator used for molecular simulations are that it should:

- Be fast and preferably only require one energy evaluation per time step.
- Require as little computer memory as possible.
- Allow the use of a reasonably long, time step.

- Show good conservation of energy.

The most widely used method in molecular dynamics to integrate the equations of motion are variations of the Verlet algorithm [263]. The advantage of using this algorithm is that it requires only one energy evaluation per step, require moderate memory, and allows for a relatively large time step to be used [264].

Verlet velocity integrator

Equation 6 - The Verlet velocity algorithm

$$r(t + \Delta t) = r(t) + \Delta t v(t) + \frac{\Delta t^2 a(t)}{2}$$

$$a(t + \Delta t) = \frac{f(t + \Delta t)}{m}$$

$$v(t + \Delta t) = v(t) + \frac{1}{2} \Delta t [a(t) + a(t + \Delta t)]$$

where $r(t)$, $v(t)$, and $a(t)$, which are the position, velocity, and acceleration at time t respectively.

2.8.3.2 Statistical ensembles

Although using Newton's equation of motion allows the constant energy surface to be explored, it is not a replica of the natural phenomenon of the system when exposed to external pressure or temperature. Under these conditions, extended forms of molecular dynamics are required to study the system.

There are several methods available for controlling temperature and pressure i.e. NVT, NVE, NPH and NPT [265]. Depending on which state variables are kept fixed - such as number of particles, volume, temperature, pressure and energy - different statistical ensembles can be generated [266].

Molecular dynamic simulations performed in this study uses the NVT ensemble.

NVT Ensemble

The NVT ensemble, also known as the canonical ensemble, keeps the number of particles, volume, and temperature constant [267]. The temperature control method is based on the Nosé-Hoover thermostat that is used for performing constant-temperature dynamics that produces true canonical ensembles in both coordinate space and momentum space [268].

Equation 7 - NVT Ensemble

$$H = \langle \Psi | \hat{H}_e | \Psi \rangle + \frac{1}{2} \sum_{i=1}^N \sum_{j=1}^N \frac{z_i z_j}{|R_i - R_j|} + \sum_{i=1}^N \frac{p_i^2}{2M_i} + \sum_{i=1}^M \frac{P_{\xi i}^2}{2Q_i} + N_f k_B T \xi_1 + k_B T \sum_{i=2}^M \xi_i$$

Where:

Q_i are the thermostat fictitious masses

ξ_i are the thermostat degrees of freedom

Nosé-Hoover dynamics adds an additional degree of freedom to the structure which represents the interaction of the structure with the heat bath [269].

Equation 8 - Nosé-Hoover dynamics

$$H_* = \sum_{i=1}^N \frac{p_i^2}{2m_i} + \phi(q) + \frac{Q}{2} \zeta^2 + N_f k_B T_0 \ln S$$

where ϕ is the interaction potential and ζ and $\ln S$ play the role of the velocity and position of the extra degree of freedom, with associated mass Q .

NVE Ensemble

NVE Ensemble, also known as the microcanonical ensemble, is a constant-energy, constant-volume ensemble what is obtained by solving the standard Newton equation

without any temperature and pressure control. When this ensemble is generated, the energy is conserved. NVE conditions are used during the equilibrium phase of the dynamics.

Equation 9 - NVE Ensemble

$$H = \langle \Psi | \hat{H}_e | \Psi \rangle + \frac{1}{2} \sum_{i=1}^N \sum_{j=1}^N \frac{z_i z_j}{|R_i - R_j|} + \sum_{i=1}^N \frac{p_i^2}{2M_i}$$

Where N is the number of particles and M_i is mass of atom i .

2.8.3.3 Forcite Anneal

The Forcite Anneal task can be used to investigate conformational space for low energy structures by periodically increasing and then decreasing the temperature of a structure or model [270]. This avoids restricting the structure in a conformation that represents a local energy minimum. The forcite anneal task consists of dynamics calculation with a change in temperature to follow a specific anneal schedule followed by optional geometry optimization.

2.8.3.4 Equilibrium

Particle velocities are assigned at random from a Maxwell-Boltzmann distribution at the start of a simulation and an integration is then performed in the microcanonical ensemble [271]. This would show a decline in temperature as some of the kinetic energy is transferred to potential energy. To ensure a simulation is at equilibrium, it is important to run it for moderately long time before analysis. In most cases, a thermostat can facilitate an equilibrium [272]. A system at equilibrium can be defined by plotting the energy or temperature against time and determining whether the numbers fluctuate around the constant averages [273].

2.9 Chapter conclusion

This chapter introduced the pharmaceutical drugs, co-crystals and polymers used in the research. The current approaches to improve the dissolution of poorly soluble drugs, the challenges in formulation and solutions to overcome these issues were discussed. The detailed explanation and several key issues about co-crystals were presented, including co-crystal design mechanisms, co-former selection, different types of co-crystal formation methods, co-crystal characterization techniques and co-crystal physicochemical properties. The key problem of co-crystals during dissolution, solution media phase transformation, was discussed as well as methods to overcome the problems. Some information about the materials that were used in this study were introduced, including FFA, FFA co-crystals, NIC, TP, PEG, PVP and PVP-VA. Finally, molecular modelling and molecular dynamics were discussed including the different types of forcefields, geometry optimisation methods and the different algorithms used in dynamics.

Chapter 3 – Materials and Methods

3.1 Chapter overview

This chapter presents materials and analytical methods used in the current research. All materials used are listed in detail, including the name, level of purity and the manufacturers. Analytical methods including ATR-FTIR, DSC, XRPD, Raman, Non-contact AFM, SEM and NMR are fully described. These methods were used to identify the co-crystals and characterise their physicochemical properties. ATR-FTIR, DSC, XRPD and Raman were used to perform qualitative analysis of formed samples, and the Raman spectrometer was also used for quantitative analysis of the phase transition of samples during the dissolution process. SEM and non-contact AFM were used to characterize the morphology of solid compacts. NMR was used to look at the interaction of the molecules in solution. Properties such as non-bond energies, hydrogen bonding, radial distribution function and mean square displacement were calculated using Materials studio.

3.2 Materials

All materials were used as received, without further processing. The details of materials were presented in the table below.

Table 1 - List of materials used in this study

Materials	Formula	Purity/grade	Manufacturer
Flufenamic Acid	$C_{14}H_{10}F_3NO_2$	97%	Sigma-Aldrich Company Ltd., Dorset, UK
Carbamazepine form III	$C_{15}H_{12}N_2O$	≥99.0%	Sigma-Aldrich Company Ltd., Dorset, UK
Nicotinamide	$C_6H_6N_2O$	≥99.5%	Sigma-Aldrich Company Ltd., Dorset, UK
Theophylline	$C_7H_8N_4O_2$	≥99.5%	Sigma-Aldrich Company Ltd.,

Methanol	CH ₃ OH	HPLC grade	Fisher Scientific Loughborough, U.K.
Ethanol	CH ₃ CH ₂ OH	Lab grade	Fisher Scientific Loughborough, U.K.
Acetonitrile	CH ₃ CN	HPLC grade	Fisher Scientific Loughborough, U.K.
Chloroform-d	CDCl ₃	99.8%	Cambridge Isotope Laboratories, Inc, USA
Double distilled water	H ₂ O	Double distilled	Lab made by Bi-Distiller (WSC044.MH3.7, Fistream International Limited, Loughborough, UK)
Ethyl acetate	C ₄ H ₈ O ₂	HPLC grade	Fisher Scientific Loughborough, U.K.
PEG 4000	C _{2n} H _{4n+2} O _{n+1}	-	Sigma-Aldrich Company Ltd., Dorset, UK
PVP K30	(C ₆ H ₉ NO) _n	-	Ashland Inc. (Schaffhausen, Switzerland)
PVP-VA	(C ₆ H ₉ NO) _n (C ₄ H ₆ O ₂) _m	-	Ashland Inc. (Schaffhausen, Switzerland)

3.3 Methods

3.3.1 Preparation and synthesis

3.3.1.1 Co-crystal synthesis

FFA-TP co-crystals were synthesized by cooling crystallization method. A 1:1 molar ratio of FFA and TP was completely dissolved in a co-solvent of (7:3) acetonitrile and water with stirring at 70°C. After the solid had completely dissolved, the solution was placed into an ice bath until the crystals had separated out from the solution. The crystals of FFA-TP CO were collected by vacuum filtration using the Cat No 1001 110

filter papers with 100mm qualitative circles. A physical mixture of FFA-TP was produced by mixing thoroughly a 1:1 ratio of FFA and TP. Single co-crystals of FFA-TP were synthesised using the remaining solution from co-crystal synthesis. A film containing small holes was used to cover the solution and the solution was left in a fume cabinet over a period of 3 days for the single co-crystals to form. The co-crystals, single co-crystals and the physical mixtures were characterized and validated using Different scanning calorimetry (DSC), Fourier transform infrared spectroscopy (FTIR) and X-ray powder diffraction (XRPD).

The FFA-NIC Co-crystal was prepared by using the solvent evaporation method. 1:1 equimolar mixture of FFA and NIC was completely dissolved in acetonitrile with stirring at 70°C. The solution was placed in a fume cabinet overnight for solvent evaporation. A physical mixture of FFA-NIC was produced by mixing thoroughly a 1:1 ratio of FFA and NIC. Single co-crystals of FFA-NIC CO were produced by solvent evaporation method by dissolving a 1:1 ratio of FFA and NIC in a co-solvent of (7:3) acetonitrile and water. FFA-NIC CO was added as seeds into the solution and the solution was then covered with a film containing small holes and was left to evaporate over a period of 3 days.

CBZ-NIC Co-crystals were prepared by the cooling crystallisation method. A 1:1 molar ratio mixture of CBZ III and NIC was completely dissolved in Ethyl Acetate (EtOAc) by stirring at 50°C. The solution was put in an ice bath for two hours and the suspension was then filtered through 0.45 µm filters (thermo Scientific Nalgene) to collect the solid residue of CBZ-NIC co-crystals. A physical mixture of CBZ-NIC was prepared by thoroughly mixing a 1:1 ratio of CBZ and NIC. Single co-crystals of CBZ-NIC CO were produced by solvent evaporation method. A 1:1 ratio of CBZ III and NIC was dissolved completely in Ethyl Acetate at 50°C. The solution was then covered with a film containing small holes and was left to evaporate over a period of 5 days.

3.3.1.2 Single co-crystals synthesis

The FFA-NIC cocrystal powders were added as seeds to newly prepared FFA and NIC cosolvent solution. The solution was then covered with a film containing small holes and was left to evaporate over a period of three days. FFA-NIC single co-crystals were harvested by filtration of the mother solutions.

Single co-crystals of FFA-TP were directly synthesised using the acetonitrile-water cosolvent. A film containing small holes was used to cover the solution which was left in a fume cabinet over a period of three days for formation of the single co-crystals. FFA-TP single co-crystals were harvested by filtration of the mother solutions.

Single co-crystals of CBZ-NIC were produced by dissolving 1:1 ratio of CBZ and NIC in ethyl acetate. A film containing small holes was used to cover the solution which was left in a fume cabinet over a period of three days for the single co-crystals to form. CBZ-NIC single co-crystals were harvested by filtration of the mother solution.

3.3.2 Analytical techniques

3.3.2.1 *Attenuated total reflection Fourier transform infrared (ATR-FTIR)*

Infrared Spectroscopy is the analysis of infrared light interacting with a molecule and can be analysed in three ways by measuring the absorption, emission, and reflection [274]. The 2D infra-red spectra contains information on the molecular structure of materials and can be used to find the functional groups of molecules based on a sequence of laser IR pulses [275].

ATR-FTIR can provide information on identity of unknown materials, determine the quality or consistency of a sample and determine the components in a mixture. ATR-FTIR can work with weak signals, provide high spectral resolutions, results can be acquired quickly with high spectral accuracy [276]. ATR-FTIR consists of a Source, Interferometer, Sample compartment and a detector. Infrared energy is emitted from the source and enters the interferometer. Molecules absorb specific frequencies of infra-red light that are characteristic to their structure [277]. Sample molecules, when exposed to infra-red radiation will absorb radiation of specific wavelengths which alters the dipole moment. This causes the energy levels of the sample molecules to transfer from 'ground state' to 'excited state'. The change in the dipole moment and transition in the energy levels is related to the intensity of the absorption peaks [278]. The 2D infra-red spectra contain information on the molecular structure of materials and can be used to find the functional groups of molecules based on a sequence of laser IR pulses. The method requires a very small amount of a sample it is fast and produces 2D-IR spectra resembling those of the NMR correlation spectroscopy [279].

Infra-red spectrums are created by passing a beam of infra-red light through an interferometer, then through the sample. Specific frequencies of energy that are uniquely characteristic to the sample are absorbed and the beam passes to the detector. The detector measures the interferogram signal and is sent to the computer for the FTIR spectrum to be produced. The resulting spectrum creates a fingerprint of the sample, representing the molecular absorption and transmission [280]. Different materials have different combinations of atoms therefore no two compounds produce the same FTIR spectrum.

In this experiment, a Perkin Elmer FTIR was used. The resolution was set at 2, sample scan time was set at 30 minutes and the wavelength was set to produce from 4000-400nm.

3.3.2.2 Differential scanning calorimetry (DSC)

DSC is a thermo-analytical technique which measures the difference in the amount of heat required to increase the temperature of a sample and a reference that is measured as a function of temperature. The sample holder temperature increases linearly as a function of time [281]. The temperatures of the sample and reference are maintained throughout the experiment. When a sample undergoes phase transition the amount of heat required to maintain the temperature varies in comparison to the reference. Whether a high or a low temperature required is dependent on the type of process such as exothermic or endothermic [282]. By observing the difference in heat flow between the sample and reference, differential scanning calorimeters are able to measure the amount of heat absorbed or released during such transitions. A number of characteristic properties of samples can be measured using DSC such as crystallization and glass transition temperatures [233].

The main applications of DSC include the phase transition characterization, such as melting point [117], glass transition [283], determination of crystallinity [284], kinetic studies [285], drug transformation and physical stability tests [286], material fingerprinting and purity control [287]. DSC is the most often used thermal analysis method, mainly because of its speed, simplicity, and convenience.

In this experiment a Perkin Elmer differential scanning calorimetry was used. Samples weighing between 3-12mg were weighed using an analytical balance in aluminium pans. The lids were clamped and the sample was placed in a sample holder. The

samples were heated at a constant rate of 20°C/min with the temperature ranging was from 50°C to 320°C.

3.3.2.3 X-ray powder diffraction (XRPD)

Single co-crystal and powder diffraction data contain the same structural information, except this information is distributed in three-dimensional (3D) space in the single co-crystal diffraction pattern, and is compressed into one dimension in the powder diffraction pattern [288]. It is important to fully characterise an API to define its crystal structure [289]. Different crystal structures comprise of distinct XRD patterns known as the 'fingerprint region' which allows for identification of different APIs, solvates, salts and co-crystals [290]. The structure determination shows the chemical composition of the crystal and provides geometric information about the molecules, the interplanar distances and the geometries of intermolecular interactions [291].

X-ray powder diffraction (XRPD) is a rapid analytical technique used for phase identification of a crystalline material and can provide information on unit cell dimensions [292].

In XRPD, the crystalline atoms cause a beam of incident X-rays to diffract in many specific directions. The angles and intensities of these diffracted beams can be measured to produce a 3D picture of the density of the electrons within the crystal. The mean position of the atoms, their chemical bonds and the states of disorder can be calculated from this 3D image [293]. The regular array of atoms in the crystals scatter the X-ray. An X-ray striking the electron produces an array of spherical waves in a phenomenon known as elastic scattering. Although these waves cancel one another out in most direction through destructive interference, they add constructively in a few directions, determined by Bragg's Law shown below.

Equation 10 - Bragg's Law

$$2d\sin\theta = n\lambda$$

Here d is the spacing between diffracting planes, θ is the incident angle, n is any integer, and λ is the wavelength of the beam. These specific directions appear as spots on the diffraction pattern called reflections. Thus, X-ray diffraction results

from an electromagnetic wave impacting on a regular array of scatters. These diffracted X-rays are then detected, processed, and counted. By scanning the sample through a range of 2θ angles, all possible diffraction directions of the lattice should be attained due to the random orientation of the powdered material. Conversion of the diffraction peaks to d-spacings allows identification of the mineral because each mineral has a set of unique d-spacings. This is achieved by comparison of d-spacings with standard reference patterns [294].

Single co-crystal and powder diffraction data contain the same structural information, except this information is distributed in three-dimensional (3D) space in the single co-crystal diffraction pattern, and is compressed into one dimension in the powder diffraction pattern [288].

A D2 PHASER diffractometer (Bruker U.K. Limited, Coventry, UK) of the PXRD provided the results from 5° to 35° at a scanning rate of $0.3^\circ (2\theta) \text{ min}^{-1}$. Cu $K\beta$ was the radiation source, and it was used at 30 kV, 10 mA.

3.3.2.4 Raman Spectroscopy

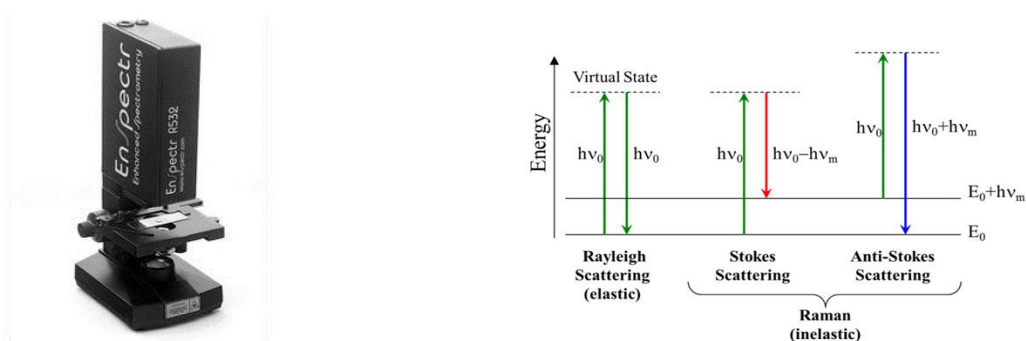
Raman spectroscopy has been effectively used in many studies of polymorphs, co-crystals, salts and solvates and involves their identification, structural characterisation, phase transformations and quantification in mixtures [295]–[297]. Raman spectroscopy is used to observe vibrational, rotational and other low-frequency modes in systems and provides information about molecular vibrations that can be used for sample identification and quantitation. It relies on Raman scattering of monochromatic light, usually from a laser in the visible, near-infrared or near-ultraviolet ranges on a sample and detecting the scattered light [298]. The Raman effect occurs when electromagnetic radiation affects a molecule and interacts with the polarisable electron density and the bonds of the molecule. For the spontaneous Raman effect, which is a form of inelastic light scattering, a photon excites the molecule from the ground state to a virtual energy state for a short period of time shown in Figure 11.

When the molecule relaxes it emits a photon and it returns to a different rotation or vibration state. The resulting scattered photon which is “emitted” or “scattered” can be of either higher – Stokes scattering- or lower – anti-stokes scattering - energy than the incoming photon [299]. In Raman scattering, the final vibrational state of the molecule

would be in a different rotational or vibrational state in comparison to the original molecule, before interacting with the incoming photon.

The difference in energy between the original state and this final state gives information about the vibration modes in the system, due to the vibration information being specific to the chemical bonds and symmetry of molecules. It therefore provides a fingerprint by which the molecule can be identified [300]. Raman technique is used for providing both structural and electronic insight into species of interest. Raman spectroscopy can be used for both qualitative and quantitative applications [295]. Raman bands are inherently sharper than their infrared counterparts; isolated bands are often present in the spectrum for more straightforward quantitative analysis. Raman spectroscopy has been used for the structure determination of nanoparticles [301], polymers [302], [303] and co-crystals [304], [305].

Figure 16 - EnSpectr R532 Raman Spectrometry and the Raman effect



Raman spectroscopy analysis is regarded as non-destructive, although lengthy irradiation with ultraviolet (UV) or visible light lasers in some samples can cause photodecomposition. As the Raman spectrum is acquired from a very small area, special care must be taken to make it representative for the whole material [299], [306].

In this experiment, En Spectr R532 Raman spectroscopy was used to study single co-crystals before and after dissolution in distilled water and water containing various polymers. The samples were placed in the sample holder. Single crystals were scanned at exposure time = 200ms and number of frames to collect = 600. Co-crystals were scanned at exposure time = 200ms and number of frames to collect = 100.

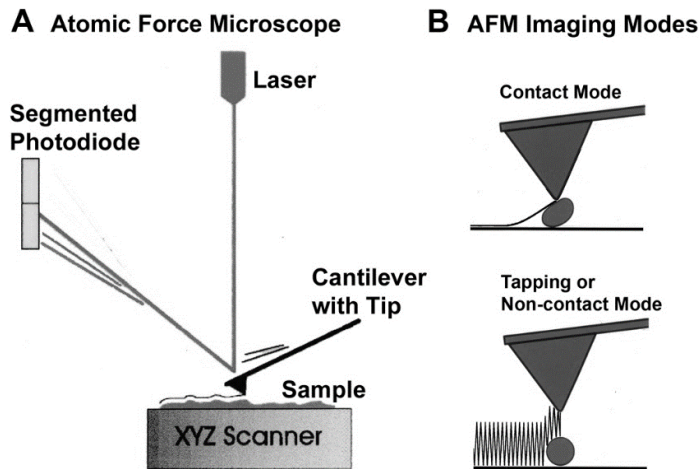
3.3.2.5 *Non-contact Atomic force Microscopy*

Atomic force microscopy (AFM) was invented in the early 1980s and has since had a major impact on the characterisation of surface structures. Increasingly, however, the method is being applied in looking at the topographic layer of crystals. AFM operate by measuring the force between a probe – a sharp tip with 15-40nm end radius- and a sample [307]. The probe is brought into close proximity of the sample surface and then scanned in a systematic manner. An image is acquired by measuring the vertical and lateral deflections of the cantilever by using an optical lever that works by reflecting a laser beam off the cantilever [308]. The reflected laser beam strikes a position-sensitive photo-detector that indicates the position of the laser spot on the detector and therefore the angular deflections of the cantilever. Direct contact of the tip with sample surfaces may damage the sample in some cases, therefore non-contact AFM is used. The non-contact forces the cantilever oscillation at resonance frequency [309]. The oscillating probe will be influenced by the close surface and therefore due to van der Waals attractive forces, produces a frequency shift in the resonance frequency. The signals recorded in non-contact mode are therefore related to the variation between cantilever resonance frequency and free oscillation of the system. This gives an estimate of the tip to sample interaction forces intensities [310].

The images produced by non-contact AFM may be determined by frequency variations related to fluctuations in frequency shift as a direct signal or as a feedback-loop signal. As a consequence, resonance frequency and oscillation amplitude both corresponds to the surface image formation [309]. Moreover, in order to minimize the attractive forces onto the tip close to the surface, the spring constant used in non-contact mode is greater than in contact mode. In recent years, atomic force microscopy has been used extensively to study various aspects of molecular crystals such as the mechanism of crystal growth [311] and additive-induced crystal growth inhibition [312].

The advantage of using AFM over other conventional microscopy techniques is that AFMs probe the sample and make measurements in three dimensions, x, y, and z, therefore enabling the presentation of three-dimensional images of a sample surface [313]. Major drawbacks of non-contact mode concern low lateral resolution and constrained use of the tip in air environment [314]. The operation of AFM is shown in the diagram below.

Figure 17 - AFM and Imaging Modes



3.3.2.6 Scanning electron microscopy

A scanning electron microscope (SEM) scans samples by scanning it with a focused beam which produces images.

The main SEM components include:

- Source of electrons
- Column down which electrons travel with electromagnetic lenses
- Electron detector
- Sample chamber
- Computer and display to view the images

Electrons are produced at the top of the column, accelerated down and passed through a combination of lenses and apertures to produce a focused beam of electrons which hits the surface of the sample [315]. The electrons would interact with atoms in the sample, that produces various measurable signals containing information about the sample's surface topography and composition. The electron beam is generally scanned in a raster scan pattern, and the beam's position is combined with the detected signal to produce an image [316].

In this study, SEM micrographs were photographed by a ZEISS EVO HD 15 scanning electron microscope (Carl Zeiss NTS Ltd., Cambridge, UK). The sample compacts

were mounted with Agar Scientific G3347N carbon adhesive tab on Agar Scientific G301 0.5" aluminium specimen stub (Agar Scientific Ltd., Stansted, UK) and photographed at a voltage of 10.00 kV. The manual sputter coating S150B was used for gold sputtering of SEM samples.

3.3.2.7 Nuclear Magnetic Resonance

NMR is a spectroscopy absorbs and re-emits electromagnet radiation in a magnate field which is used to study the chemical, physical and structural information of molecule in solution and to study molecular physics and crystals as well as non-crystalline materials [317].

The theory of NMR involves three consecutive steps [318]:

- The alignment of the magnetic nuclear spins in an applied, constant magnetic field.
- The distress of this alignment of the nuclear spins by a weak oscillating magnetic field known as a radio-frequency (RF) pulse.
- The NMR signal is detected during or after the RF pulse, due to the voltage being induced in a detection coil by precession of the nuclear spins.

All nuclei present in a molecule are charged and molecules with an odd number of electrons have a spin which creates a magnetic field [319]. A proton and neutron will have lower energy when their spins are parallel which causes an energy transfer to take place from a ground state to an excited state by absorbing radio frequency. The energy is then emitted when the excited state of the nuclei returns to its ground state [320]. The emitted frequency is converted to the chemical shift in ppm in an NMR spectrum. For proton NMR, the reference molecule is tetramethyl silane (TMS).

A change in the chemical shift occurs when the electron density around the nucleus is altered [321]. A high electron density around the nucleus leads to the shielding of the nucleus and causes a low chemical shift and triggers the signal to move up-field and vice versa.

Equation 11 - NMR chemical shift

$$\delta = \left(\frac{H_{ref} - H_{sub}}{H_{machine}} \right) \times 10^6$$

where H_{ref} = is the resonance frequency of the reference, H_{sub} = is the resonance frequency of the substance, and $H_{machine}$ = is the operating frequency of the spectrometer.

DOSY results are displayed as 2D spectra with the NMR chemical shift on the horizontal axis and the derived diffusion coefficients on the vertical axis.

An NMR spectrum gives the following information:

- The number of peaks indicate the different types of nucleus present.
- The location of the peak indicates the type of nucleus its chemical environment.
- The relative areas of the peaks give the relative number of each type of nucleus.
- Disruption in the peak, indicates that affected nuclei

NMR spectroscopy has been successfully used to study molecular structures of small molecules [322], characterise protein-ligand interactions [323] and in polymorph and co-crystal investigation [324] and polymer characterisation [325].

Diffusion-ordered spectroscopy (DOSY)

Diffusion-ordered spectroscopy (DOSY) is used to analyse a mixture based on pulsed field gradient spin (PFGSE) or stimulated (PFGSTE) echo measurements. Diffusion coefficient is characteristic of a given molecule, therefore, the NMR signals from species of different sizes can be easily distinguished [326]. One of the earliest methods of determining diffusion coefficient was to use the Stokes-Einstein equation. However, a more acceptable method now is by Wilke and Chang who have suggested a more general formula based on extensive experimental investigations.

Equation 12 - Diffusion coefficient by Wilke and Chang

$$D = \frac{7.4 \times 10^{-12} (\phi_s M_s)^{\frac{1}{2}}}{\eta_s V_D^{0.6}}$$

Where D is the diffusion coefficient, ϕ_s is a constant characteristic of a solvent; M_s is the molar mass of the solvent; T is the absolute temperature; η_s is the viscosity of the solvent; V_D is the LeBas molar volume.

Both ^1H NMR and DOSY-NMR measurements for each of the samples were carried with JEOL ECZ 600R series FT-NMR Spectrometer (JEOL Ltd, Tokyo, Japan). ^1H proton spectra were achieved after 64 scans, with a relaxation delay of 7s at a controlled temperature of 25°C. ^1H NMR spectra chemical shifts were analysed using Mnova 14.2.0 by Mestrelab. For DOSY-NMR measurements, stimulated spin echo with bipolar gradient pulses was employed to determine the molecule self-diffusion coefficient. DOSY spectra were achieved after 32 scans, with a relaxation delay of 6s, at a controlled temperature of 25°C. The gradient was from 0.3 – 300 mT/m with 14 gradual increments. The spectra were analysed using GNAT (General NMR Analysis Toolbox) and the diffusion coefficient was found from the table generated. DOSY results are displayed as 2D spectra with the NMR chemical shift on the horizontal axis and the derived diffusion coefficients on the vertical axis.

3.3.3 Calculating molecular dynamic properties

All equations were taken from the BIOVIA Materials studio handbook [258].

Binding energy ΔE_{bind} can accurately reflect the features of the components to study the interactions between the crystal surface and polymer because an interaction system can be formed between a polymer and crystal surface after the MD simulation. The molecular interaction can be evaluated by a single point total energy of each component in the system as shown in the equation below.

Equation 13 - Binding energy

$$\Delta E_{bind} = E_{system} - (E_{polymer} - E_{surface})$$

Where E_{system} is the total energy of the bonded polymer and crystal surface system, $E_{polymer}$ is the energy of the polymer and $E_{surface}$ is the energy of the surface.

3.3.3.1 Non-bond energies

Electrostatic (Coulombic) and van der Waals interactions are referred to collectively as non-bond interactions and are usually divided by the forcefield.

Electrostatic interactions

The electrostatic interaction arises from the unequal distribution of charge in a molecule which can be modelled by placing point charges at each atomic position using a forcefield [327]. Electrostatic interactions can be calculated by using the equation below.

Equation 14 - Electrostatic interaction

$$E_{elec} = \frac{1}{4\pi\epsilon_0} \frac{q_i q_j}{r_{ij}}$$

where ϵ_0 is the permittivity of free space, q_i are atomic charges, and r_{ij} is the distance between i and j.

Van der Waals interactions

Van der Waals interactions consists of all interactions between the atoms not covered by the electrostatic interactions [328]. This includes the dispersion, repulsion, and induction forces as well as others. Correlation between electrons in different atoms leads to dispersion interactions which attracts the atoms towards each other due to the reduced energy [329]. The overlapping of two electron clouds of two different atoms leads to repulsion forces. The distortion of the charge distribution of an atom or molecule in comparison to neighboring molecules leads to induction interactions [330].

Van der Waals forces shows large positive values of atomic repulsion at small distances and at large distances the dispersion interaction gives small negative values. This behaviour can be shown by the Lennard-Jones potential [331], shown below.

Equation 15 - Van der Waals interactions

$$E_{vdw}^{LJ} = 4\epsilon_{ij} \left[\left(\frac{\sigma_{ij}}{r_{ij}} \right)^{12} - \left(\frac{\sigma_{ij}}{r_{ij}} \right)^6 \right]$$

Where ϵ_{ij} is the Van der Waals well depth and σ_{ij} is the distance at which $E_{vdw}^{LJ} = 0$.

3.3.3.2 Hydrogen bonding

Hydrogen bonding is a dipole-dipole attraction between molecules that results from the attractive force between a hydrogen atom covalently bonded to a very electronegative atom such as a N, O, or F atom and another very electronegative atom [332].

Hydrogen bonds can occur between separate molecules known as intermolecular bonding or can occur among parts of the same molecule known as intramolecular bonding [333]. They are stronger than Van der Waals interactions and weaker than covalent bonds. The functional form of the hydrogen bond potential is shown below.

Equation 16 - Hydrogen bond

$$E_{hb} = \epsilon \left[\left(\frac{\sigma}{R_{D-A}} \right)^6 - \left(\frac{\sigma}{R_{D-A}} \right)^4 \right] \cos^4(\theta - \theta_0) SW(R_{D-A})$$

where ϵ is a weight or strength of the hydrogen bond interaction and σ is related to the distance R_0 at minimal potential.

Hydrogen bonds are the crucial to many phenomena, including molecular recognition [334], [335] and drug binding [336]. It also plays an important role in the structure of polymers [337], [338], both synthetic and natural.

3.3.3.3 Radial distribution function

Radial distribution function, also known as the pair correlation function, measures the probability that, given the existence of an atom at the origin of a random reference frame, there will be an atom with its center positioned in a spherical shell of minute thickness at a distance, r , from the reference atom [339]. This theory also states that the atom at the origin and the atom at distance r may be of different chemical types. The form for radial distribution function is shown below.

Equation 17 -Radial distribution function

$$x_{\alpha}x_{\beta}\rho g_{\alpha\beta}(r) = \frac{1}{N} \left[\sum_{i=1}^{N_{\alpha}} \sum_{j=1}^{N_{\beta}} \delta(r - r_i + r_j) \right]$$

Where x_{α} is the mole fraction of chemical type α , N_{α} is the number of atoms of chemical type α , N is the total number of atoms, and ρ is the overall number density.

Radial distribution function has been applied in structural investigations of local packing structures of both solids and liquids [340], in studying hydrogen bonding [341] and in statistical mechanical theories of liquids and mixtures [342].

3.3.3.4 Mean square displacement

Mean square displacement (MSD) analysis determines the average displacement of particles followed over time. It can be helpful in determining whether the particle is freely diffusing, being transported, or bound [343]. MSD can also estimate the parameters of movement i.e diffusion coefficient for freely moving molecules [344], [345]. MSD can be acquired from particle positions in an MD simulation.

In an equilibrium ensemble, the mean squared displacement must be independent of the time t , and can be averaged out, giving the mean square displacement over an interval Δt as shown below.

Equation 18 - Mean square displacement

$$MSD(\Delta t) = \frac{1}{r - \Delta t} \int_0^{r-\Delta t} [r(t - \Delta t) - r(t)]^2 dt$$

or

$$= \langle [r(t - \Delta t) - r(t)]^2 \rangle$$

where $r(t)$ is the position at time and t is the total simulation time.

3.4 Chapter conclusion

This chapter presented the materials, preparation and synthesis, analytical techniques and molecular dynamic properties used in this study. The name, formula, purity, and manufacturer of materials were presented followed by the working principle, application, instrumental setting, operation procedure and instrumental models of analytical techniques such as ATR-FTIR, DSC, XRPD, Raman spectroscopy, non-contact AFM, SEM and NMR. Finally, the molecular dynamic calculations to calculate properties such as non-bond energies, hydrogen bonding, radial distribution function and mean square displacement were shown.

Chapter 4 – Characterisation of Samples

4.1 Chapter Overview

In this chapter, FFA-NIC CO, FFA-TP CO and CBZ-NIC CO were prepared by using solvent evaporation and cooling crystallization methods. More detail on the preparation methods is given in Chapter 3. Different analytical techniques such as ATR-FTIR and XRPD were used to confirm the formation of co-crystals by comparing the spectra of individual components (FFA I, NIC, TP and CBZ) to the co-crystals FFA-NIC CO, FFA-TP CO and CBZ-NIC CO and physical mixtures to identify new chemical peaks. Physical mixtures are constituent substances not chemically combined. DSC was used to check whether a change in the melting point had occurred. The results of these analytical techniques show that all co-crystals were successfully synthesized.

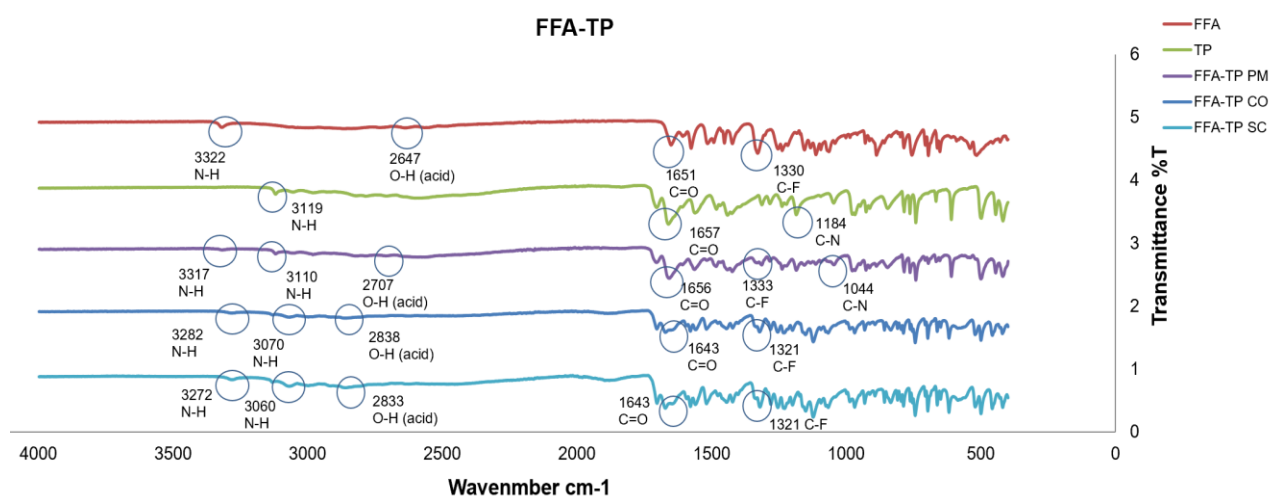
4.2 Materials and Methods

FFA I, NIC, TP, CBZ III, ethyl acetate, acetonitrile and double distilled water were used in this chapter and detailed introduction of this materials can be found in chapter 3. FFA-NIC CO and CBZ-NIC CO were formed by solvent evaporation method and FFA-TP CO was formed by cooling crystallization method. ATR-FTIR, DSC, XRPD and Raman have been used to characterize the formation of co-crystals. Details of co-crystals synthesis methods and these techniques were described in Chapter 3.

4.3 Results - Characterisation of cocrystals

4.3.1 ATR-FTIR

Figure 18 - ATR-FTIR spectra of FFA-TP

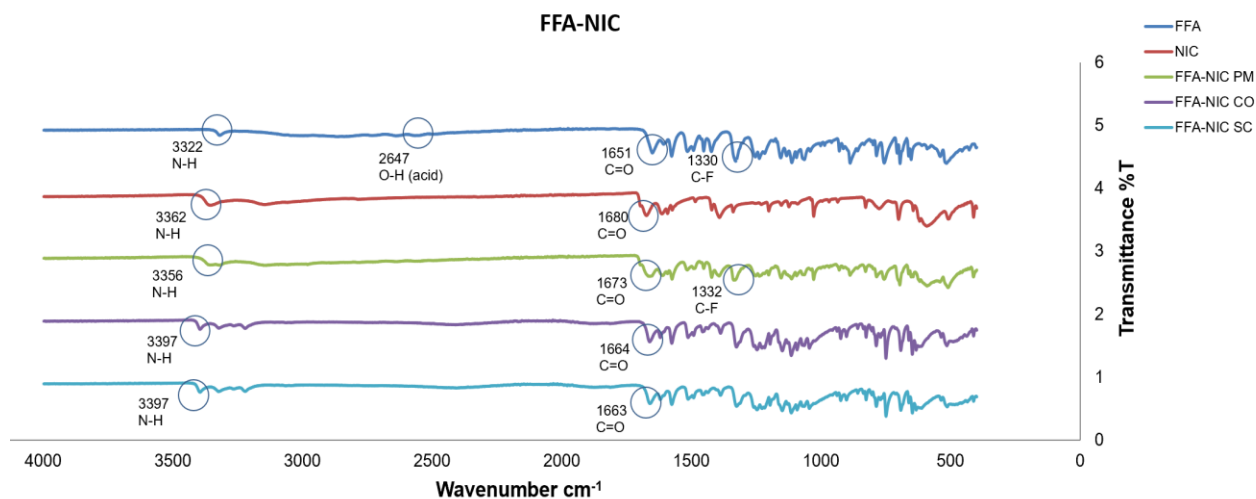


FFA-TP co-crystals are formed via hydrogen bonding. The carboxamide functional groups from both the FFA and TP provide hydrogen bonding donors and acceptors. The FTIR spectrum for FFA contains peaks at 3322 cm⁻¹ and 1651 cm⁻¹ which corresponds to bonds N-H stretch and C=O stretch forming the carboxamide functional group. The IR spectrum of the co-crystal contains two peaks at 3282 cm⁻¹ and 3070 cm⁻¹ corresponding to the N-H groups.

The spectrum shows a shift in the N-H bond contained in the FFA from 3322 cm⁻¹ to 3282 cm⁻¹ and a shift of the N-H in TP from 3119 cm⁻¹ to 3070 cm⁻¹. Further two shifts are also observed at 1651 cm⁻¹ and 1657 cm⁻¹ corresponding to the C=O group found in TP and FFA respectively. The table detailing the bonds and the frequency shifts can be found in Appendices A1. Therefore, the shifts of the IR spectrum suggest that FFA and TP are reformed in a new phase. The physical mixture shows a similar trend as the co-crystal, but the spectrum is very similar to the FFA and TP suggesting no new functional groups have been formed. FFA spectrum contains a peak at 1330 cm⁻¹ corresponding to the bond C-F. This bond is found in the physical mixture but has shifted in the co-crystal. All these changes that occurred in the spectrum indicates an interaction between FFA and TP hence the formation of the co-crystal. The single co-

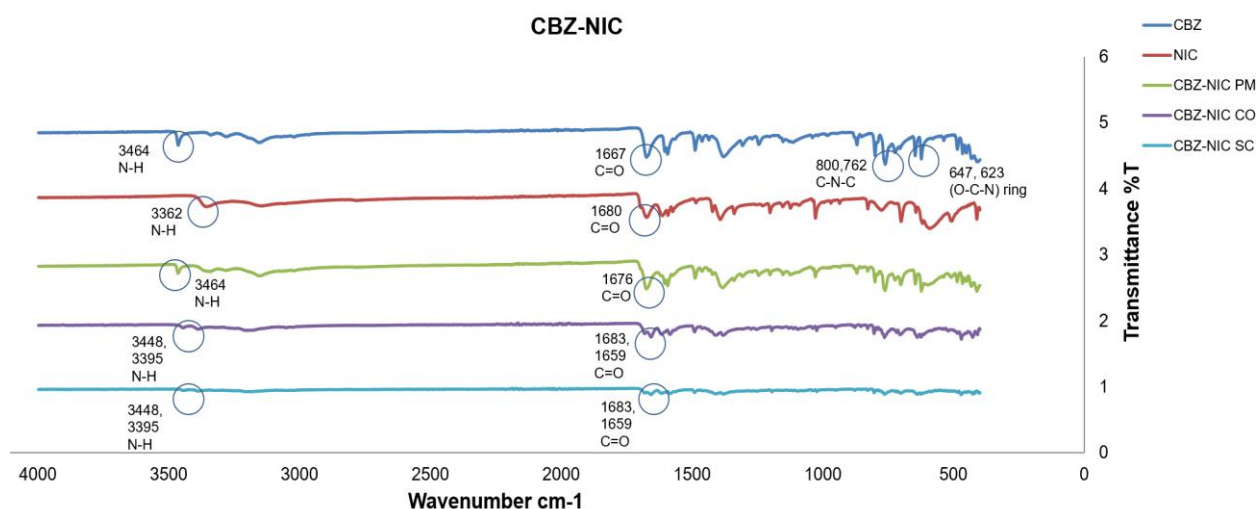
crystal contains the same peak as the co-crystal indicating the same structure for both. A list of the peak positions and assignments can be found in the Appendices Table 1 under ATR-FTIR.

Figure 19 - ATR-FTIR spectra of FFA-NIC



As shown in the figure above and Table 2 (Appendices), due to the formation of FFA-NIC Co-crystal, the NH bond in FFA has shifted to a higher frequency from 3322 cm^{-1} to 3397 cm^{-1} which indicates the formation of the carboxamide group. FFA contains a shift from 1651 cm^{-1} to 1664 cm^{-1} that attributes to the C=O stretching which suggests that the carbonyl group is taking part in the formation of hydrogen bond in the co-crystal. A shift is seen in the NIC from 3362 cm^{-1} to 3397 cm^{-1} contributing to the N-H group and a shift from 1680 cm^{-1} to 1664 cm^{-1} corresponding to the C=O bond (Appendices A1). This suggests that FFA and NIC have been reformed in a new phase. The single co-crystal contains the same peak as the co-crystal indicating the same structure for both.

Figure 20 - ATR-FTIR spectra of CBZ-NIC



CBZ-NIC co-crystals are formed via hydrogen bonds in which the carboxamide groups from both CBZ and NIC provide hydrogen bonding donors and acceptors. The spectra of CBZ-NIC co-crystals is different from those of CBZ and NIC, suggesting that both molecules are present in a new phase. CBZ's carboxamide N-H and C=O stretching frequencies shifted to 3448 and 1683 cm⁻¹ respectively. While NIC's N-H stretching frequency shifted to 3395 cm⁻¹ and the C=O stretching shifted to 1659 cm⁻¹ (Appendices A1). The spectrum of the CBZ-NIC physical mixture peaked at 3464 and 1676 cm⁻¹ due to the presence of CBZ III. A summary of IR peak identities for CBZ III, NIC and CBZ-NIC co-crystals and a mixture is shown in Table 3 in Appendices.

4.3.2 Differential Scanning Calorimetry

4.3.2.1 FFA-TP

Figure 21 - DSC spectra of FFA-TP

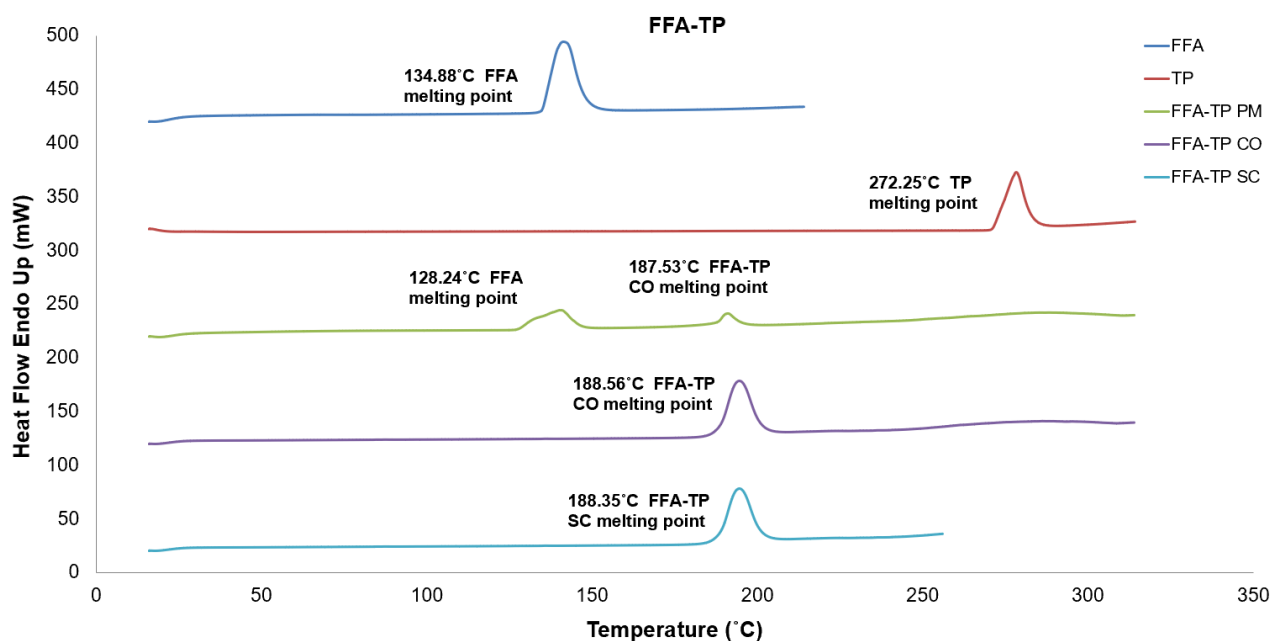


Table 2 - DSC onset and peak values of FFA-TP

Sample	Onset (°C)	Peak (°C)
FFA	134.88	141.11
TP	272.25	277.88
FFA-TP PM	128.24, 187.53	139.75, 191.15
FFA-TP CO	188.56	194.64
FFA-TP SC	188.35	193.99

The DSC curve shows that FFA melted at around 134.88°C and TP melted at around 272.25°C. FFA-TP physical mixture exhibited two major thermal events, with the first endothermic-exothermic peak at 128.24°C due to the melting of FFA and the co-crystallisation of FFA-TP co-crystals. The later endothermic peak, at around 187.53°C, results from the melting of newly formed FFA-TP co-crystals. Approximately 41.6% of

the physical mixture had converted to a co-crystal. For FFA-TP co-crystal, a single, sharp, endothermic peak was exhibited at 188.56°C. The melting point of the co-crystal also differs from the single components suggesting the formation of a new compound that is pure. These results are identical to results reported by Guo [140].

4.3.2.2 FFA-NIC

Figure 22 - DSC spectra of FFA-NIC

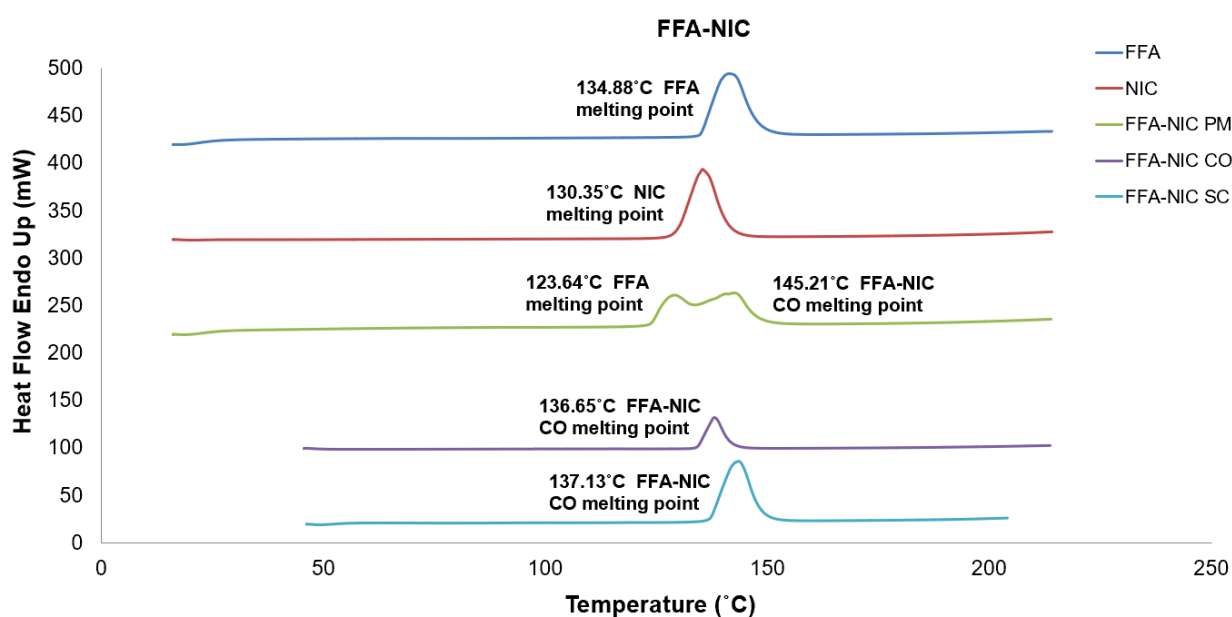


Table 3 – DSC onset and peak values of FFA-NIC

Sample	Onset (°C)	Peak (°C)
FFA	134.88	141.11
NIC	129.62	135.08
FFA-NIC PM	126.10, 157.87	130.14, 161.86
FFA-NIC CO	156.33	159.31
FFA-NIC SC	156.43	158.09

A DSC curve of pure NIC had a single peak at 129.62°C which contributes to the melting of NIC under heating. The DSC curve of FFA-NIC co-crystal shows a single

endothermic transition peak at 156.33°C resulting from the pure FFA-NIC Co-crystal. FFA-NIC Co-crystal had an obvious difference thermal behavior compared with pure FFA I, NIC and FFA-NIC physical mixture, demonstrating that FFA-NIC CO is a new compound. The findings are consistent with previous results published by Lazlo Fabian [155]. The DSC curve of FFA-NIC PM had a complex thermal behavior that showed two endothermic peaks compared with pure FFA and NIC. The first peak was due to the melting of NIC, and the later endothermic peak at 157.87°C is due to the melting of FFA-NIC CO. The results obtained from DSC of FFA-NIC CO agree with the results of Raman and FTIR. The single co-crystals also showed a similar thermal behaviour as the co-crystal.

4.3.2.3 CBZ-NIC

Figure 23 - DSC spectra of CBZ-NIC

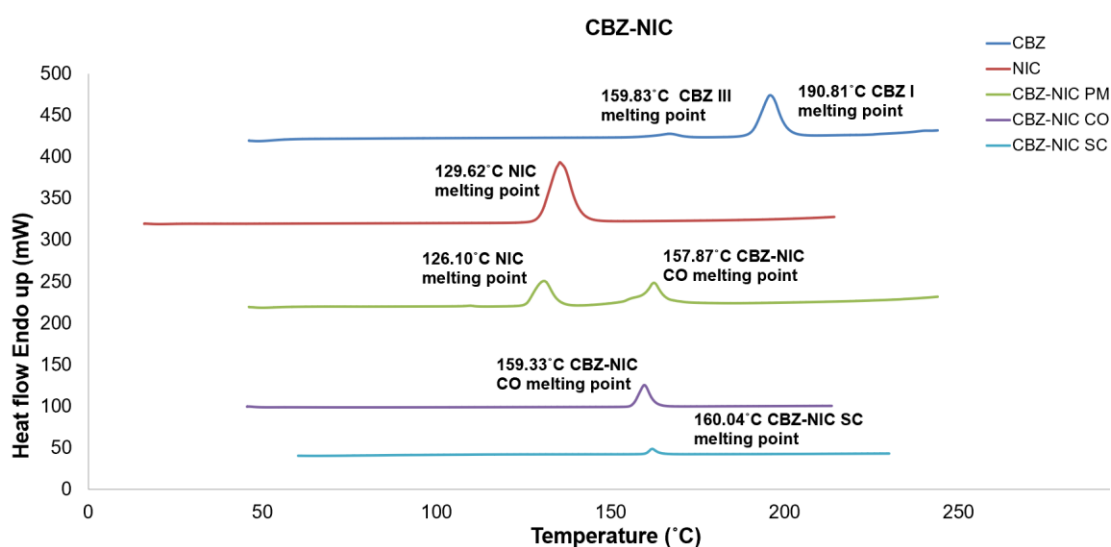


Table 4 - DSC onset and peak values of FFA-NIC

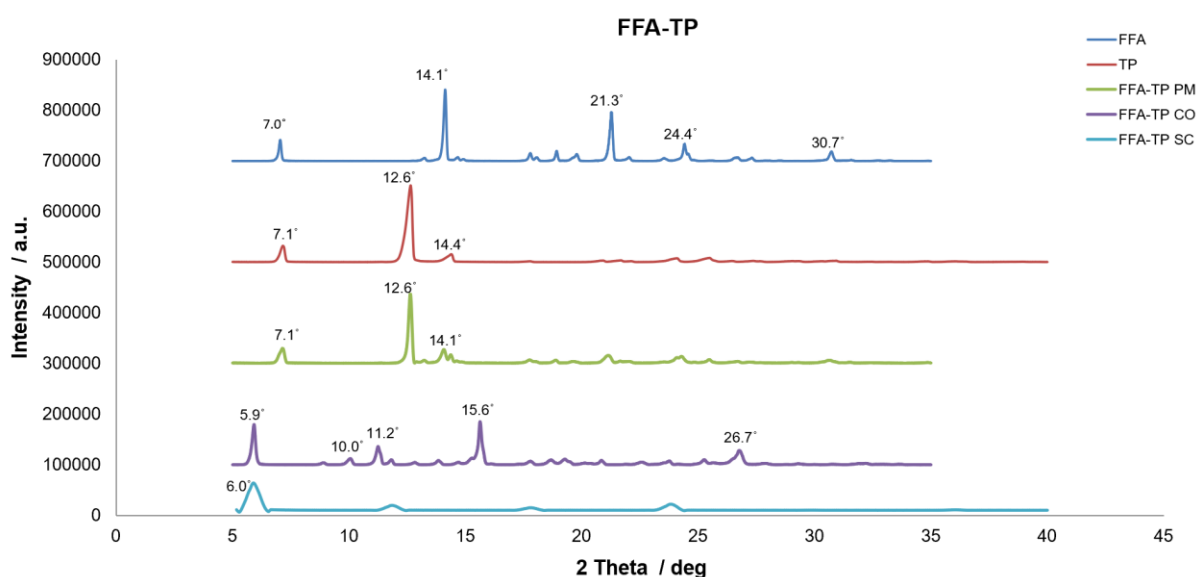
Sample	Onset (°C)	Peak (°C)
CBZ	159.83, 190.81	166.59, 195.59
NIC	129.62	135.08
CBZ-NIC PM	126.10, 157.87	130.14, 161.86
CBZ-NIC CO	159.33	160.31
CBZ-NIC SC	160.04	161.09

DSC curves patterns of CBZ III, NIC, CBZ-NIC co-crystals and a CBZ-NIC mixture are shown in Fig 19 and DSC data shown in Table 4.1. NIC melted at 129.62°C and the CBZ-NIC co-crystals had a single melted point of 156.33°C suggesting the formation of a new, pure compound. The CBZ-NIC mixture exhibited two major thermal events: the first endothermic-exothermic one being at 126.10°C due to the melting of NIC and the co-crystallisation of CBZ-NIC co-crystals, while the second endothermic peak, at 157.87°C contributes to the melting of newly formed CBZ-NIC co-crystals under DSC heating. These results are identical to those reported [346].

4.3.3 X-Ray powder diffraction

4.3.3.1 FFA-TP

Figure 24 - XRPD spectra of FFA-TP

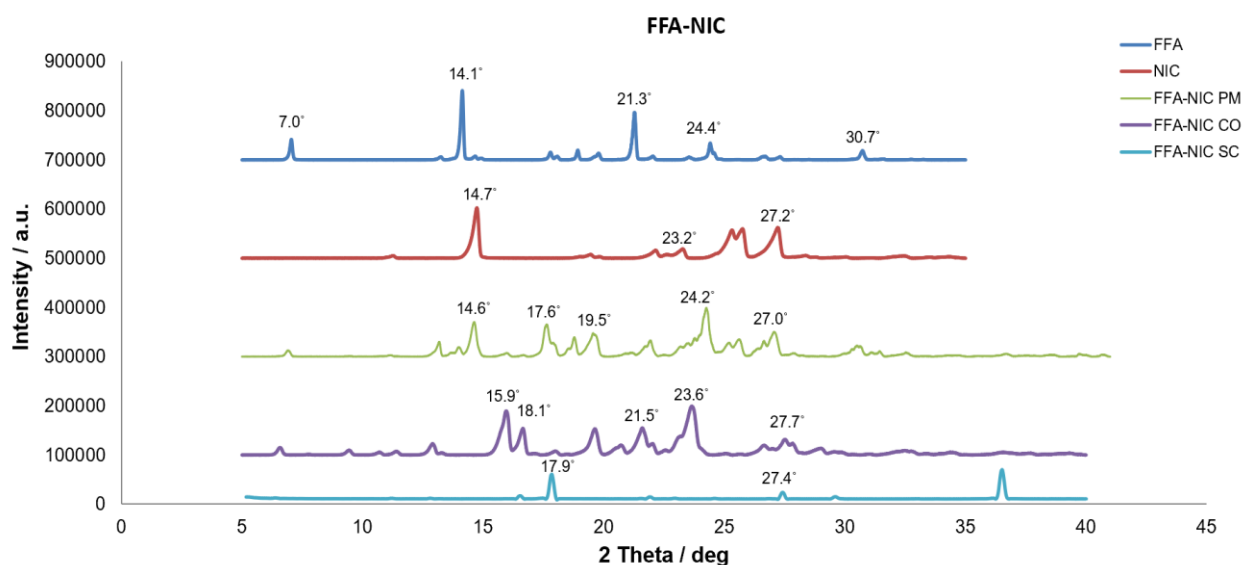


The characteristic peaks of FFA I are at $2\theta = 7.0^\circ$, 14.1° , 21.3° and 24.4° and 30.7° , all of which are identical to data reported by Guo [146]. TP's characteristic diffraction peaks are at $2\theta = 7.1^\circ$, 12.6° and 14.4° . FFA-TP co-crystals show the characteristic diffraction peaks at $2\theta = 5.9^\circ$, 10.0° , 11.2° , 15.6° and 26.7° , which agrees with previous reports. The physical mixtures showed the characteristic peaks of both FFA and TP at $2\theta = 7.1^\circ$, 12.6° and 14.1° respectively while the co-crystals show new peaks which corresponds to the formation of crystal structures. This indicates that the co-crystals

are of a completely new material and are not the same as the individual components or the physical mixture.

4.3.3.2 FFA-NIC

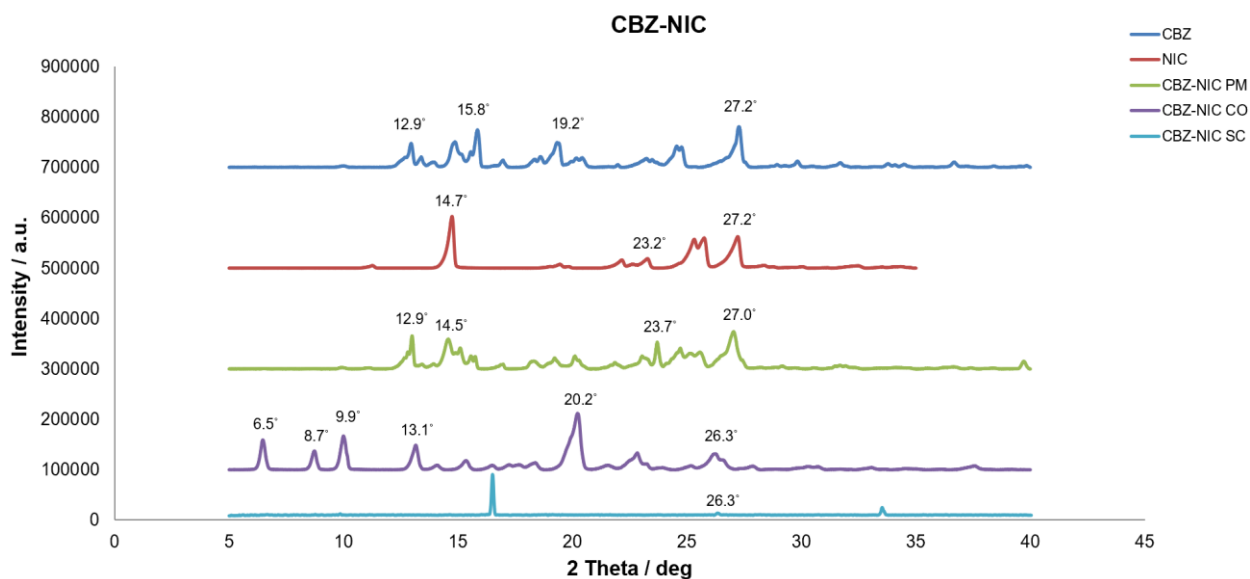
Figure 25 - XRPD spectra of FFA-NIC



NIC's characteristic diffraction peaks are at $2\theta = 14.7^\circ$, 23.2° and 27.2° . FFA-NIC co-crystals show the characteristic diffraction peaks at $2\theta = 15.9^\circ$, 19.6° , 21.5° , 15.6° and 23.6° , which agrees with previous reports [146]. The physical mixtures (not chemically bound) showed the characteristic peaks of both FFA and TP at $2\theta = 14.6^\circ$, 17.6° , 19.5° , 24.2° and 27.0° respectively while the co-crystals show new peaks which corresponds to the formation of a new crystal structure. The results agree with the DSC and FTIR data suggesting the formation of a new compound.

4.3.3.3 CBZ-NIC

Figure 26 - XRPD spectra of CBZ-NIC



The characteristic diffraction peaks of CBZ III are at $2\theta = 12.9^\circ$, 15.8° , 19.2° and 20.1° , all of which are identical to those of the reported data. NIC's characteristic diffraction peaks are at $2\theta = 14.7^\circ$, 23.2° and 27.2° . CBZ-NIC co-crystals show the characteristic diffraction peaks at $2\theta = 6.5^\circ$, 8.7° , 9.9° , 13.1° and 20.2° , which agrees with previous reports [346]. The physical mixtures showed the characteristic peaks of both CBZ III and NIC while the co-crystals show new peaks which indicate that the co-crystals are of a completely new material and are not the same as the individual components or the physical mixture.

4.4 Chapter Conclusion

In this chapter, samples of FFA I, NIC, TP, CBZ, 1:1 FFA-NIC CO, 1:1 FFA-TP CO and 1:1 CBZ-NIC CO were characterized by ATR-FTIR, DSC and XRPD. All characterized results demonstrated that FFA-NIC CO, FFA-TP CO and CBZ-NIC CO were formed successfully. DSC analysis showed the co-crystals had distinct melting points compared to its individual components. FTIR spectrum shows the hydrogen bonding formation between FFA with NIC or TP and between CBZ and NIC during co-crystals formation via $-\text{NH}_2$ and $-(\text{C}=\text{O})-$ bonding. XRPD spectra exhibited new characteristic diffraction peaks existing in co-crystals compared with the pure FFA I, NIC and TP which indicates the resulting component was not a physical mixture, but a new solid-state formation had been generated.

Chapter 5 – Investigating the effects of polymers on single crystals using experimental methods

5.1 Chapter overview

In this study, dissolution mechanisms of co-crystals in solution in the absence and presence of a pre-dissolved polymer was investigated. At the molecular level, we probed into how a co-crystal surface interacted with a polymer by investigating the etching pattern changes observed by using AFM, SEM and Raman spectroscopy in the presence/absence of polymers. To reduce the effect of viscosity, a low polymer concentration of 0.2mg/mL was used. The big faces of FFA I, FFA-TP CO, FFA-NIC CO, CBZ III and CBZ-NIC CO single co-crystals were determined using X-ray diffraction and molecular scale models of their morphologies were created using Mercury 3.9 (The Cambridge crystallographic Data Centre, Cambridge, UK). These morphology models were also used to explain the properties of each face of a single co-crystal. AFM and SEM was used to detect precipitation of the parent drug onto the surface of the single co-crystals and Raman spectroscopy was used to identify the precipitates. The surface roughness of the AFM measurements was calculated to give statistical data for comparison.

5.2 Materials and Methods

5.2.1 Materials

FFA I, NIC, TP, CBZ III, FFA-TP CO, FFA-NIC CO, CBZ-NIC CO, PEG, PVP, PVP-VA, ethyl acetate, acetonitrile and double distilled water were used in this chapter. Detailed information about these materials can be found in Chapter 3.

5.2.2 Powder FFA and CBZ Co-crystals Preparation

Co-crystals of FFA-NIC CO, FFA-TP CO and CBZ-NIC CO were used in this chapter, the detailed method can be found in chapter 3.

5.2.2 Experimental methods

5.2.1.1 Dissolution experiments of single co-crystals

Single co-crystals with well-defined and visually flat faces were carefully selected under a microscope for the etching dissolution studies. A single co-crystal was first mounted onto a cover glass using double-sided seal tape, in which the face of interest displayed at the top. The samples were then immersed in a beaker containing 20 mL of distilled water in the presence or absence of 0.2 mg/ml of PEG, PVP or PVP-VA. After a predetermined time interval shown in Table 5, the sample was taken from the solution and carefully patted using soft tissue papers to absorb the excess water. Finally, the sample was air-dried for at least 30 minutes before being studied by AFM, Raman spectroscopy and SEM.

Table 5 - Predetermined time intervals of dissolution studies

	Face index	Time (minutes)			
		DW (distilled water)	DW with PEG	DW with PVP	DW with PVP-VA
FFA-TP	(0,0,1)	10	10	10	10
FFA-NIC	(0,-1,1)	7	7	7	7
CBZ-NIC	(0,0,1)	2	2	2	2

5.2.1.2 AFM experiments

The big faces of single co-crystals of FFA-TP, FFA-NIC, and CBZ-CIN before and after the etching dissolution tests were observed using an atomic force microscopy (AFM). The measurements were carried out using non-contact mode at room temperature using an AFM (Park XE100 by Park Systems) with high-aspect-ratio and tapping mode probe tips (Team Nanotech, Wetzlar, Germany). Three scans were taken on the same area at $10 \times 10 \mu\text{m}^2$ for single co-crystals of FFA-TP and FFA-NIC and $5 \times 5 \mu\text{m}^2$ for single co-crystals of CBZ-NIC. The resolution of measurement was 512×512 points with equal steps along the x and y directions. Based on the 2D etching patterns, 3D images of the surfaces were constructed using XEI software programme (version. 4.3.0).

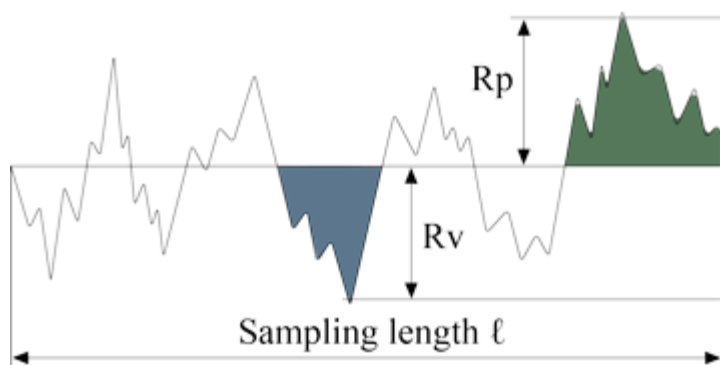
Build5, Park Systems) and the surface roughness (Ra) was calculated using the equation below (Equation 19). Ra is calculated as an average of the surface roughness measured by calculating microscopic peaks and valleys. Peak to valley height is a measurement of the maximum peak height and the maximum depth of the surface irregularities over a given sample length. The largest peak or depth is then accepted for measurement as shown in figure 27. The value is obtained by measuring the area of the material above the arbitrarily chosen base line in the baseline in the section and the enveloping rectangle.

Equation 19 - Surface Roughness (Ra)

$$Ra = \left(\frac{1}{L}\right) \int_0^L |Z(x)| dx$$

where L is the evaluation length and Z(x) is the profile height function.

Figure 27 - Peak to valley height measurement



5.2.1.3 Raman Spectroscopy

The surfaces of the single co-crystals before and after the etching dissolution tests were studied by Raman spectroscopy. In order to determine the precipitation behaviour of the parent drugs of single co-crystals after dissolution in distilled water in the absence and presence of various polymers, an EnSpectr R532[®] Raman spectroscopy (Enhanced Spectrometry, Inc. Torrance, USA) was used. The samples

were placed in the sample holder and scanned at room temperature using 20-30mV output power laser source with a wavelength of 532 nm. The integration time was 200ms, and each spectrum was obtained based on an average of 100 scans.

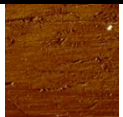
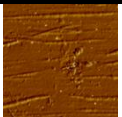
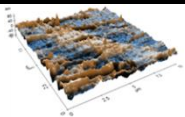
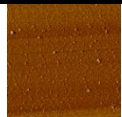
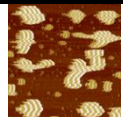
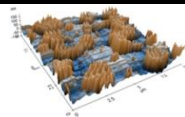
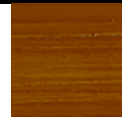
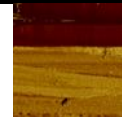
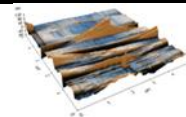
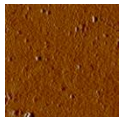
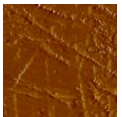
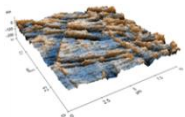
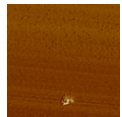

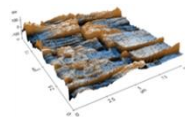
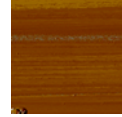

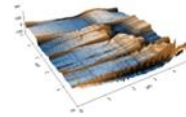
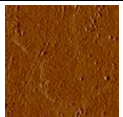
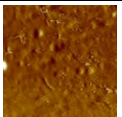
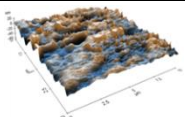
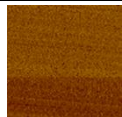

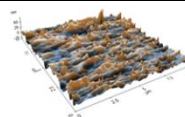


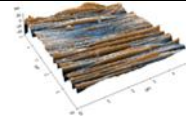
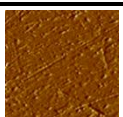

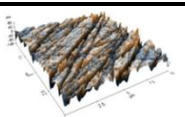

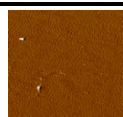
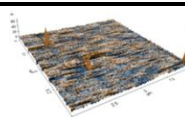
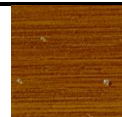
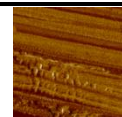
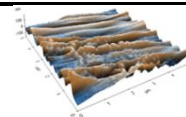
5.2.1.4 Scanning Electron Microscope

The surface topology of single co-crystals after the etching dissolution experiment was observed by scanning electron microscope (SEM) as the final step. In this study, SEM micrographs were photographed by a ZEISS EVO HD 15 scanning electron microscope (Carl Zeiss NTS Ltd., Cambridge, UK). The samples were first mounted with Agar Scientific G3347N carbon adhesive tab on Agar Scientific G301 0.5" aluminium specimen stub (Agar Scientific Ltd., Stansted, UK) and photographed at a voltage of 10.00 kV. The manual sputter coating S150B was used for gold sputtering of SEM samples. The thickness of gold coating was 15 nm. The results show the before and after dissolution images and indicates whether any parent drug has precipitated on the surface of the single co-crystals

5.3 Results

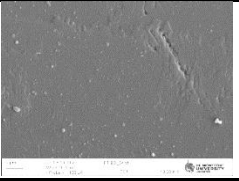
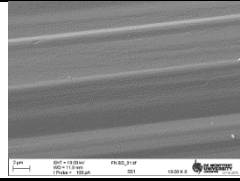
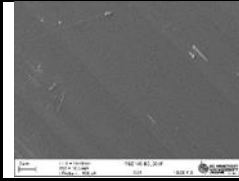
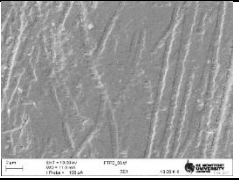
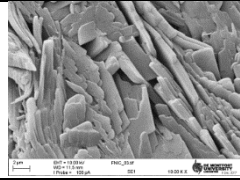
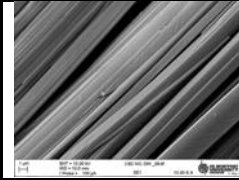
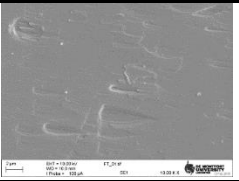
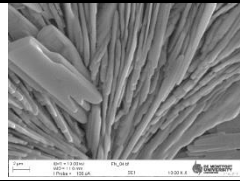
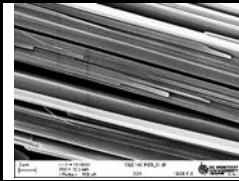

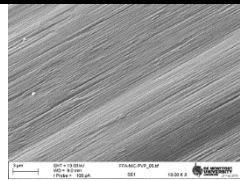
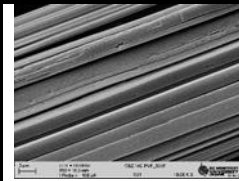
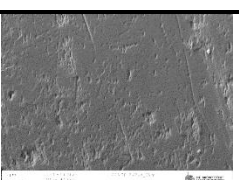
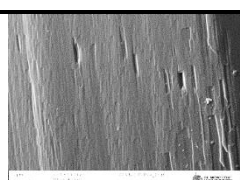
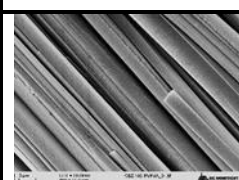
5.3.1 AFM results

Table 6 - AFM etching results of FFA-TP, FFA-NIC and CBZ-NIC co-crystal surfaces

	FFA-TP			FFA-NIC			CBZ-NIC		
	Before	After	3D and % increase	Before	After	3D and % increase	Before	After	3D and % increase
Distilled Water									
Ra (μm)	2.5	11.1	345	1.2	34.4	2862	0.9	10.7	1122
PEG									
Ra (μm)	3.3	20.8	522	2.2	24.9	1037	3.5	25.7	643
PVP									
Ra (μm)	3.4	7.2	115	1.9	7.6	300	1.0	4.0	316
PVP-VA									
Ra (μm)	6.6	20.1	206	0.6	2.6	325	0.8	34.1	3960

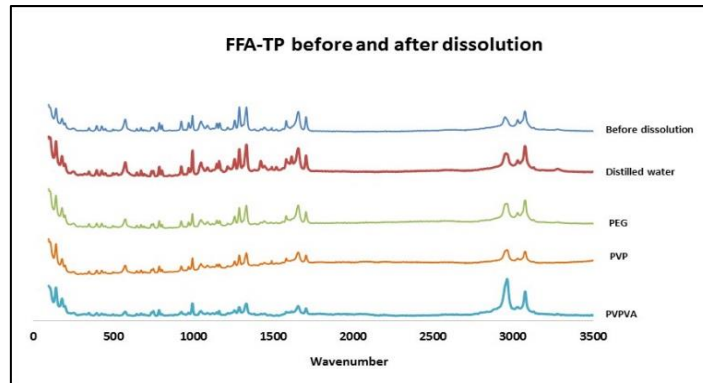
5.3.2 SEM experiments

Table 7 - SEM etching results of FFA-TP, FFA-NIC and CBZ-NIC co-crystal surfaces

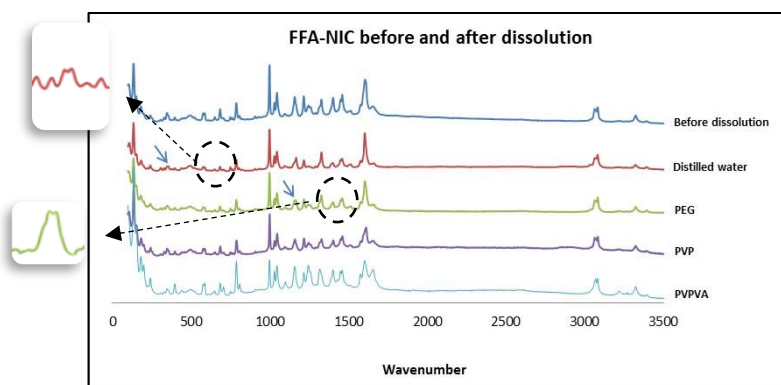
	FFA-TP	FFA-NIC	CBZ-NIC
Before dissolution			
Distilled water			
PEG			
PVP			
PVP-VA			

5.3.3 Raman experiments

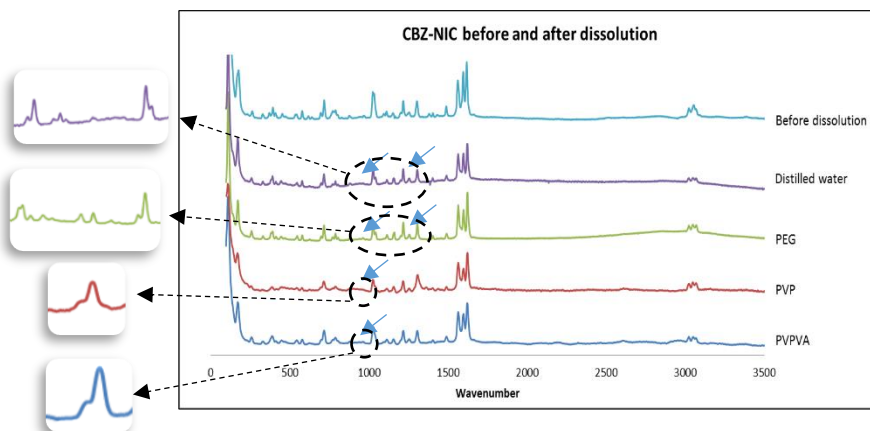
Figure 28 - Raman spectroscopy results of the co-crystal surfaces before and after etching experiments



(a) FFA-TP surface



(b) FFA-NIC surface



(c) CBZ-NIC surface

5.4 Discussion

The images created by the non-contact AFM of the faces of single co-crystals before and after the etching experiments were shown in Table 6. Prior to the etching experiments, the face (0-11) of FFA-NIC was relatively flat with its Ra valued from 0.6 to 2.2 μm . In comparison, the face (001) of FFA-TP and the face (011) of CBZ-NIC showed a high roughness from 2.5 to 6.6 μm and from 0.8 to 3.5 μm respectively. After etching in distilled water with or without PEG or PVP-VA, many small interpenetrating rectangle pits along with several long ditches formed on the face (001) of FFA-TP. On the other hand, circular pits appeared after etching with PVP. The roughness of the face (001) of FFA-TP increased after dissolution in all solutions, with a maximum increase of 522% in the presence of PEG and around 350% in distilled water. PVP caused a small increase of Ra, which was around 115%, and this was in contrast with the moderate increase caused by PVP-VA, which was about 206%.

The face (0-11) of FFA-NIC, showed no pits after etching in distilled water or in the presence of PEG. However, the roughness of the face significantly increased to 2862% after etching in distilled water and to 1037% in the presence of PEG. Small pits appeared on the same face (0-11) after etching in the presence of PVP or PVP-VA, accompanied by a moderate increase of roughness to 300% in the presence of PVP and to 324% in the presence of PVP-VA.

No pits were formed on the face (001) of CBZ-NIC after etching in distilled water with or without PEG, PVP or PVP-VA. A significant increase of the roughness was observed after etching in distilled water and in the presence of PVP-VA, 1122% in distilled water and 3960% in the presence of PVP-VA. A moderate increase of roughness, with a Ra of 643%, was seen for the same face (001) in the presence of PEG, and this was in contrast with that observed in the presence of PVP, which was 316%. AFM images and Ra values for the parent drug of FFA and CBZ can be found in Appendices A2.

SEM was used to detect changes in the surface of the co-crystals and to validate the images revealed by the AFM. Raman spectroscopy was used to detect any altered chemical properties of the etched co-crystal surfaces (Fig. 27). No change was observed for FFA-TP, indicating no precipitation occurred during etching. This was in consistent with that observed with SEM (Table 7), in which no particle was found on the co-crystal surfaces.

The characteristic peaks of FFA III were seen in Raman spectra after etching of FFA-NIC single co-crystal in distilled water and in the presence of PEG. It showed double peaks, one at 370 cm^{-1} after dissolution of FFA-NIC in distilled water and one at 1170 cm^{-1} after dissolution in PEG, which was characteristic to FFA III. This indicates that FFA III might have crystallised on the surfaces of FFA-NIC surfaces during etching. This proposal was supported by the SEM images (Table 7), demonstrating the presence of rectangular shaped crystals on the dissolving surfaces of FFA-NIC. There was no change observed for the surfaces of FFA-NIC in the presence of PVP or PVP-VA (Table 6). This seemed to be consistent with the results obtained by SEM (Table 7), which showed pits on the surface of the co-crystal. These results indicated that the recrystallization of the parent drug, FFA, might have been inhibited during co-crystal dissolution due to the effect of PVP or PVP-VA.

The particles that had recrystallised were clearly shown on the surfaces of CBZ-NIC (Table 7) after etching with or without PEG, PVP or PVP-VA. While the Raman spectra of the same surfaces (Fig. 27) showed that, in the absence or presence of PEG, the surfaces of CBZ-NIC were the same as those of CBZ dihydrate, from which the characteristic double peaks of 1030 cm^{-1} and triple peaks between 780 cm^{-1} to 820 cm^{-1} were shown. This suggested that the CBZ dihydrate could have recrystallised and completely covered the surfaces of CBZ-NIC. In the presence of PVP or PVP-VA, the Raman spectra of the surfaces of CBZ-NIC surfaces displayed as combined spectra of CBZ-NIC and CBZ dihydrate (Fig.27), indicating that PVP or PVP-VA during the dissolution of the co-crystal should be able to partially prevent the recrystallization of CBZ dihydrate. The SEM images for the parent drugs FFA and CBZ can be found in Appendices A3.

The etching experiments carried out in this research exhibited FFA-NIC and CBZ-NIC as surface precipitation co-crystals, and FFA-TP as bulk precipitation co-crystals. Both PVP and PVP-VA proved to be good surface precipitation inhibitors for FFA-NIC, and demonstrated they could completely inhibit the recrystallization of FFA III on the surface of FFA-NIC. In contrast, PVP and PVP-VA could only partially inhibit the recrystallization of CBZ dihydrate on the surface of CBZ-NIC while PEG was not considered as surface crystallization inhibitor for FFA-NIC and CBZ-NIC. The presence of PVP or PVP-VA decreased the dissolution rate of FFA-TP, lowering the solubility and dissolution of the co-crystals. Therefore, for bulk precipitation co-crystals, an addition of a solubilizer, such as PEG, to the formulation should greatly enhance the efficiency of dissolution.

5.5 Chapter conclusion

In this chapter, the effects of PEG, PVP and PVP-VA was investigated as surface precipitation inhibitors. AFM and SEM were used to look at etching patterns on the surfaces of co-crystals before and after dissolution in distilled water in presence of with/without PEG, PVP or PVP-VA. Raman spectroscopy was used to identify the chemical change on the surface of co-crystals which would indicate recrystallisation of parent drug. FFA-NIC and CBZ-NIC showed recrystallisation on the surface – identified using Raman spectroscopy - as the parent drug of FFA III and CBZ dihydrate had recrystallized on the surface of FFA-NIC and CBZ-NIC respectively. FFA-NIC and CBZ-NIC exhibited surface precipitation while FFA-TP showed no precipitation on the surface but could have precipitated in the bulk solution. Both PVP and PVP-VA proved to be good surface precipitation inhibitors for FFA-NIC and could only partially inhibit the precipitation of CBZ-NIC.

Chapter 6 - Investigating the influence of polymers on co-crystal dissolution using Molecular Modelling Techniques

6.1 Chapter overview

In this chapter, the influence of polymers PEG, PVP and PVP-VA on co-crystal dissolution surfaces was investigated using molecular modelling techniques. The morphology of single co-crystals and XRPD patterns were predicted and compared to the experimental shapes and XRPD patterns. Polymers of PEG, PVP and PVP-VA were built using a polymer builder and were energy minimised using anneal dynamics. The polymer-co-crystal surface system was built and molecular dynamic simulations were run. The molecular interactions – hydrogen bonding, electrostatic attractions and van der Waals – were calculated as well as the mean square displacement.

6.2 Molecular modelling methods

6.2.1 Single co-crystal morphology prediction and face indexing

To detect the exposed co-crystal faces to the dissolution media during AFM measurements, the morphologies of the co-crystals were produced using Mercury CSD 4.1.2 (The Cambridge crystallographic Data Centre, Cambridge, UK). Using Conquest 2.0.1 (reference codes: ZIQDUA for FFA-TP, EXAQAW for FFA-NIC, and UNEZES for CBZ-NIC) from the Cambridge Structural Database (CSD), the unit cells of single co-crystals were obtained. The morphology of a single co-crystal was predicted using the Bravais-Friedel-Donnay-Harker (BFDH) crystal morphology tool. The predicted morphologies were then validated through comparing the predicted XRD patterns using Powder diffraction in the Reflex module (BIOVIA Material studio 2017 R2) with experimental measurements. The index of a crystal face was determined by comparing the observed crystal shape with the simulated morphology.

6.2.1 Building of polymer using polymer builder

Polymers of PEG, PVP and PVPVA were built using the polymer builder in Material studio. It would have been ideal to build a whole polymer chain of each polymer used in the simulations, as the number of monomers would affect its properties and the interactions of polymer molecules with the crystal surface. However, to save computational time and resources and to generate comparable results with experiments, the polymers of PEG and PVP built represented 20% of the real polymer weights, i.e., the numbers of monomer units were given as 18 for PEG and 72 for PVP. The chemical structure of a monomer of PEG or PVP was illustrated, from which the head and tail atoms were specified to expand the required chain length of the polymer at a torsion angle of 180° . For PVP-VA however, it was a bit complicated and had to be made smaller (Table 8). The number of monomers of PVP used was 303 and the number of VA was 202 in the etching experiments shown in Table 9. To confine PVP-VA in the simulation box, the number of monomers had to be decreased to 10% of its real polymer weight, i.e., 31 for PVP monomers and 21 for VA monomers. The monomers of PVP and VA were drawn individually and were then connected randomly as a copolymer of PVP-VA using the polymer builder.

For the conformational structure of a polymer, in order to find the global minimum of potential energy, anneal dynamics was performed by periodically increasing and then decreasing the temperature from 100 to 1000K over 10 annealing cycles. Anneal dynamics was performed at NVT (constant number of particles, constant volume, and constant temperature) ensemble at the time step of 1fs. The lowest energy of the polymer configuration was selected for MD simulation. The illustration of the procedure is shown in Fig. 29. The final structure of each of the polymers with minimised energy is shown below (Table 8).

Table 8 - Structure of polymers built using the polymer builder

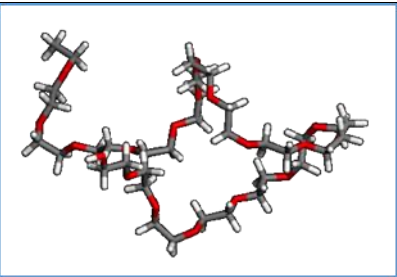
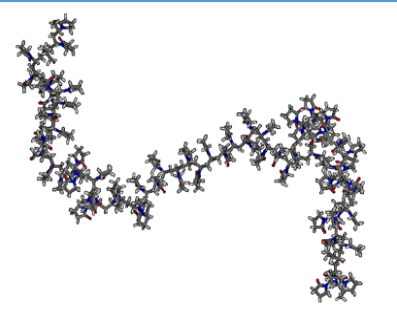
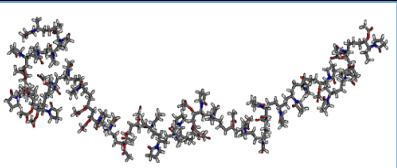
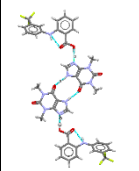
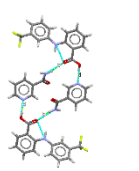
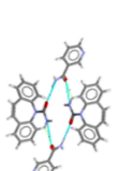
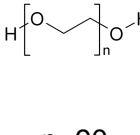
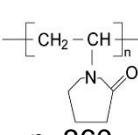
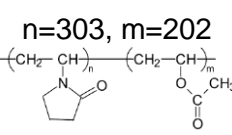
Polymer	Structure	Total energy (kcal/mol)
PEG		109.960825
PVP		1728.680229
PVP-VA		3218.723873

Table 9 - The molecular structures, weights, and no. of monomers of co-crystals and polymers

	FFA-TP	FFA-NIC	CBZ-NIC	PEG	PVP	PVP-VA
Molecular structure				 n=90	 n=360	 n=303, m=202
Molar weight of material used in the experiments	922.78	806.70	716.78	4000	40,000	51,000
Number of monomers used in the simulations	-	-	-	N=18	N=72	N=31, M=21

6.2.2 Building of crystal surface

The unit cells of co-crystals of FFA-TP, FFA-NIC, and CBZ-NIC which was taken from CSD were imported to material studio. Steepest descent algorithm in Forcite module for energy minimization was used to optimise the geometries of the unit cells. Details of each unit cell after the geometry optimisation as well as the size of the simulation boxes can be found in the table below (Table 10). The surfaces of each individual crystals with a depth of two unit-cells was then generated by cleaving the required face corresponding to the AFM measurements. For the polymers to be contained, the crystal surfaces were extended at U and V directions at different magnitudes shown in Table 10. Above the crystal surface, a thick vacuum slab of 100Å was built for each of crystals studied which forms the simulation box.

Table 10 - Simulation box details on FFA-TP, FFA-NIC and CBZ-NIC

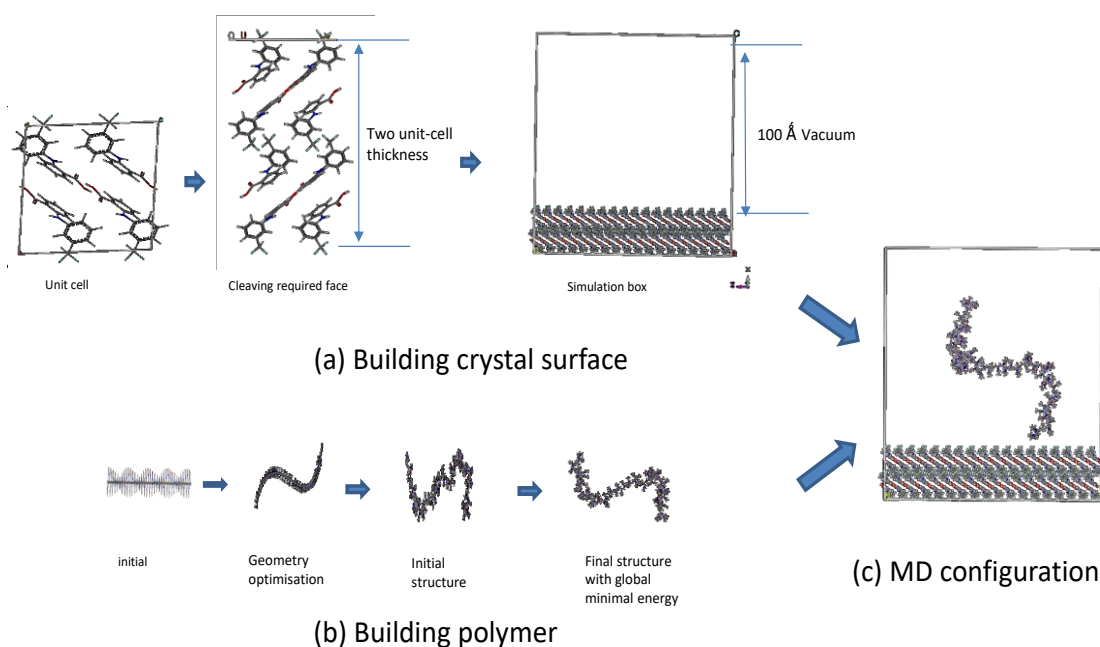
Drug	Surface index	Number of Unit cells for crystal layer			Dimensions of the simulation box (Å)		
		U	V	thickness	a	b	c
FFA-TP	(0,0,1)	12	11	2	83.9172	111.397	136.017
FFA-NIC	(0,-1,1)	18	4	2	91.8972	109.106	129.989
CBZ-NIC	(0,0,1)	18	5	2	91.7298	131.870	126.690

6.2.3 Building polymer and crystal surface together

Prior to a MD simulation, each of the polymers was placed approximately 5Å away from the centre of a crystal surface. The initial position of a polymer on the crystal surface could vary slightly, but it was found that the simulation results were not affected. The polymer-crystal system was first subjected to geometry optimisation by using the steepest descent algorithm until the energy had reached a minimum. The crystal surface was fixed before starting a MD simulation and therefore only the polymer was movable during the time of simulation. MD simulations were performed using periodic boundary conditions at NVT ensemble and the temperature was set at 298K. The cut-

off for non-bonded interactions of van der Waals and electrostatic were 12.5\AA and for Hydrogen bonds it was 4.5\AA . Simulations were run for 150ps at a time step of 1fs until equilibrium had reached evidenced by a plateau on the energy vs time graph (Appendices A4 Table 1). Nosé–Hoover thermostat algorithm was used to control the temperature. MD simulations were then proceeded for a further 50ps at the same settings for data analysis. Data was saved every 5ps for each of the MD simulations. Forcite analysis tools was used to analyse the MD results, including mean square displacement (MSD) and binding energy between the polymer and crystal surface.

Figure 29 - Illustration of molecular dynamic procedure

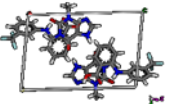
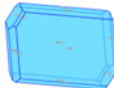

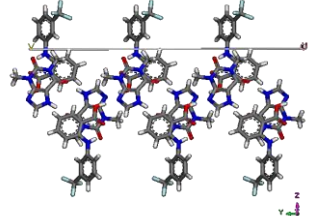
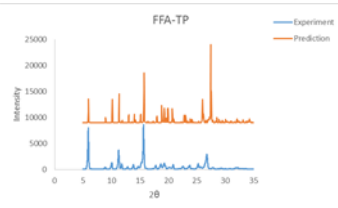
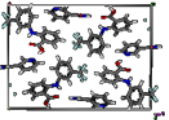
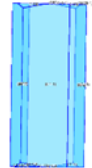

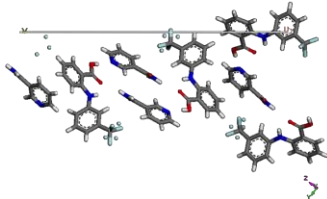
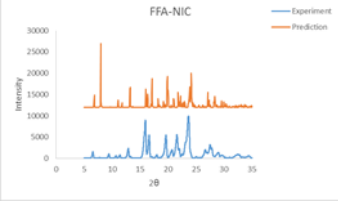
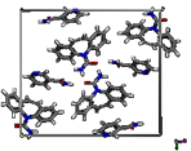
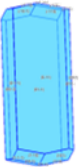
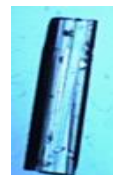
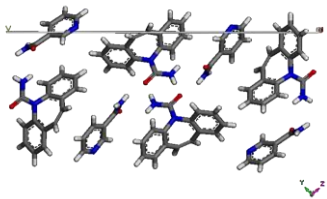
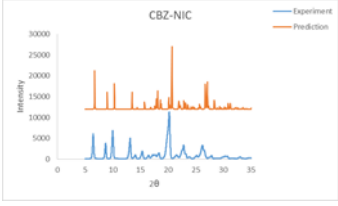


6.3 Results

6.3.1 Morphology prediction and face indices of co-crystals

The morphologies of the co-crystals were predicted using Mercury CSD 4.1.2 (Table 11), which was consistent with the observed images of the co-crystals. Comparison of the predicted XRD patterns with the experimental XRPD results (Table 11) confirmed the structures of the predicted co-crystals, verifying all the key characteristic peaks of the co-crystal allowing to be predicted accurately. The predicted morphology of FFA-TP showed dominant big faces of (001) and (00-1), large side faces of (0-10) and (010) and smaller side faces of (100) and (-100). The dominant face of (001) exposes trifluoromethylbenzene from the FFA at a perpendicular angle. This suggested that the reactive functional groups had the least exposure on the dominant faces, whereas the side faces were more reactive due to the existence of more hydrogen-bond donors and acceptors. The predicted morphology of FFA-NIC showed the dominant faces of (0-11) and (01-1), the smaller faces of (011) and (0-1-1) and the smallest faces of (-100) and (100). The functional group exposed on the dominant face (0-1-1) were carbon, fluorine and hydrogen atoms. The morphology of CBZ-NIC displayed the dominant faces of (011) and (0-1-1), and the smaller faces of (01-1) and (0-11), where the face (011) exposed the ring from Carbamazepine and nicotinamide which comprised of the N atom.

Table 11 - Predicted morphologies, surface and XRD comparison of single co-crystals

	Reference code	Unit cell	Morphology prediction	Experimental morphology	Face index (figure showing chemistry)	Surface studied	XRD Comparison
FFA-TP	ZIQDUA				(0,0,1)		
FFA-NIC	EXAQAW				(0,-1,1)		
CBZ-NIC	UNEZES				(0,1,1)		

6.3.2 Using MD simulation to identify the effect of polymers on co-crystal dissolution

Molecular dynamic simulations were conducted to determine the dynamic behaviour change of polymers on the surfaces of co-crystals. A simple system was chosen by not including any solvent molecules in the work. This was differed from the real system; the simulated results only aimed to serve as qualitative indicators of the inhibitory effects of polymers on the precipitation of the parent drug during dissolution. Nonetheless, the MD simulation allowed the visualization of the kinetic effects of polymers on the surfaces of co-crystals. Tables 12-14 shows the polymers approaching the surfaces of FFA-TP, FFA-NIC and CBZ-NIC and a summary of the polymer stabilisation time is presented in Table 15. The final polymer conformations on the surfaces of the co-crystals and the interaction energies are presented in Table 16 and Table 17 respectively.

Table 13 shows the mechanism of PEG, PVP and PVP-VA as it approaches and adsorbs on the surface (0-11) of FFA-NIC. PEG reached equilibrium within 30ps on the surface of FFA-NIC. There was a stable adsorption of PEG on the crystal surface. Both PVP and PVP-VA were able to move towards and interact with the surface of FFA-NIC after 10 ps. PVP started to adsorb on the surface after 60ps, and the whole PVP coiled and distributed evenly. Whereas some fragments of PVP-VA chain seemed to be quite far away from the surface, the PVP-VA chain distributed evenly on the co-crystal surface after 150 ps. These indicates that PVP-VA have the lowest adsorbing rate on the surface when compared to the other polymers. When comparing the face (001) of FFA-TP and CBZ-NIC, PEG had the fastest adsorbing rate and PVP-VA had the lowest one. The snapshots taken at different simulation times were shown in Table 12 and Table 14, respectively.

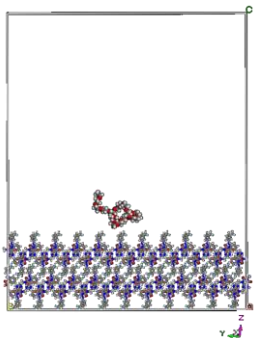
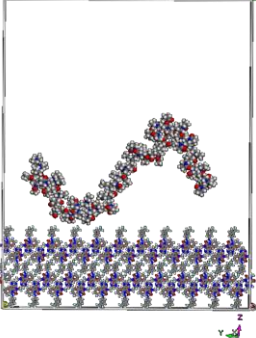
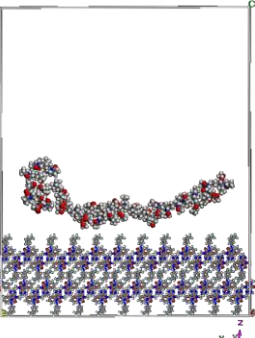
The conformation of polymers on the surfaces of co-crystals at the equilibrium point of 200ps is shown in table 16. The intermolecular interaction energies between the polymers and the surfaces of co-crystals surfaces were calculated at the same time (Table 17). All of the calculations showed negative values, implying that the adsorption process of the polymers on the surfaces of co-crystals were exothermic. Among the chosen polymers, PEG had the lowest binding, electrostatic and van der Waals energies and laid flat and straight against the surfaces of the co-crystals (table 16). PEG could only form hydrogen bonding with the surface (001) of FFA-TP, due the arisen O from TP and OH from PEG (table 16), with the energy of the hydrogen bond being

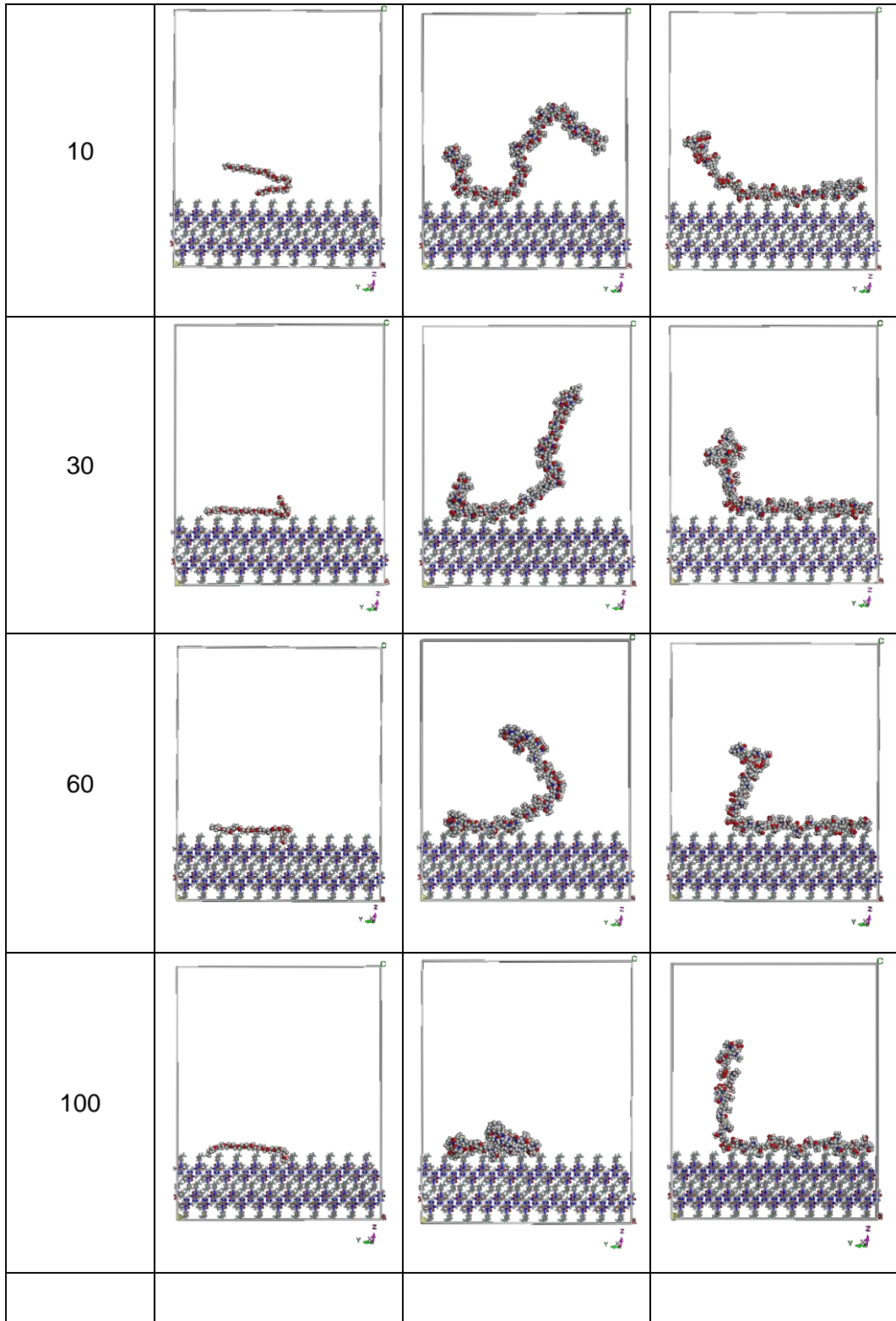
extremely low. Neither the face (0-11) of FFA-NIC nor the face (011) of CBZ-NIC formed hydrogen bonds with PEG, due to the lack of hydrogen bond donor or receptor on the surfaces of the co-crystals (Table 11). The binding and van der Waals energies for PVP and PVP-VA were comparable (Table 17), and no hydrogen bonding was observed between PVP or PVP-VA on the surfaces of the co-crystals.

The negative electrostatic energy for PVP was strong whereas the van der Waals interaction was weak. As shown from the conformations at equilibrium (table 16), PVP did not spread out on the surfaces of the co-crystals. Instead, it coiled up, particularly for the surface (0-11) of FFA-NIC. The van der Waals energies and electrostatic attractions between PVP-VA and the surfaces of the co-crystals were similar. And PVP-VA was able to spread out and bind to the surfaces of the co-crystals (table 16).

Table 18 shows the mean squared displacement and demonstrates the mobility of the polymers on the surfaces of the co-crystals. It seemed that PVP-VA had the highest mobility for the surface (001) of FFA-TP and the surface (0-11) of FFA-NIC. PVP had a slightly higher mobility than PEG for the surface (0-11) of FFA-NIC. No significant difference was observed for the mobility of PEG, PVP or PVP-VA for the surface (011) of CBZ-NIC.

Table 12 - Snapshots of polymers on FFA-TP surfaces at 298k at 0, 10, 30, 60, 100 and 150ps

Time (ps)	FFA-TP		
	PEG	PVP	PVP-VA
0			



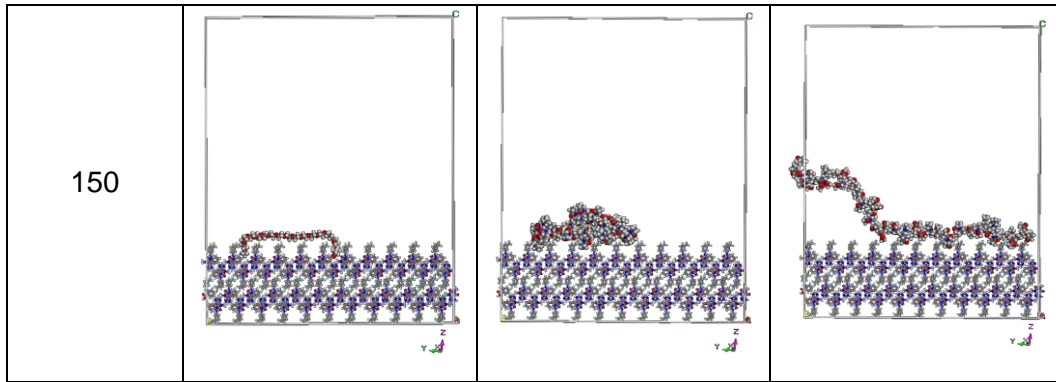


Table 13 - Snapshots of polymers on FFA-NIC surfaces at 298k at 0, 10, 30, 60, 100 and 150ps

Time (ps)	FFA-NIC (0-11) surface		
	PEG	PVP	PVP-VA
0			
10			
30			

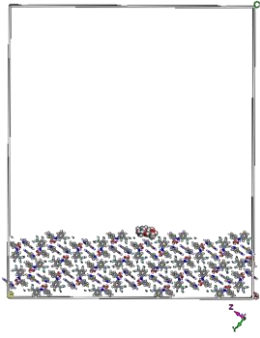
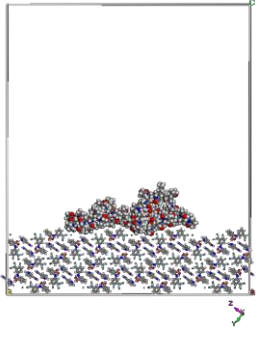
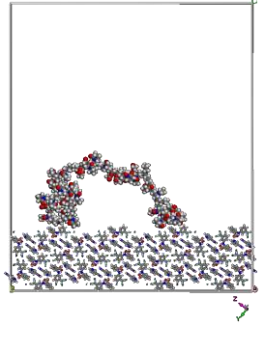
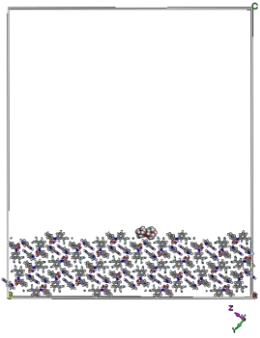
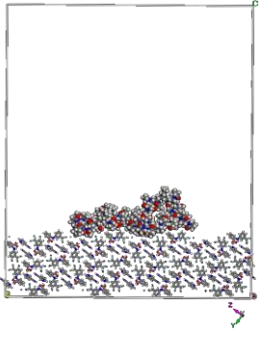
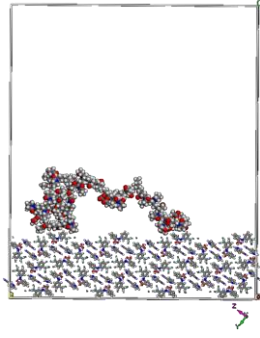
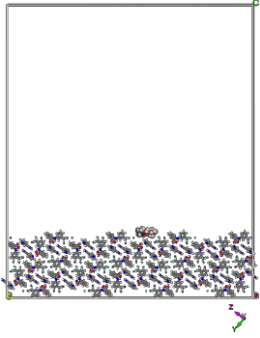
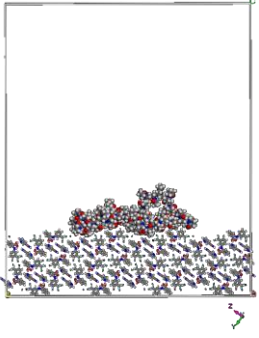
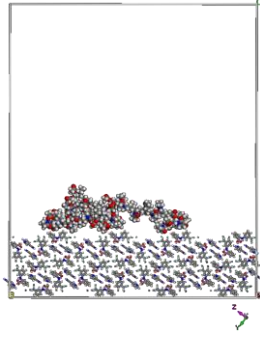
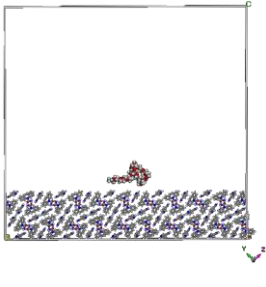
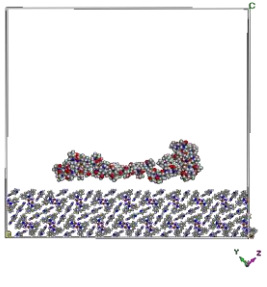
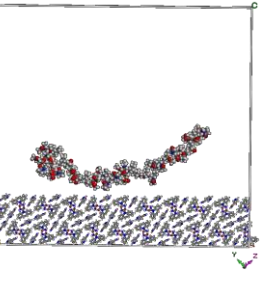
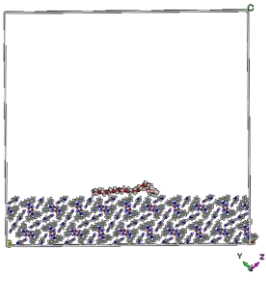
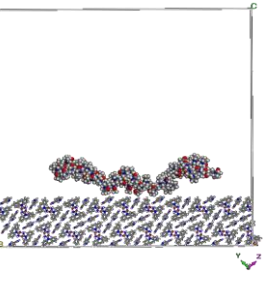
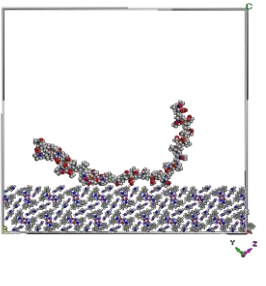
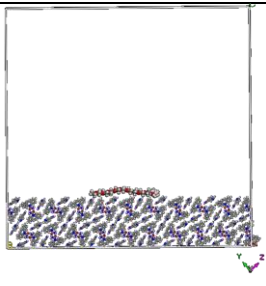
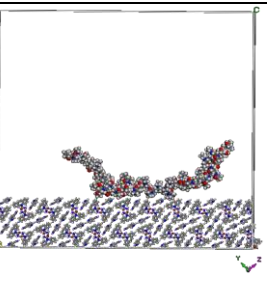
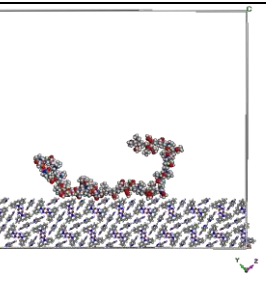
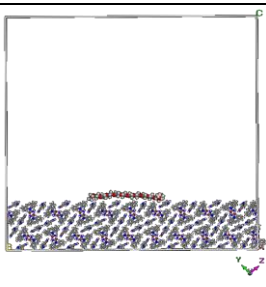
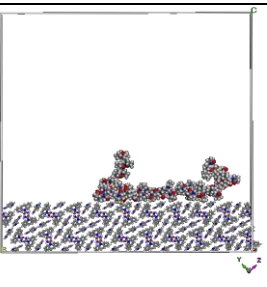
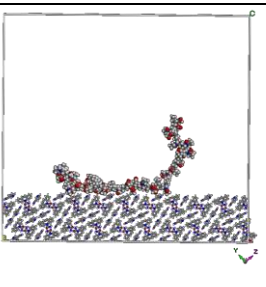
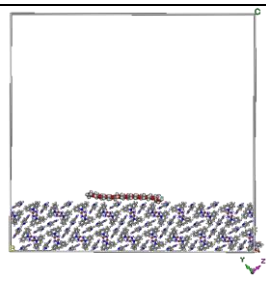
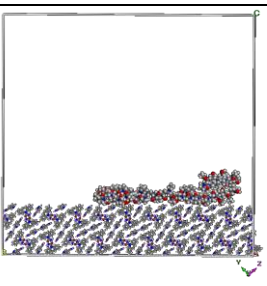
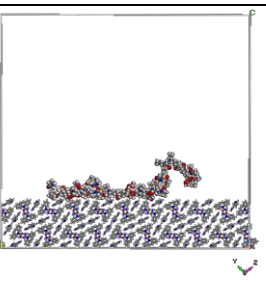
60			
100			
150			

Table 14 - Snapshots of polymers on CBZ-NIC surfaces at 298k at 0, 10, 30, 60, 100 and 150ps

Time (ps)	CBZ-NIC (011) surface		
	PEG	PVP	PVP-VA
0			
10			
30			
60			
100			

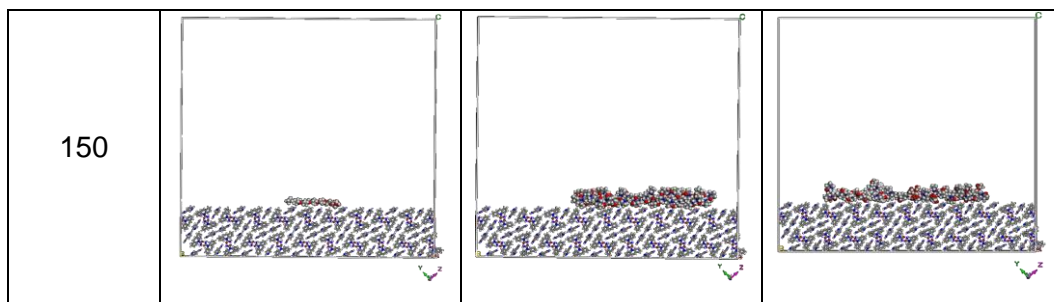
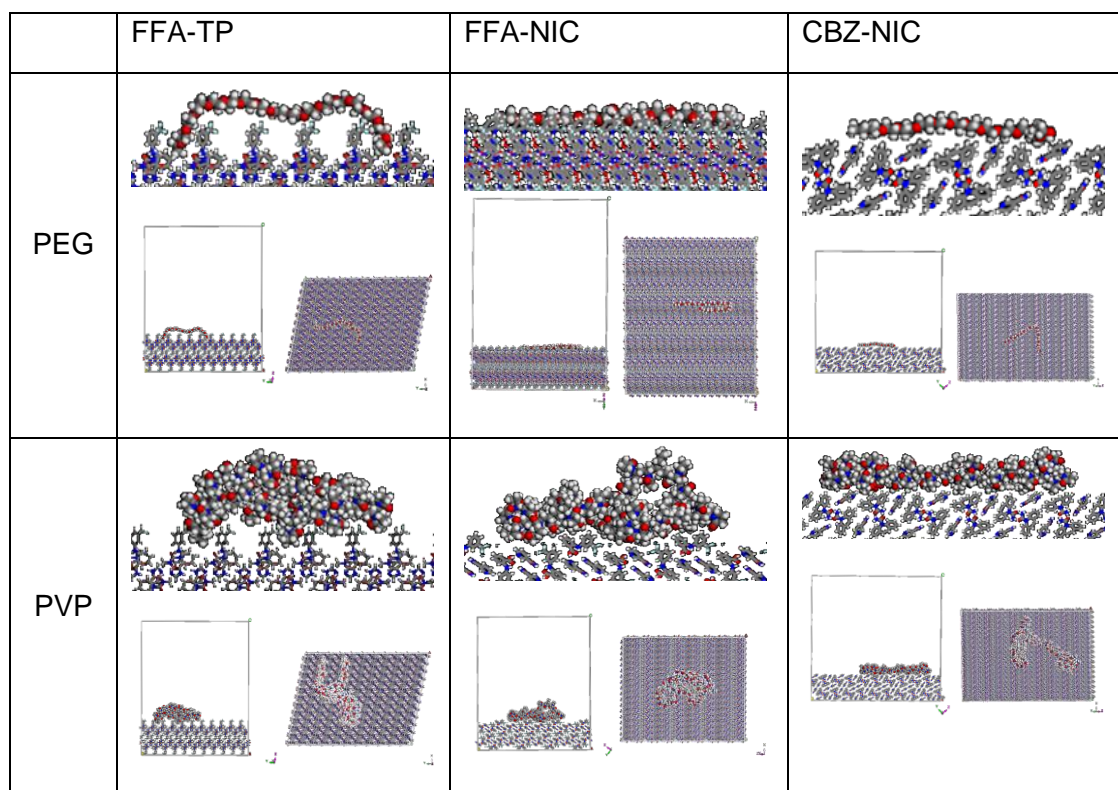


Table 15 - Summary of polymer stabilisation time

	Stabilisation time (ps)		
	FFA-TP	FFA-NIC	CBZ-NIC
PEG	30	30	10
PVP	100	60	100
PVPVA	150	150	150

Table 16 - Conformation of polymers on co-crystal surfaces at equilibrium at 298K and 200ps



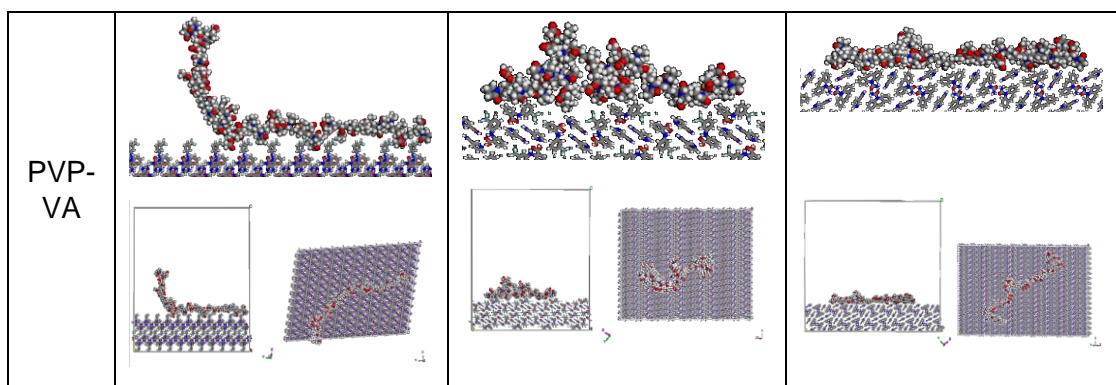


Table 17 - Binding energy, hydrogen bonding, van der Waals and electrostatic attractions on co-crystal surfaces

Crystal and polymer		Energy (kcal/mol)			
		Binding energy	Hydrogen bonding	van der Waals	Electrostatic
FFA-TP	PEG	-44.415	-0.016	14.55	-12.17
	PVP	-149.05	0	351.075	-1734.36
	PVP-VA	-90.48	0	318.27	-490.02
FFA-NIC	PEG	-54.823	0	7.948	-10.271
	PVP	-161.68	0	360.30	-1740.83
	PVP-VA	-122.90	0	255.91	-490.84
CBZ-NIC	PEG	-45.151	0	16.185	-13.816
	PVP	-208.835	0	350.682	-1729.835
	PVP-VA	-161.156	0	216.367	-483.479

Table 18 - Mean square displacement of a polymer on the crystal surface at equilibrium

<p>FFA-TP</p>	<p>FFA-TP</p> <p>MSD (nm²)</p> <p>Time (ps)</p> <p>Legend: PEG (blue), PVP (red), PVPVA (green)</p> <table border="1"> <caption>Approximate MSD values for FFA-TP</caption> <thead> <tr> <th>Time (ps)</th> <th>PEG (nm²)</th> <th>PVP (nm²)</th> <th>PVPVA (nm²)</th> </tr> </thead> <tbody> <tr><td>0</td><td>0.0</td><td>0.0</td><td>0.0</td></tr> <tr><td>10</td><td>0.1</td><td>0.2</td><td>0.5</td></tr> <tr><td>20</td><td>0.1</td><td>0.3</td><td>2.5</td></tr> <tr><td>30</td><td>0.1</td><td>0.5</td><td>4.5</td></tr> <tr><td>40</td><td>0.1</td><td>0.8</td><td>7.0</td></tr> <tr><td>50</td><td>0.2</td><td>1.0</td><td>10.5</td></tr> </tbody> </table>	Time (ps)	PEG (nm ²)	PVP (nm ²)	PVPVA (nm ²)	0	0.0	0.0	0.0	10	0.1	0.2	0.5	20	0.1	0.3	2.5	30	0.1	0.5	4.5	40	0.1	0.8	7.0	50	0.2	1.0	10.5
Time (ps)	PEG (nm ²)	PVP (nm ²)	PVPVA (nm ²)																										
0	0.0	0.0	0.0																										
10	0.1	0.2	0.5																										
20	0.1	0.3	2.5																										
30	0.1	0.5	4.5																										
40	0.1	0.8	7.0																										
50	0.2	1.0	10.5																										
<p>FFA-NIC</p>	<p>FFA-NIC</p> <p>MSD (nm²)</p> <p>Time (ps)</p> <p>Legend: PEG (blue), PVP (red), PVPVA (green)</p> <table border="1"> <caption>Approximate MSD values for FFA-NIC</caption> <thead> <tr> <th>Time (ps)</th> <th>PEG (nm²)</th> <th>PVP (nm²)</th> <th>PVPVA (nm²)</th> </tr> </thead> <tbody> <tr><td>0</td><td>0.0</td><td>0.0</td><td>0.0</td></tr> <tr><td>10</td><td>0.05</td><td>0.1</td><td>0.5</td></tr> <tr><td>20</td><td>0.2</td><td>0.15</td><td>1.5</td></tr> <tr><td>30</td><td>0.1</td><td>0.1</td><td>1.9</td></tr> <tr><td>40</td><td>0.1</td><td>0.1</td><td>1.8</td></tr> <tr><td>50</td><td>0.15</td><td>0.1</td><td>1.7</td></tr> </tbody> </table>	Time (ps)	PEG (nm ²)	PVP (nm ²)	PVPVA (nm ²)	0	0.0	0.0	0.0	10	0.05	0.1	0.5	20	0.2	0.15	1.5	30	0.1	0.1	1.9	40	0.1	0.1	1.8	50	0.15	0.1	1.7
Time (ps)	PEG (nm ²)	PVP (nm ²)	PVPVA (nm ²)																										
0	0.0	0.0	0.0																										
10	0.05	0.1	0.5																										
20	0.2	0.15	1.5																										
30	0.1	0.1	1.9																										
40	0.1	0.1	1.8																										
50	0.15	0.1	1.7																										
<p>CBZ-NIC</p>	<p>CBZ-NIC</p> <p>MSD (nm²)</p> <p>Time (ps)</p> <p>Legend: PEG (blue), PVP (red), PVPVA (green)</p> <table border="1"> <caption>Approximate MSD values for CBZ-NIC</caption> <thead> <tr> <th>Time (ps)</th> <th>PEG (nm²)</th> <th>PVP (nm²)</th> <th>PVPVA (nm²)</th> </tr> </thead> <tbody> <tr><td>0</td><td>0.0</td><td>0.0</td><td>0.0</td></tr> <tr><td>10</td><td>0.02</td><td>0.08</td><td>0.07</td></tr> <tr><td>20</td><td>0.04</td><td>0.12</td><td>0.10</td></tr> <tr><td>30</td><td>0.05</td><td>0.14</td><td>0.10</td></tr> <tr><td>40</td><td>0.10</td><td>0.15</td><td>0.13</td></tr> <tr><td>50</td><td>0.17</td><td>0.17</td><td>0.13</td></tr> </tbody> </table>	Time (ps)	PEG (nm ²)	PVP (nm ²)	PVPVA (nm ²)	0	0.0	0.0	0.0	10	0.02	0.08	0.07	20	0.04	0.12	0.10	30	0.05	0.14	0.10	40	0.10	0.15	0.13	50	0.17	0.17	0.13
Time (ps)	PEG (nm ²)	PVP (nm ²)	PVPVA (nm ²)																										
0	0.0	0.0	0.0																										
10	0.02	0.08	0.07																										
20	0.04	0.12	0.10																										
30	0.05	0.14	0.10																										
40	0.10	0.15	0.13																										
50	0.17	0.17	0.13																										

6.4 Discussion

The interactions of the polymers on the surfaces of the co-crystals played an essential role in controlling the dissolution and morphological changes of the co-crystals during the dissolution process. The MD simulations as well as the etching experiments indicate that, when compared to PVP or PVP-VA, very low interaction energy existed between PEG and the surfaces of the co-crystals. PEG therefore, was not an effective inhibitor. In contrast to PVP-VA, PVP had greater interaction energies (Table 17). It is worth noting that the calculated interaction energy for PVP was based on 20% of its actual polymer weight, and PVP-VA was based on 10% of its actual polymer weight. Therefore, it was predicted theoretically that PVPVA had stronger interaction with the surfaces of FFA-NIC or CBZ-NIC in comparison to PVP.

Interestingly, the above theory could not be applied to the observations derived from the etching experiments which demonstrates that PVP was more effective in inhibiting parent drug precipitation in comparison to PVP-VA. This observation was consistent with previous dissolution performance parameter (DPP) investigations for FFA-NIC, demonstrating a 64% increase of AUC (area under curve) in the presence of PVP whereas a 60% increase in the presence of PVP-VA [140]. The results indicated that other factors, such as non-covalent bonds existed between the polymers and the surfaces of co-crystals or the polymer mobility and conformation, might play an important role in modulating the co-crystal dissolution and parent drug precipitation.

The etching experiments in chapter 5 and the simulations carried out for this research looked at the biggest and most stable faces of the co-crystals, which were from the hydrophilic regions of the molecules. The studies showed that PVP had weak van der Waals interaction and greater electrostatic energy (Table 17), which contributes to its low mobility on the surfaces of co-crystals (Table 18). PVP adsorption on the surfaces of co-crystals led to the formation of a steric hindrance layer, which prevented solvent molecules from contacting the co-crystal surface particles and subsequently reducing the dissolution rate. Furthermore, the layer prevented the parent drug supersaturation around the dissolution surface and inhibited the precipitation of the parent drug.

Additionally, a conformational change was observed for PVP when it displayed the inhibitory effect by coiling up when they adsorbed on the surfaces of the co-crystals. This contrasted with PVP-VA, which became more mobile on the surfaces of the co-crystals (Table 18), making it difficult to form a stable steric hindrance layer. Therefore, PVP-VA was a less effective precipitation inhibitor for FFA-NIC and CBZ-NIC.

6.5 Chapter Conclusion

This research provided insights into the mechanisms of co-crystal dissolution and described inhibitory functions of polymers for precipitation, which is of great value to the development of novel co-crystal based formulations. It was highly promising that such approaches would be set up as an essential tool during the routine process of manufacturing pharmaceutical co-crystals. The results showed that PEG was not an effective inhibitor while PVP and PVP-VA was effective. In contrast to PVP-VA, PVP had greater interaction energies and was more effective in inhibiting parent drug precipitation in comparison to PVP-VA

It is also worth noting that the MD simulations without considering the dissolution medium may be too simplistic as a tool for the selection of polymeric excipients in the formulation because nucleation and growth of the parent drug could take place in the diffusion layer. Therefore, a full MD simulation will be required to provide a comprehensive understanding of the dissolution and recrystallisation mechanisms of pharmaceutical co-crystals.

Chapter 7 - Influence of polymers on the diffusion coefficient of drug molecules using NMR techniques

7.1 Chapter overview

To gain understanding into the mechanism of the supersaturated solution in the presence of polymers, the atomic-level of molecular interactions among the parent drug, co-formers and polymers were studied using one-dimensional proton nuclear magnetic resonance (^1H NMR) spectroscopy and DOSY spectroscopy. Solution ^1H NMR is a powerful tool for investigating and understanding the molecular level of drugs, in order to examine interactions such as hydrogen bonding and aggregation properties. The chemical shifts in ^1H NMR spectra indicates differences in the chemical environment of molecules and widths of the reflect molecular mobility [140]. ^1H NMR studies were conducted in singular, binary and ternary components in solutions containing parent drugs of FFA or CBZ, co-former and polymer to determine the possibility of interactions of drug/co-former, drug/polymer and co-former/polymer in low polarity solvent deuterated chloroform (CDCl_3). DOSY spectroscopy was used to calculate the diffusion coefficient of the drugs, co-formers and polymers in CDCl_3 .

7.2 Materials and methods

FFA I, NIC, TP, CBZ III, PEG, PVP, PVP-VA, acetonitrile, ethyl acetate, CDCl_3 and double distilled water were used in this study. Detailed information of these materials can be found in Chapter 3.

7.2.1 Powder FFA and CBZ Co-crystals Preparation

Co-crystals of FFA-NIC CO, FFA-TP CO and CBZ-NIC CO were used in this chapter, the detailed method can be found in chapter 3.

7.2.2 NMR and DOSY Measurements

JEOL ECZ 600R series FT-NMR Spectrometer was used to identify the interactions occurring between the drug, co-former and polymer in deuterated chloroform solution. Tetramethylsilane (TMS) spectra was used as the internal standard.

^1H NMR and DOSY experiments were used to probe interactions among drug, co-former and polymer in solution. The spectra of Singular components (FFA, TP, NIC, CBZ, PEG, PVP, PVP-VA) the binary components (FFA-TP, FFA-NIC, CBZ-NIC, FFA-PEG, FFA-PVP, FFA-PVP-VA, CBZ-PEG, CBZ-PVP, CBZ-PVP-VA, NIC-PEG, NIC-PVP, NIC-PVP-VA, TP-PEG, TP-PVP, TP-PVP-VA) and the ternary components (FFA-TP-PEG, FFA-TP-PVP, FFA-TP-PVP-VA, FFA-NIC-PEG, FFA-NIC-PVP, FFA-NIC-PVP-VA, CBZ-NIC-PEG, CBZ-NIC-PVP, CBZ-NIC-PVP-VA) were analysed for any interactions between the components. 2 different concentrations of parent drug were prepared including 2.4mg/ml and 2mg/ml. 2.4mg/ml drug concentration was studied in the presence of 0.3mg/ml PEG, PVP or PVP-VA and 2mg/ml drug concentration was studied in the presence of 0.5mg/ml and 1mg/ml PEG, PVP or PVP-VA. In order to investigate the effect of self-dissociation of the drug, it was necessary to study a slightly higher concentration of the drug (2.4mg/ml) at low polymer concentrations (0.3mg/ml). To mimic a co-crystal system, an equal molar concentration of a co-former as that of FFA or CBZ was prepared in solution. NMR techniques was used to calculate the proton shift and diffusion coefficient of API and co-former molecules in singular, binary, and ternary systems. ^1H proton spectra were achieved after 64 scans, with a relaxation delay of 7s at a controlled temperature of 25°C. For DOSY, stimulated spin echo with bipolar gradient pulses was employed for self-diffusion coefficient measurement. DOSY spectra were achieved after 32 scans, with a relaxation delay of 6s, at a controlled temperature of 25°C. The gradient was from 0.3 – 300 mT/m with 14 gradual increments.

7.3 Results

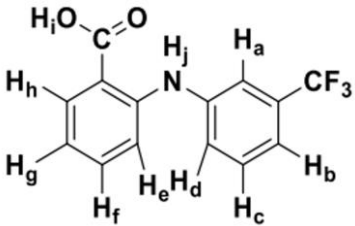
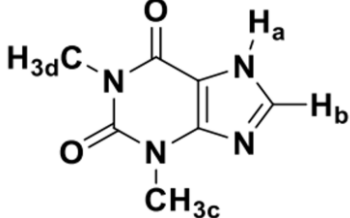
¹H NMR experiments were carried out to investigate the interactions among FFA, CBZ, co-formers and polymers in solution. This research focused on examining the characteristic chemical shifts of the protons in each of the molecules of FFA, TP, CBZ and NIC affected by their hydrogen bonding interactions and self-aggregation properties in solution in the presence or absence of a polymer of PEG, PVP or PVP-VA. Drug structures with the proton identification and with the respective peak positions are presented in Table 19 and Table 20.

Investigations were carried out for:

- i) the chemical shifts of the singlet peak of H_j and two doublet peaks of H_i of FFA;
- ii) the chemical shifts of H_a, H_b and H_c of NIC;
- iii) the chemical shifts of H_a, H_b, H_c and H_d of TP;
- iv) the chemical shifts of H_a and H_b of CBZ.

The proton details of each molecule can be found in the table below (Table 19).

Table 19 - Drug and structure with proton identification

Drug	Structure and proton identification
FFA I	
TP	

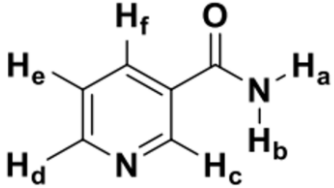
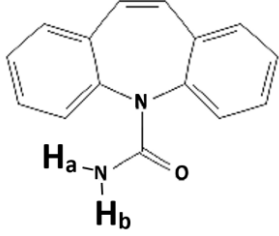
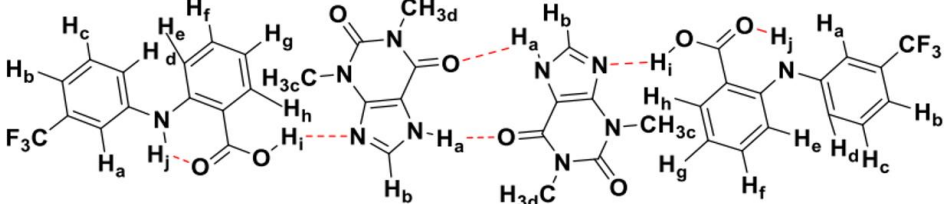
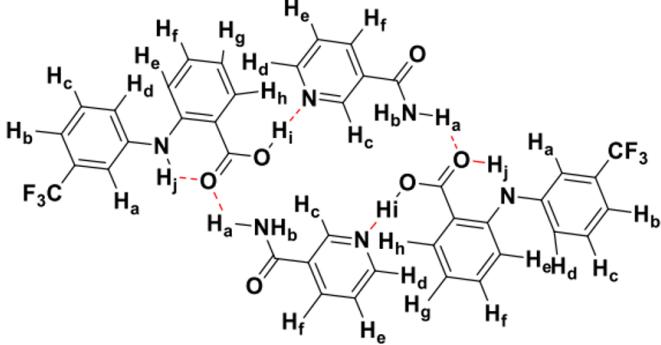
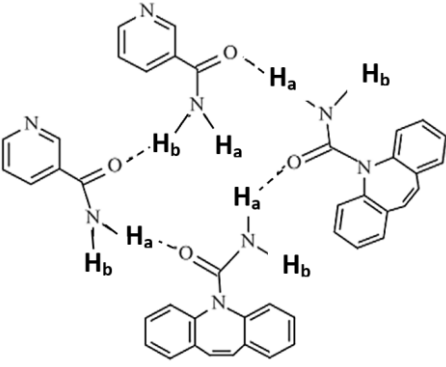
NIC	
CBZ III	
FFA-TP	
FFA-NIC	
CBZ-NIC	

Table 20 - Peak position and proton identification of the drugs

Drug	Peak position	Proton Identification
FFA	9.4	Hj
	8.0	Hh
TP	7.8	Hb
	3.6	Hc
	3.4	Hd
NIC	9.0	Hc
	5.9	Ha, Hb
CBZ	6.9	Ha
	4.3	Hb

7.3.1 ¹H NMR Analysis of Binary Components

The results below show the ¹H NMR analysis of singular and binary components of 2 different concentrations of parent drug including 2.4mg/ml and 2mg/ml of FFA and CBZ with 0.3mg/ml, 0.5mg/ml and 1mg/ml PEG, PVP or PVP-VA. The proton graphs were analysed using Mnova 14.2.0 by Mestrelab. The full NMR spectra can be found under A5 Table 1-4 in Appendices.

7.3.1.1 In presence of 0.3mg/ml PEG, PVP or PVP-VA

Table 21 - Singular and binary component NMR analysis of FFA, TP and NIC with 0.3mg/ml PEG, PVP or PVP-VA

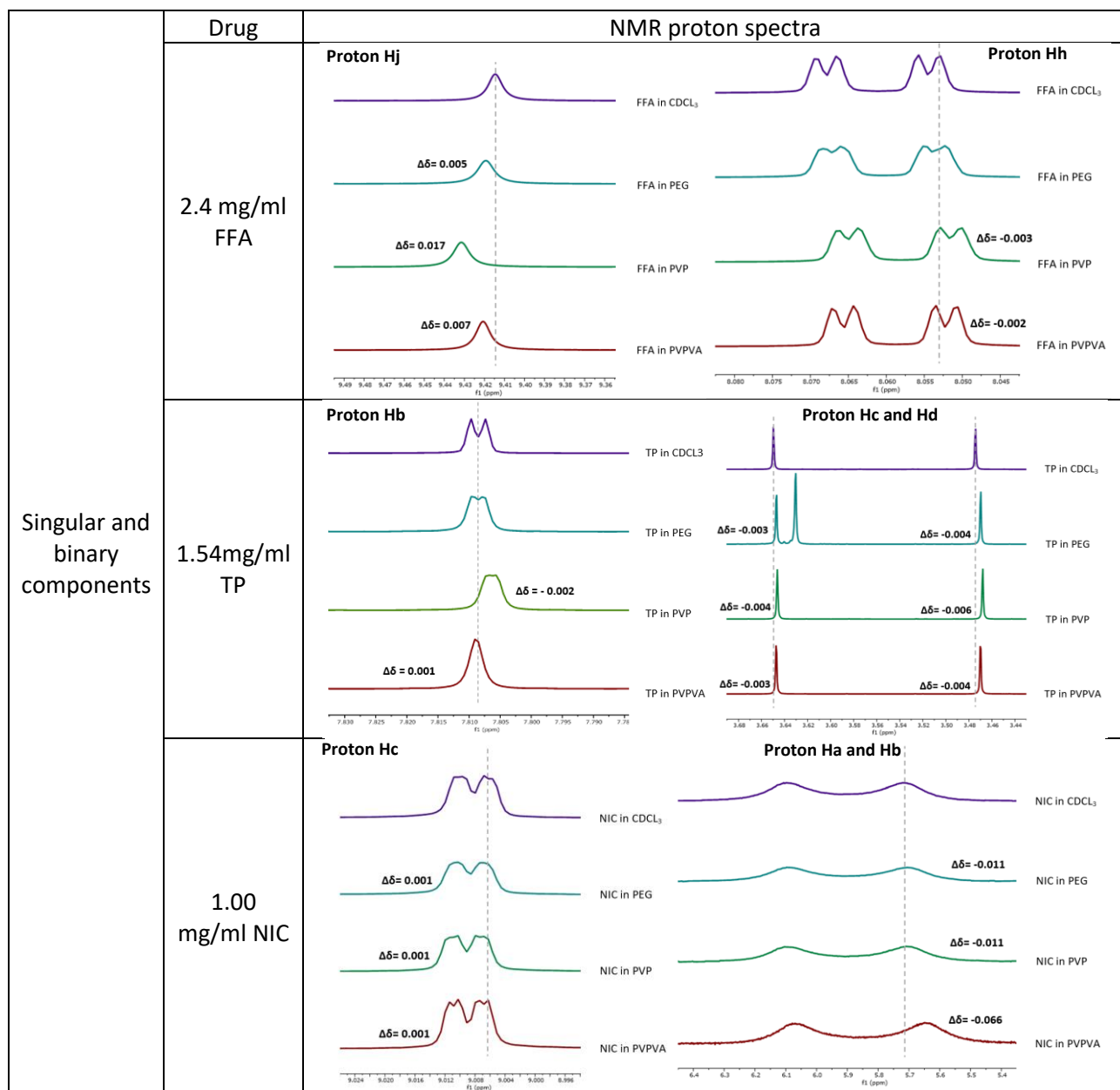
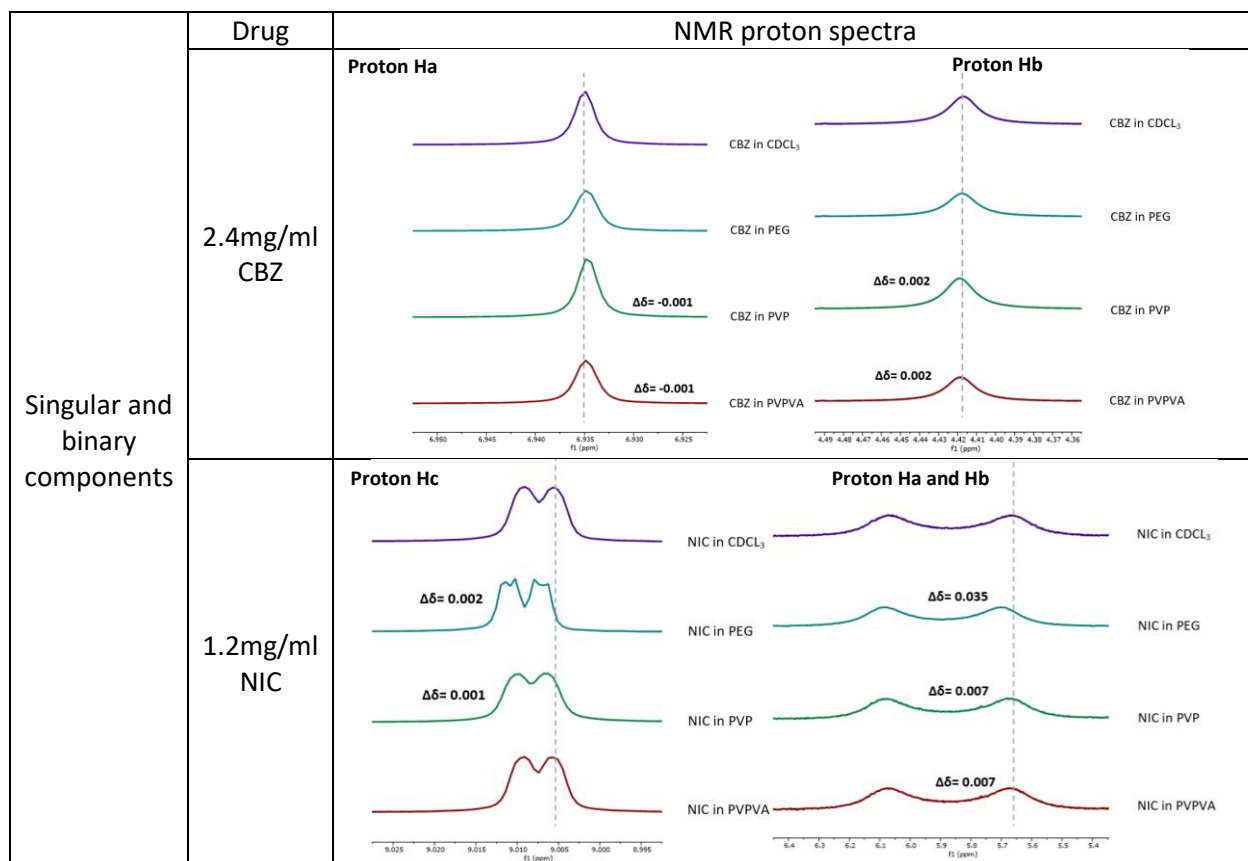


Table 22 - Singular and binary component NMR analysis of CBZ and NIC with 0.3mg/ml PEG, PVP or PVP-VA



7.3.1.2 In presence of 0.5mg/ml PEG/PVP/PVP-VA

Table 23 - Singular and binary component NMR analysis of FFA, TP and NIC with 0.5mg/ml PEG, PVP or PVP-VA

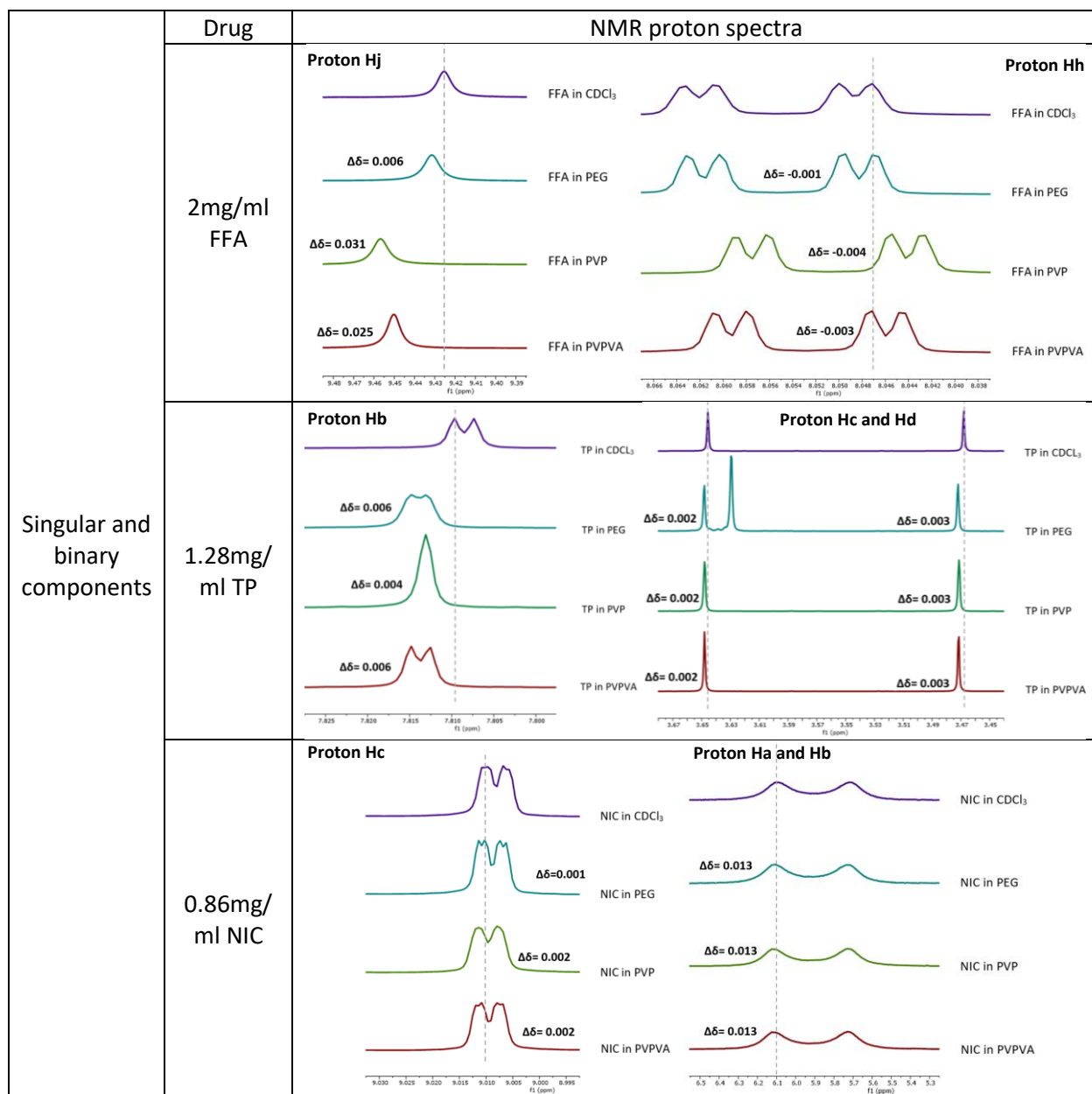
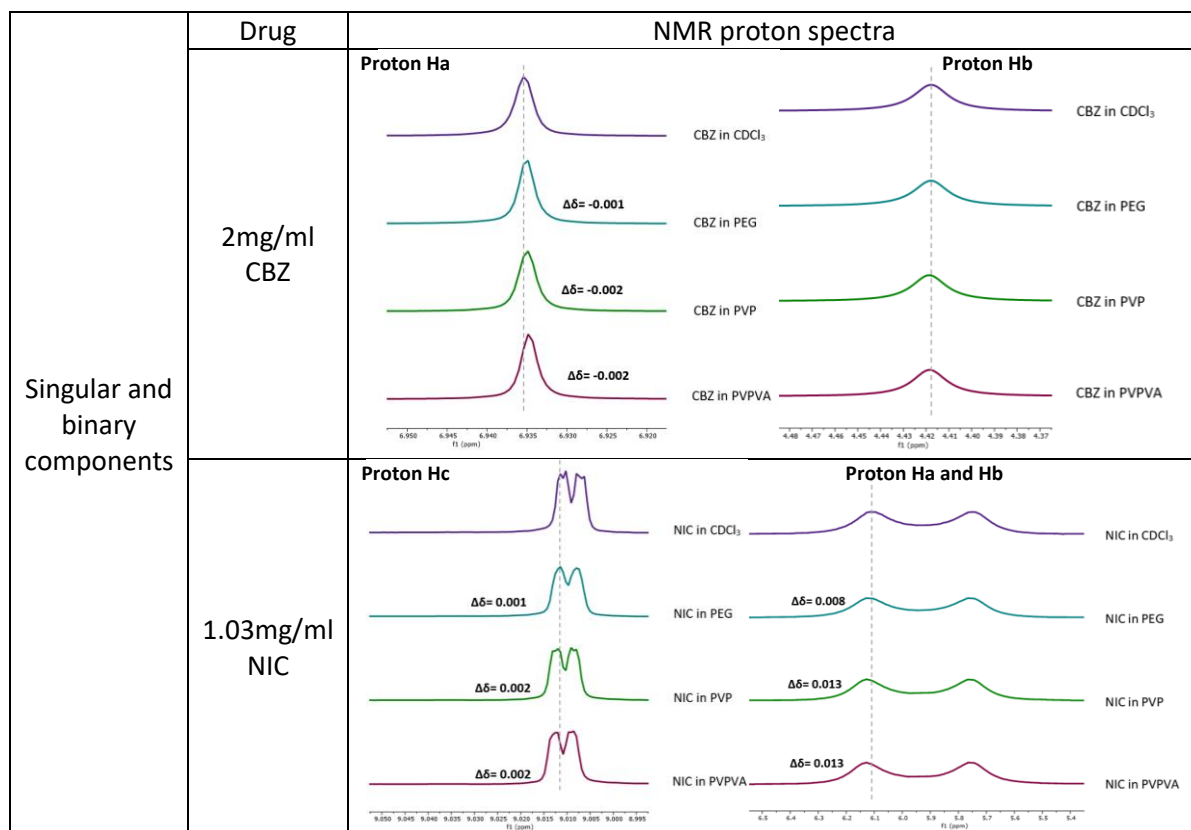
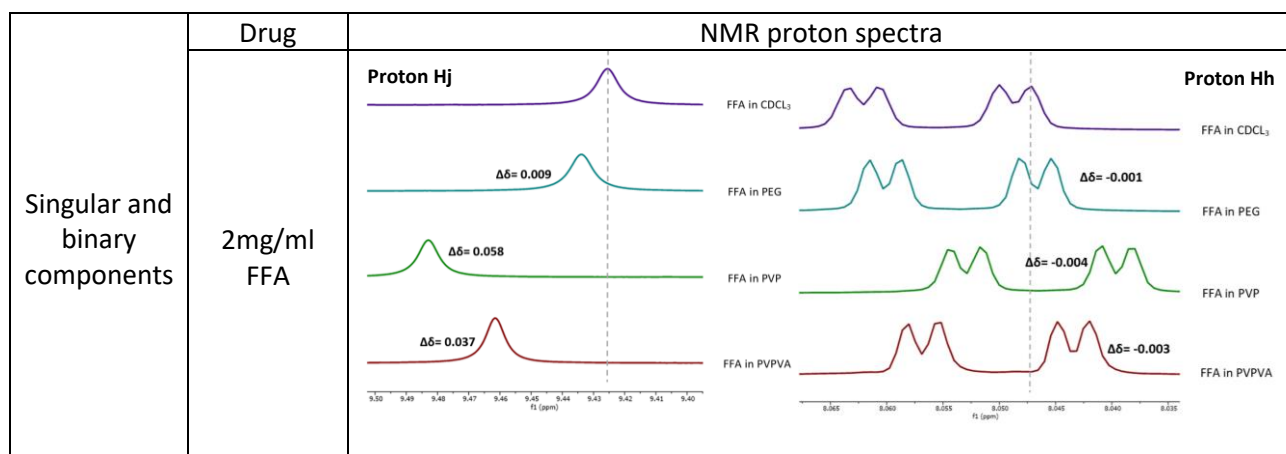


Table 24 - Singular and binary component NMR analysis of CBZ and NIC with 0.5mg/ml PEG, PVP or PVP-VA



7.3.1.3 In presence of 1mg/ml PEG, PVP or PVP-VA

Table 25 - Singular and binary component NMR analysis of FFA, TP and NIC with 1mg/ml PEG, PVP or PVP-VA



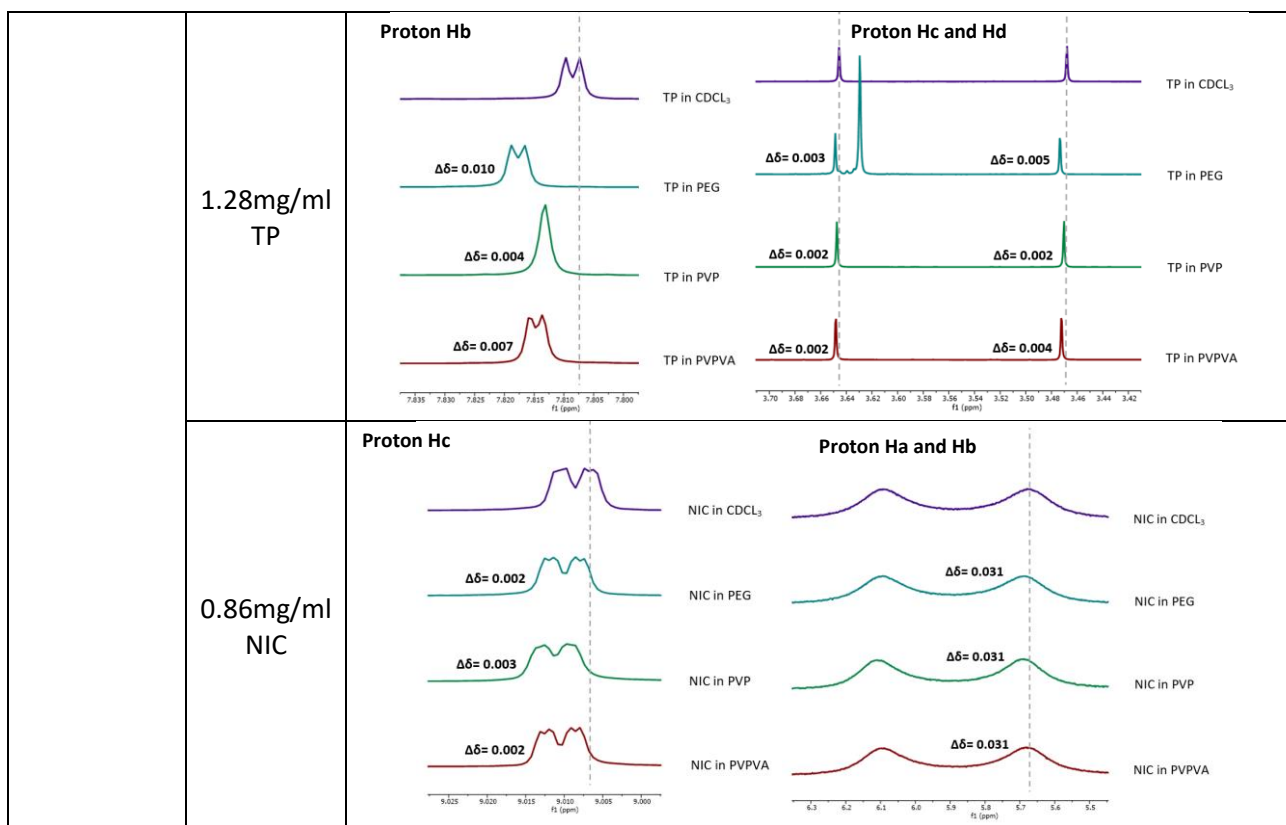
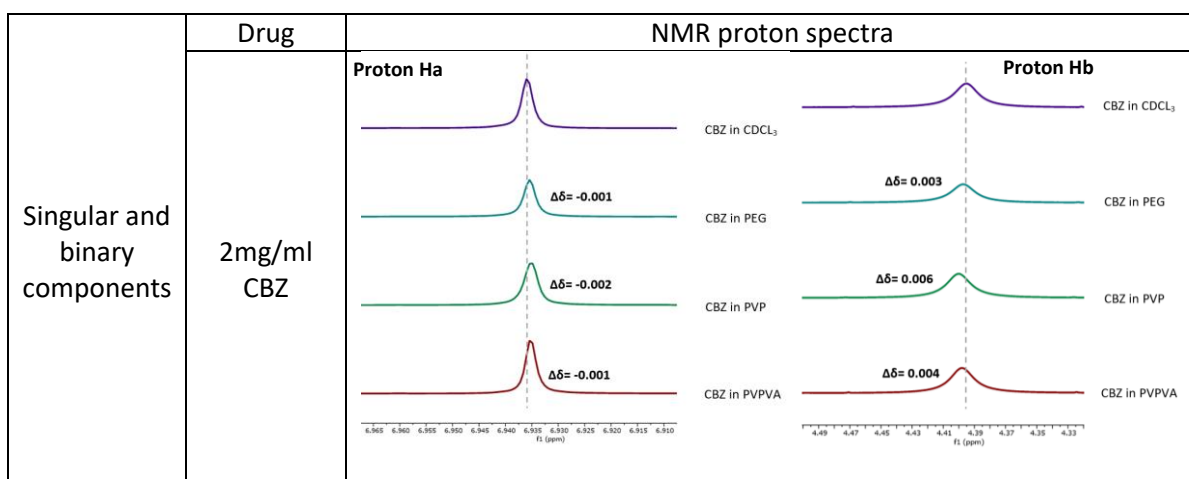


Table 26 - Singular and binary component NMR analysis of CBZ and NIC with 1mg/ml PEG, PVP or PVP-VA



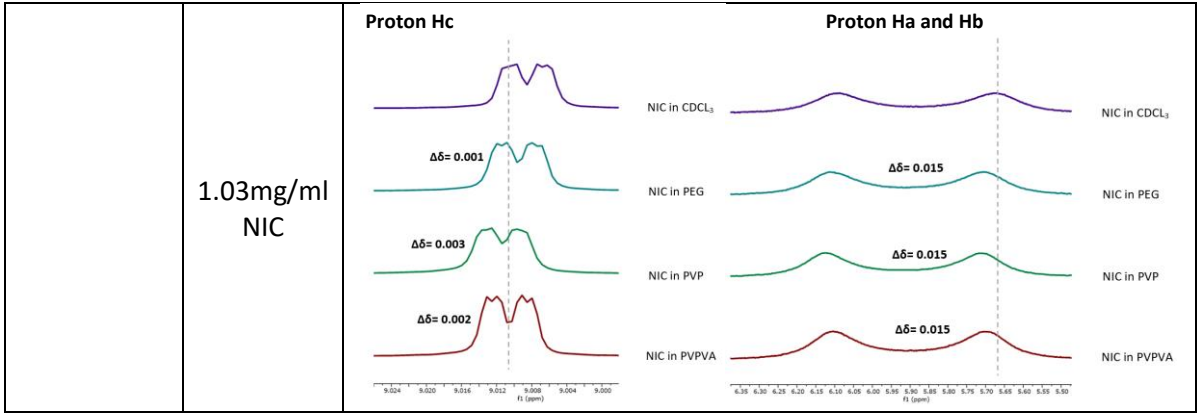


Table 27 - Summary of the peak shift differences in singular and binary components

Compound	Characteristic peak	Difference of peak shift								
		PEG	PVP	PVPVA	PEG		PVP		PVPVA	
-	-	0.3mg/ml	0.3mg/ml	0.3mg/ml	0.5mg/ml	1mg/ml	0.5mg/ml	1mg/ml	0.5mg/ml	1mg/ml
2mg/ml FFA	9.425	0.005	0.017	0.007	0.006	0.009	0.031	0.058	0.025	0.037
	8.047	0	-0.003	-0.002	-0.001	-0.002	-0.004	-0.009	-0.003	-0.005
1.28mg/ml TP	7.809	0	-0.002	0.001	0.006	0.01	0.004	0.004	0.006	0.007
	3.646	-0.003	-0.004	-0.003	0.002	0.003	0.002	0.002	0.002	0.002
	3.468	-0.004	-0.006	-0.004	0.003	0.005	0.003	0.002	0.003	0.004
0.86mg/ml NIC	9.006	0.001	0.001	0.001	0.001	0.002	0.002	0.003	0.002	0.002
	5.671	-0.011	-0.011	-0.066	0.053	0.031	0.053	0.031	0.053	0.031

In this study FFA and CBZ cocrystals were analysed in the presence of three different concentrations of polymers – 0.3mg/ml, 0.5mg/ml and 1mg/ml of PEG, PVP or PVP-VA. Table 21 and 22 show the chemical shifts of the characteristic peaks of FFA-TP, NIC and CBZ in 0.3mg/ml PEG, PVP or PVP-VA. Peak shift details can be found in the Appendices under A5 Table 6.

At low polymer concentration, for all three polymers, the chemical shift of H_j of FFA showed downfield shift - $\Delta\delta = 0.005$ with PEG, $\Delta\delta = 0.017$ with PVP and $\delta\Delta = 0.007$ with PVP-VA - indicates hydrogen bond interaction between the O-H of the carboxylic acid functional group of FFA with the carbonyl O functional group of PEG, PVP or PVP-VA. The chemical shift of H_h of FFA showed an up-field shift in the presence of PVP and PVPVA – $\Delta\delta = -0.003$ and $\Delta\delta = -0.002$ respectively which indicates a different type of interaction is taking place. Although the functional group, O=C of the carboxylic acid on the FFA is not involved with the interaction with the polymers, the long backbone chains of polymers can disturb the intramolecular interaction of N-H_j...O=C and subsequently affect the confirmation of the FFA. In the presence of 0.5mg/mL polymer concentration (Table 23), the effect of both down-fielding and up-fielding was increased for FFA, with the highest increase being in the presence of PVP as the H_j showed a downfield shift of – $\Delta\delta = 0.031$. PEG showed a slight increase (– $\Delta\delta = 0.006$) and PVP-VA showed a moderate increase (– $\Delta\delta = 0.025$). The chemical shift of H_h showed an upfield shift of – $\Delta\delta = -0.001$ for PEG, – $\Delta\delta = -0.004$ for PVP and – $\Delta\delta = -0.003$ for PVP-VA. In the presence of 1mg/ml polymer (Table 25), there was a further increase in the down-fielding and up-fielding effect. H_j proton showed a chemical shift of – $\Delta\delta = 0.009$ for PEG, – $\Delta\delta = 0.058$ for PVP and – $\Delta\delta = 0.037$ for PVP-VA while the chemical shift for H_h did not change. In all three polymer concentrations, PVP had the highest hydrogen bond interactions between the O-H of FFA and the carbonyl O of PVP, followed by a moderate interaction of PVP-VA and low interaction of PEG. Furthermore, in comparison to PVP-VA, PVP showed a slightly broader peak, demonstrating that PVP can significantly suppress the mobility of FFA molecules in solution.

¹H NMR spectra of TP samples are complex, as they can be affected by solute-solvent, solute-solute and solute-polymer interactions [178]. In CDCl₃, dimerization of TP molecules is found to be the controlling factor affecting the ¹H chemical shifts of TP [347]. Due to TPs being good proton donors, PVP-VA can disrupt TP dimers in solution, indicating shifts of proton of TP at a low polymer concentration of 0.3mg/mL as shown in Table 21. The chemical shift of H_b, in the presence of PEG showed no change while the H_c and H_d proton showed an up-field shift of $\Delta\delta = -0.003$ and $\Delta\delta = -0.004$ respectively. PVP showed an up-field shift for all three protons while PVP-VA showed

an up-field shift for Hb proton and a downfield shift for Hc and Hd proton. In all three concentrations, a peak change was seen for the Hb proton, where the double peak had changed to a narrow single peak.

The chemical shifts of NIC (corresponding to the FFA ratio) shows a slight downfield shift of $\Delta\delta = 0.001$ for the Hc proton in the presence of all three polymers. Ha protons show an up-field shift in the presence of the polymers with $\Delta\delta = -0.011$ in the presence of PEG and PVP and $\Delta\delta = -0.066$ in the presence of PVP-VA (Table 21). In of 0.5mg/ml polymer, the chemical shift of Hc proton showed an increase in the down-fielding effect in presence of PVP and PVP-VA ($\Delta\delta = 0.002$) while Ha protons showed a chemical shift of $\Delta\delta = 0.013$ for all three polymers as seen in Table 23. 1mg of polymer further increased the Ha protons in the presence of PEG ($\Delta\delta = 0.002$) and PVP ($\Delta\delta = 0.003$) while PVP-VA remained the same (Table 25). The chemical shift of Hc protons had an increase in the up-fielding shift where the change was $\Delta\delta = -0.031$ for all three polymers. Due to no significant change for the chemical shift of Ha protons, it can be implied that the changes are due to hydrophobic or hydrophilic environments in the presence of polymers rather than due to any hydrogen bonding. On the other hand, hydrogen bonding is present between the Hc proton and the carbonyl O functional group of 0.3mg/ml PVP-VA and 1mg/ml PEG, PVP and PVP-VA.

The chemical shifts of NIC (corresponding to the CBZ ratio) showed similar changes as the NIC corresponding to FFA. However, in the presence of 0.3mg/ml a down-fielding chemical shift of $\Delta\delta = 0.035$ was seen for the Hc proton. It is worth noting that the concentration of the drug in the presence of 0.3mg/ml polymer is slightly higher (2.4mg/ml) in comparison to the drug concentration in the other two polymers. This high drug concentration – low PEG polymer concentration could have resulted in hydrogen bond formation.

The chemical shift of the Hb in CBZ showed no change in the presence of PEG and an up-field shift of $\delta\Delta = -0.001$ for both PVP and PVP-VA which indicates a hydrogen bond interaction between the N-H of the CBZ and the carbonyl O functional group of the polymers. In contrast, the chemical shift of Ha showed a downfield shift of $\Delta\delta = 0.002$ for both PVP and PVP-VA. No change was found in the presence of PEG. In the presence of 0.5mg/ml polymer (Table 24), the up-fielding shift of Ha in CBZ only showed a slight increase of $\delta\Delta = -0.001$ for PEG, $\delta\Delta = -0.002$ for PVP and -0.002 for PVP-VA. The chemical shift of Hb showed no change. Increasing the polymer concentration to 1mg/ml (Table 26) showed slight difference in the chemical shift for Ha proton in comparison to 0.5mg/ml of polymer where PEG and PVP showed no difference and

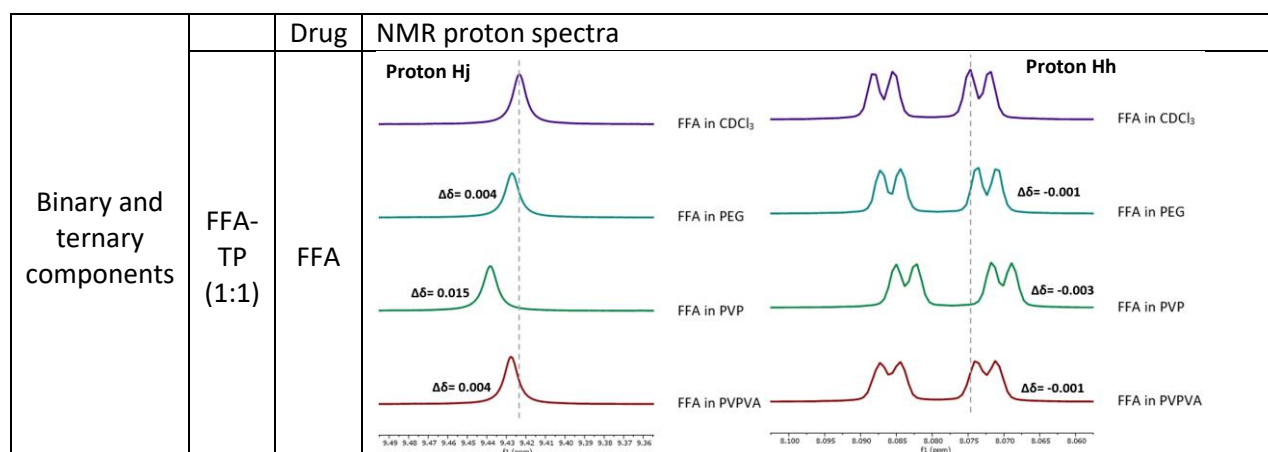
PVP-VA increased slightly downfield to $\delta\Delta = -0.001$. On the other hand, the chemical shift of Hb in CBZ, showed a moderate increase in the down-field effect in the presence of PEG ($\delta\Delta = 0.003$), PVP (0.006) and PVP-VA ($\delta\Delta = 0.004$). NMR data strongly suggests CBZ does not interact much in the presence of polymers which indicates that the chemical environment of CBZ in each solution was not significantly different. CBZ in the presence of PVP showed a slightly broader peak for the Ha proton which attributed to the changes in molecular mobility where the suppression of the molecular mobility is occurring. The chemical shift of the Ha proton in CBZ drug peak can be attributed to the differences in the chemical environment surrounding the drug, for example, hydrophobic or hydrophilic environments in the presence of polymers, rather than any hydrogen bond interactions [348].

7.3.2 ^1H NMR Analysis of Ternary Components

The results below show the ^1H NMR analysis of the binary and ternary components of co-crystals with 2 different concentrations of parent drug including 2.4mg/ml and 2mg/ml of 1:1 FFA-TP, 1:1 FFA-NIC and 1:1 CBZ-NIC with 0.3mg/ml, 0.5mg/ml and 1mg/ml PEG, PVP or PVP-VA. The full NMR spectra of the components can be found under A5 Table 1-4 in appendices.

7.3.2.1 In presence of 0.3mg/ml PEG/PVP/PVP-VA

Table 28 - Binary and ternary component NMR analysis of 1:1 FFA-TP and FFA-NIC with 0.3mg/ml PEG, PVP or PVP-VA



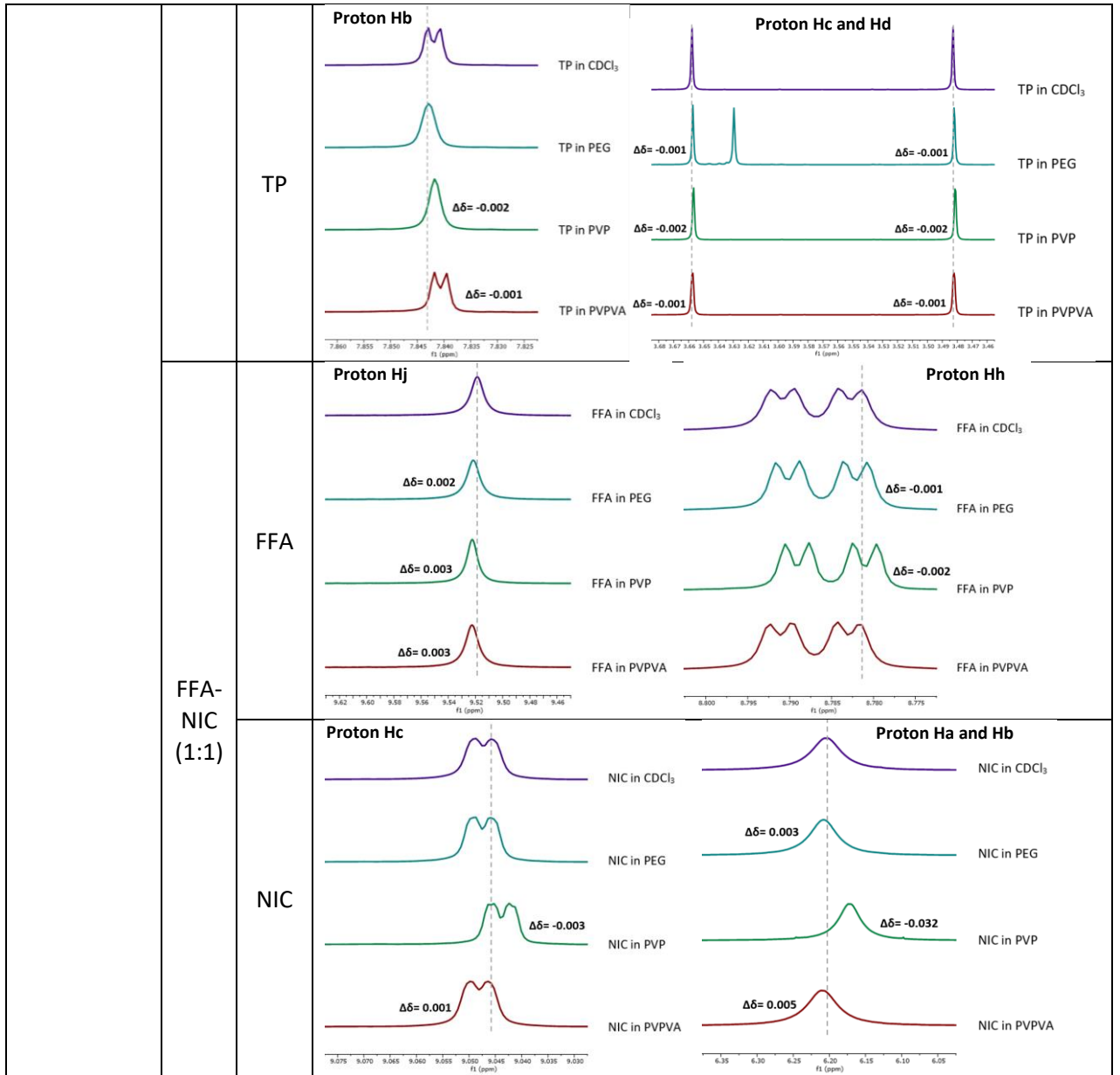
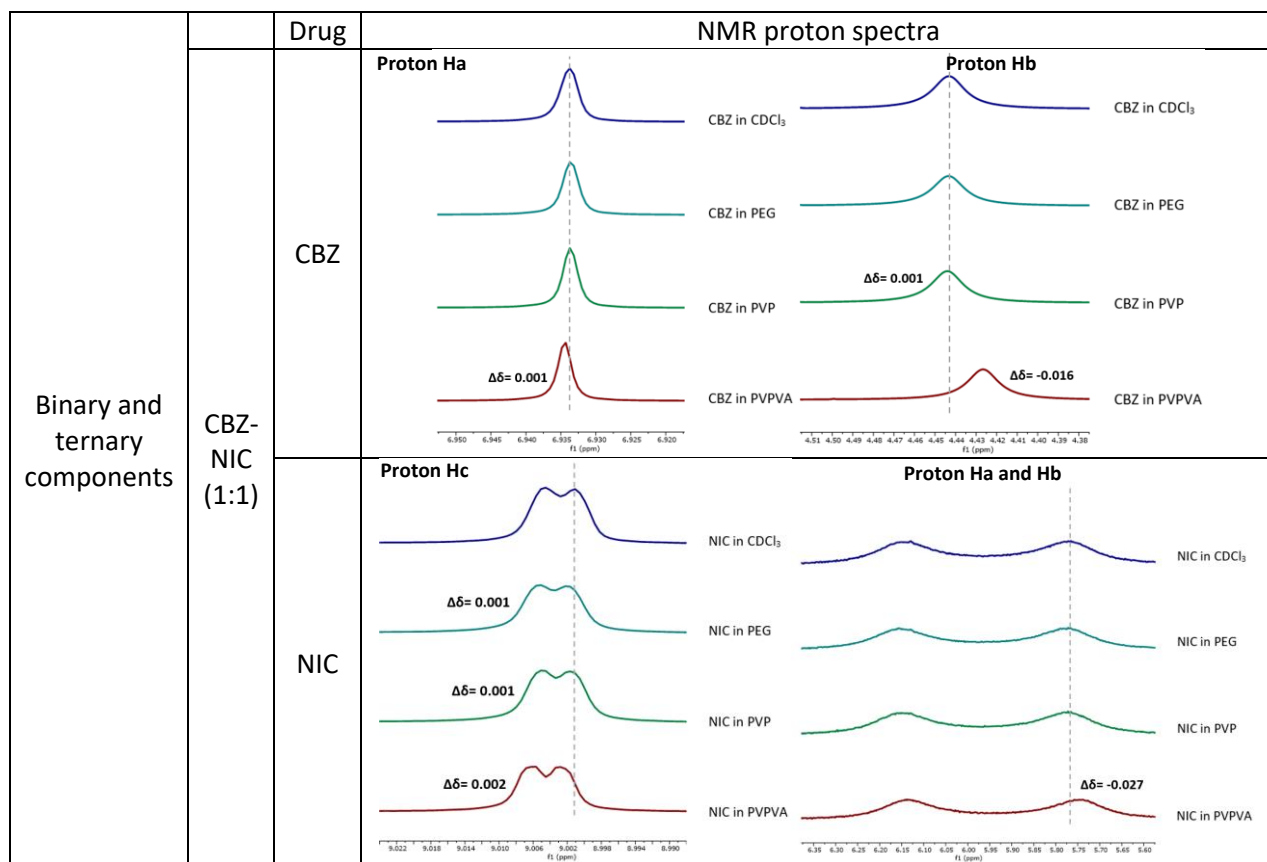
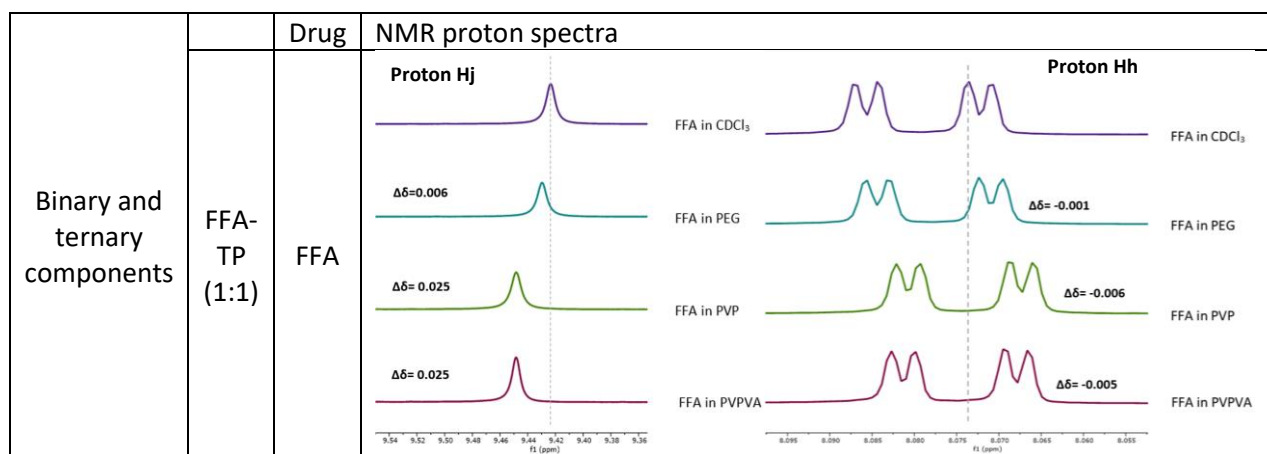


Table 29 - Binary and ternary component NMR analysis of 1:1 CBZ-NIC with 0.3mg/ml PEG, PVP or PVP-VA



7.3.2.2 In presence of 0.5mg/ml PEG, PVP or PVP-VA

Table 30 - Binary and ternary component NMR analysis of 1:1 FFA-TP and 1:1 FFA-NIC with 0.5mg/ml PEG, PVP or PVP-VA



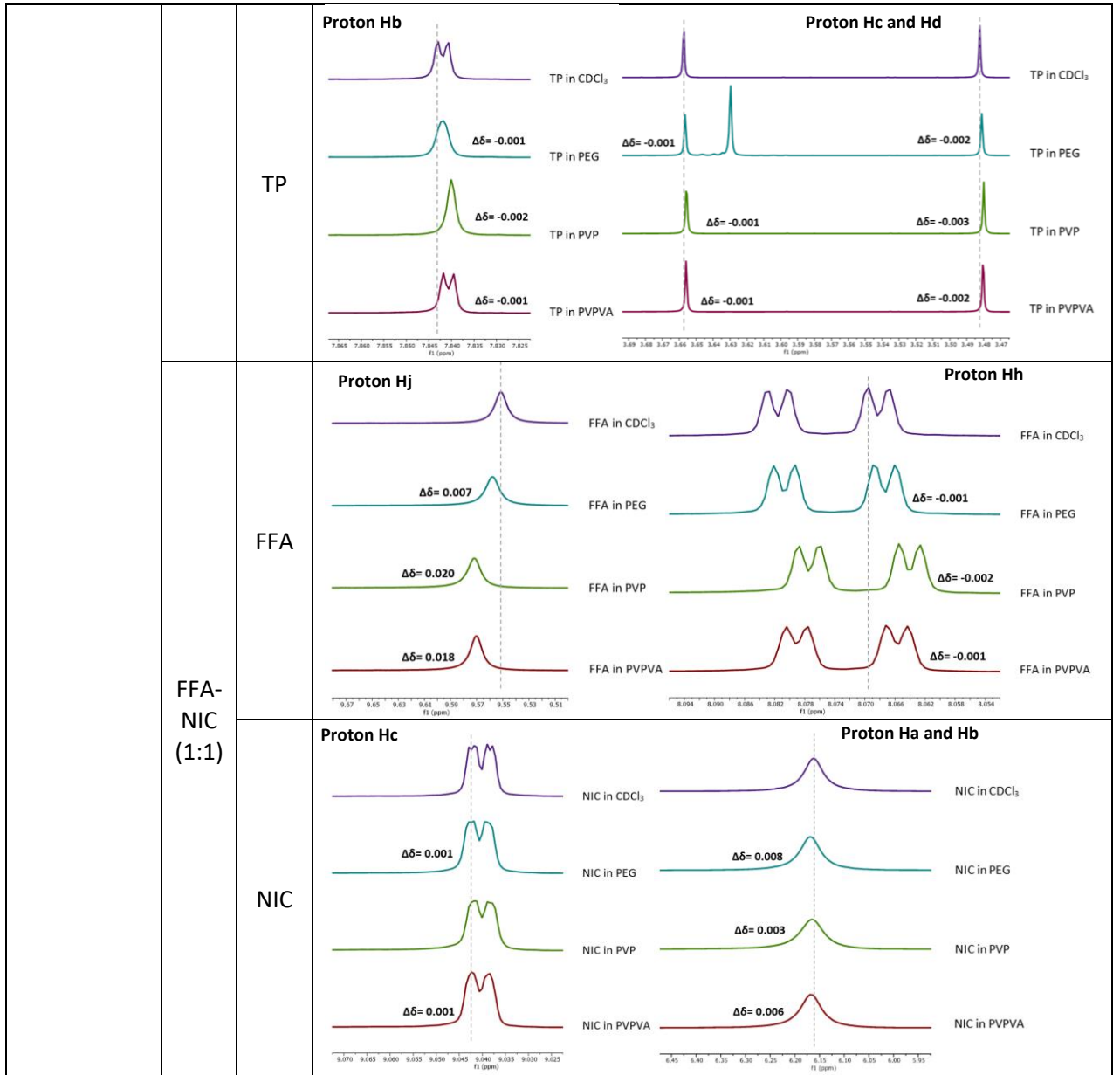
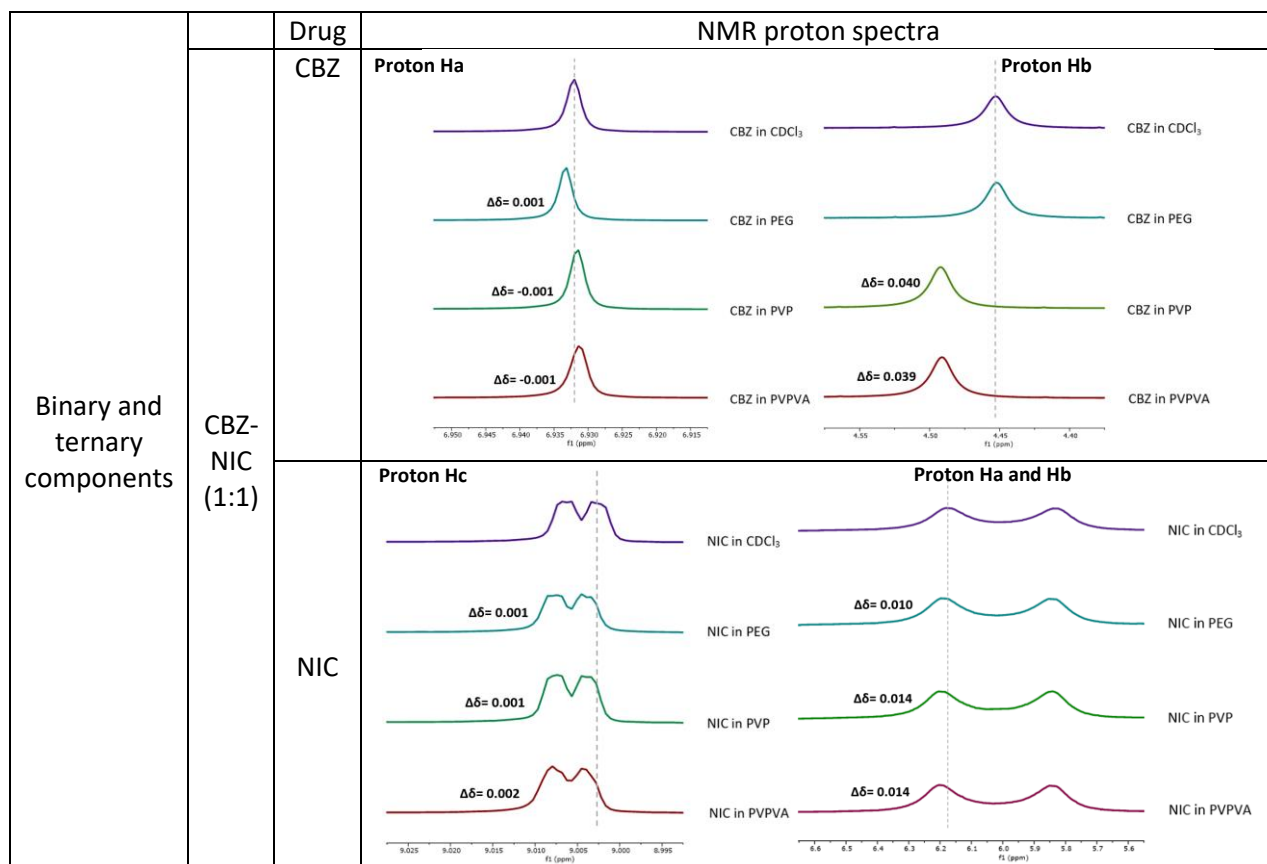
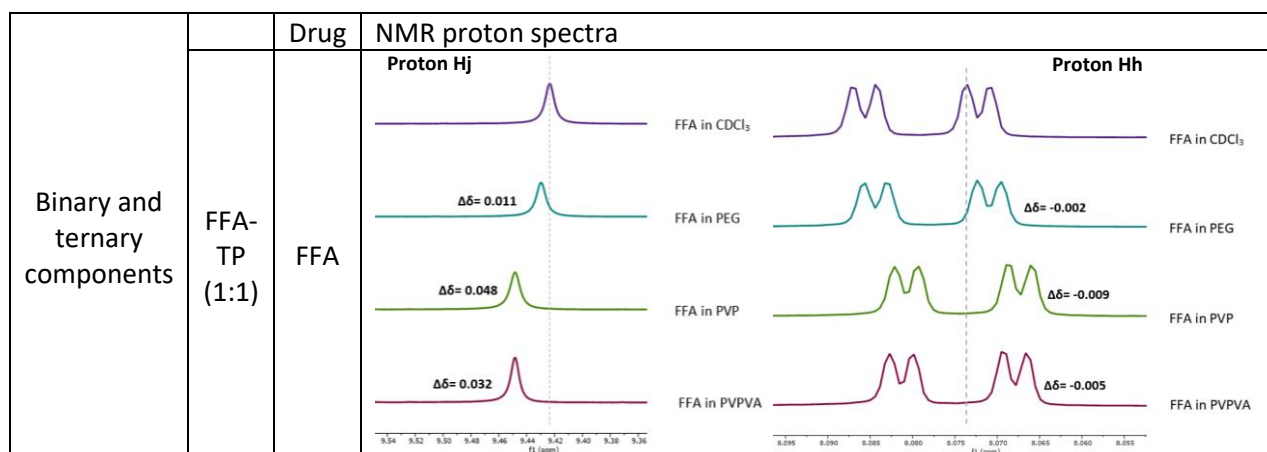


Table 31 - Binary and ternary component NMR analysis of CBZ-NIC with 0.5mg/ml PEG, PVP or PVP-VA



7.3.2.3 In presence of 1mg/ml PEG/PVP/PVP-VA

Table 32 - Binary and ternary component NMR analysis of 1:1 FFA-TP and 1:1 FFA-NIC with 1mg/ml PEG, PVP or PVP-VA



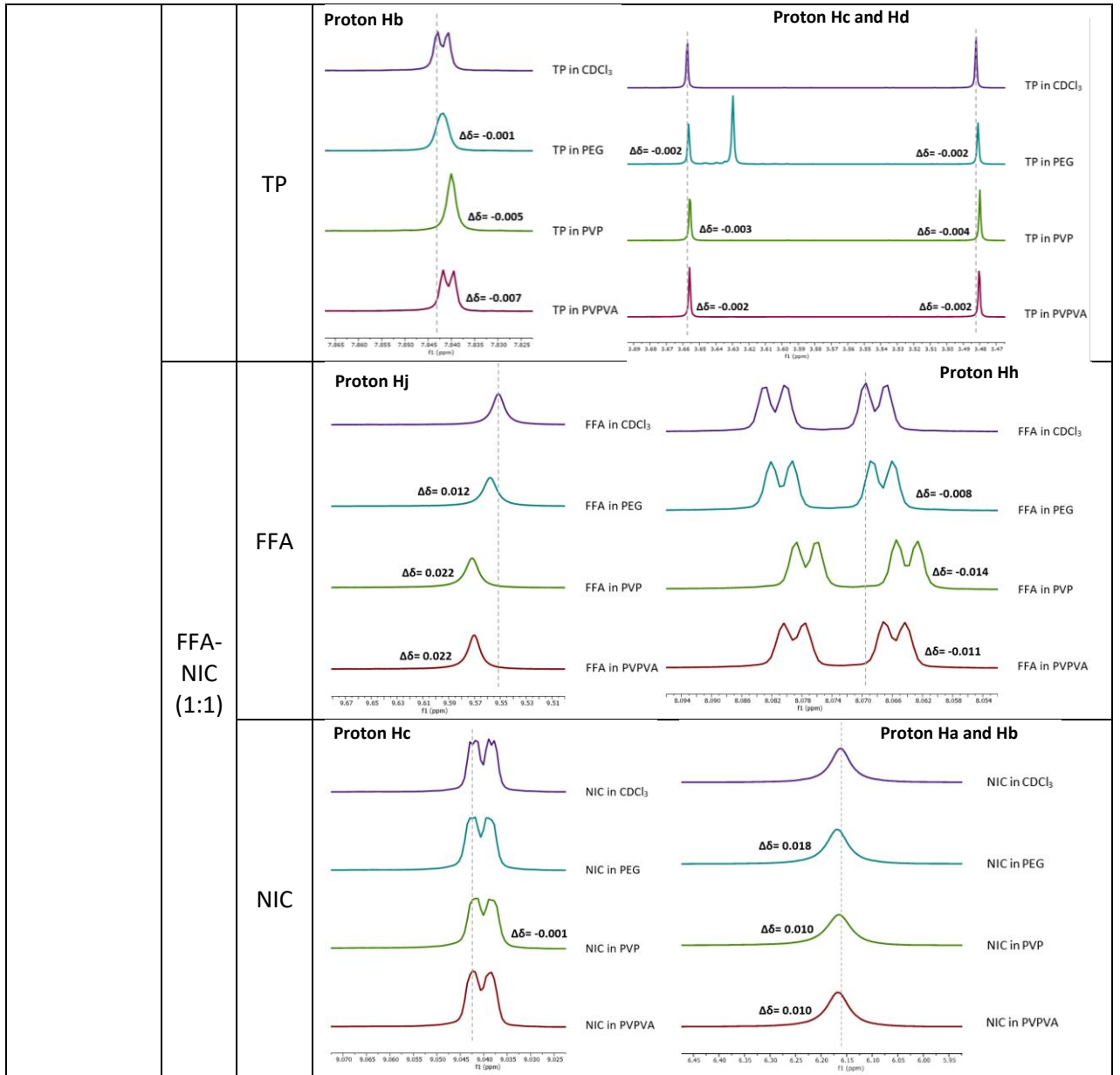


Table 33 - Binary and ternary component NMR analysis of 1:1 CBZ-NIC with 1mg/ml PEG, PVP or PVP-VA.

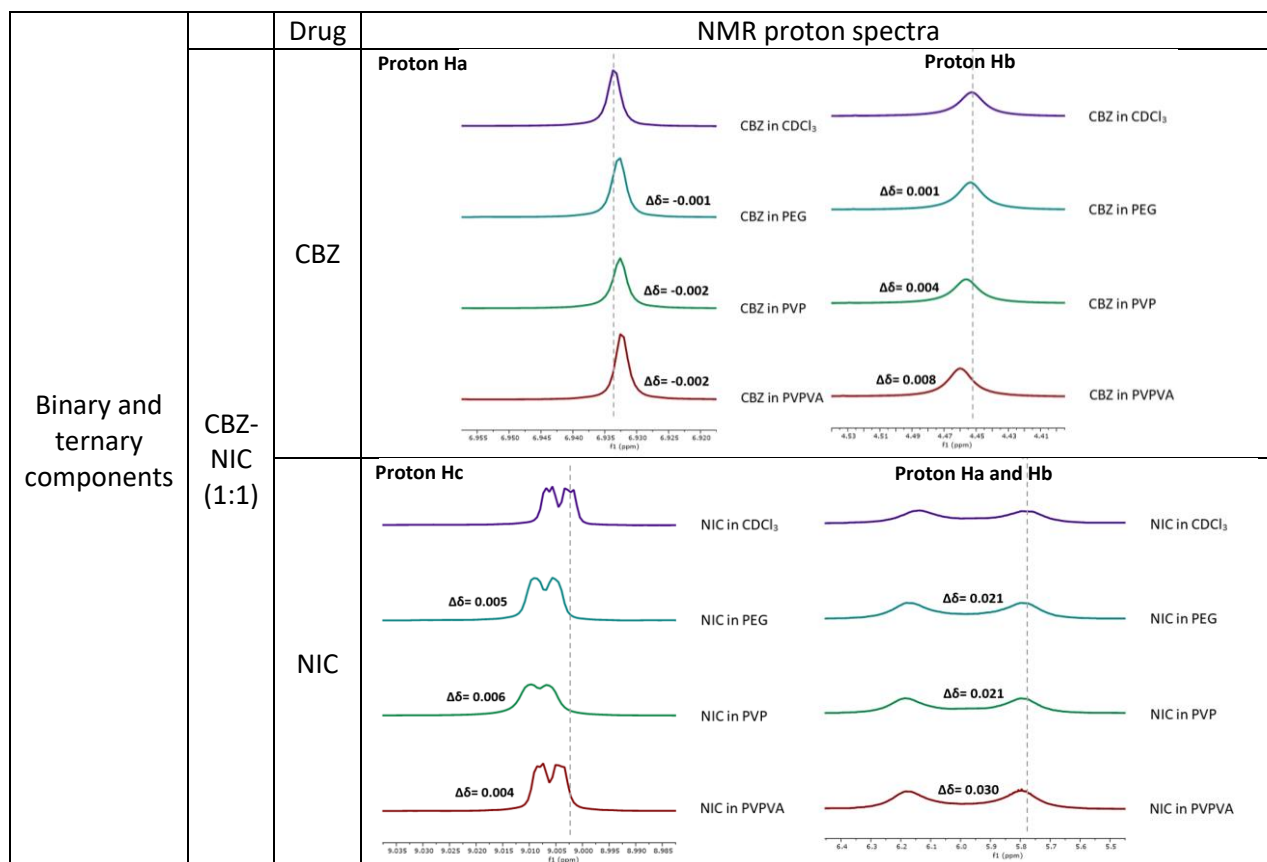


Table 34 - Summary of peak shift differences of binary and ternary components

Compound		Characteristic peak	Difference of peak shift								
			PEG	PVP	PVPVA	PEG	PVP	PVPVA	PEG	PVP	PVPVA
-		-	0.3mg/ml	0.3mg/ml	0.3mg/ml	0.5mg/ml	1mg/ml	0.5mg/ml	0.3mg/ml	0.3mg/ml	0.3mg/ml
FFA-TP	FFA	9.423	0.004	0.015	0.004	0.006	0.011	0.025	0.048	0.025	0.032
		8.071	-0.001	-0.003	-0.001	-0.001	-0.002	-0.006	-0.009	-0.005	-0.005
	TP	7.841	0	-0.002	-0.001	-0.001	-0.001	-0.002	-0.005	-0.001	-0.007
		3.657	-0.001	-0.002	-0.001	-0.001	-0.002	-0.001	-0.003	-0.001	-0.002
FFA-NIC	FFA	9.551	0.002	0.003	0.003	0.007	0.012	0.02	0.022	0.018	0.022
		8.067	-0.001	-0.002	0	-0.001	-0.008	-0.003	-0.014	-0.004	-0.011
	NIC	9.038	0	-0.003	0.001	0.001	0	0	-0.001	0.001	0
		6.161	0.003	-0.032	0.005	0.008	-0.01	0.003	-0.01	0.006	-0.018
2mg/ml CBZ		6.935	0	-0.001	-0.001	0	-0.001	-0.001	-0.002	-0.001	-0.001
		4.394	0	0.002	0.002	0	0.003	0	0.006	0	0.004
1.03mg/ml NIC		9.007	0.002	0.001	0	0.001	0.001	0.002	0.003	0.002	0.002
		5.742	0.035	0.007	0.007	0.008	0.015	0.013	0.015	0.013	0.015
CBZ-NIC	CBZ	6.932	0	0	0.001	0.001	-0.001	-0.001	-0.002	-0.001	-0.002
		4.452	0	0.001	-0.016	0	0.001	0.04	0.004	0.039	0.008
	NIC	9.002	0.001	0.001	0.002	0.001	0.005	0.001	0.006	0.002	0.004
		5.767	0	0	-0.027	0.01	0.021	0.014	0.021	0.014	0.03

Ternary components consisted of the mixtures of FFA and CBZ at a concentration of 2mg/mL or 2.4mg/ml with its equal molar concentration of a co-former of NIC or TP in different concentrations of a polymer in CDCl₃ presented in Tables 28-33. The concentrations of the polymers remained at 0.3mg/ml, 0.5mg/ml or 1mg/ml of PEG, PVP or PVP-VA.

Regarding mixture of FFA and TP in CDCl₃, in the presence of 0.3mg/ml PEG, the H_j proton of FFA had a downfield shift of $\Delta\delta = 0.004$, PVA showed a shift of $\Delta\delta = 0.015$ and PVP-VA, $\Delta\delta = 0.004$. The H_h protons showed an up-field shift for all three polymers. The H_b proton of TP showed no change in the presence of PEG and a downfield shift in the presence of PVP and in the presence of PVP-VA, which contrasted with TP in PVP-VA alone (Table 28). This indicates that hydrogen bonds between FFA and TP were disturbed by the polymer as well as the dimerization of the TP molecules. In the presence of 0.5mg/ml (Table 30), a slight change was seen for the H_j proton in the presence of PEG and a large change was seen in the presence of PVP and PVP where the down-fielding effect increased to $\Delta\delta = 0.025$ for both. The H_h proton also showed an increase in the up-field shift of $\Delta\delta = -0.001$, $\Delta\delta = -0.006$ and $\Delta\delta = -0.005$ for PEG, PVP and PVP-VA respectively.

The chemical shifts of the H_b, H_c and the H_d protons did not show significant change indicating that the chemical environments of the TP protons did not change much. In the presence of 1mg/ml polymer (Table 32), a further increase was seen for the chemical shifts of H_j protons of FFA in the presence of PVP and PVP-VA - $\Delta\delta = 0.048$ for PVP and $\Delta\delta = -0.032$ for PVP-VA. H_h protons also showed a slight increase in the presence of PEG and PVP - $\Delta\delta = -0.002$ and $\Delta\delta = -0.009$ respectively – while PVP-VA remained the same. Furthermore, the H_b proton showed a slight increase in the presence of PVP and PVP-VA and no change in the presence of PEG. The chemical environments for H_c and H_d protons remained the same. The results indicate that PVP interacted the most with the carbonyl functional group of FFA followed by PVP-VA then PEG. The 1mg/ml PVP-VA interacted with the dimerization of TP while no significant change was seen in the presence of other polymers in all three concentrations. This indicates that the chemical environment change was due to the hydrophobic/hydrophilic nature of the polymer and not due to hydrogen bond formation.

Regarding the FFA-NIC co-crystal, at a low polymer concentration of 200 μ g/mL in CDCl₃, characteristic chemical shifts of the H_j proton of FFA moved downfield while H_h protons in the presence of PEG and PVP moved up-field. The H_c proton on the NIC showed no change in the presence of PEG, an up-field shift of $\Delta\delta = -0.003$ in the

presence of PVP and a downfield shift of $\Delta\delta = 0.001$ in the presence of PVP-VA. The Ha protons show a downfield shift ($\Delta\delta = 0.003$) in the presence of PEG, a large upfield shift ($\Delta\delta = -0.032$) in the presence of PVP and a downfield shift ($\Delta\delta = 0.005$) in the presence of PVP-VA. In the presence of 0.5mg/ml polymer (Table 32), a large downfield shift was seen for the Hj proton on FFA in the presence of PVP and PVPVA ($\Delta\delta = 0.020$ and $\Delta\delta = 0.018$ respectively) and a moderate up field shift for the Hh proton. No significant change was seen for the Hc protons of NIC and a moderate down-field shift was seen in the presence of PEG ($\Delta\delta = 0.008$) and PVP-VA ($\Delta\delta = 0.006$). In the presence of 1mg/ml polymer, a high down-fielding shift occurred for the Hj proton on FFA in the presence of PVP and PVP-VA ($\Delta\delta = 0.022$) and a moderate up-field shift for the Hh proton in the presence of all three polymers. No significant change was seen for the Hc proton on NIC and a large downfield shift was seen for the Ha proton in the presence of PEG ($\Delta\delta = 0.018$), PVP ($\Delta\delta = 0.010$) and PVP-VA ($\Delta\delta = 0.010$). These results suggest that some of hydrogen bonds between FFA and NIC have been disrupted due to the interactions of FFA and polymer with PVP being the best polymer.

In the solid state of 1:1 FFA-NIC co-crystal structure, hydrogen bonds are formed by two FFA and two NIC molecules, where Hj of carboxyl acid of the FFA and aromatic N of the first NIC form a hydrogen bond and the amide Ha or Hb of the second NIC forms a hydrogen bond with the carbonyl O atom of the acid of the same FFA [140]. It seems that same interactions of FFA and NIC are formed in CDCl_3 , indicating the de-shielding of chemical shifts of the Hj of FFA and Ha of NIC to a down-field when equal molar of FFA and NIC are dissolved in CDCl_3 and therefore disrupting the intramolecular N-Hj...O=C bond of the co-crystal.

For CBZ-NIC, in the presence of 0.3mg/ml polymer (Table 29), no significant change was seen for the chemical shift of Ha proton of CBZ in the presence of PEG and PVP and a small downfield effect was seen in the presence of PVP-VA ($\Delta\delta = 0.001$). For the Hb proton, no change was seen in the presence of PEG, a slight down-field shift of $\Delta\delta = 0.001$ was seen in the presence of PVP and a large up-field shift of $\Delta\delta = -0.16$ was seen in the presence of PVP-VA. The Hc bond of NIC shows a down-field shift in the presence of PEG ($\Delta\delta = 0.001$), PVP ($\Delta\delta = 0.001$) and PVP-VA ($\Delta\delta = 0.002$). The Ha proton showed an up-field shift of $\Delta\delta = -0.027$ in the presence of PVP-VA which suggests that PVP-VA was able to disrupt the bonds formed by CBZ and NIC. Increasing the polymer concentration to 0.5mg/ml (Table 31) the Ha proton of CBZ shows a slight downfield change in the presence of all three polymers. The Ha proton of NIC shows a moderate down-field shift in the presence of PEG ($\Delta\delta = 0.010$), PVP and PVP-VA ($\Delta\delta = 0.014$). In the presence of 1mg/ml polymers, no significant change

was seen for the CBZ Ha proton, and Hb proton showed a moderate down-field shift in the presence of PVP-VA whereas Hc proton on NIC shows a moderate downfield shift and Ha proton shows a large down field shift in the presence of PEG, PVP ($\Delta\delta = 0.021$) and PVP-VA ($\Delta\delta = 0.030$). The results indicate that PVP and PVP-VA at a concentration of 0.5mg/ml showed the best interaction with CBZ.

7.3.3 Diffusion coefficient

7.3.3.1 In presence of 0.3mg/ml of PEG/PVP/PVP-VA

Table 35 – Singular, binary, and ternary components FFA-TP, FFA-NIC and CBZ-NIC with 0.3mg/ml PEG, PVP or PVP-VA

Drug	Components	Characteristic peak	Diffusion coefficient 10 ¹⁰ cm ² /sec			
			Without polymers	PEG	PVP	PVPVA
W/O drug	-	-	-	2.185	1.149, 1.582, 1.324	1.637
2.4mg/ml FFA	FFA	9.425	8.597	8.235	8.501	8.751
		8.047, 8.061	8.301, 8.612	8.041, 8.561	8.212, 8.593	8.580, 8.766
	Polymer	-	-	1.954	1.594, 1.764, 1.663	2.444
1.54mg/ml TP	TP	7.812	8.886	9.083	8.93524	8.567
		3.646	9.251	8.445	9.36306	8.476
		3.470	8.877	9.112	9.03541	8.672
	Polymer	-	-	2.303	1.424, 2.104, 1.413	1.733

1.00mg/ml NIC	NIC	9.006	13.687	13.341	13.489	12.877
	Polymer	-	-	2.201	1.634, 1.766, 1.245	1.516
(1:1) FFA- TP	FFA	9.425	8.309	8.452	8.285	8.465
		8.047, 8.061	8.159, 8.135	8.385, 8.003	8.128, 7.891	8.483, 8.075
	TP	7.812	8.392	8.284	8.367	8.466
		3.646	8.357	8.287	8.497	8.432
		3.470	8.552	8.311	8.564	8.344
	Polymer	-	-	2.196	0.916, 0.979, 1.846	2.079
(1:1) FFA- NIC	FFA	9.425	8.869	8.665	8.264	7.852
		8.047, 8.061	8.293, 8.386	8.274, 8.327	7.970, 8.529	7.742, 7.568
	NIC	9.006	11.882	11.620	11.223	10.930
	Polymer	-	-	2.079	1.290, 2.040, 1.463	1.296
2.4mg/ml CBZ	CBZ	6.935	10.562	9.994	10.012	9.790
		4.418	9.769	9.963	10.077	9.811
	Polymer	-	-	2.340	1.381, 1.165, 1.360	2.100
	NIC	9.006	12.975	12.638	13.614	13.540

1.2mg/ml NIC	Polymer	-	-	2.936	1.707, 2.404, 2.280	2.263
(1:1) CBZ- NIC	CBZ	6.935	9.764	9.965	9.415	9.820
		4.418	9.582	9.659	9.545	9.667
	NIC	9.006	12.624	12.932	12.267	13.011
	Polymer	-	-	2.396	1.150, 1.807, 1.176	1.948

7.3.3.2 In presence of 0.5mg/ml and 1mg/ml of PEG/PVP/PVP-VA

Table 36 - Singular, binary, and ternary components FFA-TP, FFA-NIC and CBZ-NIC with 0.5mg/ml and 1mg/ml PEG, PVP or PVP-VA

System	Components	Characteristic peaks	W/O polymers	Diffusion coefficient 10 ¹⁰ cm ² /sec in PEG		Diffusion coefficient 10 ¹⁰ cm ² /sec in PVP		Diffusion coefficient 10 ¹⁰ cm ² /sec in PVPVA	
				0.5mg/ml	1mg/ml	0.5mg/ml	1mg/ml	0.5mg/ml	1mg/ml
	Polymer	-	-	2.019	2.113	1.709, 1.880, 1.699	1.256, 1.064, 1.077	1.628	1.599
2mg/ml FFA	FFA	9.425	8.543	8.392	8.445	8.241	7.933	8.389	8.276
		8.047, 8.061	8.243, 8.580	8.355, 8.541	8.552, 8.289	8.081, 8.371	7.881, 7.797	8.149, 8.428	8.297, 8.104
	Polymer	-	-	1.824	2.177	1.771, 2.465, 1.512	1.324, 2.497, 1.275	1.787	1.745
1.28mg/ml TP	TP	7.812	8.827	9.000	8.661	8.663	8.338	8.969	8.500
		3.646	9.210	8.25911	7.938	8.604	8.307	8.780	8.285
		3.470	8.820	8.97918	8.342	8.480	8.406	8.975	8.332
	Polymer	-	-	2.09781	1.950	1.480, 1.999, 1.250	1.389, 2.391, 1.455	1.683	1.551
	NIC	9.006	13.635	13.712	12.634	12.209	12.567	12.843	12.893

0.86mg/ml NIC	Polymer	-	-	2.434	2.059	0.1691 0.218, 0.858	1.107, 1.213, 1.150	1.619	1.453
FFA-TP (1:1)	FFA	9.425	8.268	8.140	8.270	8.010	7.689	8.015,	7.911
		8.047, 8.061	8.137, 8.089	8.151, 8.072	8.061, 8.558	7.975, 7.872	7.494, 7.832	7.888, 7.884	7.770, 7.959
	TP	7.812	8.392	8.529	8.540	8.143	8.326	8.465	8.293
		3.646	8.330	7.268	8.416	8.438	8.409	8.549	8.292
		3.470	8.543	8.622	9.076	8.130	8.384	8.653	8.387
Polymer	-	-	2.140	2.058	1.765, 1.622, 1.627	1.039, 2.012, 1.231	1.876	1.561	
FFA-NIC (1:1)	FFA	9.425	8.824	8.396	8.657	8.298	7.838	8.247	8.224
		8.047, 8.061	8.271, 8.367	8.146, 8.272	8.232, 8.948	7.988, 7.751	7.759, 8.114	8.047, 7.907	7.769, 8.578
	NIC	9.006	11.860	11.621	11.561	11.620	11.320	11.648	11.508
	Polymer	-	-	2.255	2.391	1.133, 1.524, 1.503	1.234, 2.102, 1.206	1.821	1.520
2mg/ml CBZ	CBZ	6.935	10.501	9.838	9.707	9.762	10.226	9.776	9.708
		4.418	9.737	9.671	9.435	9.683	9.827	9.648	9.617
	Polymer	-	-	2.120	2.238	1.600, 1.326, 1.484	1.770, 1.455, 1.681	1.473	1.472

1.03mg/ml NIC	NIC	9.006	12.932	13.025	12.603	13.109	12.506	12.920	12.613
	Polymer	-	-	2.225	1.975	1.299, 1.749, 1.425	1.224, 1.148, 1.353	1.668	1.567
CBZ-NIC (1:1)	CBZ	6.935	9.719	9.385	9.385	10.071	9.492	10.688	9.413
		4.418	9.556	9.429	9.233	9.482	9.808	9.458	9.275
	NIC	9.006	12.609	12.34009	11.990	12.574	12.270	13.067	12.083
	Polymer	-	-	2.117	3.432	1.507, 1.504, 1.919	1.314, 1.372, 1.383	1.718	1.585

Table 37 - Summary of Diffusion coefficient corresponding to the H_j peak of FFA

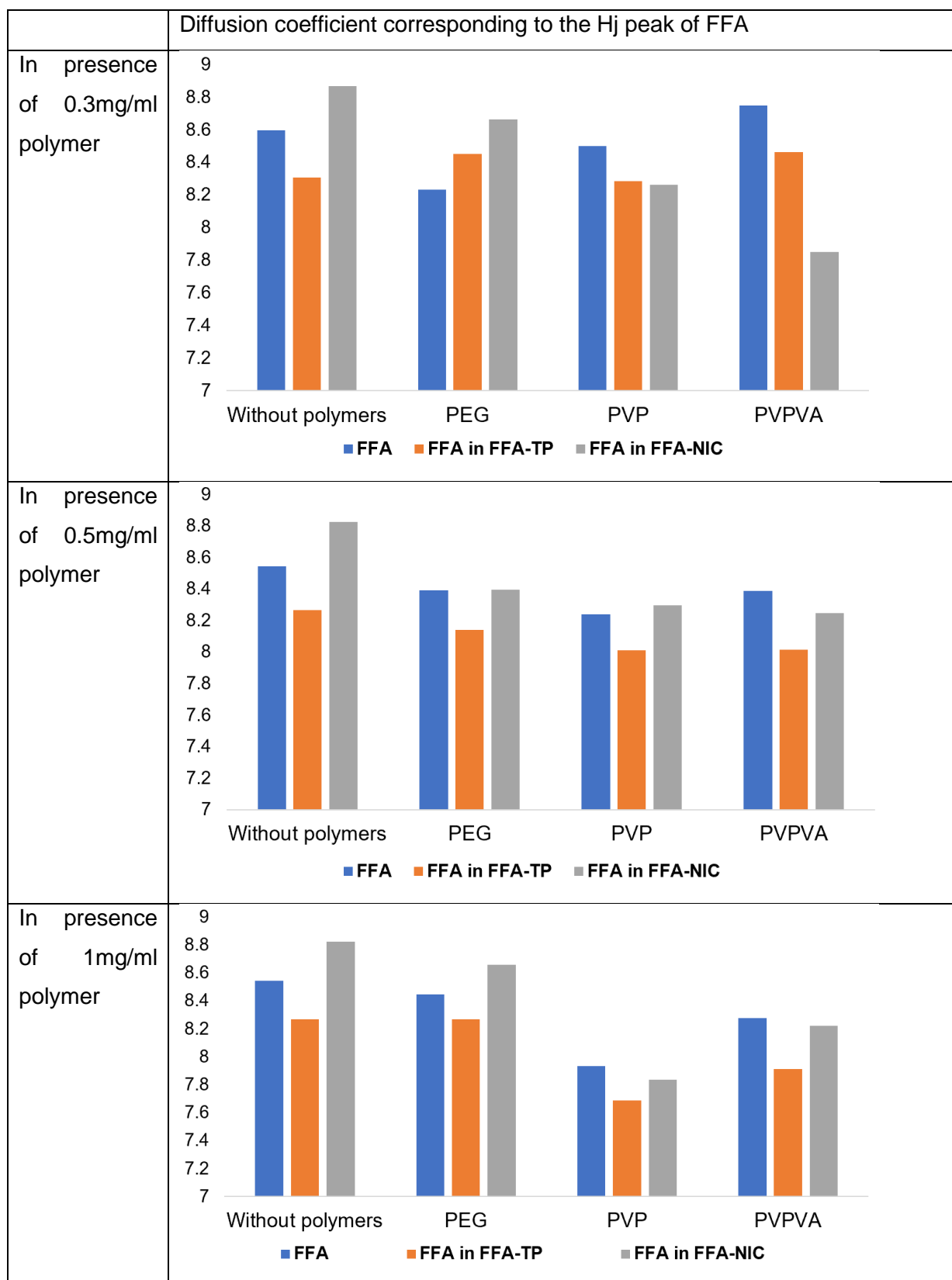
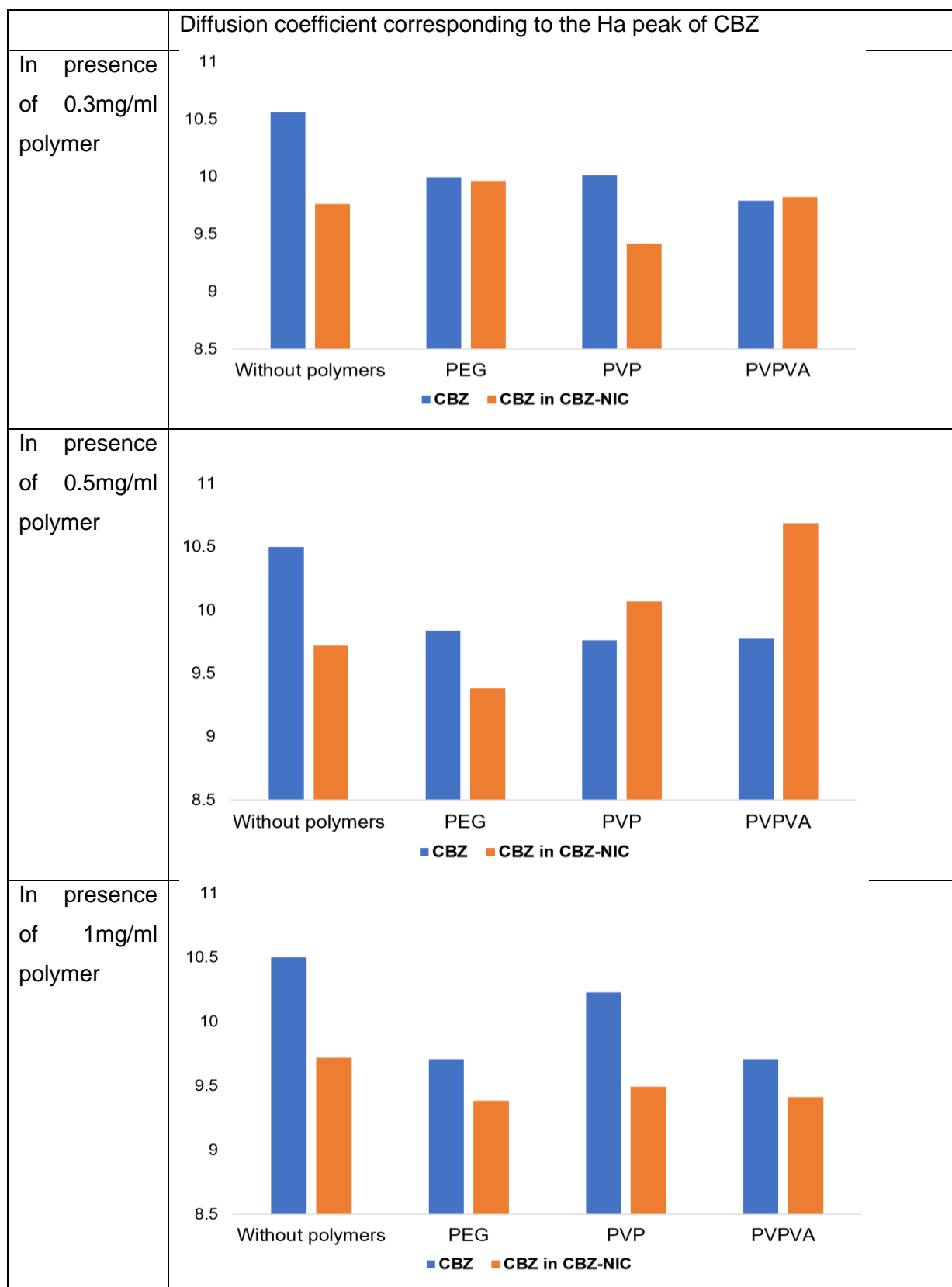
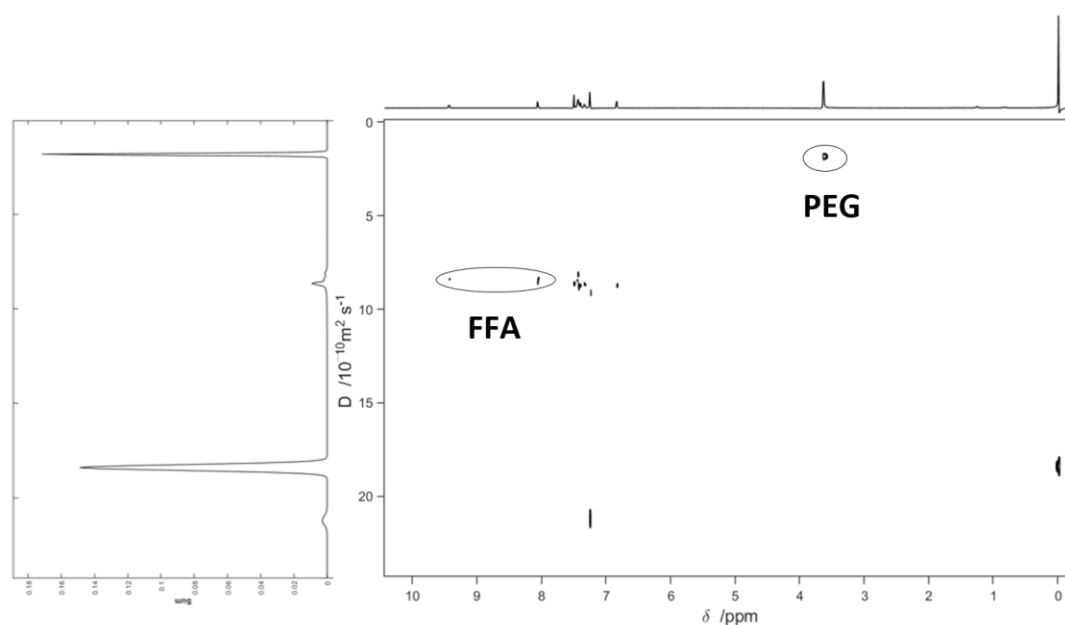


Table 38 - Summary of Diffusion coefficient corresponding to the Ha peak of CBZ



Diffusion coefficient (DC) can be used as a means to measure the size and structural information of particles [349]. 2D DOSY spectra were measured and the diffusion coefficient of the drugs, co-formers and polymers were identified based on the characteristic peaks. The values of DC are shown in tables 35 and 36 followed by a summary of the H_j peak of FFA and H_a peak of CBZ in Tables 37 and 38 respectively. An example of the 2D spectrum of FFA in the presence of PEG is shown below. All 2D DOSY spectra can be found in the Appendices A6.

Figure 30 - 2D DOSY spectrum of FFA and PEG in CDCl₃



Addition of 0.3mg/ml polymers to FFA drug molecules in chloroform altered the diffusion coefficient of the drug. In the presence of PVPVA, the diffusion coefficient increased to 8.751 from 8.597 but decreased in the presence of PEG and PVP. The diffusion coefficients of PEG decreased while an increase was seen for PVP and PVP-VA (Table 35). Increasing the polymer concentration to 0.5mg/ml and 1mg/ml polymer (Table 36), the diffusion coefficient of FFA decreased all three polymers, with the biggest decrease seen in the presence of PVP as shown in table 37 which suggests hydrogen bond formation between FFA and PVP molecules.

TP, in the presence of 0.3mg/ml and 0.5mg/ml, the diffusion coefficient corresponding to the characteristic peak 7.8 (H_b proton), increased in the presence of PEG and PVP and decreased in the presence of PVP-VA. In 0.3mg/ml polymer, the DC corresponding to the 3.6 characteristic peak (H_c proton), decreased in the presence of PEG and PVP-

VA and increased in the presence of PVP while the peak corresponding to 3.4 (Hd proton), decreased in the presence of PEG and PVP-VA and increased in the presence of PVP (Table 35). The diffusion coefficient of PEG, PVP and PVP-VA also increased which suggests no interaction was taking place between the polymers and TP. A decrease in the DC of the drug could be due to the self-association of the TP molecules. In the presence of 0.5mg/ml polymer, the DC decreased for the 3.6 characteristic peak (Hc proton) in the presence of all three polymers while the 3.4 peak shows an increase in the presence of PEG and PVP-VA and a decrease in the presence of PVP. In the presence of 1mg/ml polymer, a decrease in the DC was seen for all characteristic peaks of TP. A decrease in the polymer DC was seen in the presence of 1mg/ml PEG, 0.5mg/ml PVP and 1mg/ml PVP which suggests hydrogen bond formation between the TP molecules and polymers in the specified concentrations (Table 36).

NIC (corresponding to the ratio of FFA) shows an increase in the DC in the presence of 0.5mg/ml PEG and a decrease in the presence of all other polymers in 0.3mg/ml, 0.5mg/ml and 1mg/ml concentrations. NIC (corresponding to the ratio of CBZ), in 0.3mg/ml concentration, decreased in the presence of PEG, and increased in the presence of PVP and PVP-VA. DC of NIC increased in the presence of 0.5mg/ml and 1mg/ml PEG and decreased in the presence of all other polymers.

In the presence of 0.3mg/ml polymer the 6.9 characteristic peak of CBZ showed a decrease in the presence of all three polymers while the 4.4 characteristic peak showed an increase the presence of all three polymers. The DC of the polymers also increased suggesting that no interactions were taking place between the polymer and CBZ molecules. In the presence of 0.5mg/ml and 1mg/ml polymers, the DC of CBZ decreased in all three polymers. The DC of polymers decreased in the presence of 0.5mg/ml PVP and PVP-VA and in 1mg/ml PVP-VA suggesting hydrogen bond interactions with CBZ.

The DC of FFA in FFA-TP decreased in comparison to FFA alone. In 0.3mg/ml polymer concentration, the DC was further decreased in the presence PVP while an increase was seen in the presence of PEG and PVP-VA. A large decrease was also seen on the DC of PVP which suggests hydrogen bond formation between PVP and FFA molecules. 0.5mg/ml and 1mg/ml polymer concentration also show a decrease in the DC of FFA molecules with the largest decrease seen in the presence of 1mg/ml PVP as seen in Table 37. The DC of FFA in FFA-NIC also decreased in the presence of all three polymers in both 0.5 and 1mg/ml concentrations with the largest decrease seen in the

presence of 1mg/ml PVP. In the presence of 0.3mg/ml, the largest decrease was seen in the presence of PVP-VA.

Regarding CBZ-NIC, the DC of CBZ decreased in comparison to CBZ alone. An increase was seen in the DC of CBZ in the presence of 0.3mg/ml PEG and PVP-VA polymer while a decrease was seen in the presence of PVP. Increasing the polymer concentration to 0.5mg/ml, the 6.9 characteristic peak showed an increase in the DC of CBZ in the presence of PVP and PVP-VA while a decrease was seen in the presence of PEG. The DC corresponding to the characteristic peak 4.4, showed a decrease in the presence of all three polymers. Increasing the polymer concentration to 1mg/ml showed a decrease in the DC for CBZ in the presence of all polymers, except for DC corresponding to the characteristic peak 4.4 in the presence of PVP. DC of polymer shows a decrease for 0.5mg/ml PVP and 1mg/ml PVP-VA indicating hydrogen bond formation.

7.4 Discussion

In this chapter, we have demonstrated the molecular interactions between drugs (FFA and CBZ) and co-formers (TP and NIC) in the presence of 0.3mg/ml, 0.5mg/ml and 1mg/ml polymers (PEG, PVP and PVP-VA) in CDCl₃. The mechanism of the effects of the polymers on the dissolution surface of co-crystals has been explored in our recent publication [350], and in the previous chapter indicating that a pre-dissolved polymer can interact with the crystal surface to alter the co-crystal dissolution properties, therefore inhibiting the drug precipitation. PEG, PVP and PVP-VA are water soluble polymers. However, due to their differences in molecular structures, the intermolecular interactions of polymer/drug and polymer/co-former are different, which affects the dissolution properties.

PEG showed very little interaction with either FFA or CBZ in solution. At higher concentrations of 0.5mg/ml and 1mg/ml, and in the presence of TP or NIC, a moderate downfield shift was seen for FFA. No significant interactions were seen for CBZ. Our recently published research, also presented in chapter 6, suggested PEG forms very weak interactions with the surfaces of co-crystals and AFM and SEM results (chapter 5) showed recrystallization of the parent drug suggesting PEG was not a good precipitation inhibitor [350]. NMR spectroscopy and DOSY spectroscopy also supports this conclusion as no significant interaction was seen with the drug molecules, regardless of the concentration. Increasing the concentration also did not significantly

alter the diffusion coefficient values suggesting any decreased values could be due to recrystallisation or self-association of the drug and not due to interactions with the polymer.

The downfield chemical shifts of H_i of FFA in FFA-TP or FFA-NIC co-crystal indicated the formation of the hydrogen bonding interactions of FFA with PVP or PVP-VA in solution, with PVP showing a greater effect. This was also supported by the diffusion coefficient values decreasing in the presence of PVP or PVP-VA. Compared with PVP, PVP-VA is more hydrophobic and flexible due to the presence of a hydrophobic monomer vinyl acetate (VA), and leads to the formation of micelles at a higher concentration. PVP-VA micelle formation has been studied by our research group and it was found that critical micelle formation occurred at 1mg/ml of PVP-VA and at concentrations above 1mg/ml, solubility of PVP was elevated [178].

The up-field chemical shifts of H_j of FFA in a higher PVP-VA concentration suggests the encapsulation of FFA in PVP-VA micelles. In the presence of a co-former of NIC or TP in solution, a significant increase in the solubilization ability of PVP-VA was observed. This was consistent with the diffusion coefficient values which decreased in the presence of PVP-VA due to interactions between the drug and polymer. The downfield shift H_b proton in CBZ in the presence of PVP-VA suggests interactions between the drug and polymer, also supported by a reduction in the diffusion coefficient value. A further decrease in the diffusion coefficient of CBZ was seen in the presence of NIC. Increasing the concentration of PVP-VA from 0.3mg/ml to 1mg/ml increased the interaction with FFA or CBZ with PVP-VA suggesting PVP-VA to be a good solubilising agent regardless of its concentration. This was consistent with previously published research by Guo who concluded PVP-VA to be a good solubilising agent and PVP to be a good stabilising agent for FFA [178].

The elevated solution concentrations obtained by PVP-VA are fundamentally different from supersaturation solutions generated in the presence of the stabilizing agent PVP. Solubilizing additives increase concentration by increasing the equilibrium solubility rather than increasing the chemical potential. In conclusion, the solubility of FFA or CBZ co-crystal formulation is determined by the combination of several factors such as the type of a polymer, the polymer concentration and co-former present: in particular, the interaction between a polymeric excipient with the co-former.

7.5 Chapter conclusion

In this work, the mechanism of the supersaturated solution in the presence of polymers, the atomic-level information of molecular interactions among the parent drug, co-formers and polymers were studied using one-dimensional proton nuclear magnetic resonance (^1H NMR) spectroscopy and DOSY spectroscopy. The study showed that the type of a polymer, its concentration, and the interaction of the polymer with a co-former in solution will significantly affect the FFA and CBZ co-crystals. It was found that PEG did not make a significant effect on the parent drugs. Furthermore, the role of PVP as a stabilising agent did not change for FFA even in the presence of co-formers. PVP-VA on the other hand acts as a good solubilizer even at low concentrations.

Solution ^1H NMR and DOSY spectrometry is a powerful tool in which the atomic-level knowledge of molecular interactions among parent drug (FFA and CBZ), co-formers and polymers have been uncovered. In conclusion, to design an optimal co-crystal formulation, the scientific approaches through mechanistic understanding of the molecular state of drug molecules among API, co-former and polymeric excipients need to be explored to determine the optimal solubility for the performance of oral drug products.

Chapter 8 – Investigating the influence of polymers on drug molecules in solution using Molecular Modelling Techniques

8.1 Chapter overview

Molecular interactions between small drug molecules, water and polymer play a key role in the formulation of medicinal products. It is important to investigate the fundamental chemical interactions underlying dissolution of the co-crystals at molecular level in the presence of polymers. Although these interactions are well understood using experimental methods, using computational methods to accurately calculate binding energies still remain challenging. Molecular dynamics simulations are a powerful and promising approach to calculate binding energies between molecules.

Previously our research focused on preventing surface precipitation by modelling the interaction of polymer molecules on the surface of single co-crystals. However, water molecules could not be incorporated due to increased computational time. This research focusses on the interaction of free co-crystal molecules in water in the presence of PEG, PVP or PVPVA. Interaction energies between drug-water, polymer-water, co-crystal-polymer and co-former-polymer was calculated as well as the distance between the API molecules (length evolution and length distribution), mean squared displacement and radial distribution function. The pharmaceutical co-crystals used for this study are FFA-TP, FFA-NIC and CBZ-NIC. In previous research, these co-crystals have been extensively studied and characterized, showing that their dissolution behaviors could be regulated by including a polymeric excipient in the dissolution media. However, the behavior of these molecules freely in solution is yet to be studied.

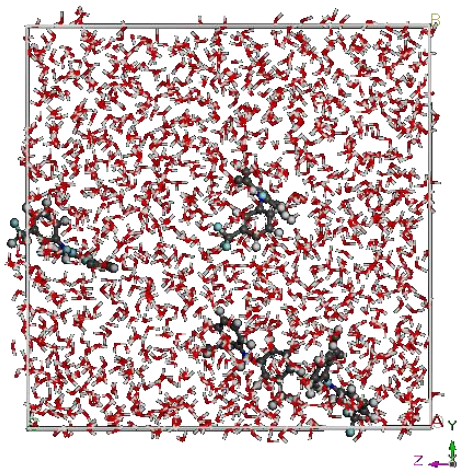
8.2 Methods

CSD 4.1.2 (The Cambridge crystallographic Data Centre, Cambridge, UK) and BIOVIA Material studio 2017 R2 was used to construct the simulation models.

8.2.1 Construction of simulation model

API and co-formers molecules were input from CSD and were geometry optimised (GO). Polymers were built using polymer builder on Materials studio and was GO. Anneal dynamics was performed from 100K to 1000K for 3 cycles to find the conformation of the polymers at minimum energy level. For the model, a 1:1 ratio of 4 FFA/CBZ to co-former molecules was used along with 1500 water molecules and 2 monomer units PEG/ 7 monomer units PVP or 6:4 monomer units PVPVA (6 monomers of PVP and 4 monomers of VA). Amorphous cell Calculation module on Materials studio was used for the construction of models. The density was set at 0.997g/cm^3 to represent the density of water. COMPASS forcefield was used for all geometry optimisation and dynamics simulation methods as it is a widely used and reliable forcefield. The summation method used was Ewald for both Electrostatic and van der Waals forces respectively. The output structure was then geometry optimised using Steepest descent algorithm until minimum was reached. A visual representation of the system containing FFA and water is shown below after geometry optimisation. All other systems can be found in Appendices under A7.

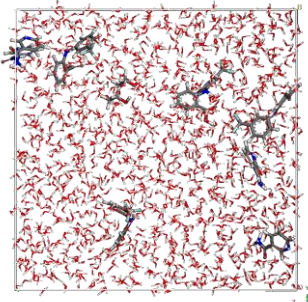
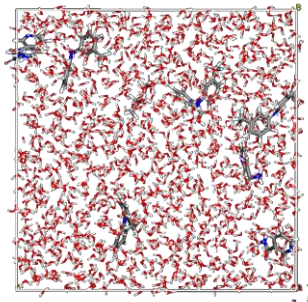
Figure 31 - Simulation box containing FFA and water molecules after geometry optimisation.

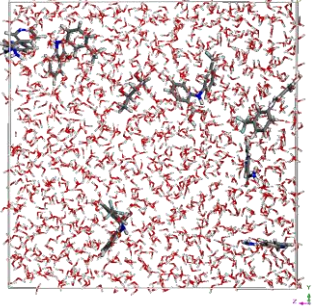
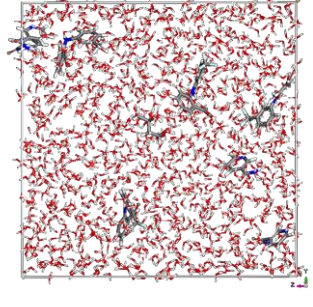
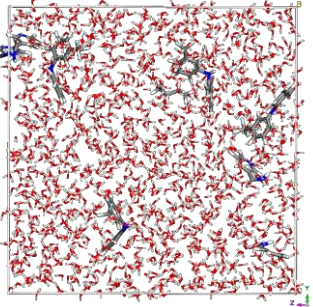


8.2.2 Dynamics simulations

In order to contain all the water molecules inside the simulation box, the O atoms of each water molecule along the edges of the box was fixed in place by using the constraint method. The edged water molecules were allowed to rotate and change conformation in a fixed position while the other water molecules were free to move around. The simulations were performed using COMPASS forcefield, periodic boundary conditions at NVT ensemble, and a temperature of 298K for 50ps to equilibrate the system. The cut-off for non-bonded attractions, i.e., van der Waals and electrostatic forces, were 12.5Å. The simulations were then performed for another 50ps at NVE ensemble in order to acquire the production run needed for analysis with a frame output every 2ps. A visual representation of the system over time containing FFA-NIC and PEG in water is shown in Table 39.

Table 39 - Simulation of FFA-NIC, PEG and Water at 0, 10, 20, 30 and 50ps

Time (ps)	Model
0	
10	

20	
30	
50	

8.2.3 Calculating properties

Length evolution and length distribution

Length evolution and distribution was calculated by selecting the API molecules of interest and selecting 'length evolution' or 'length distribution' from the list of properties on the Forcite analysis dialog.

Mean square displacement

Mean square displacement (MSD) can determine the mode of displacement of particles followed over a defined period. It can help in determining whether the particle is freely diffusing, transported, or bound. The API molecules of interest were selected and 'mean square displacement' was selected from the properties on the Forcite analysis dialog.

Radial distribution function

Radial distribution function describes how density varies as a function of distance from a reference particle. The API-API radial distribution function is defined as the normalized probability of finding an atom of an API molecule at a radial distance r from an atom of any other API molecule. The oxygen atoms of the APIs and polymer were selected and 'radial distribution function' was selected from the properties on the Forcite analysis dialog.

8.3 Results

8.3.1 Calculating the energy of API molecules

The Forcite module in materials studio was used to construct an energy expression that represents the potential energy surface by which the particles of a specified system interact. The total energy, van der Waals and electrostatic interactions of the API in the system containing API, polymer and water molecules was calculated at the start and end of the production simulation (NVE) time of 50ps. The results are shown in the tables below.

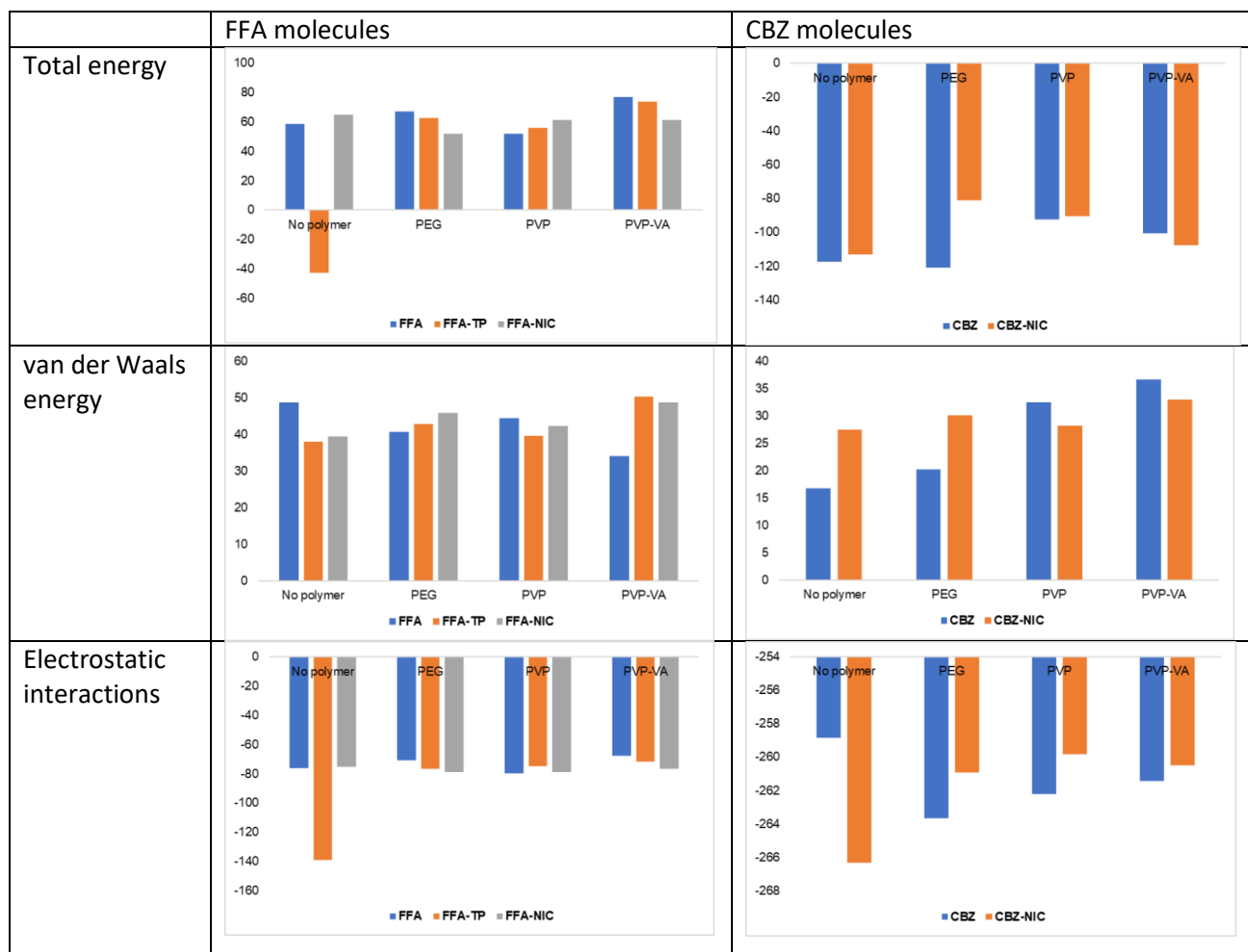
Table 40 - Total energy, van der Waals and electrostatic interactions of API at the start of the production run in the presence of PEG, PVP and PVP-VA

-	Energy of API molecules in systems containing various polymers kcal/mol											
	No polymer			PEG			PVP			PVPVA		
-	Total energy	vdW	Electrostatic	Total energy	vdW	Electrostatic	Total energy	vdW	Electrostatic	Total energy	vdW	Electrostatic
FFA	78.35	34.88	-79.59	65.06	51.74	-78.80	63.97	38.60	-71.55	73.88	41.80	-66.99
FFA-TP	61.83	46.32	-78.90	49.19	45.56	-82.07	55.57	47.96	-76.30	66.07	31.97	-66.47
FFA-NIC	52.69	41.87	-74.89	63.93	37.76	-76.37	55.85	40.10	-75.13	72.68	44.75	-78.71
CBZ	-115.11	24.54	-258.33	-133.84	19.81	-263.63	-93.72	29.82	-259.12	-72.69	31.75	-250.77
CBZ-NIC	-105.09	30.04	-261.03	-89.30	28.00	-261.52	-92.48	31.92	-265.78	-77.99	37.61	-263.29

Table 41 - Total energy, van der Waals and electrostatic interactions of API at the end of the production run in the presence of PEG, PVP and PVP-VA

-	Energy of API molecules in systems containing various polymers kcal/mol											
	No polymer			PEG			PVP			PVPVA		
-	Total energy	vdW	Electrostatic	Total energy	vdW	Electrostatic	Total energy	vdW	Electrostatic	Total energy	vdW	Electrostatic
FFA	58.82	48.81	-76.06	67.03	40.69	-71.01	52.16	44.41	-79.82	76.79	34.13	-67.82
FFA-TP	-42.83	38.08	-138.88	62.73	42.74	-76.71	56.08	39.65	-75.01	73.65	50.39	-71.58
FFA-NIC	65.03	39.35	-75.35	52.01	45.78	-79.05	61.31	42.29	-78.984	61.56	48.76	-76.40
CBZ	-117.29	16.81	-258.85	-120.78	20.25	-263.65	-92.56	32.51	-262.20	-100.82	36.72	-261.44
CBZ-NIC	-112.95	27.53	-266.32	-81.26	30.16	-260.93	-90.32	28.20	-259.82	-107.71	33.00	-260.49

Table 42 - Summary of total energy, van der Waals and electrostatic interactions of API at the end of the production run in the presence of PEG, PVP and PVP-VA



The API in FFA and FFA-TP systems shows a total energy decrease at the end of the production run (Table 41) in comparison to the start in the presence of no polymers (Table 40). FFA in FFA-TP also shows a large increase in the electrostatic attraction which indicates agglomeration of API molecules are occurring by the end of the simulation in the presence of no polymers. The total energy for FFA in FFA-NIC increases to 65.03 kcal/mol while the vdW and electrostatic interactions does not show much change which indicates FFA is more soluble in the presence of NIC. Previously in our research group we concluded FFA-TP shows bulk precipitation in the solvent while FFA-NIC and CBZ-NIC leads to surface precipitation [178], [350].

In the presence of PEG, an increase in the total energy was seen for the API in FFA and FFA-TP systems (Table 42) while a decrease was seen for the electrostatic interactions which indicates the API is soluble in the presence of PEG. For FFA-NIC, a decrease was seen in the total energy while an increase was seen in the vdW and electrostatic interactions. In the presence of PVP, an increase in the total energy was seen for the FFA in FFA-TP system and a large decrease was observed for the electrostatic interactions, while a total energy decrease was seen for the FFA and FFA in FFA-NIC systems and an increase in the electrostatic interactions. This proposes PVP as a good precipitation inhibitor for FFA-TP CO while it is not effective for FFA-NIC CO.

In the presence of PVPVA, there is an increase in the total energy for FFA and FFA in FFA-TP system and a decrease in the electrostatic attractions is observed while the FFA in FFA-NIC showed a very slight increase as shown by table 42. CBZ in the presence of PVP and PVP-VA showed a decrease in the total energy while an increase was seen for the electrostatic interactions in the presence of all three polymers. On the other hand, CBZ in CBZ-NIC showed a decrease in the total potential energy as well as a decrease in the electrostatic interactions in the presence of all three polymers, with the biggest decrease being in the presence of PVP.

The calculation of the energies of the API molecules indicate polymers do play an essential part in the formulation of co-crystals. The large decrease in the electrostatic attraction of FFA in FFA-TP at the end of the production run in comparison the start of the production run points towards agglomeration of the API molecules. Electrostatic interactions of FFA in FFA-TP are significantly decreased in the presence of polymers which indicates that the agglomeration of the FFA molecules are being disrupted by the presence of all three polymers, especially PVP-VA. The results obtained agree with the NMR and DOSY experiments presented in chapter 7 and shows that PVP-VA is the best polymer to use for FFA-TP and FFA-NIC COs while PVP is best suitable for CBZ-NC CO.

8.3.2 Calculating the kinetic properties of API molecules

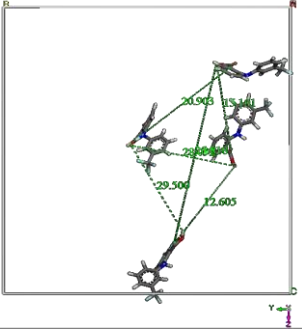
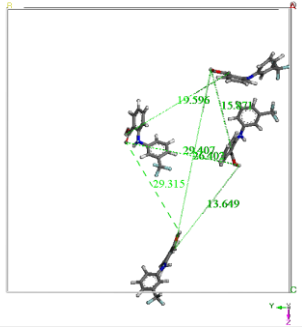
Forcite analysis tools were then used to analyse the simulation results during the production run in order to analyse the distance between the API molecules over a 50ps time period. Plots can be produced showing the evolution of various different lengths of the APIs as the simulation progresses. The mean length evolution, length distribution,

mean squared displacement and radial distribution function was calculated for all FFA and CBZ molecules in various systems in the presence of PEG, PVP or PVP-VA.

Length evolution and length distribution

For visual purposes, only the FFA molecules of the of FFA-PVPVA model is shown below (Table 43) without the polymer and water molecules at different time interval. This model was used to calculate the length evolution and length distribution of the API molecules. All other models can be found in Appendices under A7. The length evolution and length distribution of the API in various systems was observed during the NVE production simulation run of 50ps.

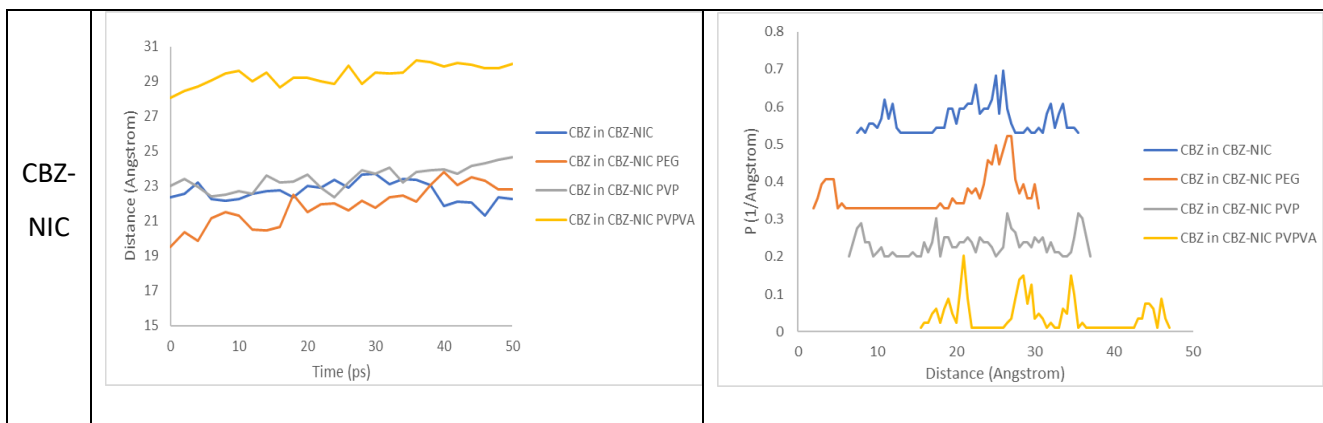
Table 43 - The evolution of bond lengths of FFA molecules at various time intervals in a 50ps production run.

Time (ps)	Model
0	
10	

20	<p>Molecular structure diagram showing bond angles: 114.411, 128.825, 130.190, 13.960, and 22.846 degrees.</p>
30	<p>Molecular structure diagram showing bond angles: 114.416, 128.655, 130.831, 13.875, and 22.158 degrees.</p>
50	<p>Molecular structure diagram showing bond angles: 114.415, 128.863, 130.972, 13.339, and 22.516 degrees.</p>

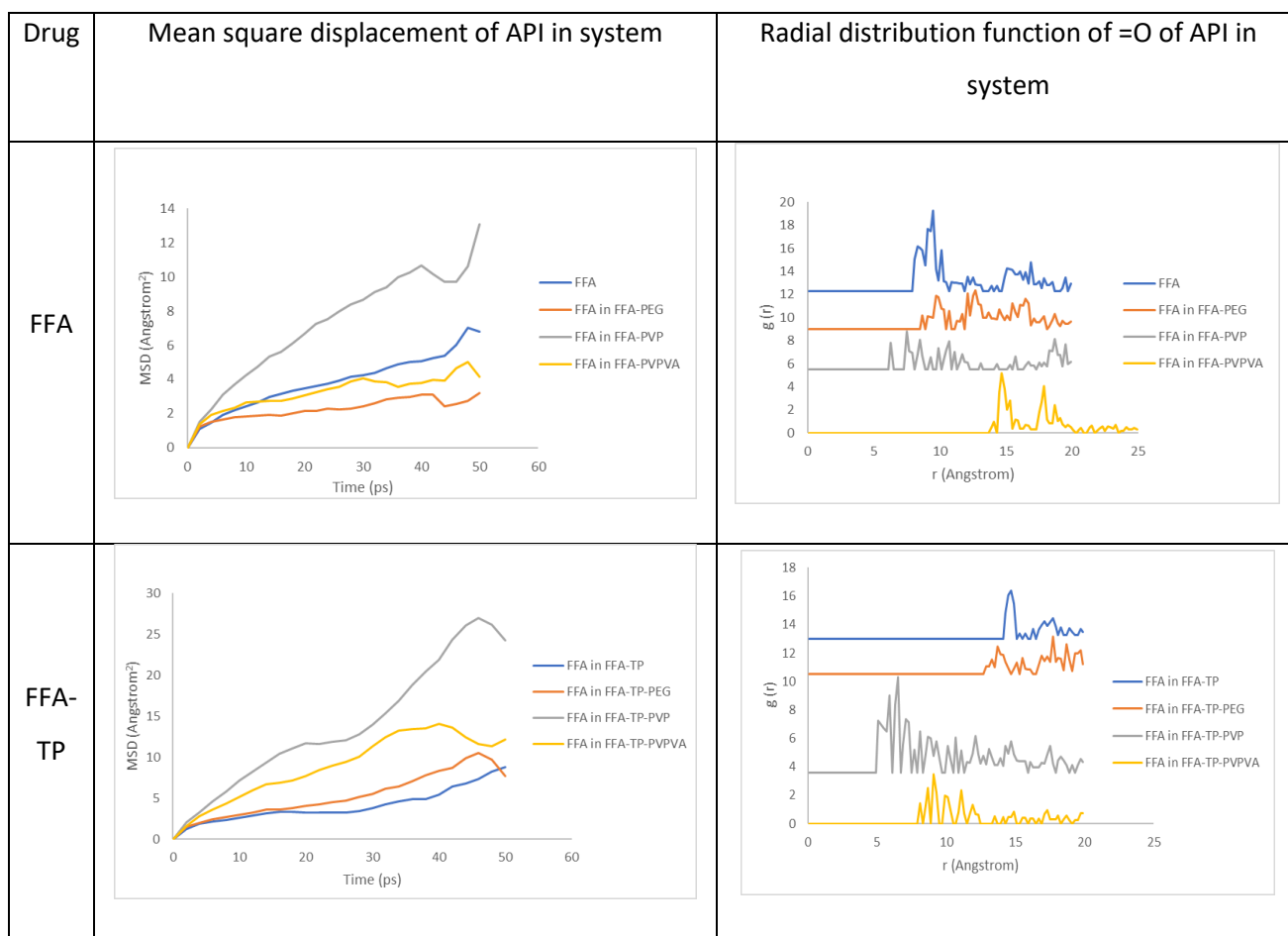
Table 44 - Length evolution and length distribution of APIs with/without polymers over a 50ps production run.

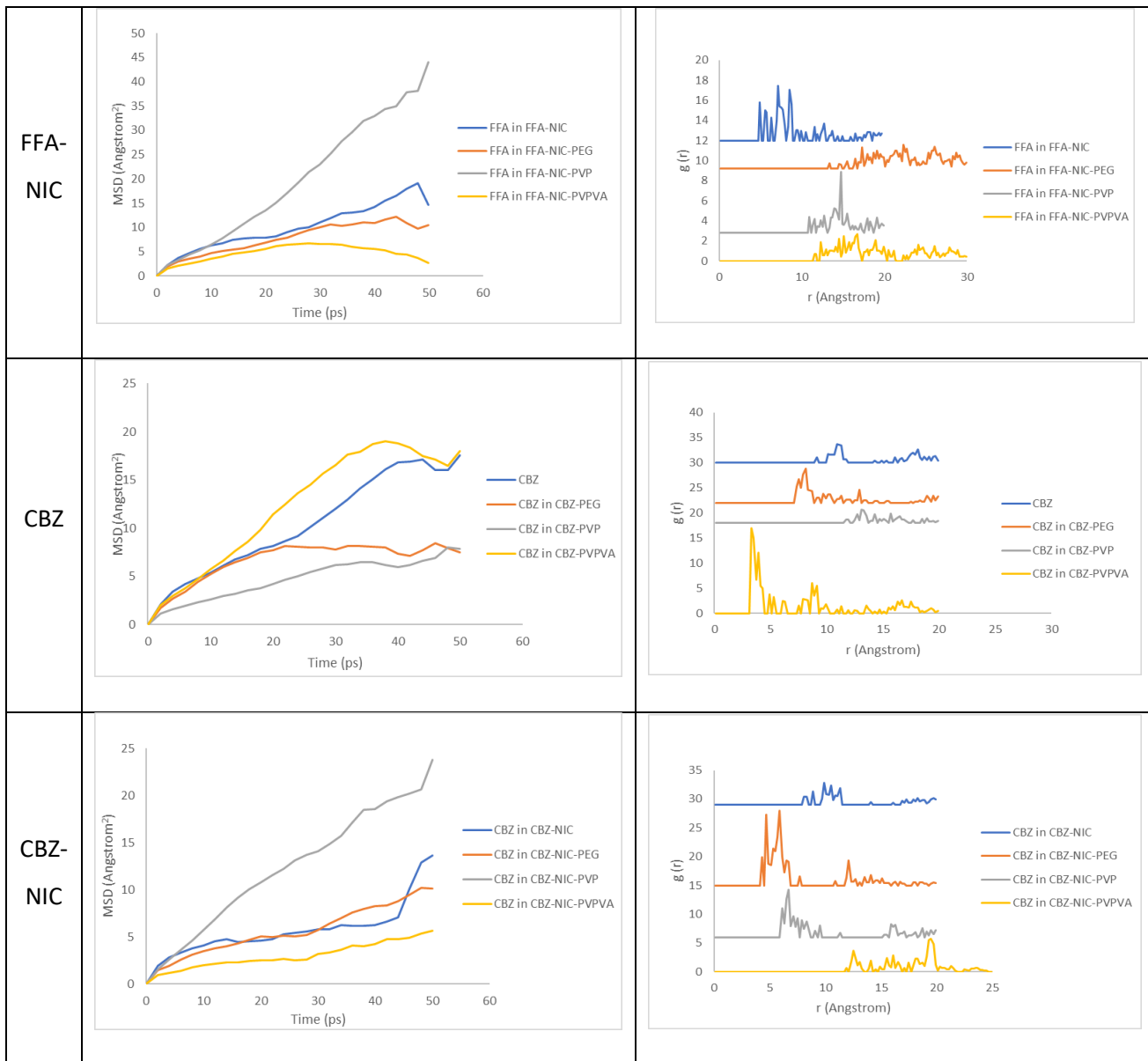




Mean squared displacement and radial distribution function

Table 45 - Mean square displacement and radial distribution functions of API molecules.





8.4 Discussion

The length evolution and length distribution of the APIs in various systems presented in Table 44, was observed after during the production simulation run of 50ps. FFA in the presence of polymers showed slight increase in the distances between the API while FFA alone showed a decrease. This is also supported by the length distribution graph where the probability of finding the API molecules at a shorter distance is higher than in comparison to the API molecules in the presence of polymers. Mean square displacement show the greatest movement for FFA was in the presence of PVP while the radial distribution function suggests strong interactions between the molecules as observed in the graphs in Table 45. The weakest interactions are seen in the presence of PVP-VA.

FFA in FFA-TP and in the presence of PEG and PVP-VA show a stable distance between the APIs over the 50ps time period. FFA in FFA-TP in the presence of PVP however, show a distance of 18Å, at the start of the production run which is much lower in comparison to the FFA alone or in the presence of PEG and PVP-VA (Table 44). The distance then continues to decrease over the course of time which suggests agglomeration of the API molecules is occurring in solution. The length distribution graph is also in agreement with the probability of finding the API molecules is at a distance of less than 30Å. FFA in the presence of FFA-TP also shows the largest mean square displacement in the presence of PVP with radial distribution function also showing the largest interactions between the O atoms (Table 45). Both FFA and TP molecules are able to self-associate with other molecules of the same species. In the presence of polymers, the self-association is disrupted, therefore agglomeration is not occurring.

FFA molecules in FFA-NIC shows a similar pattern to FFA-TP with the API molecules precipitating in the presence of PVP. The probability of finding the molecules close together at short distances are higher in comparison to FFA-TP. Both the length evolution and length distribution (Table 44) suggest PEG and PVP-VA to be a good precipitation inhibitor as they prevent the API molecules from moving close together and the probability of finding the molecules close are low as shown by the length distribution graph. FFA molecules in FFA-NIC show the greatest movement in the presence of PVP as shown by the mean square displacement. However, the greatest interaction between the API molecules was seen in the presence of no polymers. FFA and NIC molecules are able to interact with each other and this interaction is disrupted by the presence of polymers.

CBZ alone and in the presence of PEG and PVP-VA shows a short stable distance between the molecules over the production run. In the presence of PVP, on the other hand, longer distances are seen at the start of the production run which is maintained throughout. The distribution of the bond length shows that majority of the distances are above 22Å (Table 44). Mean square displacement for CBZ shows the largest movement in the presence of PVP-VA with the largest interactions also being present between the molecules in the presence of PEG and PVP-VA (Table 45).

CBZ in CBZ-NIC however, show a promising effect in the presence of PVP-VA. The length between the API molecules is large in comparison to CBZ in the other systems. This is also supported by the bond length distribution which shows the probability of PVP-VA molecules found at longer distances in comparison to others (Table 44). CBZ molecules show the largest movement in the presence of PVP and the lowest movement in the presence of PVP-VA. Radial distribution function also show the lowest interactions in the presence of PVP-VA (Table 45).

From the results gathered, it can be deduced that FFA molecules in FFA-TP and FFA-NIC agglomerate in solution. Precipitation can be inhibited by the addition of polymers as both the NMR (Chapter 7) and molecular modelling results suggest. PVP is the worst polymer for FFA-TP and FFA-NIC formulations while PEG and PVP-VA show effects of inhibiting precipitation. PVP is the best polymer for CBZ formulation while PVP-VA is the most effective for CBZ-NIC formulations.

8.5 Chapter conclusion

This study explores the molecular interactions between the API molecules of FFA or CBZ in the presence of co-formers, various polymers and water molecules. The study showed that the type of a polymer and the interaction of the polymer with the drug in solution will significantly affect the FFA and CBZ co-crystals. It was found that in the presence of PVP, the FFA molecules in FFA-TP and FFA-NIC showed short distances and high interactions suggesting agglomeration of the drug is occurring. PVP-VA however is an effective precipitation inhibitor. Molecular modelling techniques proved to be a powerful tool which can be used to probe into the interactions of the drug molecules at molecular level in order to design effective drug formulations.

Chapter 9 – Conclusion and future work

9.1 Conclusion

This thesis has focussed on the dissolution properties of FFA-TP CO, FFA-NIC CO and CBZ-NIC CO in the presence of three different polymers using a combined experimental and molecular modelling techniques. Both the surface dissolution mechanism and the mechanism of molecular dissolution in solution has been investigated in order to give a better understanding for the formulation of the co-crystals. The specific aims of this study were to:

- 1) explore the surface dissolution of single co-crystals in the presence/absence of polymers in solution by the use of non-contact Atomic force microscopy, Raman spectroscopy and Scanning electron microscopy to detect any surface change.
- 2) at interaction of polymers on surface of single co-crystals by using molecular modelling techniques.
- 3) explore the interactions of drug-drug, drug-polymer and co-former-polymer in solution by using NMR spectroscopy and DOSY.
- 4) explore the interactions of free drug molecules, co-former molecules and monomers in the presence of water molecules using molecular modelling techniques.

The influence of the three polymers PEG, PVP, and PVP-VA on the surface recrystallisation of FFA-TP CO, FFA-NIC CO and CBZ-NIC CO has been investigated using non-contact atomic force microscopy and scanning electron microscopy. FFA-NIC and CBZ-NIC showed recrystallisation on the surface which was identified using Raman spectroscopy. The parent drug of FFA III and CBZ dihydrate had recrystallized on the surface of FFA-NIC CO and CBZ-NIC CO respectively while FFA-TP showed no precipitation on the surface but could have precipitated in the bulk solution.

The dissolution mechanisms of FFA-TP CO are controlled by the defect sites of the crystal surface and by precipitation of the parent drug as individual crystals in the bulk fluid. In contrast, the dissolution mechanisms of FFA-NIC CO are controlled by the surface layer removal and by a surface precipitation mechanism, where the parent drug precipitates directly onto the surface of the dissolving co-crystals as a coating layer.

Both PVP and PVP-VA proved to be good surface precipitation inhibitors for FFA-NIC and could only partially inhibit the precipitation of CBZ-NIC.

Molecular modelling techniques used to investigate the surface dissolution of the co-crystals in the presence of polymers showed that PEG was not an effective inhibitor while PVP and PVP-VA was effective. In contrast to PVP-VA, PVP had greater interaction energies and was more effective in inhibiting parent drug precipitation in comparison to PVP-VA.

Solution ^1H NMR and DOSY spectrometry proved to be a powerful tool in which the atomic-level knowledge of molecular interactions among parent drug, co-formers and polymers can be explored. It was found that the type of a polymer, its concentration, and the interaction of the polymer with a co-former in solution will significantly affect the FFA and CBZ co-crystals. Results show that PEG did not make a significant effect on the parent drugs. Furthermore, the role of PVP as a stabilising agent did not change for FFA even in the presence of co-formers. PVP-VA on the other hand acts as a good solubilizer even at low concentrations.

Finally, molecular modelling of the drug molecules in solution in the presence of co-formers, polymers and water molecules showed that in the presence of PVP, the FFA molecules in FFA-TP and FFA-NIC showed short distances and high interactions suggesting agglomeration of the drug is occurring. PVP-VA however is an effective precipitation inhibitor.

9.2 Future work

The future directions can focus on carrying out animals testing and finally commercial co-crystal products. Up until now, animal studies to explore bioavailability of co-crystals are rare. Current research on pharmacokinetic (PK) studies of co-crystals have been focussing on comparing the bioavailability of co-crystals with pure drugs. However, little is known about the modification of PK of the studied drugs due to the presence of co-former molecules in the GI tract. The underlying mechanisms of PK interactions of drugs, co-formers and polymers needs to be explored before commercial co-crystals products can be produced.

References

- [1] E. Shefter and T. Higuchi, "Dissolution behavior of crystalline solvated and nonsolvated forms of some pharmaceuticals," *J. Pharm. Sci.*, vol. 52, no. 8, pp. 781–791, 1963, doi: 10.1002/jps.2600520815.
- [2] Y. Ishizuka *et al.*, "Effect of Drug-Polymer Interactions through Hypromellose Acetate Succinate Substituents on the Physical Stability on Solid Dispersions Studied by Fourier-Transform Infrared and Solid-State Nuclear Magnetic Resonance," *Mol. Pharm.*, vol. 16, no. 6, pp. 2785–2794, 2019, doi: 10.1021/acs.molpharmaceut.9b00301.
- [3] M. S. Jasani, D. P. Kale, I. P. Singh, and A. K. Bansal, "Influence of Drug-Polymer Interactions on Dissolution of Thermodynamically Highly Unstable Cocrystal," *Mol. Pharm.*, vol. 16, no. 1, pp. 151–164, 2019, doi: 10.1021/acs.molpharmaceut.8b00923.
- [4] P. K. Jha and R. G. Larson, "Assessing the efficiency of polymeric excipients by atomistic molecular dynamics simulations," *Mol. Pharm.*, vol. 11, no. 5, pp. 1676–1686, 2014, doi: 10.1021/mp500068w.
- [5] B. D. Anderson, "Predicting Solubility/Miscibility in Amorphous Dispersions: It Is Time to Move Beyond Regular Solution Theories," *J. Pharm. Sci.*, vol. 107, no. 1, pp. 24–33, 2018, doi: 10.1016/j.xphs.2017.09.030.
- [6] W. A. Birru *et al.*, "Computational Models of the Gastrointestinal Environment. 2. Phase Behavior and Drug Solubilization Capacity of a Type I Lipid-Based Drug Formulation after Digestion," *Mol. Pharm.*, vol. 14, no. 3, pp. 580–592, 2017, doi: 10.1021/acs.molpharmaceut.6b00887.
- [7] C. J. Schram, L. S. Taylor, and S. P. Beaudoin, "Influence of Polymers on the Crystal Growth Rate of Felodipine: Correlating Adsorbed Polymer Surface Coverage to Solution Crystal Growth Inhibition," *Langmuir*, vol. 31, no. 41, pp. 11279–11287, 2015, doi: 10.1021/acs.langmuir.5b02486.
- [8] A. Dalpiaz, V. Ferretti, V. Bertolasi, B. Pavan, A. Monari, and M. Pastore, "From Physical Mixtures to Co-Crystals: How the Cofomers Can Modify Solubility and Biological Activity of Carbamazepine," *Mol. Pharm.*, vol. 15, no. 1, pp. 268–278, 2018, doi: 10.1021/acs.molpharmaceut.7b00899.
- [9] C. J. Schram, S. P. Beaudoin, and L. S. Taylor, "Impact of polymer conformation on the crystal growth inhibition of a poorly water-soluble drug in aqueous solution," *Langmuir*, vol. 31, no. 1, pp. 171–179, 2015, doi: 10.1021/la503644m.
- [10] S. Moghadam and R. G. Larson, "Assessing the efficacy of poly(N-isopropylacrylamide) for drug delivery applications using molecular dynamics simulations," *Mol. Pharm.*, vol. 14, no. 2, pp. 478–491, 2017, doi: 10.1021/acs.molpharmaceut.6b00942.
- [11] H. Nie *et al.*, "Investigating the Interaction Pattern and Structural Elements of a Drug-Polymer Complex at the Molecular Level," *Mol. Pharm.*, vol. 12, no. 7, pp. 2459–2468, 2015, doi: 10.1021/acs.molpharmaceut.5b00162.

- [12] D. Prasad, H. Chauhan, and E. Atef, "Role of Molecular Interactions for Synergistic Precipitation Inhibition of Poorly Soluble Drug in Supersaturated Drug-Polymer-Polymer Ternary Solution," *Mol. Pharm.*, vol. 13, no. 3, pp. 756–765, 2016, doi: 10.1021/acs.molpharmaceut.5b00655.
- [13] F. Keramatnia, A. Shayanfar, and A. Jouyban, "Thermodynamic Solubility Profile of Carbamazepine-Cinnamic Acid Cocrystal at Different pH," *J. Pharm. Sci.*, vol. 104, no. 8, pp. 2559–2565, 2015, doi: 10.1002/jps.24525.
- [14] M. Karimi-Jafari, L. Padrela, G. M. Walker, and D. M. Croker, "Creating cocrystals: A review of pharmaceutical cocrystal preparation routes and applications," *Crystal Growth and Design*, vol. 18, no. 10. American Chemical Society, pp. 6370–6387, Oct. 03, 2018, doi: 10.1021/acs.cgd.8b00933.
- [15] Y. Yani, P. S. Chow, and R. B. H. Tan, "Molecular simulation study of the effect of various additives on salbutamol sulfate crystal habit," *Mol. Pharm.*, vol. 8, no. 5, pp. 1910–1918, 2011, doi: 10.1021/mp200277u.
- [16] Y. Yani, P. Kanaujia, P. S. Chow, and R. B. H. Tan, "Effect of API-Polymer Miscibility and Interaction on the Stabilization of Amorphous Solid Dispersion: A Molecular Simulation Study," *Ind. Eng. Chem. Res.*, vol. 56, no. 44, pp. 12698–12707, 2017, doi: 10.1021/acs.iecr.7b03187.
- [17] J. P. Zeng, Y. Dai, W. Y. Shi, J. L. Shao, and G. X. Sun, "Molecular dynamics simulation on the interaction between polymer inhibitors and anhydrite surface," *Surf. Interface Anal.*, vol. 47, no. 9, pp. 896–902, 2015, doi: 10.1002/sia.5792.
- [18] B. Prathab, V. Subramanian, and T. M. Aminabhavi, "Molecular dynamics simulations to investigate polymer-polymer and polymer-metal oxide interactions," *Polymer (Guildf.)*, vol. 48, no. 1, pp. 409–416, 2007, doi: 10.1016/j.polymer.2006.11.014.
- [19] Z. Tong, Y. Xie, and Y. Zhang, "Molecular dynamics simulation on the interaction between polymer inhibitors and β -dicalcium silicate surface," *J. Mol. Liq.*, vol. 259, pp. 65–75, 2018, doi: 10.1016/j.molliq.2018.03.018.
- [20] M. Yazdanian, K. Briggs, C. Jankovsky, and A. Hawi, "The 'High Solubility' Definition of the Current FDA Guidance on Biopharmaceutical Classification System May Be Too Strict for Acidic Drugs," *Pharm. Res.*, vol. 21, no. 2, pp. 293–299, 2004, doi: 10.1023/B:PHAM.0000016242.48642.71.
- [21] R. Löbenberg and G. L. Amidon, "Modern bioavailability, bioequivalence and biopharmaceutics classification system. New scientific approaches to international regulatory standards," *Eur. J. Pharm. Biopharm.*, vol. 50, no. 1, pp. 3–12, 2000, doi: 10.1016/S0939-6411(00)00091-6.
- [22] N. K. Sachan, A. Bhattacharya, S. Pushkar, and A. Mishra, "Biopharmaceutical classification system: A strategic tool for oral drug delivery technology," *Asian J. Pharm.*, vol. 3, no. 2, pp. 76–81, 2009, doi: 10.4103/0973-8398.55042.
- [23] M. Yasir, M. Asif, A. Kumar, and A. Aggarwal, "Biopharmaceutical Classification System :An Account Article in," 2010. [Online]. Available: <https://www.researchgate.net/publication/266213316>.
- [24] M. S. Ku, "Use of the biopharmaceutical classification system in early drug development," *AAPS J.*, vol. 10, no. 1, pp. 208–212, Mar. 2008, doi: 10.1208/s12248-008-9020-0.

- [25] M. Yazdani, K. Briggs, C. Jankovsky, and A. Hawi, "The 'High Solubility' Definition of the Current FDA Guidance on Biopharmaceutical Classification System May Be Too Strict for Acidic Drugs," *Pharm. Res.*, vol. 21, no. 2, pp. 293–299, Feb. 2004, doi: 10.1023/B:PHAM.0000016242.48642.71.
- [26] M. G. Papich and M. N. Martinez, "Applying Biopharmaceutical Classification System (BCS) Criteria to Predict Oral Absorption of Drugs in Dogs: Challenges and Pitfalls," doi: 10.1208/s12248-015-9743-7.
- [27] S. Baghel, H. Cathcart, and N. J. O'Reilly, "Polymeric Amorphous Solid Dispersions: A Review of Amorphization, Crystallization, Stabilization, Solid-State Characterization, and Aqueous Solubilization of Biopharmaceutical Classification System Class II Drugs," *Journal of Pharmaceutical Sciences*, vol. 105, no. 9. Elsevier B.V., pp. 2527–2544, Sep. 01, 2016, doi: 10.1016/j.xphs.2015.10.008.
- [28] G. G. Liversidge and K. C. Cundy, "Particle size reduction for improvement of oral bioavailability of hydrophobic drugs: I. Absolute oral bioavailability of nanocrystalline danazol in beagle dogs," *Int. J. Pharm.*, vol. 125, no. 1, pp. 91–97, Oct. 1995, doi: 10.1016/0378-5173(95)00122-Y.
- [29] V. L. Campo, D. F. Kawano, D. B. da Silva, and I. Carvalho, "Carrageenans: Biological properties, chemical modifications and structural analysis - A review," *Carbohydrate Polymers*, vol. 77, no. 2. Elsevier, pp. 167–180, Jun. 10, 2009, doi: 10.1016/j.carbpol.2009.01.020.
- [30] P. B. Shekhawat and V. B. Pokharkar, "Understanding peroral absorption: regulatory aspects and contemporary approaches to tackling solubility and permeability hurdles," *Acta Pharmaceutica Sinica B*, vol. 7, no. 3. Chinese Academy of Medical Sciences, pp. 260–280, May 01, 2017, doi: 10.1016/j.apsb.2016.09.005.
- [31] K. T. Savjani, A. K. Gajjar, and J. K. Savjani, "Drug Solubility: Importance and Enhancement Techniques," *ISRN Pharm.*, vol. 2012, pp. 1–10, 2012, doi: 10.5402/2012/195727.
- [32] J. I. Jinno *et al.*, "Effect of particle size reduction on dissolution and oral absorption of a poorly water-soluble drug, cilostazol, in beagle dogs," *J. Control. Release*, vol. 111, no. 1–2, pp. 56–64, Mar. 2006, doi: 10.1016/j.jconrel.2005.11.013.
- [33] G. G. Liversidge and P. Conzentino, "Drug particle size reduction for decreasing gastric irritancy and enhancing absorption of naproxen in rats," *Int. J. Pharm.*, vol. 125, no. 2, pp. 309–313, Oct. 1995, doi: 10.1016/0378-5173(95)00148-C.
- [34] J. O. Morales, A. B. Watts, and J. T. McConville, "Mechanical particle-size reduction techniques," in *AAPS Advances in the Pharmaceutical Sciences Series*, vol. 22, Springer Verlag, 2016, pp. 165–213.
- [35] S. Verma, R. Gokhale, and D. J. Burgess, "A comparative study of top-down and bottom-up approaches for the preparation of micro/nanosuspensions," *Int. J. Pharm.*, vol. 380, no. 1–2, pp. 216–222, Oct. 2009, doi: 10.1016/j.ijpharm.2009.07.005.
- [36] J. Salazar, R. H. Müller, and J. P. Möschwitzer, "Performance Comparison of two Novel Combinative Particle-Size-Reduction Technologies," *J. Pharm. Sci.*, vol. 102, no. 5, pp. 1636–1649, May 2013, doi: 10.1002/jps.23475.

- [37] H. de Waard, W. L. J. Hinrichs, and H. W. Frijlink, "A novel bottom-up process to produce drug nanocrystals: Controlled crystallization during freeze-drying," *J. Control. Release*, vol. 128, no. 2, pp. 179–183, Jun. 2008, doi: 10.1016/j.jconrel.2008.03.002.
- [38] J. Salazar, R. H. Müller, and J. P. Möschwitzer, "Combinative Particle Size Reduction Technologies for the Production of Drug Nanocrystals," *J. Pharm.*, vol. 2014, pp. 1–14, 2014, doi: 10.1155/2014/265754.
- [39] F. Cansell, C. Aymonier, and A. Loppinet-Serani, "Review on materials science and supercritical fluids," *Curr. Opin. Solid State Mater. Sci.*, vol. 7, no. 4–5, pp. 331–340, Aug. 2003, doi: 10.1016/j.cossms.2004.01.003.
- [40] E. Reverchon, "Supercritical fluid extraction and fractionation of essential oils and related products," *Journal of Supercritical Fluids*, vol. 10, no. 1. Elsevier, pp. 1–37, Apr. 14, 1997, doi: 10.1016/S0896-8446(97)00014-4.
- [41] J. Szafraniec *et al.*, "Planetary ball milling and supercritical fluid technology as a way to enhance dissolution of bicalutamide," *Int. J. Pharm.*, vol. 533, no. 2, pp. 470–479, Nov. 2017, doi: 10.1016/j.ijpharm.2017.03.078.
- [42] S. G. Kazarian, "Polymer Processing with Supercritical Fluids," *Polym. Sci. Ser. C*, vol. 42, pp. 78–101, 2000.
- [43] M. Moneghini, I. Kikic, D. Voinovich, B. Perissutti, and J. Filipović-Grčić, "Processing of carbamazepine - PEG 4000 solid dispersions with supercritical carbon dioxide: Preparation, characterisation, and in vitro dissolution," *Int. J. Pharm.*, vol. 222, no. 1, pp. 129–138, 2001, doi: 10.1016/S0378-5173(01)00711-6.
- [44] K. Gong, R. Viboonkiat, I. U. Rehman, G. Buckton, and J. A. Darr, "Formation and characterization of porous indomethacin-PVP coprecipitates prepared using solvent-free supercritical fluid processing," *J. Pharm. Sci.*, vol. 94, no. 12, pp. 2583–2590, 2005, doi: 10.1002/jps.20474.
- [45] Arun Rasheed, "Cyclodextrins as Drug Carrier Molecule: A Review," *Sci. Pharm.*, vol. 76, no. 4, pp. 567–598, Nov. 2008, doi: 10.3797/scipharm.0808-05.
- [46] P. Jansook, N. Ogawa, and T. Loftsson, "Cyclodextrins: structure, physicochemical properties and pharmaceutical applications," 2017, doi: 10.1016/j.ijpharm.2017.11.018.
- [47] R. L. Carrier, L. A. Miller, and I. Ahmed, "The utility of cyclodextrins for enhancing oral bioavailability," *J. Control. Release*, vol. 123, no. 2, pp. 78–99, Nov. 2007, doi: 10.1016/j.jconrel.2007.07.018.
- [48] T. LOFTSSON and D. DUCHENE, "Cyclodextrins and their pharmaceutical applications," *Int. J. Pharm.*, vol. 329, no. 1–2, pp. 1–11, Feb. 2007, doi: 10.1016/j.ijpharm.2006.10.044.
- [49] X. Wang, V. Parvathaneni, S. K. Shukla, D. D. Kanabar, A. Muth, and V. Gupta, "Cyclodextrin Complexation for Enhanced Stability and Non-invasive Pulmonary Delivery of Resveratrol—Applications in Non-small Cell Lung Cancer Treatment," *AAPS PharmSciTech*, vol. 21, no. 5, pp. 1–14, Jul. 2020, doi: 10.1208/s12249-020-01724-x.
- [50] L. Leibler, H. Orland, and J. C. Wheeler, "Theory of critical micelle concentration for solutions of block copolymers," *J. Chem. Phys.*, vol. 79, no. 7, pp. 3550–3557, Oct. 1983, doi: 10.1063/1.446209.

- [51] D. A. Chiappetta and A. Sosnik, "Poly(ethylene oxide)-poly(propylene oxide) block copolymer micelles as drug delivery agents: Improved hydrosolubility, stability and bioavailability of drugs," *European Journal of Pharmaceutics and Biopharmaceutics*, vol. 66, no. 3. Elsevier, pp. 303–317, Jun. 01, 2007, doi: 10.1016/j.ejpb.2007.03.022.
- [52] K. Kataoka, A. Harada, and Y. Nagasaki, "Block copolymer micelles for drug delivery: Design, characterization and biological significance," *Adv. Drug Deliv. Rev.*, vol. 47, no. 1, pp. 113–131, Mar. 2001, doi: 10.1016/S0169-409X(00)00124-1.
- [53] S. Sinha, M. Ali, S. Baboota, A. Ahuja, A. Kumar, and J. Ali, "Solid dispersion as an approach for bioavailability enhancement of poorly water-soluble drug ritonavir," *AAPS PharmSciTech*, vol. 11, no. 2, pp. 518–527, Jun. 2010, doi: 10.1208/s12249-010-9404-1.
- [54] H. Al-Hamidi, A. A. Edwards, M. A. Mohammad, and A. Nokhodchi, "To enhance dissolution rate of poorly water-soluble drugs: Glucosamine hydrochloride as a potential carrier in solid dispersion formulations," *Colloids Surfaces B Biointerfaces*, vol. 76, no. 1, pp. 170–178, Mar. 2010, doi: 10.1016/j.colsurfb.2009.10.030.
- [55] S. Onoue *et al.*, "Formulation design and photochemical studies on nanocrystal solid dispersion of curcumin with improved oral bioavailability," *J. Pharm. Sci.*, vol. 99, no. 4, pp. 1871–1881, 2010, doi: 10.1002/jps.21964.
- [56] Y. D. Yan *et al.*, "Novel valsartan-loaded solid dispersion with enhanced bioavailability and no crystalline changes," *Int. J. Pharm.*, vol. 422, no. 1–2, pp. 202–210, Jan. 2012, doi: 10.1016/j.ijpharm.2011.10.053.
- [57] V. Gall, M. Runde, and H. P. Schuchmann, "Extending applications of high-pressure homogenization by using simultaneous emulsification and mixing (SEM) - An overview," *Processes*, vol. 4, no. 4, 2016, doi: 10.3390/pr4040046.
- [58] S. H. Park, S. G. Min, Y. J. Jo, and J. Y. Chun, "Effect of high pressure homogenization on the physicochemical properties of natural plant-based model emulsion applicable for dairy products," *Korean Journal for Food Science of Animal Resources*, vol. 35, no. 5. Korean Society for Food Science of Animal Resources, pp. 630–637, 2015, doi: 10.5851/kosfa.2015.35.5.630.
- [59] K. S. Yadav and K. Kale, "High Pressure Homogenizer in Pharmaceuticals: Understanding Its Critical Processing Parameters and Applications," *J. Pharm. Innov.*, vol. 15, no. 4, pp. 690–701, 2020, doi: 10.1007/s12247-019-09413-4.
- [60] G. L. Perlovich and A. N. Manin, "Design of pharmaceutical cocrystals for drug solubility improvement," *Russ. J. Gen. Chem.*, vol. 84, no. 2, pp. 407–414, 2014, doi: 10.1134/S107036321402042X.
- [61] E. Skořepová *et al.*, "Increase in solubility of poorly-ionizable pharmaceuticals by salt formation: A case of agomelatine sulfonates," *Cryst. Growth Des.*, vol. 17, no. 10, pp. 5283–5294, 2017, doi: 10.1021/acs.cgd.7b00805.
- [62] S. F. Chow, M. Chen, L. Shi, A. H. L. Chow, and C. C. Sun, "Simultaneously improving the mechanical properties, dissolution performance, and hygroscopicity of ibuprofen and flurbiprofen by cocrystallization with nicotinamide," *Pharm. Res.*, vol. 29, no. 7, pp. 1854–1865, 2012, doi: 10.1007/s11095-012-0709-5.

- [63] M. Akshay Vitthalrao, F. Neeraj Kumar, and B. Kailash Radheshyam, "COCRYSTALIZATION: AN ALTERNATIVE APPROACH FOR SOLID MODIFICATION," *J. Drug Deliv. Ther.*, vol. 2013, no. 3, p. 166, 2011, [Online]. Available: <http://jddtonline.info>.
- [64] D. Douroumis, S. A. Ross, and A. Nokhodchi, "Advanced methodologies for cocrystal synthesis," *Advanced Drug Delivery Reviews*, vol. 117. Elsevier B.V., pp. 178–195, Aug. 01, 2017, doi: 10.1016/j.addr.2017.07.008.
- [65] N. Schultheiss and A. Newman, "Pharmaceutical cocrystals and their physicochemical properties," *Crystal Growth and Design*, vol. 9, no. 6. pp. 2950–2967, Jun. 03, 2009, doi: 10.1021/cg900129f.
- [66] K. Wittering, J. King, L. H. Thomas, and C. C. Wilson, "From evaporative to cooling crystallisation: An initial co-crystallisation study of cytosine and its fluorinated derivative with 4-chloro-3,5-dinitrobenzoic acid," *Crystals*, vol. 4, no. 2, pp. 123–140, Jun. 2014, doi: 10.3390/cryst4020123.
- [67] J. J. Du *et al.*, "Exploring the solubility of the carbamazepine-saccharin co-crystal; a charge density study," *Cryst. Growth Des.*, p. acs.cgd.8b01111, Dec. 2018, doi: 10.1021/acs.cgd.8b01111.
- [68] C. Chen *et al.*, "Supramolecular structural motifs in compounds of acetoguanamine and various carboxylic acids: N-H···O heterosynthons and N-H···N homosynthons," *J. Mol. Struct.*, vol. 1170, pp. 60–69, Oct. 2018, doi: 10.1016/j.molstruc.2018.05.079.
- [69] N. Blagden, M. de Matas, P. T. Gavan, and P. York, "Crystal engineering of active pharmaceutical ingredients to improve solubility and dissolution rates," *Adv. Drug Deliv. Rev.*, vol. 59, no. 7, pp. 617–630, Jul. 2007, doi: 10.1016/j.addr.2007.05.011.
- [70] E. J. Corey, "General methods for the construction of complex molecules," *Pure Appl. Chem.*, vol. 14, no. 1, pp. 19–38, Jan. 1967, doi: 10.1351/pac196714010019.
- [71] K. M. Hutchins, "Functional materials based on molecules with hydrogen-bonding ability: applications to drug co-crystals and polymer complexes," *R. Soc. Open Sci.*, vol. 5, no. 6, p. 180564, Jun. 2018, doi: 10.1098/rsos.180564.
- [72] J. J. Devogelaer, S. J. T. Brugman, H. Meekes, P. Tinnemans, E. Vlieg, and R. De Gelder, "Cocrystal design by network-based link prediction," *CrystEngComm*, vol. 21, no. 44, pp. 6875–6885, Nov. 2019, doi: 10.1039/c9ce01110b.
- [73] T. T. Duignan, M. D. Baer, G. K. Schenter, and C. J. Mundy, "Real single ion solvation free energies with quantum mechanical simulation," *Chem. Sci.*, vol. 8, no. 9, pp. 6131–6140, 2017, doi: 10.1039/c7sc02138k.
- [74] T. E. Gartner and A. Jayaraman, "Modeling and Simulations of Polymers: A Roadmap," *Macromolecules*, vol. 52, no. 3. American Chemical Society, pp. 755–786, Feb. 12, 2019, doi: 10.1021/acs.macromol.8b01836.
- [75] D. Shivakumar, Y. Deng, and B. Roux, "Computations of absolute solvation free energies of small molecules using explicit and implicit solvent model," *J. Chem. Theory Comput.*, vol. 5, no. 4, pp. 919–930, 2009, doi: 10.1021/ct800445x.
- [76] L. Fábíán, "Cambridge structural database analysis of molecular complementarity in cocrystals," *Cryst. Growth Des.*, vol. 9, no. 3, pp. 1436–1443, Mar. 2009, doi: 10.1021/cg800861m.

- [77] N. Sarkar, A. S. Sinha, and C. B. Aakeroý, "Systematic investigation of hydrogen-bond propensities for informing co-crystal design and assembly," *CrystEngComm*, vol. 21, no. 40, pp. 6048–6055, 2019, doi: 10.1039/c9ce01196j.
- [78] G. Kuminek, F. Cao, A. Bahia de Oliveira da Rocha, S. Gonçalves Cardoso, and N. Rodríguez-Hornedo, "Cocrystals to facilitate delivery of poorly soluble compounds beyond-rule-of-5," *Advanced Drug Delivery Reviews*, vol. 101, Elsevier B.V., pp. 143–166, Jun. 01, 2016, doi: 10.1016/j.addr.2016.04.022.
- [79] N. Qiao, M. Li, W. Schlindwein, N. Malek, A. Davies, and G. Trappitt, "Pharmaceutical cocrystals: An overview," *Int. J. Pharm.*, vol. 419, no. 1–2, pp. 1–11, 2011, doi: 10.1016/j.ijpharm.2011.07.037.
- [80] D. D. Gadade and S. S. Pekamwar, "Pharmaceutical cocrystals: Regulatory and strategic aspects, design and development," *Advanced Pharmaceutical Bulletin*, vol. 6, no. 4, Tabriz University of Medical Sciences, pp. 479–494, 2016, doi: 10.15171/apb.2016.062.
- [81] N. Huang and N. Rodríguez-Hornedo, "Engineering cocrystal thermodynamic stability and eutectic points by micellar solubilization and ionization," *CrystEngComm*, vol. 13, no. 17, pp. 5409–5422, 2011, doi: 10.1039/c1ce05381g.
- [82] Y. Gao *et al.*, "Coformer selection based on degradation pathway of drugs: A case study of adefovir dipivoxil-saccharin and adefovir dipivoxil-nicotinamide cocrystals," *Int. J. Pharm.*, vol. 438, no. 1–2, pp. 327–335, Nov. 2012, doi: 10.1016/j.ijpharm.2012.09.027.
- [83] I. Tomaszewska, S. Karki, J. Shur, R. Price, and N. Fotaki, "Pharmaceutical characterisation and evaluation of cocrystals: Importance of in vitro dissolution conditions and type of coformer," *Int. J. Pharm.*, vol. 453, no. 2, pp. 380–388, Sep. 2013, doi: 10.1016/j.ijpharm.2013.05.048.
- [84] K. C. Müllers, M. Paisana, and M. A. Wahl, "Simultaneous formation and micronization of pharmaceutical cocrystals by Rapid Expansion of Supercritical Solutions (RESS)," *Pharm. Res.*, vol. 32, no. 2, pp. 702–713, 2015, doi: 10.1007/s11095-014-1498-9.
- [85] S. Aitipamula, P. S. Chow, and R. B. H. Tan, "Trimorphs of a pharmaceutical cocrystal involving two active pharmaceutical ingredients: Potential relevance to combination drugs," *CrystEngComm*, vol. 11, no. 9, pp. 1823–1827, 2009, doi: 10.1039/b904616j.
- [86] V. Sládková, O. Dammer, G. Sedmak, E. Skořepová, and B. Kratochvíl, "Ivabradine hydrochloride (S)-mandelic acid co-crystal: In situ preparation during formulation," *Crystals*, vol. 7, no. 1, Jan. 2017, doi: 10.3390/cryst7010013.
- [87] M. Liu *et al.*, "Development of a pharmaceutical cocrystal with solution crystallization technology: Preparation, characterization, and evaluation of myricetin-proline cocrystals," *Eur. J. Pharm. Biopharm.*, vol. 107, pp. 151–159, Oct. 2016, doi: 10.1016/j.ejpb.2016.07.008.
- [88] D. Verdoes, G. J. Arkenbout, O. S. L. Bruinsma, P. G. Koutsoukos, and J. Ulrich, "Improved procedures for separating crystals from the melt," *Appl. Therm. Eng.*, vol. 17, no. 8–10, pp. 879–888, Aug. 1997, doi: 10.1016/s1359-4311(96)00075-0.

- [89] S. Patil, K. Chaudhari, and R. Kamble, "Electrospray technique for cocrystallization of phytomolecules," *J. King Saud Univ. - Sci.*, vol. 30, no. 1, pp. 138–141, Jan. 2018, doi: 10.1016/j.jksus.2017.04.001.
- [90] A. Karagianni, M. Malamataris, and K. Kachrimanis, "Pharmaceutical cocrystals: New solid phase modification approaches for the formulation of APIs," *Pharmaceutics*, vol. 10, no. 1. MDPI AG, Mar. 01, 2018, doi: 10.3390/pharmaceutics10010018.
- [91] S. L. Childs, P. Kandi, and S. R. Lingireddy, "Formulation of a danazol cocrystal with controlled supersaturation plays an essential role in improving bioavailability," *Mol. Pharm.*, vol. 10, no. 8, pp. 3112–3127, Aug. 2013, doi: 10.1021/mp400176y.
- [92] D. J. Good and N. Rodríguez-Hornedo, "Cocrystal eutectic constants and prediction of solubility behavior," *Cryst. Growth Des.*, vol. 10, no. 3, pp. 1028–1032, 2010, doi: 10.1021/cg901232h.
- [93] S. Pal, "Mixing Effects on the Ternary Phase Diagram of Cocrystals and Gibbs Formation Energy Calculation," *Cryst. Growth Des.*, vol. 21, pp. 249–259, 2021, doi: 10.1021/acs.cgd.0c01077.
- [94] Y. Huang, X. Sun, L. Zhou, Z. Zhang, S. Zhang, and Q. Yin, "Investigation of Ternary Phase Diagrams of Carbamazepine–Nicotinamide Cocrystal in Ethanol and Ethanol/Ethyl Acetate Mixtures at 298.15 K and 313.15 K," *J. Solution Chem.*, vol. 49, no. 1, pp. 117–132, 2020, doi: 10.1007/s10953-019-00944-5.
- [95] S. L. Morissette *et al.*, "High-throughput crystallization: Polymorphs, salts, cocrystals and solvates of pharmaceutical solids," *Adv. Drug Deliv. Rev.*, vol. 56, no. 3, pp. 275–300, Feb. 2004, doi: 10.1016/j.addr.2003.10.020.
- [96] K. Fucke, S. A. Myz, T. P. Shakhtshneider, E. V. Boldyreva, and U. J. Griesser, "How good are the crystallisation methods for co-crystals? A comparative study of piroxicam," *New J. Chem.*, vol. 36, no. 10, pp. 1969–1977, 2012, doi: 10.1039/c2nj40093f.
- [97] Y. Huang *et al.*, "Preparation of theophylline-benzoic acid cocrystal and on-line monitoring of cocrystallization process in solution by raman spectroscopy," *Crystals*, vol. 9, no. 7, 2019, doi: 10.3390/cryst9070329.
- [98] T. Leyssens, N. Tumanova, K. Robeyns, N. Candoni, and S. Veessler, "Solution cocrystallization, an effective tool to explore the variety of cocrystal systems: Caffeine/dicarboxylic acid cocrystals," *CrystEngComm*, vol. 16, no. 41, pp. 9603–9611, 2014, doi: 10.1039/c4ce01495b.
- [99] M. A. Repka *et al.*, "Pharmaceutical applications of hot-melt extrusion: Part II," *Drug Development and Industrial Pharmacy*, vol. 33, no. 10, pp. 1043–1057, Oct. 2007, doi: 10.1080/03639040701525627.
- [100] X. Liu, M. Lu, Z. Guo, L. Huang, X. Feng, and C. Wu, "Improving the chemical stability of amorphous solid dispersion with cocrystal technique by hot melt extrusion," *Pharm. Res.*, vol. 29, no. 3, pp. 806–817, Mar. 2012, doi: 10.1007/s11095-011-0605-4.
- [101] A. Alhalaweh and S. P. Velaga, "Formation of Cocrystals from Stoichiometric Solutions of Incongruently Saturating Systems by Spray Drying," vol. 10, p. 22, 2010, doi: 10.1021/cg100451q.

- [102] C. A. Ober and R. B. Gupta, "Formation of itraconazole-succinic acid cocrystals by gas antisolvent cocrystallization," *AAPS PharmSciTech*, vol. 13, no. 4, pp. 1396–1406, Dec. 2012, doi: 10.1208/s12249-012-9866-4.
- [103] D. Daurio, C. Medina, R. Saw, K. Nagapudi, and F. Alvarez-Núñez, "Application of twin screw extrusion in the manufacture of cocrystals, part I: Four case studies," *Pharmaceutics*, vol. 3, no. 3, pp. 582–600, Sep. 2011, doi: 10.3390/pharmaceutics3030582.
- [104] J. Jin *et al.*, "Nucleation Control-Triggering Cocrystal Polymorphism of Charge-Transfer Complexes Differing in Physical and Electronic Properties," *ACS Appl. Mater. Interfaces*, vol. 12, no. 17, pp. 19718–19726, Apr. 2020, doi: 10.1021/acsami.9b23590.
- [105] N. Rodríguez-Hornedo, S. J. Nehm, K. F. Seefeldt, Y. Pagán-Torres, and C. J. Falkiewicz, "Reaction crystallization of pharmaceutical molecular complexes," *Mol. Pharm.*, vol. 3, no. 3, pp. 362–367, May 2006, doi: 10.1021/mp050099m.
- [106] V. S. Mandala, S. J. Loewus, and M. A. Mehta, "Monitoring cocrystal formation via in situ solid-state NMR," *J. Phys. Chem. Lett.*, vol. 5, no. 19, pp. 3340–3344, Oct. 2014, doi: 10.1021/jz501699h.
- [107] C. C. Sun and H. Hou, "Improving mechanical properties of caffeine and methyl gallate crystals by cocrystallization," *Cryst. Growth Des.*, vol. 8, no. 5, pp. 1575–1579, May 2008, doi: 10.1021/cg700843s.
- [108] N. K. Duggirala, M. L. Perry, Ö. Almarsson, and M. J. Zaworotko, "Pharmaceutical cocrystals: Along the path to improved medicines," *Chem. Commun.*, vol. 52, no. 4, pp. 640–655, 2016, doi: 10.1039/c5cc08216a.
- [109] A. Alhalaweh, H. R. H. Ali, and S. P. Velaga, "Effects of polymer and surfactant on the dissolution and transformation profiles of cocrystals in aqueous media," *Cryst. Growth Des.*, vol. 14, no. 2, pp. 643–648, Feb. 2014, doi: 10.1021/cg4015256.
- [110] A. Dalpiaz, V. Ferretti, V. Bertolasi, B. Pavan, A. Monari, and M. Pastore, "From Physical Mixtures to Co-Crystals: How the Cofomers Can Modify Solubility and Biological Activity of Carbamazepine," *Mol. Pharm.*, vol. 15, no. 1, pp. 268–278, Jan. 2018, doi: 10.1021/acs.molpharmaceut.7b00899.
- [111] F. Paquin, J. Rivnay, A. Salleo, N. Stingelin, and C. Silva, "Multi-phase semicrystalline microstructures drive exciton dissociation in neat plastic semiconductors," *J. Mater. Chem. C*, vol. 3, pp. 10715–10722, 2015, doi: 10.1039/b000000x.
- [112] M. D. Eddleston, M. Arhangelskis, L. Fábíán, G. J. Tizzard, S. J. Coles, and W. Jones, "Investigation of an Amide-Pseudo Amide Hydrogen Bonding Motif within a Series of Theophylline:Amide Cocrystals," *Cryst. Growth Des.*, vol. 16, no. 1, pp. 51–58, Jan. 2016, doi: 10.1021/acs.cgd.5b00905.
- [113] S. K. Nechipadappu, V. Tekuri, and D. R. Trivedi, "Pharmaceutical Co-Crystal of Flufenamic Acid: Synthesis and Characterization of Two Novel Drug-Drug Co-Crystal," *J. Pharm. Sci.*, vol. 106, no. 5, pp. 1384–1390, May 2017, doi: 10.1016/j.xphs.2017.01.033.

- [114] M. D. Eddleston, R. Thakuria, B. J. Aldous, and W. Jones, "An investigation of the causes of cocrystal dissociation at high humidity," *J. Pharm. Sci.*, vol. 103, no. 9, pp. 2859–2864, Sep. 2014, doi: 10.1002/jps.23865.
- [115] D. P. McNamara *et al.*, "Use of a glutaric acid cocrystal to improve oral bioavailability of a low solubility API," *Pharm. Res.*, vol. 23, no. 8, pp. 1888–1897, Aug. 2006, doi: 10.1007/s11095-006-9032-3.
- [116] A. Jayasankar, L. S. Reddy, S. J. Bethune, and N. Rodríguez-Hornedo, "Role of cocrystal and solution chemistry on the formation and stability of cocrystals with different stoichiometry," *Cryst. Growth Des.*, vol. 9, no. 2, pp. 889–897, 2009, doi: 10.1021/cg800632r.
- [117] S. Tsutsumi *et al.*, "Characterization and evaluation of miconazole salts and cocrystals for improved physicochemical properties," *Int. J. Pharm.*, vol. 421, no. 2, pp. 230–236, Dec. 2011, doi: 10.1016/j.ijpharm.2011.09.034.
- [118] A. V. Trask, W. D. S. Motherwell, and W. Jones, "Physical stability enhancement of theophylline via cocrystallization," *Int. J. Pharm.*, vol. 320, no. 1–2, pp. 114–123, Aug. 2006, doi: 10.1016/j.ijpharm.2006.04.018.
- [119] S. Patel, A. M. Kaushal, and A. K. Bansal, "Compression physics in the formulation development of tablets," *Crit. Rev. Ther. Drug Carrier Syst.*, vol. 23, no. 1, pp. 1–65, 2006, doi: 10.1615/critrevtherdrugcarriersyst.v23.i1.10.
- [120] G. Bolla and A. Nangia, "Pharmaceutical cocrystals: Walking the talk," *Chem. Commun.*, vol. 52, no. 54, pp. 8342–8360, 2016, doi: 10.1039/c6cc02943d.
- [121] M. Rehula, R. Adamek, and V. Spacek, "Stress relaxation study of fillers for directly compressed tablets," *Powder Technol.*, vol. 217, pp. 510–515, Feb. 2012, doi: 10.1016/j.powtec.2011.11.011.
- [122] S. Chatteraj, L. Shi, M. Chen, A. Alhalaweh, S. Velaga, and C. C. Sun, "Origin of deteriorated crystal plasticity and compaction properties of a 1:1 cocrystal between piroxicam and saccharin," *Cryst. Growth Des.*, vol. 14, no. 8, pp. 3864–3874, Aug. 2014, doi: 10.1021/cg500388s.
- [123] H. Ahmed, M. R. Shimpi, and S. P. Velaga, "Relationship between mechanical properties and crystal structure in cocrystals and salt of paracetamol," *Drug Dev. Ind. Pharm.*, vol. 43, no. 1, pp. 89–97, 2017, doi: 10.1080/03639045.2016.1220568.
- [124] S. Hiendrawan, B. Veriansyah, E. Widjojokusumo, S. N. Soewandhi, S. Wikarsa, and R. R. Tjandrawinata, "Physicochemical and mechanical properties of paracetamol cocrystal with 5-nitroisophthalic acid," *Int. J. Pharm.*, vol. 497, no. 1–2, pp. 106–113, Jan. 2016, doi: 10.1016/j.ijpharm.2015.12.001.
- [125] W. Jones, W. D. S. Motherwell, and A. V. Trask, "Pharmaceutical cocrystals: An emerging approach to physical property enhancement," *MRS Bull.*, vol. 31, no. 11, pp. 875–879, 2006, doi: 10.1557/mrs2006.206.
- [126] Z. Li and A. J. Matzger, "Influence of Coformer Stoichiometric Ratio on Pharmaceutical Cocrystal Dissolution: Three Cocrystals of Carbamazepine/4-Aminobenzoic Acid," *Mol. Pharm.*, vol. 13, no. 3, pp. 990–995, Mar. 2016, doi: 10.1021/acs.molpharmaceut.5b00843.
- [127] C. Saal and A. C. Petereit, "Optimizing solubility: Kinetic versus thermodynamic solubility temptations and risks," *Eur. J. Pharm. Sci.*, vol. 47, no. 3, pp. 589–595, Oct. 2012, doi: 10.1016/j.ejps.2012.07.019.

- [128] R. Thakuria, A. Delori, W. Jones, M. P. Lipert, L. Roy, and N. Rodríguez-Hornedo, "Pharmaceutical cocrystals and poorly soluble drugs," *International Journal of Pharmaceutics*, vol. 453, no. 1. Elsevier B.V., pp. 101–125, Aug. 30, 2013, doi: 10.1016/j.ijpharm.2012.10.043.
- [129] S. Ren *et al.*, "The effects of pH, surfactant, ion concentration, coformer, and molecular arrangement on the solubility behavior of myricetin cocrystals," *Acta Pharm. Sin. B*, vol. 9, no. 1, pp. 59–73, Jan. 2019, doi: 10.1016/j.apsb.2018.09.008.
- [130] S. J. Bethune, N. Huang, A. Jayasankar, and N. Rodríguez-Hornedo, "Understanding and predicting the effect of cocrystal components and pH on cocrystal solubility," *Cryst. Growth Des.*, vol. 9, no. 9, pp. 3976–3988, Sep. 2009, doi: 10.1021/cg9001187.
- [131] A. J. Smith, P. Kavuru, L. Wojtas, M. J. Zaworotko, and R. D. Shytle, "Cocrystals of quercetin with improved solubility and oral bioavailability," *Mol. Pharm.*, vol. 8, no. 5, pp. 1867–1876, Oct. 2011, doi: 10.1021/mp200209j.
- [132] M. S. Jung *et al.*, "Bioavailability of indomethacin-saccharin cocrystals," *J. Pharm. Pharmacol.*, vol. 62, no. 11, pp. 1560–1568, Nov. 2010, doi: 10.1111/j.2042-7158.2010.01189.x.
- [133] S. N. and K. J. Yadav Sanjay, Gupta Prakash Chandra, "COCRYSTALS: AN ALTERNATIVE APPROACH TO MODIFY PHYSICOCHEMICAL PROPERTIES OF DRUGS," 2015. [Online]. Available: <https://www.researchgate.net/publication/276204725>.
- [134] E. Pindelska, A. Sokal, and W. Kolodziejski, "Pharmaceutical cocrystals, salts and polymorphs: Advanced characterization techniques," *Advanced Drug Delivery Reviews*, vol. 117. Elsevier B.V., pp. 111–146, Aug. 01, 2017, doi: 10.1016/j.addr.2017.09.014.
- [135] S. L. Childs, P. Kandi, and S. R. Lingireddy, "Formulation of a danazol cocrystal with controlled supersaturation plays an essential role in improving bioavailability," *Mol. Pharm.*, vol. 10, no. 8, pp. 3112–3127, Aug. 2013, doi: 10.1021/mp400176y.
- [136] K. Greco and R. Bogner, "Solution-mediated phase transformation: Significance during dissolution and implications for bioavailability," *Journal of Pharmaceutical Sciences*, vol. 101, no. 9. John Wiley and Sons Inc., pp. 2996–3018, Sep. 01, 2012, doi: 10.1002/jps.23025.
- [137] M. Banik, S. P. Gopi, S. Ganguly, and G. R. Desiraju, "Cocrystal and salt forms of furosemide: Solubility and diffusion variations," *Cryst. Growth Des.*, vol. 16, no. 9, pp. 5418–5428, Sep. 2016, doi: 10.1021/acs.cgd.6b00902.
- [138] D. Murphy, F. Rodríguez-Cintrón, B. Langevin, R. C. Kelly, and N. Rodríguez-Hornedo, "Solution-mediated phase transformation of anhydrous to dihydrate carbamazepine and the effect of lattice disorder," *Int. J. Pharm.*, vol. 246, no. 1–2, pp. 121–134, Oct. 2002, doi: 10.1016/S0378-5173(02)00358-7.
- [139] N. Qiao, K. Wang, W. Schindwein, A. Davies, and M. Li, "In situ monitoring of carbamazepine-nicotinamide cocrystal intrinsic dissolution behaviour," *Eur. J. Pharm. Biopharm.*, vol. 83, no. 3, pp. 415–426, Apr. 2013, doi: 10.1016/j.ejpb.2012.10.005.

- [140] M. Guo, K. Wang, N. Qiao, L. Fábíán, G. Sadiq, and M. Li, "Insight into Flufenamic Acid Cocrystal Dissolution in the Presence of a Polymer in Solution: From Single Crystal to Powder Dissolution," *Mol. Pharm.*, vol. 14, no. 12, pp. 4583–4596, Dec. 2017, doi: 10.1021/acs.molpharmaceut.7b00712.
- [141] K. Sugano, M. Omori, T. Watanabe, T. Uekusa, J. Oki, and D. Inoue, "Effects of cofomer and polymer on particle surface solution-mediated phase transformation of cocrystals in aqueous media," *Mol. Pharm.*, vol. 17, no. 10, pp. 3825–3836, Oct. 2020, doi: 10.1021/acs.molpharmaceut.0c00587.
- [142] R. J. Davey, N. Blagden, S. Righini, H. Alison, and E. S. Ferrari, "Nucleation control in solution mediated polymorphic phase transformations: The case of 2,6-dihydroxybenzoic acid," *J. Phys. Chem. B*, vol. 106, no. 8, pp. 1954–1959, Feb. 2002, doi: 10.1021/jp013044i.
- [143] E. S. Ferrari and R. J. Davey, "Solution-mediated transformation of α to β L-glutamic acid: Rate enhancement due to secondary nucleation," in *Crystal Growth and Design*, Sep. 2004, vol. 4, no. 5, pp. 1061–1068, doi: 10.1021/cg0342112.
- [144] J. F. Mojica and L. L. Levenson, "Bulk-to-surface precipitation and surface diffusion of carbon on polycrystalline nickel," *Surf. Sci.*, vol. 59, no. 2, pp. 447–460, Oct. 1976, doi: 10.1016/0039-6028(76)90028-5.
- [145] A. Alvani, A. Jouyban, and A. Shayanfar, "The effect of surfactant and polymer on solution stability and solubility of tadalafil-methylparaben cocrystal," *J. Mol. Liq.*, vol. 281, pp. 86–92, May 2019, doi: 10.1016/j.molliq.2019.02.080.
- [146] M. Guo, K. Wang, N. Hamill, K. Lorimer, and M. Li, "Investigating the influence of polymers on supersaturated flufenamic acid cocrystal solutions," *Mol. Pharm.*, vol. 13, no. 9, pp. 3292–3307, Sep. 2016, doi: 10.1021/acs.molpharmaceut.6b00612.
- [147] Y. Huang, G. Kuminek, L. Roy, K. L. Cavanagh, Q. Yin, and N. Rodríguez-Hornedo, "Cocrystal Solubility Advantage Diagrams as a Means to Control Dissolution, Supersaturation, and Precipitation," *Mol. Pharm.*, vol. 16, no. 9, pp. 3887–3895, Sep. 2019, doi: 10.1021/acs.molpharmaceut.9b00501.
- [148] I. Lebrón and D. L. Suárez, "Kinetics and mechanisms of precipitation of calcite as affected by PCO₂ and organic ligands at 25°C," *Geochim. Cosmochim. Acta*, vol. 62, no. 3, pp. 405–416, Feb. 1998, doi: 10.1016/S0016-7037(97)00364-5.
- [149] D. D. Patel and B. D. Anderson, "Effect of precipitation inhibitors on indomethacin supersaturation maintenance: Mechanisms and modeling," *Mol. Pharm.*, vol. 11, no. 5, pp. 1489–1499, May 2014, doi: 10.1021/mp400658k.
- [150] D. B. Warren, H. Benameur, C. J. H. Porter, and C. W. Pouton, "Using polymeric precipitation inhibitors to improve the absorption of poorly water-soluble drugs: A mechanistic basis for utility," *Journal of Drug Targeting*, vol. 18, no. 10, Taylor & Francis, pp. 704–731, Dec. 2010, doi: 10.3109/1061186X.2010.525652.
- [151] C. Wang, Q. Tong, X. Hou, S. Hu, J. Fang, and C. C. Sun, "Enhancing Bioavailability of Dihydromyricetin through Inhibiting Precipitation of Soluble Cocrystals by a Crystallization Inhibitor," *Cryst. Growth Des.*, vol. 16, no. 9, pp. 5030–5039, Sep. 2016, doi: 10.1021/acs.cgd.6b00591.

- [152] D. D. Bavishi and C. H. Borkhataria, "Spring and parachute: How cocrystals enhance solubility," *Progress in Crystal Growth and Characterization of Materials*, vol. 62, no. 3. Elsevier Ltd, pp. 1–8, Sep. 01, 2016, doi: 10.1016/j.pcrysgrow.2016.07.001.
- [153] H. S. Gwak, J. S. Choi, and H. K. Choi, "Enhanced bioavailability of piroxicam via salt formation with ethanolamines," *Int. J. Pharm.*, vol. 297, no. 1–2, pp. 156–161, Jun. 2005, doi: 10.1016/j.ijpharm.2005.03.016.
- [154] C. Liu *et al.*, "Improving Oral Bioavailability of Sorafenib by Optimizing the 'spring' and 'parachute' Based on Molecular Interaction Mechanisms," *Mol. Pharm.*, vol. 13, no. 2, pp. 599–608, Feb. 2016, doi: 10.1021/acs.molpharmaceut.5b00837.
- [155] L. Fábíán *et al.*, "Cocrystals of fenamic acids with nicotinamide," *Cryst. Growth Des.*, vol. 11, no. 8, pp. 3522–3528, Aug. 2011, doi: 10.1021/cg200429j.
- [156] D. P. Evans, M. S. Burke, and R. G. Newcombe, "Medicines of choice in low back pain," *Curr. Med. Res. Opin.*, vol. 6, no. 8, pp. 540–547, 1980, doi: 10.1185/03007998009109484.
- [157] S. Aitipamula, A. B. H. Wong, P. S. Chow, and R. B. H. Tan, "Cocrystallization with flufenamic acid: Comparison of physicochemical properties of two pharmaceutical cocrystals," *CrystEngComm*, vol. 16, no. 26, pp. 5793–5801, Jul. 2014, doi: 10.1039/c3ce42182a.
- [158] K. T. Rajan, A. G. Hill, A. Barr, and E. Whitwell, "Flufenamic acid in rheumatoid arthritis.," *Ann. Rheum. Dis.*, vol. 26, no. 1, pp. 43–46, 1967, doi: 10.1136/ard.26.1.43.
- [159] E. H. Lee, S. X. M. Boerrigter, and S. R. Byrn, "Epitaxy of a structurally related compound on the (100) faces of flufenamic acid form i and iii single crystals," *Cryst. Growth Des.*, vol. 10, no. 2, pp. 518–527, Feb. 2010, doi: 10.1021/cg900549h.
- [160] S. P. Delaney and T. M. Korter, "Terahertz Spectroscopy and Computational Investigation of the Flufenamic Acid/Nicotinamide Cocrystal," *J. Phys. Chem. A*, vol. 119, no. 13, pp. 3269–3276, Apr. 2015, doi: 10.1021/jp5125519.
- [161] P. J. Wiffen, S. Derry, R. A. Moore, and H. J. McQuay, "Carbamazepine for acute and chronic pain in adults," in *Cochrane Database of Systematic Reviews*, no. 1, P. J. Wiffen, Ed. Chichester, UK: John Wiley & Sons, Ltd, 2011.
- [162] M. Elphick, "The clinical uses and pharmacology of carbamazepine in psychiatry," *Int. Clin. Psychopharmacol.*, vol. 3, no. 3, pp. 185–203, 1988, doi: 10.1097/00004850-198807000-00001.
- [163] K. D. Denicoff, E. E. Smith-Jackson, R. E. Disney, S. O. Ali, G. S. Leverich, and R. M. Post, "Comparative prophylactic efficacy of lithium, carbamazepine, and the combination in bipolar disorder," *J. Clin. Psychiatry*, vol. 58, no. 11, pp. 470–478, 1997, doi: 10.4088/JCP.v58n1102.
- [164] D. Loeff, P. Grimley, F. Kuller, A. Martin, and L. Shonfield, "CARBAMAZEPINE FOR PTSD," *Journal of the American Academy of Child and Adolescent Psychiatry*, vol. 34, no. 6, pp. 703–704, 1995, doi: 10.1097/00004583-199506000-00008.

- [165] S. Leucht, B. Helfer, M. Dold, W. Kissling, and J. Mcgrath, "Carbamazepine for schizophrenia," *Cochrane Database of Systematic Reviews*, vol. 2014, no. 5. John Wiley and Sons Ltd, May 02, 2014, doi: 10.1002/14651858.CD001258.pub3.
- [166] C. Simhandl and K. Meszaros, "The use of carbamazepine in the treatment of schizophrenic and schizoaffective psychoses: A review," *Journal of Psychiatry and Neuroscience*, vol. 17, no. 1. Canadian Medical Association, pp. 1–14, 1992, Accessed: Dec. 21, 2020. [Online]. Available: /pmc/articles/PMC1188379/?report=abstract.
- [167] L. J. Birkhimer, J. L. Curtis, and M. W. Jann, "Use of carbamazepine in psychiatric disorders," *Clin. Pharm.*, vol. 4, no. 4, pp. 425–434, Jul. 1985, Accessed: Dec. 21, 2020. [Online]. Available: <https://europepmc.org/article/med/2864160>.
- [168] N. J. Babu, L. S. Reddy, and A. Nangia, "Amide N-oxide heterosynthon and amide dimer homosynthon in cocrystals of carboxamide drugs and pyridine N-oxides," *Mol. Pharm.*, vol. 4, no. 3, pp. 417–434, May 2007, doi: 10.1021/mp070014c.
- [169] D. J. Good and R. H. Naír, "Solubility advantage of pharmaceutical cocrystals," *Cryst. Growth Des.*, vol. 9, no. 5, pp. 2252–2264, May 2009, doi: 10.1021/cg801039j.
- [170] M. Knip *et al.*, "Safety of high-dose nicotinamide: A review," *Diabetologia*, vol. 43, no. 11. Springer, pp. 1337–1345, 2000, doi: 10.1007/s001250051536.
- [171] S. Aitipamula, A. B. H. Wong, P. S. Chow, and R. B. H. Tan, "Polymorphism and phase transformations of a cocrystal of nicotinamide and pimelic acid," *CrystEngComm*, vol. 14, no. 23, pp. 8193–8198, Dec. 2012, doi: 10.1039/c2ce26151k.
- [172] T. Hino, J. L. Ford, and M. W. Powell, "Assessment of nicotinamide polymorphs by differential scanning calorimetry," *Thermochim. Acta*, vol. 374, no. 1, pp. 85–92, Jun. 2001, doi: 10.1016/S0040-6031(01)00491-9.
- [173] A. L. Kelly, T. Gough, R. S. Dhumal, S. A. Halsey, and A. Paradkar, "Monitoring ibuprofen-nicotinamide cocrystal formation during solvent free continuous cocrystallization (SFCC) using near infrared spectroscopy as a PAT tool," *Int. J. Pharm.*, vol. 426, no. 1–2, pp. 15–20, Apr. 2012, doi: 10.1016/j.ijpharm.2011.12.033.
- [174] A. S. Pessoa, G. P. S. Aguiar, J. Vladimir Oliveira, A. J. Bortoluzzi, A. Paulino, and M. Lanza, "Precipitation of resveratrol-isoniazid and resveratrol-nicotinamide cocrystals by gas antisolvent," *J. Supercrit. Fluids*, vol. 145, pp. 93–102, Mar. 2019, doi: 10.1016/j.supflu.2018.11.014.
- [175] F. L. F. Soares and R. L. Carneiro, "Evaluation of analytical tools and multivariate methods for quantification of co-former crystals in ibuprofen-nicotinamide co-crystals," *J. Pharm. Biomed. Anal.*, vol. 89, pp. 166–175, Feb. 2014, doi: 10.1016/j.jpba.2013.11.005.
- [176] Z. Rahman, C. Agarabi, A. S. Zidan, S. R. Khan, and M. A. Khan, "Physico-mechanical and stability evaluation of carbamazepine cocrystal with nicotinamide.," *AAPS PharmSciTech*, vol. 12, no. 2, pp. 693–704, May 2011, doi: 10.1208/s12249-011-9603-4.

- [177] S. Zhang and Å. C. Rasmuson, "The theophylline-oxalic acid co-crystal system: Solid phases, thermodynamics and crystallisation," *CrystEngComm*, vol. 14, no. 14, The Royal Society of Chemistry, pp. 4644–4655, Jul. 21, 2012, doi: 10.1039/c2ce25299f.
- [178] M. Guo, K. Wang, N. Qiao, V. Yardley, and M. Li, "Investigating Permeation Behavior of Flufenamic Acid Cocrystals Using a Dissolution and Permeation System," *Mol. Pharm.*, vol. 15, no. 9, pp. 4257–4272, Sep. 2018, doi: 10.1021/acs.molpharmaceut.8b00670.
- [179] C. Liu, K. G. H. Desai, and C. Liu, "Enhancement of Dissolution Rate of Valdecoxib Using Solid Dispersions with Polyethylene Glycol 4000," *Drug Dev. Ind. Pharm.*, vol. 31, no. 1, pp. 1–10, Jan. 2005, doi: 10.1081/DDC-43918.
- [180] "Poly Ethylene Glycol Products Description Poly Ethylene Glycol 6000 Powder (PEG 6000) Poly Ethylene Glycol 8000 Powder (PEG 8000)." Accessed: Dec. 22, 2020. [Online]. Available: <http://www.interchim.com>.
- [181] S. Janssens, H. N. de Armas, C. J. Roberts, and G. Van den Mooter, "Characterization of Ternary Solid Dispersions of Itraconazole, PEG 6000, and HPMC 2910 E5," *J. Pharm. Sci.*, vol. 97, no. 6, pp. 2110–2120, Jun. 2008, doi: 10.1002/jps.21128.
- [182] H. Bley, B. Fussnegger, and R. Bodmeier, "Characterization and stability of solid dispersions based on PEG/polymer blends," *Int. J. Pharm.*, vol. 390, no. 2, pp. 165–173, May 2010, doi: 10.1016/j.ijpharm.2010.01.039.
- [183] S. Sethia and E. Squillante, "Solid dispersion of carbamazepine in PVP K30 by conventional solvent evaporation and supercritical methods," *Int. J. Pharm.*, vol. 272, no. 1–2, pp. 1–10, Mar. 2004, doi: 10.1016/j.ijpharm.2003.11.025.
- [184] A. Modi and P. Tayade, "Enhancement of dissolution profile by solid dispersion (kneading) technique," *AAPS PharmSciTech*, vol. 7, no. 3, pp. E87–E92, Aug. 2006, doi: 10.1208/pt070368.
- [185] "7 Final Report on the Safety Assessment of Polyvinylpyrrolidone/Vinyl Acetate Copolymer," *J. Am. Coll. Toxicol.*, vol. 2, no. 5, pp. 141–159, Sep. 1983, doi: 10.3109/10915818309140719.
- [186] M. Vasanthavada, W. Q. Tong, Y. Joshi, and M. S. Kislalioglu, "Phase behavior of amorphous molecular dispersions II: Role of hydrogen bonding in solid solubility and phase separation kinetics," *Pharm. Res.*, vol. 22, no. 3, pp. 440–448, Mar. 2005, doi: 10.1007/s11095-004-1882-y.
- [187] M. Tobyn *et al.*, "Amorphous drug-PVP dispersions: Application of theoretical, thermal and spectroscopic analytical techniques to the study of a molecule with intermolecular bonds in both the crystalline and pure amorphous state," *J. Pharm. Sci.*, vol. 98, no. 9, pp. 3456–3468, Sep. 2009, doi: 10.1002/jps.21738.
- [188] Y. Huang, B. Zhang, Y. Gao, J. Zhang, and L. Shi, "Baicalein-nicotinamide cocrystal with enhanced solubility, dissolution, and oral bioavailability," *J. Pharm. Sci.*, vol. 103, no. 8, pp. 2330–2337, Aug. 2014, doi: 10.1002/jps.24048.
- [189] K. Kothari, V. Ragoonanan, and R. Suryanarayanan, "The role of drug-polymer hydrogen bonding interactions on the molecular mobility and physical stability of nifedipine solid dispersions," *Mol. Pharm.*, vol. 12, no. 1, pp. 162–170, Jan. 2015, doi: 10.1021/mp5005146.

- [190] C. Goddeeris, T. Willems, and G. Van den Mooter, "Formulation of fast disintegrating tablets of ternary solid dispersions consisting of TPGS 1000 and HPMC 2910 or PVPVA 64 to improve the dissolution of the anti-HIV drug UC 781," *Eur. J. Pharm. Sci.*, vol. 34, no. 4–5, pp. 293–302, Aug. 2008, doi: 10.1016/j.ejps.2008.05.005.
- [191] K. Wlodarski, L. Tajber, and W. Sawicki, "Physicochemical properties of direct compression tablets with spray dried and ball milled solid dispersions of tadalafil in PVP-VA," *Eur. J. Pharm. Biopharm.*, vol. 109, pp. 14–23, Dec. 2016, doi: 10.1016/j.ejpb.2016.09.011.
- [192] W. Zhang *et al.*, "Impact of polymer type, ASD loading and polymer-drug ratio on ASD tablet disintegration and drug release," *Int. J. Pharm.*, vol. 592, p. 120087, Nov. 2020, doi: 10.1016/j.ijpharm.2020.120087.
- [193] U. S. Kestur, B. Van Eerdenbrugh, and L. S. Taylor, "Influence of polymer chemistry on crystal growth inhibition of two chemically diverse organic molecules," *CrystEngComm*, vol. 13, no. 22, pp. 6712–6718, Nov. 2011, doi: 10.1039/c1ce05822c.
- [194] M. M. Knopp, J. H. Nguyen, H. Mu, P. Langguth, T. Rades, and R. Holm, "Influence of Copolymer Composition on In Vitro and In Vivo Performance of Celecoxib-PVP/VA Amorphous Solid Dispersions," *AAPS J.*, vol. 18, no. 2, pp. 416–423, Mar. 2016, doi: 10.1208/s12248-016-9865-6.
- [195] S. Bénazet, G. Jacob, and G. Pèpe, "Molecular Modeling in Crystal Engineering for Processing of Energetic Materials," *Propellants, Explos. Pyrotech.*, vol. 28, no. 6, pp. 287–295, Dec. 2003, doi: 10.1002/prop.200300020.
- [196] J. D. Durrant and J. A. McCammon, "Molecular dynamics simulations and drug discovery," *BMC Biology*, vol. 9, no. 1. BioMed Central, p. 71, Oct. 28, 2011, doi: 10.1186/1741-7007-9-71.
- [197] A. Nemkevich, H. B. Bürgi, M. A. Spackman, and B. Corry, "Molecular dynamics simulations of structure and dynamics of organic molecular crystals," *Phys. Chem. Chem. Phys.*, vol. 12, no. 45, pp. 14916–14929, Dec. 2010, doi: 10.1039/c0cp01409e.
- [198] L. Song, L. Chen, D. Cao, and J. Wang, "Solvent selection for explaining the morphology of nitroguanidine crystal by molecular dynamics simulation," *J. Cryst. Growth*, vol. 483, pp. 308–317, Feb. 2018, doi: 10.1016/j.jcrysgro.2017.09.026.
- [199] R. B. Hammond, K. Pencheva, V. Ramachandran, and K. J. Roberts, "Application of grid-based molecular methods for modeling solvent-dependent crystal growth morphology: Aspirin crystallized from aqueous ethanolic solution," in *Crystal Growth and Design*, Sep. 2007, vol. 7, no. 9, pp. 1571–1574, doi: 10.1021/cg070310u.
- [200] A. S. Larsen, M. T. Ruggiero, K. E. Johansson, J. A. Zeitler, and J. Rantanen, "Tracking dehydration mechanisms in crystalline hydrates with molecular dynamics simulations," *Cryst. Growth Des.*, vol. 17, no. 10, pp. 5017–5022, 2017, doi: 10.1021/acs.cgd.7b00889.
- [201] C. P. Tsangarides *et al.*, "Computational modelling and characterisation of nanoparticle-based tuneable photonic crystal sensors," *RSC Adv.*, vol. 4, no. 21, pp. 10454–10461, Feb. 2014, doi: 10.1039/c3ra47984f.

- [202] D. Yang *et al.*, “Structural and Computational Insights into Cocrystal Interactions: A Case on Cocrystals of Antipyrine and Aminophenazone,” *Cryst. Growth Des.*, vol. 19, no. 11, pp. 6175–6183, May 2019, doi: 10.1021/acs.cgd.9b00591.
- [203] S. Xiong, S. Chen, and S. Jin, “Molecular dynamic simulations on TKX-50/RDX cocrystal,” *J. Mol. Graph. Model.*, vol. 74, pp. 171–176, Jun. 2017, doi: 10.1016/j.jmglm.2017.03.006.
- [204] A. Kuzmanic, R. B. Pritchard, D. F. Hansen, and F. L. Gervasio, “Importance of the Force Field Choice in Capturing Functionally Relevant Dynamics in the von Willebrand Factor,” *J. Phys. Chem. Lett.*, vol. 10, no. 8, pp. 1928–1934, Apr. 2019, doi: 10.1021/acs.jpcllett.9b00517.
- [205] C. A. Becker, F. Tavazza, Z. T. Trautt, and R. A. Buarque De Macedo, “Considerations for choosing and using force fields and interatomic potentials in materials science and engineering,” 2013, doi: 10.1016/j.cossms.2013.10.001.
- [206] P. Robustelli, S. Piana, and D. E. Shaw, “Developing a molecular dynamics force field for both folded and disordered protein states,” *Proc. Natl. Acad. Sci. U. S. A.*, vol. 115, no. 21, pp. E4758–E4766, May 2018, doi: 10.1073/pnas.1800690115.
- [207] N. Okabayashi, A. Peronio, M. Paulsson, T. Arai, and F. J. Giessibl, “Vibrations of a molecule in an external force field,” *Proc. Natl. Acad. Sci. U. S. A.*, vol. 115, no. 18, pp. 4571–4576, May 2018, doi: 10.1073/pnas.1721498115.
- [208] J. Nyman, O. S. Pundyke, and G. M. Day, “Accurate force fields and methods for modelling organic molecular crystals at finite temperatures,” *Phys. Chem. Chem. Phys.*, vol. 18, no. 23, pp. 15828–15837, Jun. 2016, doi: 10.1039/c6cp02261h.
- [209] N. Vaidehi and A. Jain, “Internal coordinate molecular dynamics: A foundation for multiscale dynamics,” *J. Phys. Chem. B*, vol. 119, no. 4, pp. 1233–1242, Jan. 2015, doi: 10.1021/jp509136y.
- [210] L. ho Tam, A. Zhou, Z. Yu, Q. Qiu, and D. Lau, “Understanding the effect of temperature on the interfacial behavior of CFRP-wood composite via molecular dynamics simulations,” *Compos. Part B Eng.*, vol. 109, pp. 227–237, Jan. 2017, doi: 10.1016/j.compositesb.2016.10.030.
- [211] N. Schmid *et al.*, “Definition and testing of the GROMOS force-field versions 54A7 and 54B7,” *Eur. Biophys. J.*, vol. 40, no. 7, pp. 843–856, Jul. 2011, doi: 10.1007/s00249-011-0700-9.
- [212] T. A. Halgren, “Merck molecular force field. I. Basis, form, scope, parameterization, and performance of MMFF94,” *J. Comput. Chem.*, vol. 17, no. 5–6, pp. 490–519, Apr. 1996, doi: 10.1002/(SICI)1096-987X(199604)17:5/6<490::AID-JCC1>3.0.CO;2-P.
- [213] B. Derecskei and A. Derecskei-Kovacs, “Molecular modelling simulations to predict density and solubility parameters of ionic liquids,” *Mol. Simul.*, vol. 34, no. 10–15, pp. 1167–1175, Sep. 2008, doi: 10.1080/08927020802412362.
- [214] Y. Yamaguchi and S. Maruyama, “A molecular dynamics simulation of the fullerene formation process,” *Chem. Phys. Lett.*, vol. 286, no. 3–4, pp. 336–342, Apr. 1998, doi: 10.1016/S0009-2614(98)00102-X.
- [215] R. Gilson, “Molecular dynamics simulation of dipole interactions,” *undefined*, 2000.

- [216] W. K. Den Otter and W. J. Briels, "The calculation of free-energy differences by constrained molecular-dynamics simulations," *J. Chem. Phys.*, vol. 109, no. 11, pp. 4139–4146, Sep. 1998, doi: 10.1063/1.477019.
- [217] M. Levitt, M. Hirshberg, R. Sharon, and V. Daggett, "Potential energy function and parameters for simulations of the molecular dynamics of proteins and nucleic acids in solution," 1995.
- [218] J. Marelius, K. Kolmodin, I. Feierberg, and J. Åqvist, "Q: a molecular dynamics program for free energy calculations and empirical valence bond simulations in biomolecular systems," *J. Mol. Graph. Model.*, vol. 16, no. 4–6, pp. 213–225, Aug. 1998, doi: 10.1016/s1093-3263(98)80006-5.
- [219] D. Hossain, M. A. Tschopp, D. K. Ward, J. L. Bouvard, P. Wang, and M. F. Horstemeyer, "Molecular dynamics simulations of deformation mechanisms of amorphous polyethylene," *Polymer (Guildf.)*, vol. 51, no. 25, pp. 6071–6083, Nov. 2010, doi: 10.1016/j.polymer.2010.10.009.
- [220] M. J. P. Musgrave and J. A. Pople, "A general valence force field for diamond," *Proc. R. Soc. London. Ser. A. Math. Phys. Sci.*, vol. 268, no. 1335, pp. 474–484, Aug. 1962, doi: 10.1098/rspa.1962.0153.
- [221] H. Sun, "Compass: An ab initio force-field optimized for condensed-phase applications - Overview with details on alkane and benzene compounds," *J. Phys. Chem. B*, vol. 102, no. 38, pp. 7338–7364, Sep. 1998, doi: 10.1021/jp980939v.
- [222] M. J. McQuaid, H. Sun, and D. Rigby, "Development and validation of COMPASS force field parameters for molecules with aliphatic azide chains," *J. Comput. Chem.*, vol. 25, no. 1, pp. 61–71, Jan. 2004, doi: 10.1002/jcc.10316.
- [223] S. W. Bunte and H. Sun, "Molecular Modeling of Energetic Materials: The Parameterization and Validation of Nitrate Esters in the COMPASS Force Field," *J. Phys. Chem. B*, vol. 104, no. 11, pp. 2477–2489, Mar. 2000, doi: 10.1021/jp991786u.
- [224] T. S. Asche, P. Behrens, and A. M. Schneider, "Validation of the COMPASS force field for complex inorganic–organic hybrid polymers," *J. Sol-Gel Sci. Technol.*, vol. 81, no. 1, pp. 195–204, Jan. 2017, doi: 10.1007/s10971-016-4185-y.
- [225] A. N. Jain, K. Koile, and D. Chapman, "Compass: Predicting Biological Activities from Molecular Surface Properties. Performance Comparisons on a Steroid Benchmark," *J. Med. Chem.*, vol. 37, no. 15, pp. 2315–2327, Jul. 1994, doi: 10.1021/jm00041a010.
- [226] K. H. Kim *et al.*, "Crystal structure prediction of organic materials: Tests on the 1,4-diketo-3,6-diphenylpyrrolo(3,4-c)pyrrole and 1,4-diketo-3,6-bis(4'-dipyridyl)pyrrolo-[3,4-c]pyrrole," *Dye. Pigment.*, vol. 89, no. 1, pp. 37–43, Apr. 2011, doi: 10.1016/j.dyepig.2010.08.017.
- [227] N. D. Kondratyuk and V. V. Pisarev, "Calculation of viscosities of branched alkanes from 0.1 to 1000 MPa by molecular dynamics methods using COMPASS force field," *Fluid Phase Equilib.*, vol. 498, pp. 151–159, Oct. 2019, doi: 10.1016/j.fluid.2019.06.023.

- [228] H. Sun, "The COMPASS force field: Parameterization and validation for phosphazenes," *Comput. Theor. Polym. Sci.*, vol. 8, no. 1–2, pp. 229–246, Jan. 1998, doi: 10.1016/S1089-3156(98)00042-7.
- [229] D. Rigby, "Fluid density predictions using the COMPASS force field," *Fluid Phase Equilib.*, vol. 217, no. 1, pp. 77–87, Mar. 2004, doi: 10.1016/j.fluid.2003.08.019.
- [230] J. Yang, Y. Ren, A. M. Tian, and H. Sun, "COMPASS Force Field for 14 Inorganic Molecules, He, Ne, Ar, Kr, Xe, H₂, O₂, N₂, NO, CO, CO₂, NO₂, CS₂, and SO₂, in Liquid Phases," *J. Phys. Chem. B*, vol. 104, no. 20, pp. 4951–4957, May 2000, doi: 10.1021/jp992913p.
- [231] J. Gupta, C. Nunes, S. Vyas, and S. Jonnalagadda, "Prediction of solubility parameters and miscibility of pharmaceutical compounds by molecular dynamics simulations," *J. Phys. Chem. B*, vol. 115, no. 9, pp. 2014–2023, Mar. 2011, doi: 10.1021/jp108540n.
- [232] T. Chakraborty, A. Hens, S. Kulashrestha, N. Chandra Murmu, and P. Banerjee, "Calculation of diffusion coefficient of long chain molecules using molecular dynamics," *Phys. E Low-Dimensional Syst. Nanostructures*, vol. 69, pp. 371–377, May 2015, doi: 10.1016/j.physe.2015.01.008.
- [233] M. K. Shukla, A. Kumar, A. Yadav, and K. Sharma, "Improved mechanical properties of graphene oxide reinforced cross-linked epoxy nanocomposites: A molecular dynamics approach," in *Materials Today: Proceedings*, Jan. 2019, vol. 11, pp. 679–685, doi: 10.1016/j.matpr.2019.03.027.
- [234] S. L. Mayo, B. D. Olafson, and W. A. Goddard, "DREIDING: A generic force field for molecular simulations," *J. Phys. Chem.*, vol. 94, no. 26, pp. 8897–8909, 1990, doi: 10.1021/j100389a010.
- [235] G. A. Carlson, "Computer Simulation of the Molecular Structure of Bituminous Coal," *Energy and Fuels*, vol. 6, no. 6, pp. 771–778, Feb. 1992, doi: 10.1021/ef00036a012.
- [236] B. Arab, A. Shokuhfar, and K. Nasir, "Molecular Dynamics Simulation of Cross-Linked Epoxy Polymers: the Effect of Force Field on the Estimation of Properties," *J. Nano Electron. Phys.*, 2013.
- [237] C. Ouvrard and S. L. Price, "Toward crystal structure prediction for conformationally flexible molecules: The headaches illustrated by aspirin," *Cryst. Growth Des.*, vol. 4, no. 6, pp. 1119–1127, Nov. 2004, doi: 10.1021/cg049922u.
- [238] S. S. Jang, M. Blanco, W. A. Goddard, G. Caldwell, and R. B. Ross, "The source of helicity in perfluorinated N-alkanes," *Macromolecules*, vol. 36, no. 14, pp. 5331–5341, Jul. 2003, doi: 10.1021/ma025645t.
- [239] J. Yang *et al.*, "Hydrogen bonding energy determined by molecular dynamics simulation and correlation to properties of thermoplastic starch films," *Carbohydr. Polym.*, vol. 166, pp. 256–263, Jun. 2017, doi: 10.1016/j.carbpol.2017.03.001.
- [240] J. L. Mendoza-Cortes, Q. An, W. A. Goddard, C. Ye, and S. Zybin, "Prediction of the crystal packing of di-tetrazine-tetroxide (DTTO) energetic material," *J. Comput. Chem.*, vol. 37, no. 2, pp. 163–167, Jan. 2016, doi: 10.1002/jcc.23893.
- [241] M. J. Bearpark, M. A. Robb, and H. Bernhard Schlegel, "A direct method for the location of the lowest energy point on a potential surface crossing," *Chem. Phys. Lett.*, vol. 223, no. 3, pp. 269–274, Jun. 1994, doi: 10.1016/0009-2614(94)00433-1.

- [242] P. E. Maslen, "Geometry optimization of molecular clusters and complexes using scaled internal coordinates," *J. Chem. Phys.*, vol. 122, no. 1, p. 014104, Jan. 2005, doi: 10.1063/1.1829043.
- [243] B. Paizs, G. Fogarasi, and P. Pulay, "An efficient direct method for geometry optimization of large molecules in internal coordinates," *J. Chem. Phys.*, vol. 109, no. 16, pp. 6571–6576, Oct. 1998, doi: 10.1063/1.477309.
- [244] B. Civalleri, P. D'Arco, R. Orlando, V. R. Saunders, and R. Dovesi, "Hartree-Fock geometry optimisation of periodic systems with the CRYSTAL code," *Chem. Phys. Lett.*, vol. 348, no. 1–2, pp. 131–138, Nov. 2001, doi: 10.1016/S0009-2614(01)01081-8.
- [245] L. Iuzzolino, P. McCabe, S. L. Price, and J. G. Brandenburg, "Crystal structure prediction of flexible pharmaceutical-like molecules: density functional tight-binding as an intermediate optimisation method and for free energy estimation," *Faraday Discuss.*, vol. 211, no. 0, pp. 275–296, Oct. 2018, doi: 10.1039/c8fd00010g.
- [246] I. G. Tironi, R. Sperb, P. E. Smith, and W. F. Van Gunsteren, "A generalized reaction field method for molecular dynamics simulations," *J. Chem. Phys.*, vol. 102, no. 13, pp. 5451–5459, Apr. 1995, doi: 10.1063/1.469273.
- [247] G. M. Day and T. G. Cooper, "Crystal packing predictions of the alpha-amino acids: Methods assessment and structural observations," *CrystEngComm*, vol. 12, no. 8, pp. 2443–2453, Aug. 2010, doi: 10.1039/c002213f.
- [248] S. Vázquez, R. A. Mosquera, M. A. Rios, and C. Van Alsenoy, "AB initio gradient optimized molecular geometry and conformational analysis of 1,2-propanediol at the 4-21G level," *J. Mol. Struct. THEOCHEM*, vol. 184, no. 3–4, pp. 323–342, Feb. 1989, doi: 10.1016/0166-1280(89)85101-2.
- [249] T. H. Fischer and J. Almlöf, "General methods for geometry and wave function optimization," *J. Phys. Chem.*, vol. 96, no. 24, pp. 9768–9774, 1992, doi: 10.1021/j100203a036.
- [250] S. R. Billeter, A. J. Turner, and W. Thiel, "Linear scaling geometry optimisation and transition state search in hybrid delocalised internal coordinates," *Phys. Chem. Chem. Phys.*, vol. 2, no. 10, pp. 2177–2186, May 2000, doi: 10.1039/a909486e.
- [251] R. M. Freund, "The Steepest Descent Algorithm for Unconstrained Optimization and a Bisection Line-search Method," 2004.
- [252] R. Watrous, "Learning Algorithms for Connectionist Networks: Applied Gradient Methods of Nonlinear Optimization," *Tech. Reports*, Jul. 1988, Accessed: Dec. 27, 2020. [Online]. Available: https://repository.upenn.edu/cis_reports/597.
- [253] H. U. Simon and N. List, "SVM-Optimization and Steepest-Descent Line Search. SVM-Optimization and Steepest-Descent Line Search *," 2009. [Online]. Available: <https://www.researchgate.net/publication/221497771>.
- [254] C. C. Gonzaga and R. M. Schneider, "On the steepest descent algorithm for quadratic functions," *Comput. Optim. Appl.*, vol. 63, no. 2, pp. 523–542, Mar. 2016, doi: 10.1007/s10589-015-9775-z.

- [255] A. A. Goldstein, "On Steepest Descent," *J. Soc. Ind. Appl. Math. Ser. A Control*, vol. 3, no. 1, pp. 147–151, Jan. 1965, doi: 10.1137/0303013.
- [256] H. B. Curry and Frankord Arsenal, "NOTES-THE METHOD OF STEEPEST DESCENT FOR NON-LINEAR MINIMIZATION PROBLEMS*."
- [257] D. Eckhard and A. S. Bazanella, "Robust convergence of the steepest descent method for data-based control," *Int. J. Syst. Sci.*, vol. 43, no. 10, pp. 1969–1975, Oct. 2012, doi: 10.1080/00207721.2011.563874.
- [258] B. D. Systèmes, "BACKGROUND THEORY." 2017.
- [259] B. Y. Cao and Z. Y. Guo, "Equation of motion of a phonon gas and non-Fourier heat conduction," *J. Appl. Phys.*, vol. 102, no. 5, p. 053503, Sep. 2007, doi: 10.1063/1.2775215.
- [260] L. Susskind, "Complexity and Newton's Laws," *arXiv*, Apr. 2019, Accessed: Dec. 27, 2020. [Online]. Available: <http://arxiv.org/abs/1904.12819>.
- [261] T. C. Mo and C. H. Papas, "New equation of motion for classical charged particles," *Phys. Rev. D*, vol. 4, no. 12, pp. 3566–3571, Dec. 1971, doi: 10.1103/PhysRevD.4.3566.
- [262] H. Kamberaj, R. J. Low, and M. P. Neal, "Time reversible and symplectic integrators for molecular dynamics simulations of rigid molecules," *J. Chem. Phys.*, vol. 122, no. 22, p. 224114, Jun. 2005, doi: 10.1063/1.1906216.
- [263] Q. Spreiter and M. Walter, "Classical molecular dynamics simulation with the velocity verlet algorithm at strong external magnetic fields," *J. Comput. Phys.*, vol. 152, no. 1, pp. 102–119, Jun. 1999, doi: 10.1006/jcph.1999.6237.
- [264] R. W. Pastor, B. R. Brooks, and A. Szabo, "An analysis of the accuracy of langevin and molecular dynamics algorithms," *Mol. Phys.*, vol. 65, no. 6, pp. 1409–1419, Dec. 1988, doi: 10.1080/00268978800101881.
- [265] J. M. Ilnytskyi and M. R. Wilson, "A domain decomposition molecular dynamics program for the simulation of flexible molecules of spherically-symmetrical and nonspherical sites. II. Extension to NVT and NPT ensembles," *Comput. Phys. Commun.*, vol. 148, no. 1, pp. 43–58, Sep. 2002, doi: 10.1016/S0010-4655(02)00467-8.
- [266] J. R. Ray and A. Rahman, "Statistical ensembles and molecular dynamics studies of anisotropic solids," *J. Chem. Phys.*, vol. 80, no. 9, pp. 4423–4428, May 1984, doi: 10.1063/1.447221.
- [267] S. Labík and W. R. Smith, "Scaled particle theory and the efficient calculation of the chemical potential of hard spheres in the NYT ensemble," *Mol. Simul.*, vol. 12, no. 1, pp. 23–31, 1994, doi: 10.1080/08927029408022533.
- [268] D. J. Evans and B. L. Holian, "The Nose-Hoover thermostat," *J. Chem. Phys.*, vol. 83, no. 8, pp. 4069–4074, Oct. 1985, doi: 10.1063/1.449071.
- [269] C. Braga and K. P. Travis, "A configurational temperature Nosé-Hoover thermostat," *Journal of Chemical Physics*, vol. 123, no. 13. American Institute of PhysicsAIP, p. 134101, Oct. 03, 2005, doi: 10.1063/1.2013227.
- [270] Y. ying Lu *et al.*, "Theoretical simulations on the glass transition temperatures and mechanical properties of modified glycidyl azide polymer," *Comput. Mater. Sci.*, vol. 139, pp. 132–139, Nov. 2017, doi: 10.1016/j.commatsci.2017.07.022.

- [271] W. L. Hase and D. G. Buckowski, "Monte carlo sampling of a microcanonical ensemble of classical harmonic oscillators," *Chem. Phys. Lett.*, vol. 74, no. 2, pp. 284–287, Sep. 1980, doi: 10.1016/0009-2614(80)85159-1.
- [272] H. Frentrup, C. Avendaño, M. Horsch, A. Salih, and E. A. Müller, "Transport diffusivities of fluids in nanopores by non-equilibrium molecular dynamics simulation," *Mol. Simul.*, vol. 38, no. 7, pp. 540–553, Jun. 2012, doi: 10.1080/08927022.2011.636813.
- [273] A. Ovseevich, "A Local Feedback Control Bringing a Linear System to Equilibrium," *J. Optim. Theory Appl.*, vol. 165, no. 2, pp. 532–544, May 2015, doi: 10.1007/s10957-014-0636-1.
- [274] "Fundamentals of Fourier Transform Infrared Spectroscopy - Brian C. Smith - Google Books." https://books.google.co.uk/books?hl=en&lr=&id=LR9HkK2cP_0C&oi=fnd&pg=PP1&dq=related:BDtJxZWMIVYJ:scholar.google.com/&ots=iMzfHaUK5B&sig=4yd9DKLSlybpH6zbXiy_epUELjc#v=onepage&q&f=false (accessed Dec. 19, 2020).
- [275] S. Ishihara, Y. Hattori, and M. Otsuka, "MCR-ALS analysis of IR spectroscopy and XRD for the investigation of ibuprofen - nicotinamide cocrystal formation," *Spectrochim. Acta - Part A Mol. Biomol. Spectrosc.*, vol. 221, p. 117142, Oct. 2019, doi: 10.1016/j.saa.2019.117142.
- [276] L. Feng and K. A. Berglund, "ATR-FTIR for Determining Optimal Cooling Curves for Batch Crystallization of Succinic Acid," *Cryst. Growth Des.*, vol. 2, no. 5, pp. 449–452, Sep. 2002, doi: 10.1021/cg025545e.
- [277] S. G. Kazarian and K. L. A. Chan, "ATR-FTIR spectroscopic imaging: Recent advances and applications to biological systems," *Analyst*, vol. 138, no. 7. Royal Society of Chemistry, pp. 1940–1951, Apr. 07, 2013, doi: 10.1039/c3an36865c.
- [278] "Infrared and Raman Spectroscopy: Principles and Spectral Interpretation - Peter Larkin - Google Books." https://books.google.co.uk/books?hl=en&lr=&id=bMgpDwAAQBAJ&oi=fnd&pg=PP1&dq=ir+spectroscopy+principle&ots=_qDAvdVrhv&sig=ArGHGuN5PSTaZJsyFLDb-AMKqvs#v=onepage&q=ir spectroscopy principle&f=false (accessed Dec. 19, 2020).
- [279] A. A. Ismail, F. R. van de Voort, and J. Sedman, "Chapter 4 Fourier transform infrared spectroscopy: Principles and applications," *Tech. Instrum. Anal. Chem.*, vol. 18, no. C, pp. 93–139, Jan. 1997, doi: 10.1016/S0167-9244(97)80013-3.
- [280] B. Dziuba, A. Babuchowski, D. Nałecz, and M. Niklewicz, "Identification of lactic acid bacteria using FTIR spectroscopy and cluster analysis," *Int. Dairy J.*, vol. 17, no. 3, pp. 183–189, Mar. 2007, doi: 10.1016/j.idairyj.2006.02.013.
- [281] C. H. Spink, "Differential Scanning Calorimetry," *Methods in Cell Biology*, vol. 84. Academic Press, pp. 115–141, Jan. 01, 2008, doi: 10.1016/S0091-679X(07)84005-2.
- [282] J. Reguera, D. W. Urry, T. M. Parker, D. T. McPherson, and J. C. Rodríguez-Cabello, "Effect of NaCl on the exothermic and endothermic components of the inverse temperature transition of a model elastin-like polymer," *Biomacromolecules*, vol. 8, no. 2, pp. 354–358, Feb. 2007, doi: 10.1021/bm060936l.

- [283] P. Liu, L. Yu, H. Liu, L. Chen, and L. Li, "Glass transition temperature of starch studied by a high-speed DSC," *Carbohydr. Polym.*, vol. 77, no. 2, pp. 250–253, Jun. 2009, doi: 10.1016/j.carbpol.2008.12.027.
- [284] Y. Kong and J. N. Hay, "The measurement of the crystallinity of polymers by DSC," *Polymer (Guildf.)*, vol. 43, no. 14, pp. 3873–3878, May 2002, doi: 10.1016/S0032-3861(02)00235-5.
- [285] A. Yousefi, P. G. Lafleur, and R. Gauvin, "Kinetic studies of thermoset cure reactions: A review," *Polym. Compos.*, vol. 18, no. 2, pp. 157–168, Apr. 1997, doi: 10.1002/pc.10270.
- [286] S. Hubert *et al.*, "Process induced transformations during tablet manufacturing: Phase transition analysis of caffeine using DSC and low frequency micro-Raman spectroscopy," *Int. J. Pharm.*, vol. 420, no. 1, pp. 76–83, Nov. 2011, doi: 10.1016/j.ijpharm.2011.08.028.
- [287] A. A. van Dooren and B. W. Müller, "Purity determinations of drugs with differential scanning calorimetry (DSC)-a critical review," *International Journal of Pharmaceutics*, vol. 20, no. 3. Elsevier, pp. 217–233, Jul. 01, 1984, doi: 10.1016/0378-5173(84)90170-4.
- [288] T. Ma *et al.*, "Single-crystal x-ray diffraction structures of covalent organic frameworks," *Science (80-.)*, vol. 361, no. 6397, pp. 48–52, Jul. 2018, doi: 10.1126/science.aat7679.
- [289] H. Toraya, "Whole-powder-pattern fitting without reference to a structural model: application to X-ray powder diffraction data," *J. Appl. Crystallogr.*, vol. 19, no. 6, pp. 440–447, Dec. 1986, doi: 10.1107/s0021889886088982.
- [290] F. Vanmeert, W. De Nolf, S. De Meyer, J. Dik, and K. Janssens, "Macroscopic X-ray Powder Diffraction Scanning, a New Method for Highly Selective Chemical Imaging of Works of Art: Instrument Optimization," *Anal. Chem.*, vol. 90, no. 11, pp. 6436–6444, Jun. 2018, doi: 10.1021/acs.analchem.8b00240.
- [291] R. Das and E. A. H. S. B. Ali, "CURRENT APPLICATIONS OF X-RAY POWDER DIFFRACTION - A REVIEW.," *Rev. Adv. Mater. Sci.*, vol. 38, no. 2, pp. 95–109, Oct. 2014, Accessed: Dec. 19, 2020. [Online]. Available: <http://search.ebscohost.com/login.aspx?direct=true&db=aph&AN=99121449&site=eds-live>.
- [292] A. Newman, D. Engers, S. Bates, I. Ivanisevic, R. C. Kelly, and G. Zografi, "Characterization of amorphous API:polymer mixtures using x-ray powder diffraction," *J. Pharm. Sci.*, vol. 97, no. 11, pp. 4840–4856, Nov. 2008, doi: 10.1002/jps.21352.
- [293] R. W. James, "The Dynamical Theory of X-Ray Diffraction," *Solid State Phys. - Adv. Res. Appl.*, vol. 15, no. C, pp. 53–220, Jan. 1963, doi: 10.1016/S0081-1947(08)60592-5.
- [294] W. H. Zachariasen, "A general theory of X-ray diffraction in crystals," *Acta Crystallogr.*, vol. 23, no. 4, pp. 558–564, Oct. 1967, doi: 10.1107/s0365110x67003202.
- [295] S. Mazurek and R. Szostak, "Quantitative determination of captopril and prednisolone in tablets by FT-Raman spectroscopy," *J. Pharm. Biomed. Anal.*, vol. 40, no. 5, pp. 1225–1230, Mar. 2006, doi: 10.1016/j.jpba.2005.03.047.

- [296] K. Dégardin, Y. Roggo, F. Been, and P. Margot, "Detection and chemical profiling of medicine counterfeits by Raman spectroscopy and chemometrics," *Anal. Chim. Acta*, vol. 705, no. 1–2, pp. 334–341, Oct. 2011, doi: 10.1016/j.aca.2011.07.043.
- [297] A. Hertrampf, R. M. Sousa, J. C. Menezes, and T. Herdling, "Semi-quantitative prediction of a multiple API solid dosage form with a combination of vibrational spectroscopy methods," *J. Pharm. Biomed. Anal.*, vol. 124, pp. 246–253, May 2016, doi: 10.1016/j.jpba.2016.03.003.
- [298] S. A. Asher and R. Borrett, "Raman Instrumentation," 2000, pp. 35–54.
- [299] R. S. Das and Y. K. Agrawal, "Raman spectroscopy: Recent advancements, techniques and applications," *Vibrational Spectroscopy*, vol. 57, no. 2. Elsevier, pp. 163–176, Nov. 01, 2011, doi: 10.1016/j.vibspec.2011.08.003.
- [300] R. Merlin, A. Pinczuk, and W. H. Weber, "Overview of Phonon Raman Scattering in Solids," 2000, pp. 1–29.
- [301] J. P. Camden *et al.*, "Probing the structure of single-molecule surface-enhanced Raman scattering hot spots," *J. Am. Chem. Soc.*, vol. 130, no. 38, pp. 12616–12617, Sep. 2008, doi: 10.1021/ja8051427.
- [302] S. Parnell, K. Min, and M. Cakmak, "Kinetic studies of polyurethane polymerization with Raman spectroscopy," *Polymer (Guildf.)*, vol. 44, no. 18, pp. 5137–5144, Aug. 2003, doi: 10.1016/S0032-3861(03)00468-3.
- [303] B. H. Stuart, "Polymer crystallinity studied using Raman spectroscopy," *Vibrational Spectroscopy*, vol. 10, no. 2. Elsevier, pp. 79–87, Jan. 01, 1996, doi: 10.1016/0924-2031(95)00042-9.
- [304] M. A. Elbagerma, H. G. M. Edwards, T. Munshi, M. D. Hargreaves, P. Matousek, and I. J. Scowen, "Characterization of new cocrystals by raman spectroscopy, powder X-ray diffraction, differential scanning calorimetry, and transmission raman spectroscopy," *Cryst. Growth Des.*, vol. 10, no. 5, pp. 2360–2371, May 2010, doi: 10.1021/cg100156a.
- [305] W. W. Porter, S. C. Elie, and A. J. Matzger, "Polymorphism in carbamazepine cocrystals," *Cryst. Growth Des.*, vol. 8, no. 1, pp. 14–16, Jan. 2008, doi: 10.1021/cg701022e.
- [306] P. R. G. D.J. Gardiner, *Practical Raman Spectroscopy*. Springer Berlin Heidelberg, 1989.
- [307] N. Jalili and K. Laxminarayana, "A review of atomic force microscopy imaging systems: Application to molecular metrology and biological sciences," *Mechatronics*, vol. 14, no. 8, pp. 907–945, Oct. 2004, doi: 10.1016/j.mechatronics.2004.04.005.
- [308] E. Meyer, "Atomic force microscopy," *Prog. Surf. Sci.*, vol. 41, no. 1, pp. 3–49, Sep. 1992, doi: 10.1016/0079-6816(92)90009-7.
- [309] R. W. Seizo Morita, Franz J. Giessibl, Ernst Meyer, *Noncontact Atomic Force Microscopy: Volume 3 - Google Books*. Springer, 2015.
- [310] E. I. Altman, M. Z. Baykara, and U. D. Schwarz, "Noncontact Atomic Force Microscopy: An Emerging Tool for Fundamental Catalysis Research," *Acc. Chem. Res.*, vol. 48, no. 9, pp. 2640–2648, Sep. 2015, doi: 10.1021/acs.accounts.5b00166.

- [311] S. X. M. Boerrigter *et al.*, "MONTY: Monte Carlo crystal growth on any crystal structure in any crystallographic orientation; Application to fats," *J. Phys. Chem. A*, vol. 108, no. 27, pp. 5894–5902, Jul. 2004, doi: 10.1021/jp049804h.
- [312] J. D. Rimer *et al.*, "Crystal growth inhibitors for the prevention of L-cystine kidney stones through molecular design," *Science (80-.)*, vol. 330, no. 6002, pp. 337–341, Oct. 2010, doi: 10.1126/science.1191968.
- [313] I. Muševič, "Atomic force microscopy," *Inf. MIDEEM*, vol. 30, no. 4, pp. 223–227, Dec. 2000, doi: 10.1007/s00897960059a.
- [314] R. Jagtap and A. Ambre, "Overview literature on atomic force microscopy (AFM) : Basics and its important applications for polymer characterization," *undefined*, 2006.
- [315] A. V. Crewe, M. Isaacson, and D. Johnson, "A simple scanning electron microscope," *Rev. Sci. Instrum.*, vol. 40, no. 2, pp. 241–246, Feb. 1969, doi: 10.1063/1.1683910.
- [316] H. Seiler, "Secondary electron emission in the scanning electron microscope," *J. Appl. Phys.*, vol. 54, no. 11, pp. R1–R18, Nov. 1983, doi: 10.1063/1.332840.
- [317] Y. H. Yun and P. J. Bray, "Nuclear magnetic resonance studies of the glasses in the system Na₂O·B₂O₃·SiO₂," *J. Non. Cryst. Solids*, vol. 27, no. 3, pp. 363–380, Mar. 1978, doi: 10.1016/0022-3093(78)90020-0.
- [318] Edwin D. Becker, *High Resolution NMR: Theory and Chemical Applications*, Third edition. London: Academic Press, 2000.
- [319] J. Autschbach and B. Le Guennic, "Analyzing and interpreting NMR spin-spin coupling constants using molecular orbital calculations," *J. Chem. Educ.*, vol. 84, no. 1, pp. 156–171, 2007, doi: 10.1021/ed084p156.
- [320] S. Mukamel, D. Abramavicius, L. Yang, W. Zhuang, I. V. Schweigert, and D. V. Voronine, "Coherent multidimensional optical probes for electron correlations and exciton dynamics: From NMR to X-rays," *Acc. Chem. Res.*, vol. 42, no. 4, pp. 553–562, Apr. 2009, doi: 10.1021/ar800258z.
- [321] M. Karplus and J. A. Pople, "Theory of carbon NMR chemical shifts in conjugated molecules," *J. Chem. Phys.*, vol. 38, no. 12, pp. 2803–2807, Jun. 1963, doi: 10.1063/1.1733605.
- [322] T. E. Crowley, "Nuclear magnetic resonance spectroscopy," in *Purification and Characterization of Secondary Metabolites*, Elsevier, 2020, pp. 67–78.
- [323] S. Maity, R. K. Gundampati, and T. K. Suresh Kumar, "NMR Methods to Characterize Protein-Ligand Interactions," *Nat. Prod. Commun.*, vol. 14, no. 5, p. 1934578X1984929, May 2019, doi: 10.1177/1934578X19849296.
- [324] M. R. Chierotti and R. Gobetto, "NMR crystallography: The use of dipolar interactions in polymorph and co-crystal investigation," *CrystEngComm*, vol. 15, no. 43, pp. 8599–8612, Nov. 2013, doi: 10.1039/c3ce41026a.
- [325] S. Yusa, "Polymer characterization," in *Polymer Science and Nanotechnology*, Elsevier, 2020, pp. 105–124.
- [326] G. A. Morris, "Diffusion-Ordered Spectroscopy," in *Encyclopedia of Magnetic Resonance*, Chichester, UK: John Wiley & Sons, Ltd, 2009.
- [327] I. Sogami and N. Ise, "On the electrostatic interaction in macroionic solutions," *J. Chem. Phys.*, vol. 81, no. 12, pp. 6320–6332, Dec. 1984, doi: 10.1063/1.447541.

- [328] Y. Andersson, E. Hult, H. Rydberg, P. Apell, B. I. Lundqvist, and D. C. Langreth, "Van der Waals Interactions in Density Functional Theory," in *Electronic Density Functional Theory*, Boston, MA: Springer US, 1998, pp. 243–260.
- [329] M. Ramaswamy *et al.*, "How confinement-induced structures alter the contribution of hydrodynamic and short-ranged repulsion forces to the viscosity of colloidal suspensions," *Phys. Rev. X*, vol. 7, no. 4, p. 041005, Oct. 2017, doi: 10.1103/PhysRevX.7.041005.
- [330] A. J. Misquitta and A. J. Stone, "Accurate induction energies for small organic molecules: 1. Theory," *J. Chem. Theory Comput.*, vol. 4, no. 1, pp. 7–18, Jan. 2008, doi: 10.1021/ct700104t.
- [331] C. Zhang, H. Dai, P. Lu, L. Wu, B. Zhou, and C. Yu, "Molecular dynamics simulation of distribution and diffusion behaviour of oil–water interfaces," *Molecules*, vol. 24, no. 10, May 2019, doi: 10.3390/molecules24101905.
- [332] S. J. Grabowski, *Hydrogen bonding - New insights*. Springer Netherlands, 2006.
- [333] G. J. Zhao and K. L. Han, "Role of intramolecular and intermolecular hydrogen bonding in both singlet and triplet excited states of aminofluorenones on internal conversion, intersystem crossing, and twisted intramolecular charge transfer," *J. Phys. Chem. A*, vol. 113, no. 52, pp. 14329–14335, Dec. 2009, doi: 10.1021/jp903200x.
- [334] E. Fan, S. A. Van Arman, S. Kincaid, and A. D. Hamilton, "Molecular Recognition: Hydrogen-Bonding Receptors That Function in Highly Competitive Solvents," *J. Am. Chem. Soc.*, vol. 115, no. 1, pp. 369–370, Jan. 1993, doi: 10.1021/ja00054a066.
- [335] E. Fan, A. D. Hamilton, S. K. Chang, and D. Van Engen, "Hydrogen Bonding and Molecular Recognition: Synthetic, Complexation, and Structural Studies on Barbiturate Binding to an Artificial Receptor," *J. Am. Chem. Soc.*, vol. 113, no. 20, pp. 7640–7645, Sep. 1991, doi: 10.1021/ja00020a027.
- [336] R. Patil, S. Das, A. Stanley, L. Yadav, A. Sudhakar, and A. K. Varma, "Optimized Hydrophobic Interactions and Hydrogen Bonding at the Target-Ligand Interface Leads the Pathways of Drug-Designing," *PLoS One*, vol. 5, no. 8, p. e12029, Aug. 2010, doi: 10.1371/journal.pone.0012029.
- [337] A. Choperena and P. Painter, "Hydrogen bonding in polymers: Effect of temperature on the OH stretching bands of poly(vinylphenol)," *Macromolecules*, vol. 42, no. 16, pp. 6159–6165, Aug. 2009, doi: 10.1021/ma900928z.
- [338] R. F. M. Lange, M. Van Gorp, and E. W. Meijer, "Hydrogen-bonded supramolecular polymer networks," *J. Polym. Sci. Part A Polym. Chem.*, vol. 37, no. 19, pp. 3657–3670, Oct. 1999, doi: 10.1002/(SICI)1099-0518(19991001)37:19<3657::AID-POLA1>3.0.CO;2-6.
- [339] J. Cohn, "Theory of the radial distribution function," *J. Phys. Chem.*, vol. 72, no. 2, pp. 608–616, 1968, doi: 10.1021/j100848a037.
- [340] G. X. Li, Y. F. Liang, Z. G. Zhu, and C. S. Liu, "Microstructural analysis of the radial distribution function for liquid and amorphous Al," *J. Phys. Condens. Matter*, vol. 15, no. 14, pp. 2259–2267, Apr. 2003, doi: 10.1088/0953-8984/15/14/302.
- [341] A. A. Chialvo and P. T. Cummings, "Hydrogen bonding in supercritical water," *J. Chem. Phys.*, vol. 101, no. 5, pp. 4466–4469, Sep. 1994, doi: 10.1063/1.467432.

- [342] J. G. Kirkwood and F. P. Buff, "The statistical mechanical theory of surface tension," *J. Chem. Phys.*, vol. 17, no. 3, pp. 338–343, Mar. 1949, doi: 10.1063/1.1747248.
- [343] D. Ernst and J. Köhler, "Measuring a diffusion coefficient by single-particle tracking: Statistical analysis of experimental mean squared displacement curves," *Phys. Chem. Chem. Phys.*, vol. 15, no. 3, pp. 845–849, Jan. 2013, doi: 10.1039/c2cp43433d.
- [344] J. H. Jeon and R. Metzler, "Analysis of short subdiffusive time series: Scatter of the time-averaged mean-squared displacement," *J. Phys. A Math. Theor.*, vol. 43, no. 25, p. 252001, Jun. 2010, doi: 10.1088/1751-8113/43/25/252001.
- [345] G. Sikora, K. Burnecki, and A. Wyłomańska, "Mean-squared-displacement statistical test for fractional Brownian motion," *Phys. Rev. E*, vol. 95, no. 3, p. 032110, Mar. 2017, doi: 10.1103/PhysRevE.95.032110.
- [346] S. Qiu *et al.*, "Role of polymers in solution and tablet-based carbamazepine cocrystal formulations," *CrystEngComm*, vol. 18, no. 15, pp. 2664–2678, Apr. 2016, doi: 10.1039/c6ce00263c.
- [347] R. Bobrovs, L. Seton, and N. Dempster, "The reluctant polymorph: Investigation into the effect of self-association on the solvent mediated phase transformation and nucleation of theophylline," *CrystEngComm*, vol. 17, no. 28, pp. 5237–5251, Jul. 2015, doi: 10.1039/c4ce02484b.
- [348] K. Ueda *et al.*, "Mechanistic differences in permeation behavior of supersaturated and solubilized solutions of carbamazepine revealed by nuclear magnetic resonance measurements," *Mol. Pharm.*, vol. 9, no. 11, pp. 3023–3033, 2012, doi: 10.1021/mp300083e.
- [349] R. C. O. Sebastião, C. N. Pacheco, J. P. Braga, and D. Piló-Veloso, "Diffusion coefficient distribution from NMR-DOSY experiments using Hopfield neural network," *J. Magn. Reson.*, vol. 182, no. 1, pp. 22–28, Sep. 2006, doi: 10.1016/j.jmr.2006.06.005.
- [350] P. Kirubakaran, K. Wang, I. Rosbottom, R. B. M. Cross, and M. Li, "Understanding the Effects of a Polymer on the Surface Dissolution of Pharmaceutical Cocrystals Using Combined Experimental and Molecular Dynamics Simulation Approaches," *Mol. Pharm.*, vol. 17, no. 2, pp. 517–529, 2020, doi: 10.1021/acs.molpharmaceut.9b00955.

Appendix

A1 ATR-FTIR

Table 1: Peak position and assignment of FFA-TP

	Peak position (cm ³)	Assaignment
FFA I	3322	-N-H
	2647	O-H acid
	1651	C=O
	1330	C-F
TP	3119	-N-H
	1657	C=O
	1184	C-N
FFA-TP PM	3317, 3110	-N-H
	2707	O-H acid
	1656	C=O
	1333	C-F
	1044	C-N
FFA-TP CO	3282, 3070	-N-H
	2838	O-H (acid)
	1643	C=O
	1321	C-F
FFA-TP SC	3272, 3060	-N-H
	2833	O-H acid
	1643	C=O
	1321	C-F

Table 2: Peak position and assignment of FFA-NIC

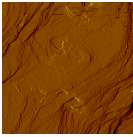
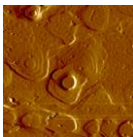
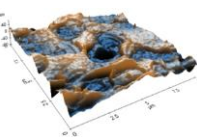
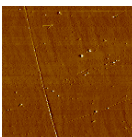
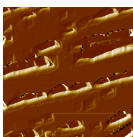
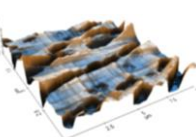
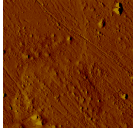
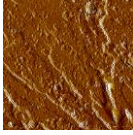
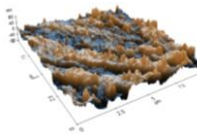
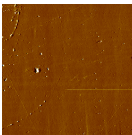
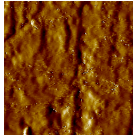
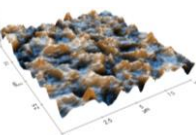
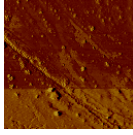
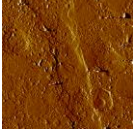
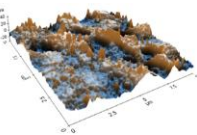
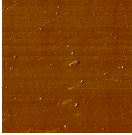
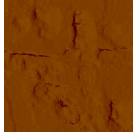
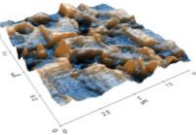
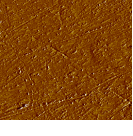
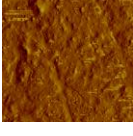
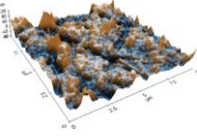
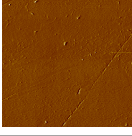
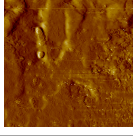
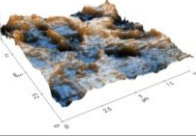
	Peak position (cm ³)	Assignment
FFA I	3322	-N-H
	2647	O-H acid
	1651	C=O
	1330	C-F
NIC	3362	-N-H
	1680	C=O
FFA-NIC PM	3356	-N-H
	1673	C=O
	1332	C-F
FFA-NIC CO	3397	-N-H
	1664	C=O
FFA-NIC SC	3397	-N-H
	1663	C=O

Table 3: Peak position and assignment of CBZ-NIC

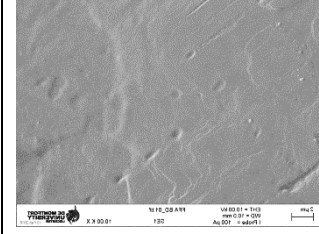
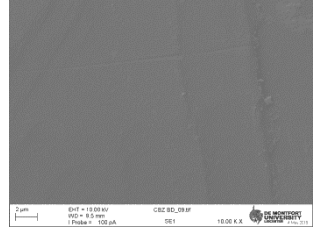
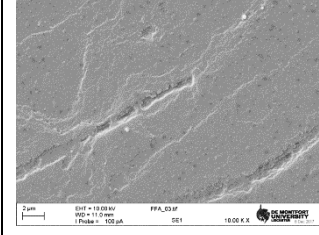
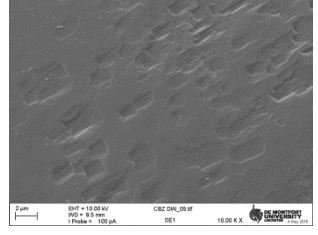
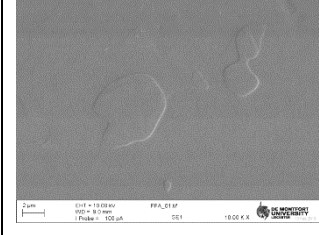
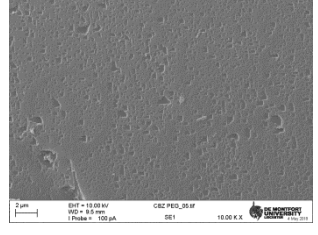
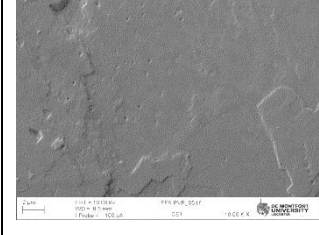
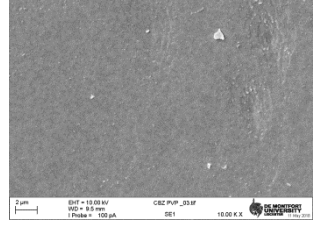

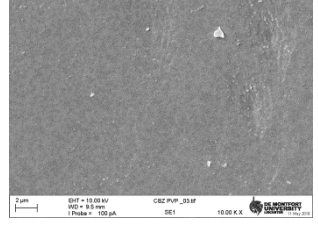
	Peak position (cm ³)	Assignment
CBZ III	3464	-N-H
	1667	C=O
	800, 762	C-N-C
	647, 623	(O-C-N) ring
NIC	3362	-N-H
	1680	C=O
CBZ-NIC PM	3464	-N-H of CBZ
	1676	C=O of NIC
CBZ-NIC CO	3448, 3395	-N-H of CBZ
	1683, 1659	C=O of NIC

CBZ-NIC SC	3448, 3395	-N-H of CBZ
	1683, 1659	C=O of NIC

A2 Atomic force microscopy

	FFA			CBZ		
	Before	After	3D and % increase	Before	After	3D and % increase
Distilled water						
Roughness, Ra (μm)	7.31	12.883	76.238	1.827	110.105	5926.546
PEG						
Roughness, Ra (μm)	10.712	18.578	73.432	1.814	21.678	1095.039
PVP						
Roughness, Ra (μm)	9.898	8.15	-17.660	1.079	31.384	2808.619
PVPVA						
Roughness, Ra (μm)	9.797	16.004	63.356	0.944	29.912	3068.644

A3 Scanning electron microscope

	FFA	CBZ
Before Dissolution	 <p>SEM image of FFA surface before dissolution. The surface appears relatively smooth with some fine, irregular texture. Technical data: X 300k, 10.00 kV, 10.00 kX, 2.00 µm scale bar.</p>	 <p>SEM image of CBZ surface before dissolution. The surface is very smooth and uniform. Technical data: 10.00 kV, 10.00 kX, 2.00 µm scale bar.</p>
Distilled water	 <p>SEM image of FFA surface after dissolution in distilled water. The surface is highly porous and fibrous, with a complex network of interconnected fibers. Technical data: 10.00 kV, 10.00 kX, 2.00 µm scale bar.</p>	 <p>SEM image of CBZ surface after dissolution in distilled water. The surface is porous and shows a layered or fibrous structure. Technical data: 10.00 kV, 10.00 kX, 2.00 µm scale bar.</p>
PEG	 <p>SEM image of FFA surface after dissolution in PEG. The surface is porous and shows a network of interconnected fibers. Technical data: 10.00 kV, 10.00 kX, 2.00 µm scale bar.</p>	 <p>SEM image of CBZ surface after dissolution in PEG. The surface is porous and shows a network of interconnected fibers. Technical data: 10.00 kV, 10.00 kX, 2.00 µm scale bar.</p>
PVP	 <p>SEM image of FFA surface after dissolution in PVP. The surface is porous and shows a network of interconnected fibers. Technical data: 10.00 kV, 10.00 kX, 2.00 µm scale bar.</p>	 <p>SEM image of CBZ surface after dissolution in PVP. The surface is porous and shows a network of interconnected fibers. Technical data: 10.00 kV, 10.00 kX, 2.00 µm scale bar.</p>
PVPVA	 <p>SEM image of FFA surface after dissolution in PVPVA. The surface is porous and shows a network of interconnected fibers. Technical data: 10.00 kV, 10.00 kX, 2.00 µm scale bar.</p>	 <p>SEM image of CBZ surface after dissolution in PVPVA. The surface is porous and shows a network of interconnected fibers. Technical data: 10.00 kV, 10.00 kX, 2.00 µm scale bar.</p>

A4 MD Simulations

Table 1: Energy graph of FFA-NIC and PEG

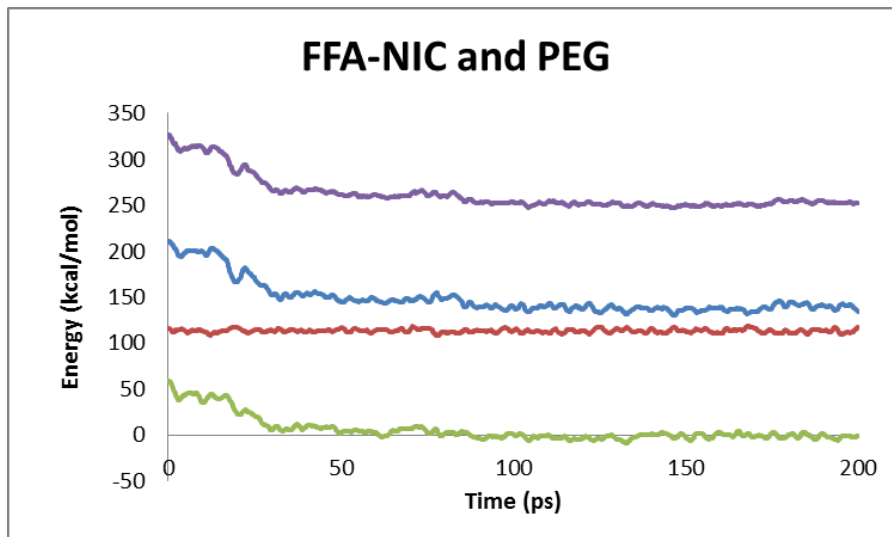
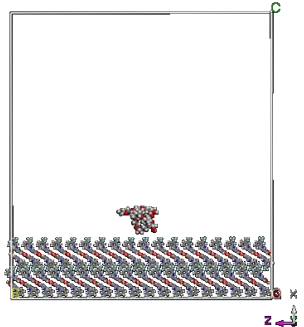
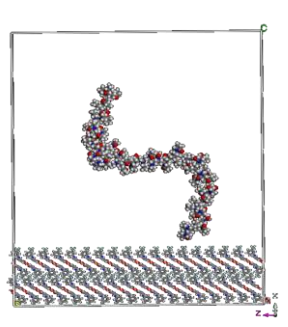
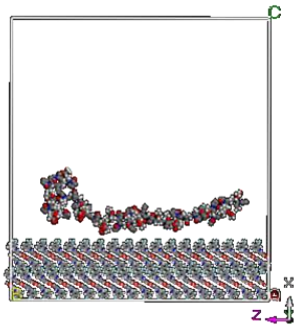


Table 2: Snapshot of a polymer on FFA (100) crystal surface at 298K at different simulation times

Time (ps)	FFA		
	PEG	PVP	PVP-VA
0			

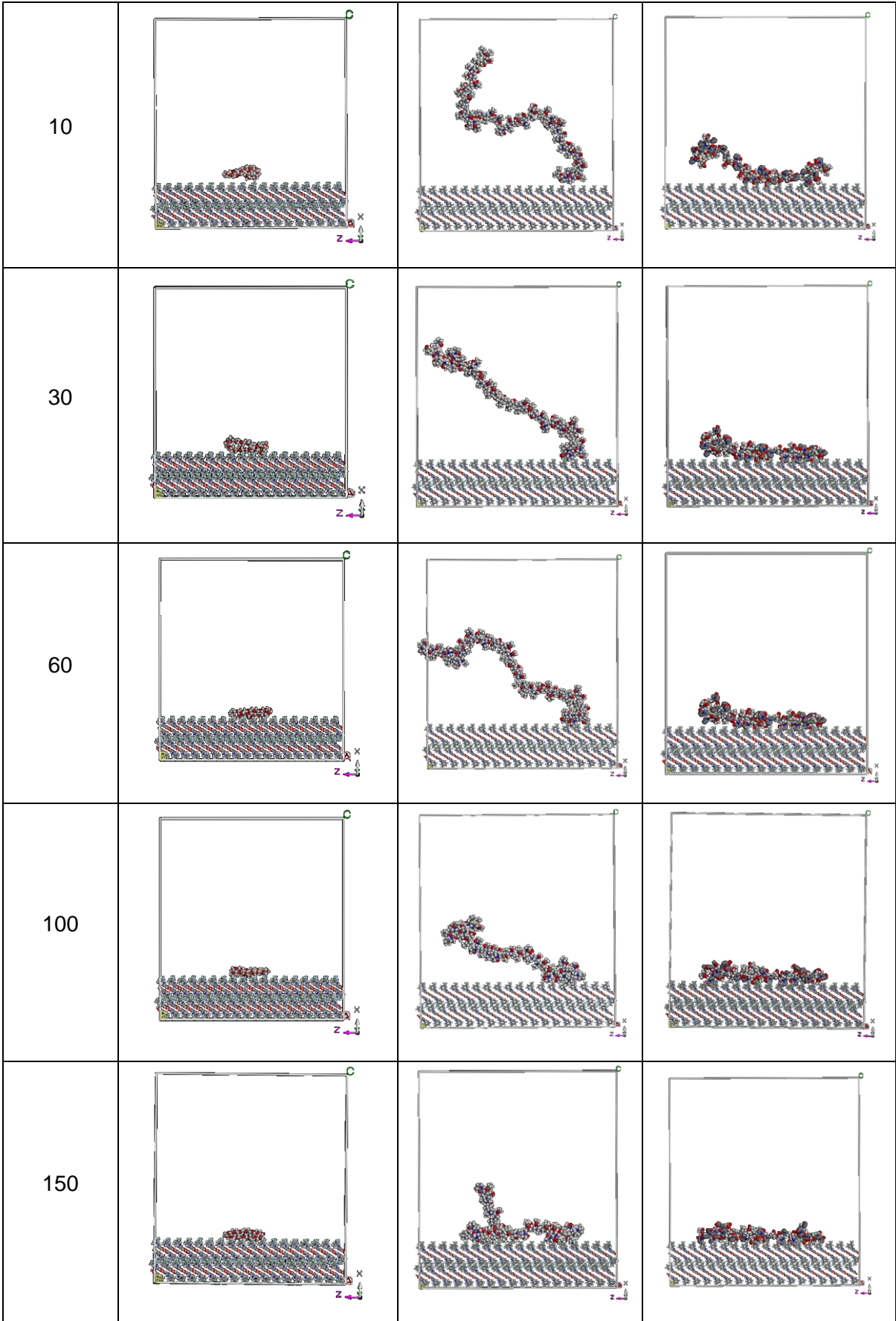
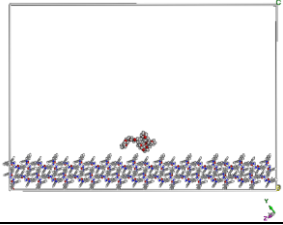
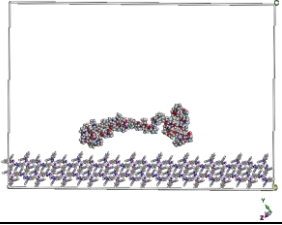
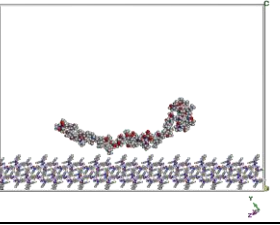
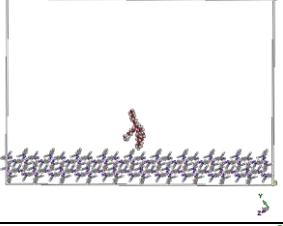
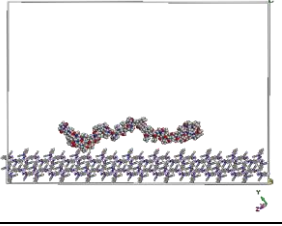
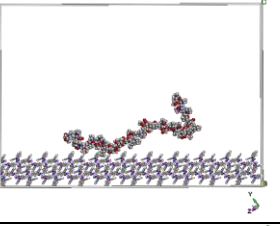
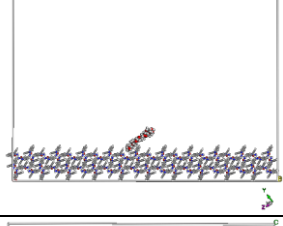
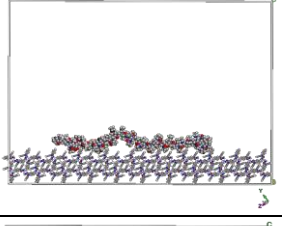
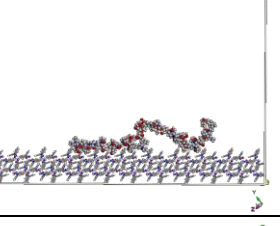
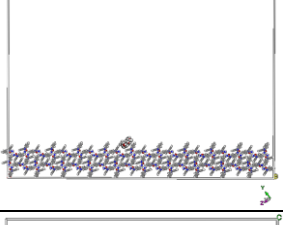
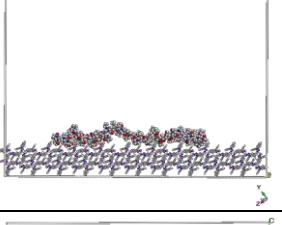
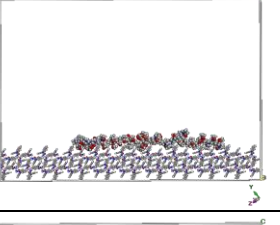
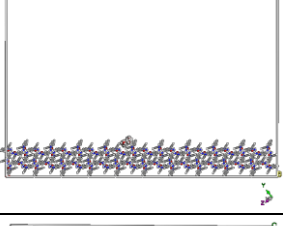
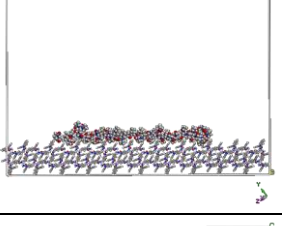
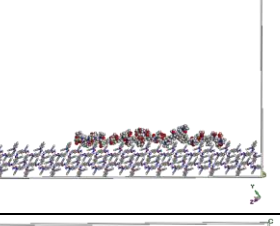
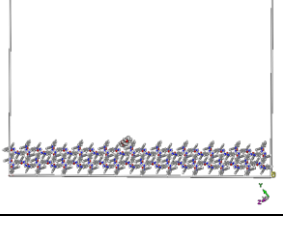
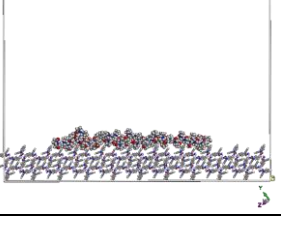
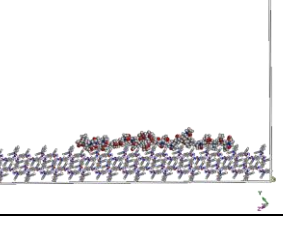
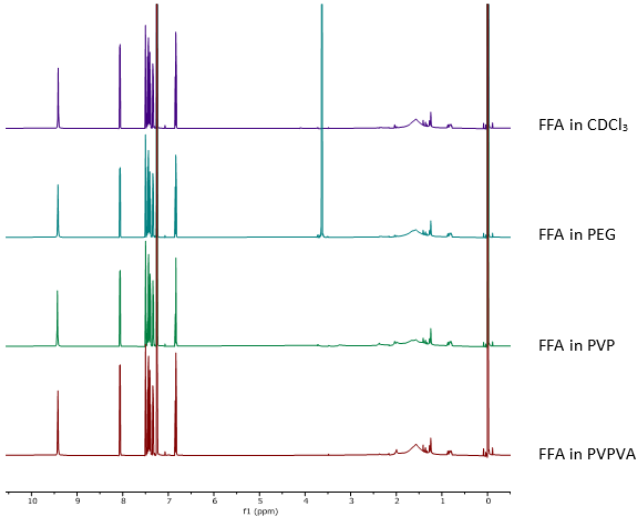
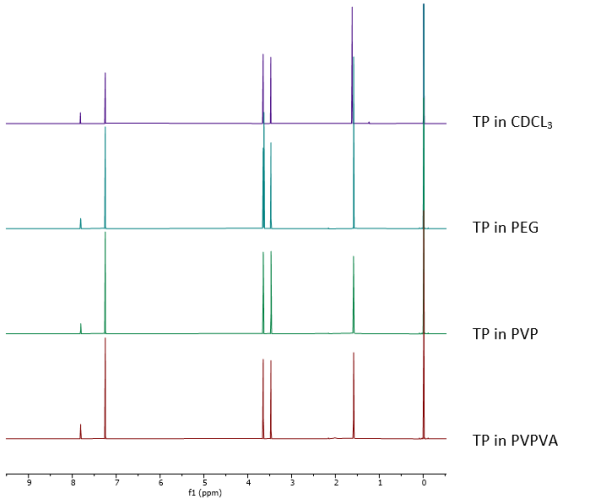


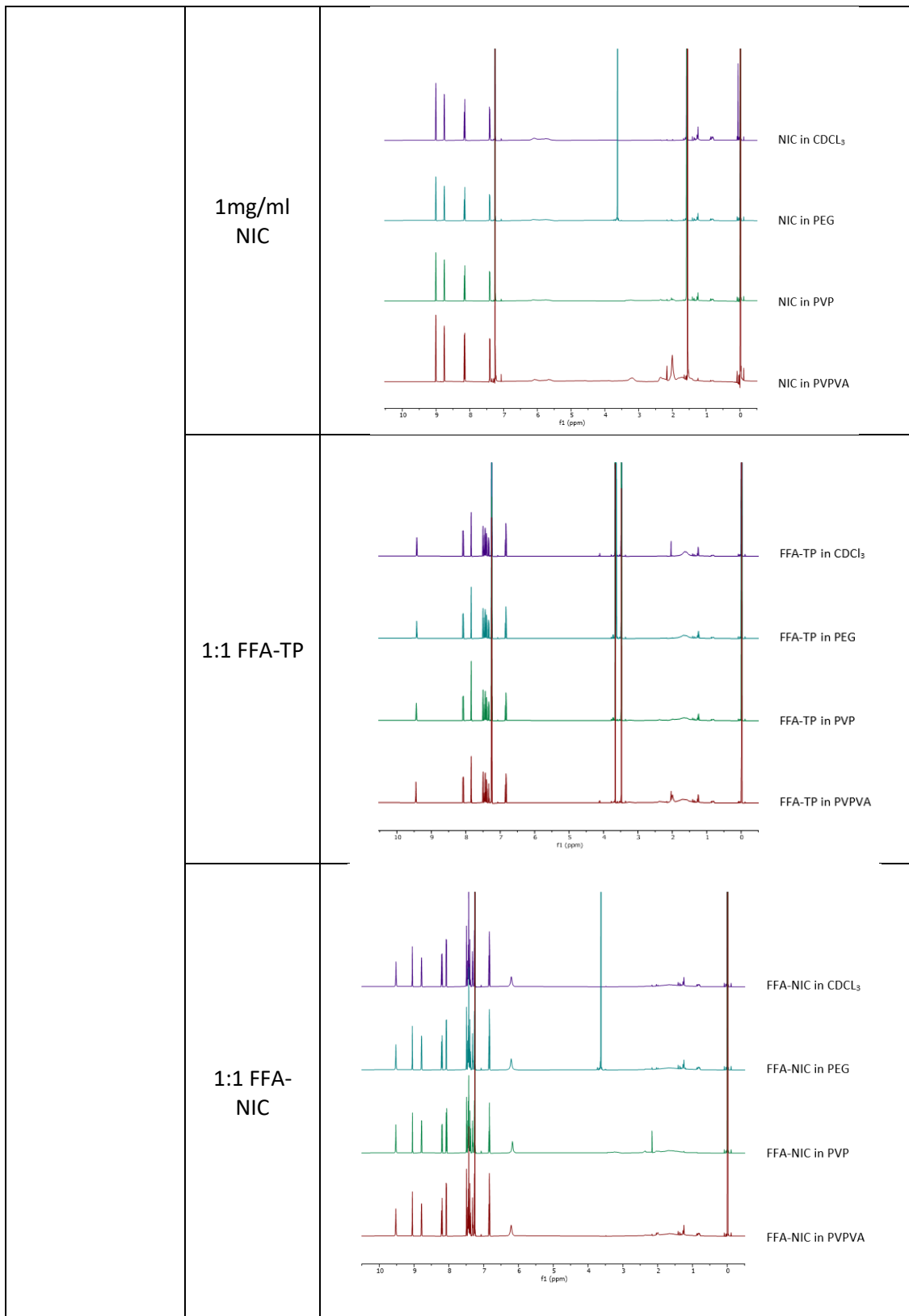
Table 3: Snapshot of a polymer on CBZ (0,1,-1) crystal surface at 298K at different simulation times.

Time (ps)	CBZ		
	PEG	PVP	PVP-VA
0			
10			
30			
60			
100			
150			

A5 NMR Spectra

Table 1: NMR spectra of the drugs and co-crystals in 0.3mg/ml polymer.

	Drug	NMR proton spectra
Components	2.4mg/ml FFA	 <p>FFA in CDCl₃</p> <p>FFA in PEG</p> <p>FFA in PVP</p> <p>FFA in PVPVA</p>
	1.54mg/ml TP	 <p>TP in CDCl₃</p> <p>TP in PEG</p> <p>TP in PVP</p> <p>TP in PVPVA</p>



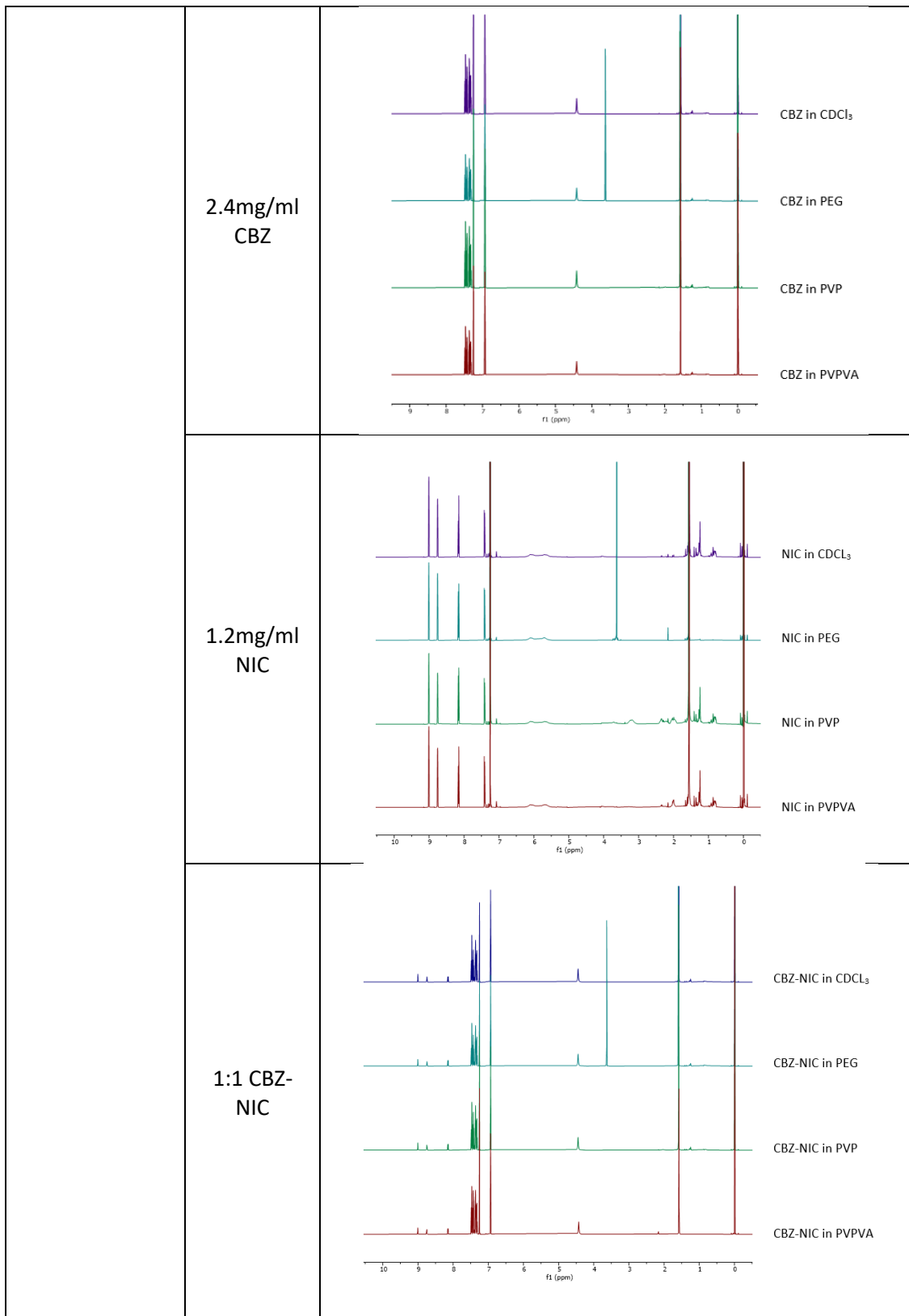
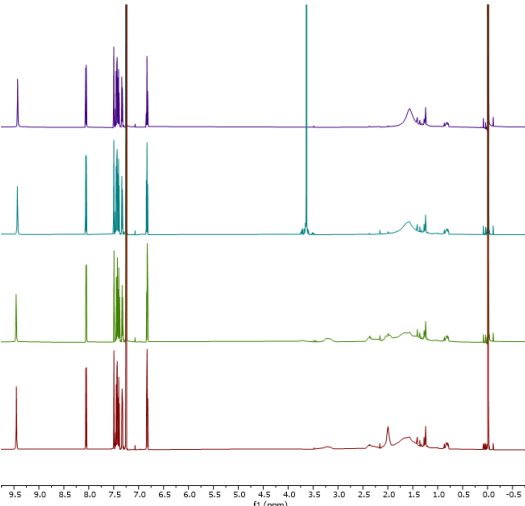
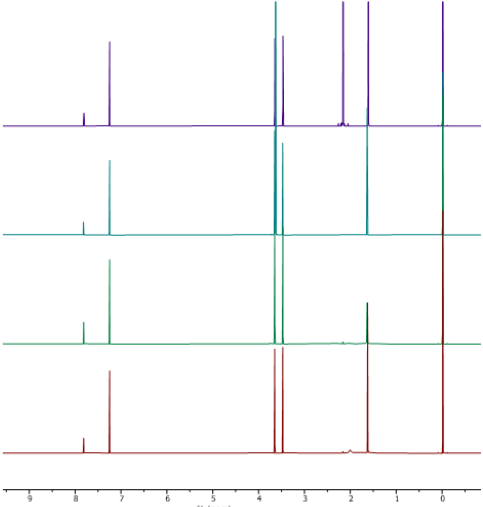
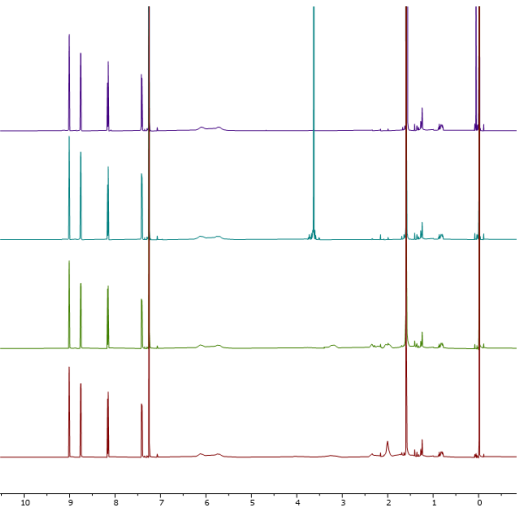
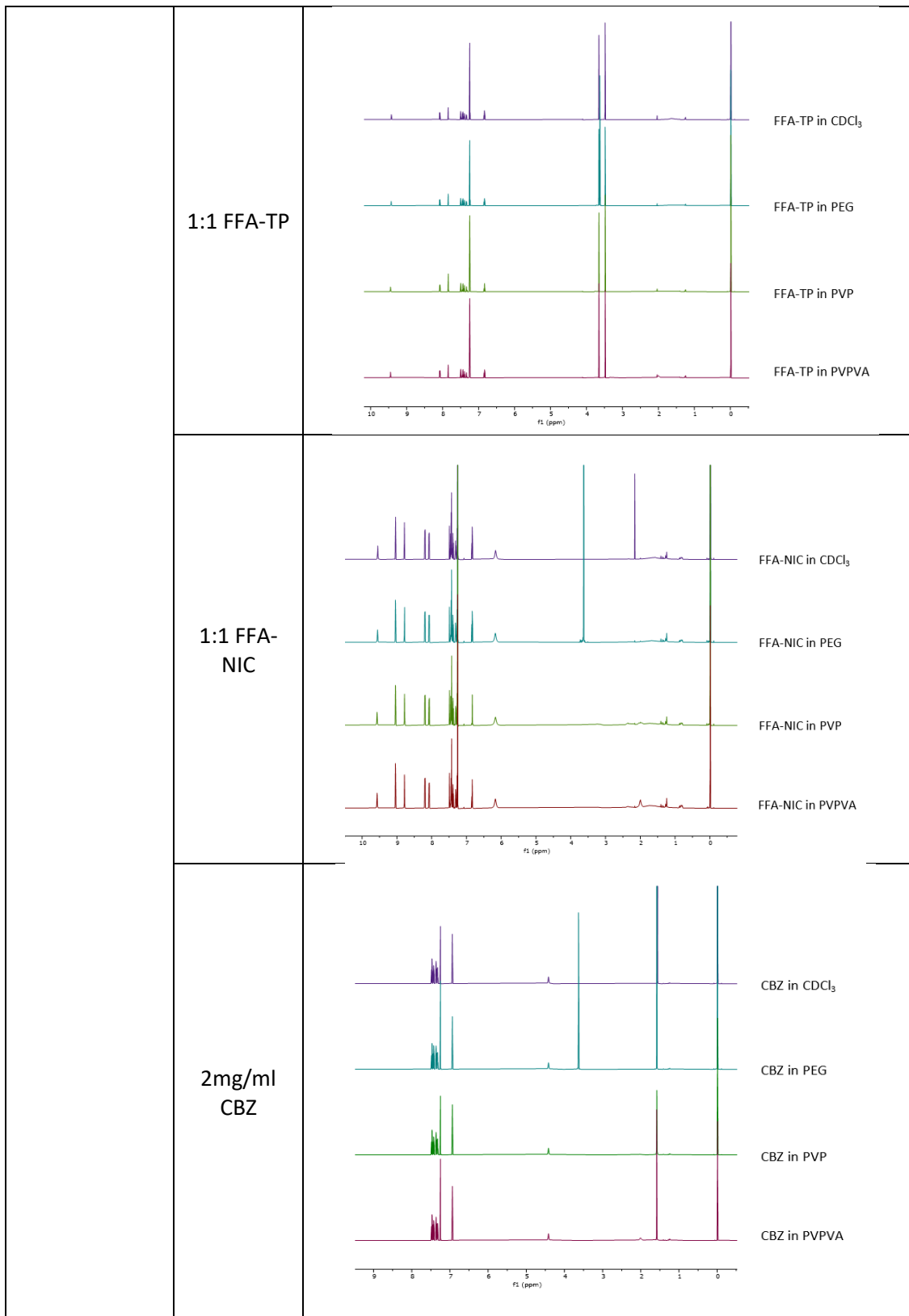


Table 2: NMR spectra of drugs and polymer in 0.5mg/ml polymer.

	Drug	NMR proton spectra
Components	2mg/ml FFA	 <p>FFA in CDCl₃</p> <p>FFA in PEG</p> <p>FFA in PVP</p> <p>FFA in PVPVA</p> <p>f1 (ppm)</p>
	1.28mg/ml TP	 <p>TP in CDCl₃</p> <p>TP in PEG</p> <p>TP in PVP</p> <p>TP in PVPVA</p> <p>f1 (ppm)</p>
	0.86mg/ml NIC	 <p>NIC in CDCl₃</p> <p>NIC in PEG</p> <p>NIC in PVP</p> <p>NIC in PVPVA</p> <p>f1 (ppm)</p>



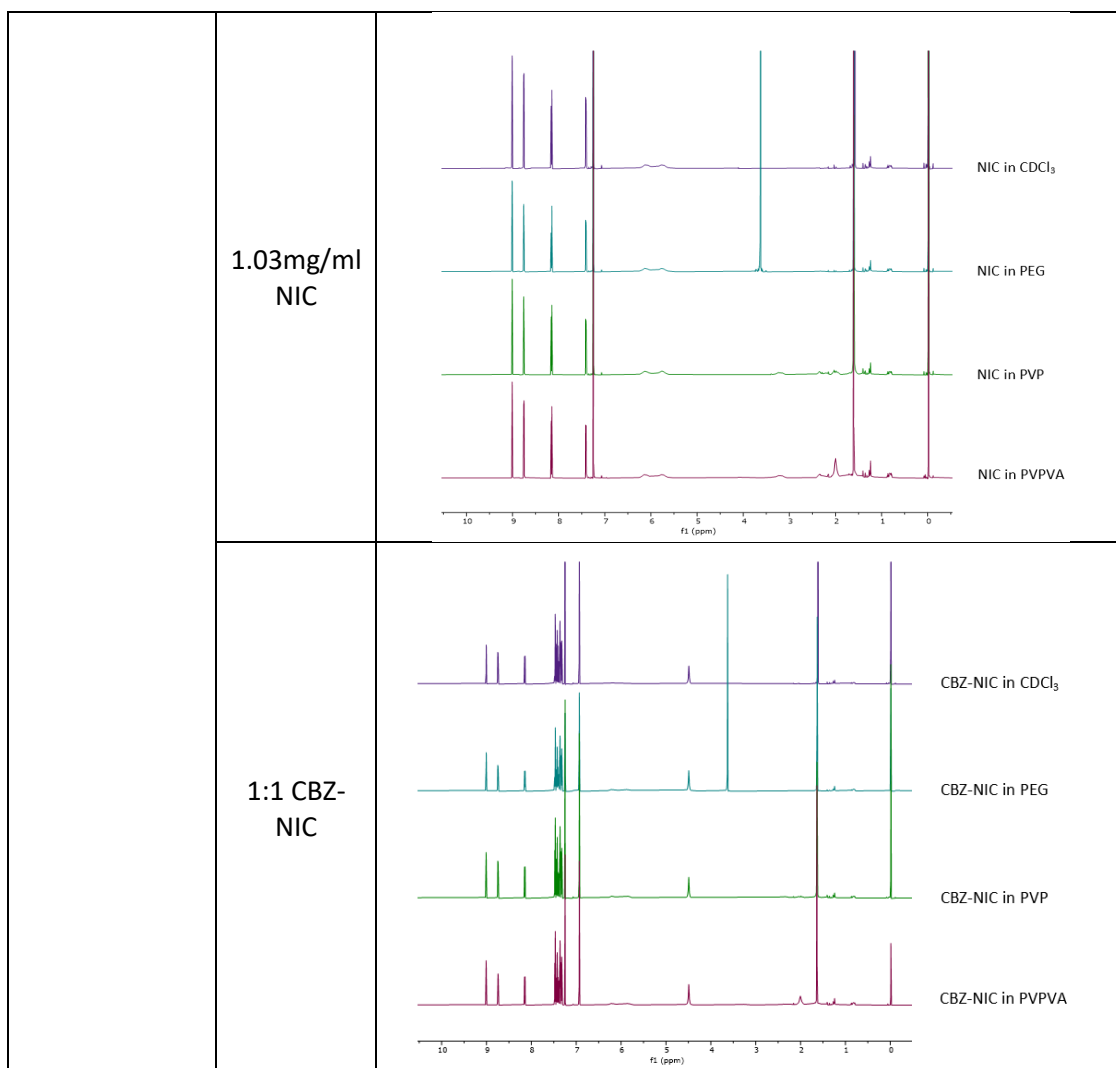
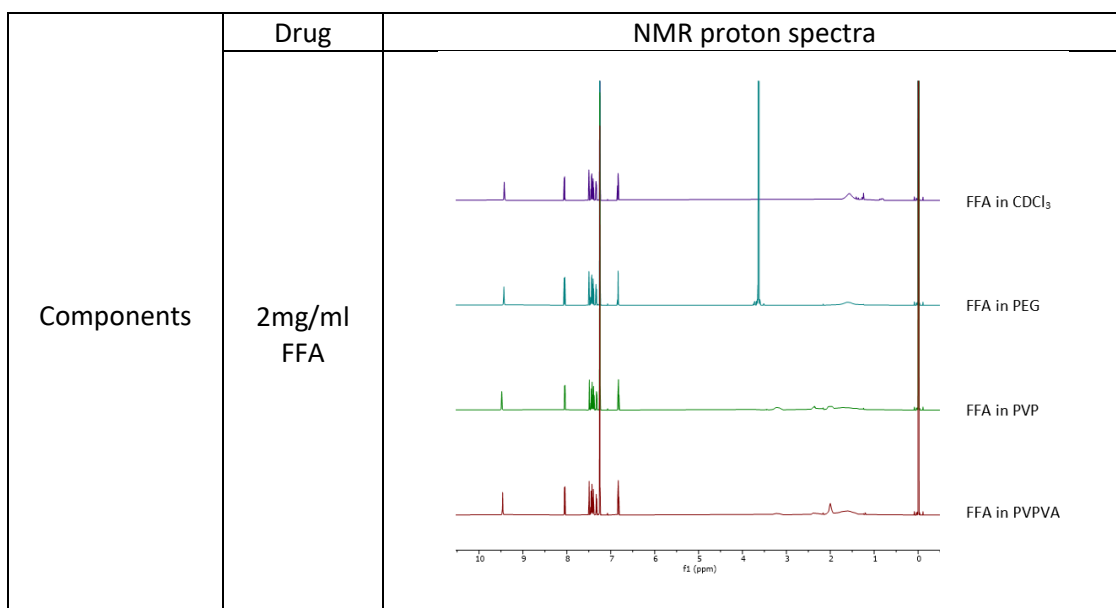
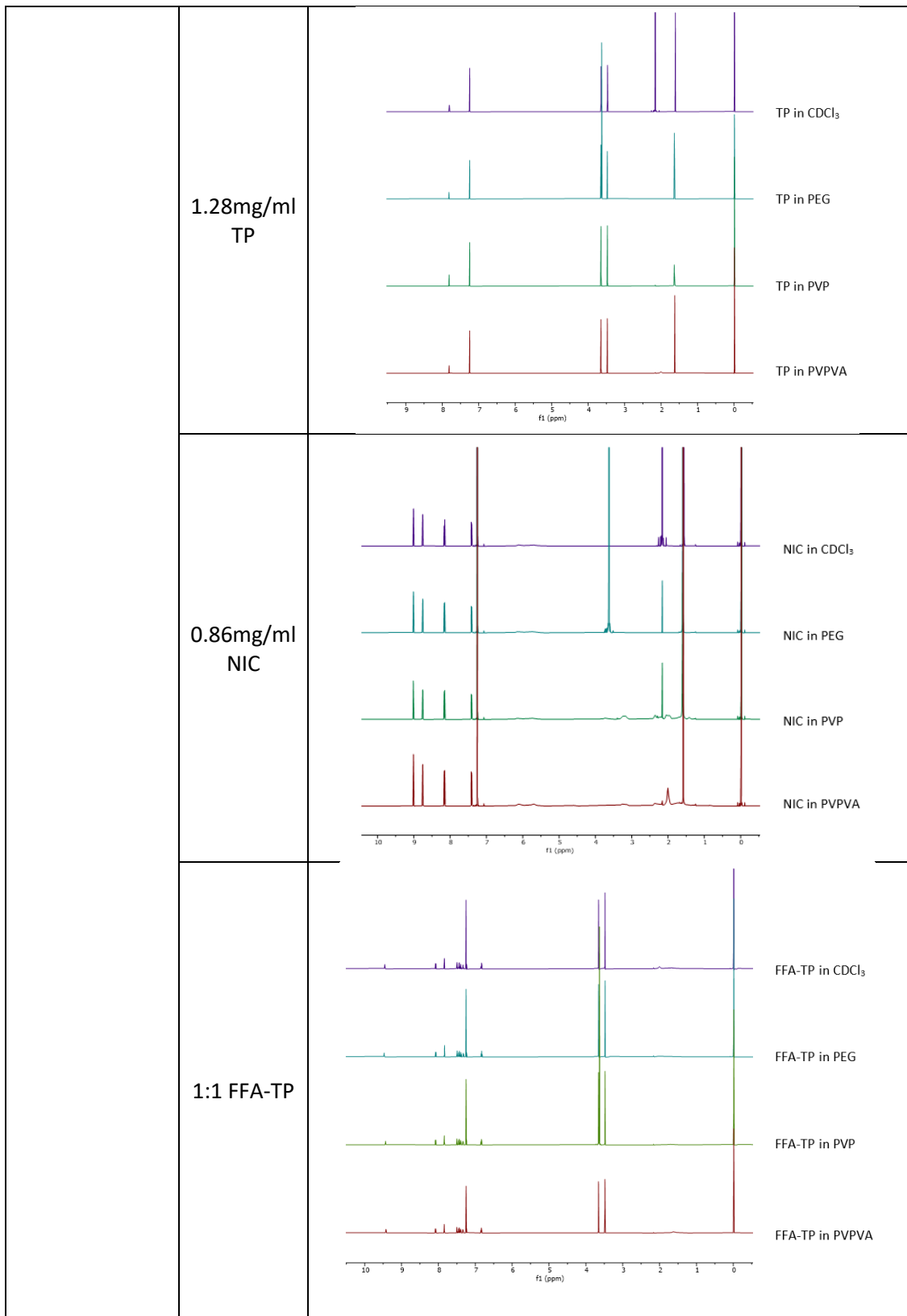
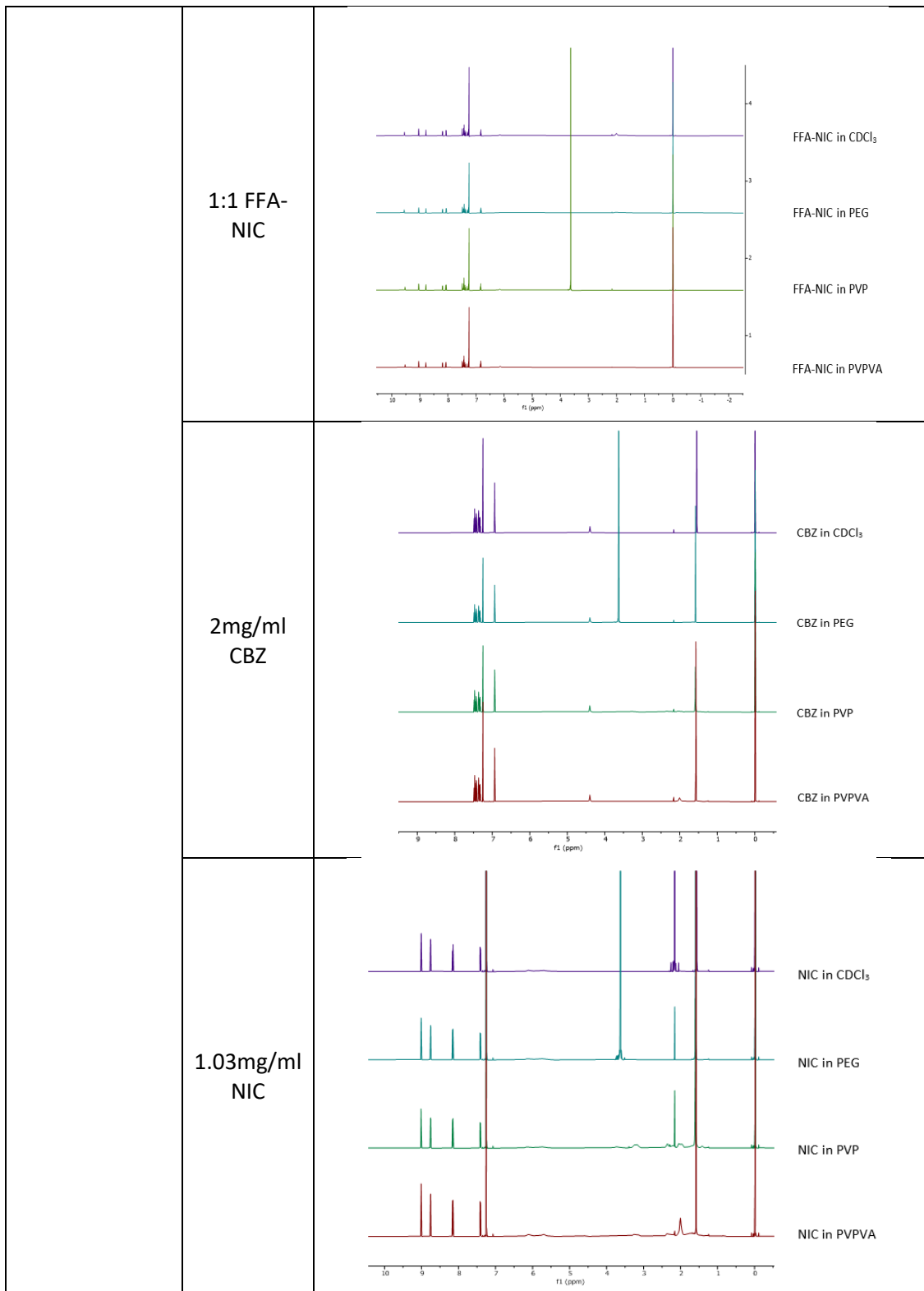


Table 3: NMR spectra of drugs and co-crystals in 1mg/ml polymer.







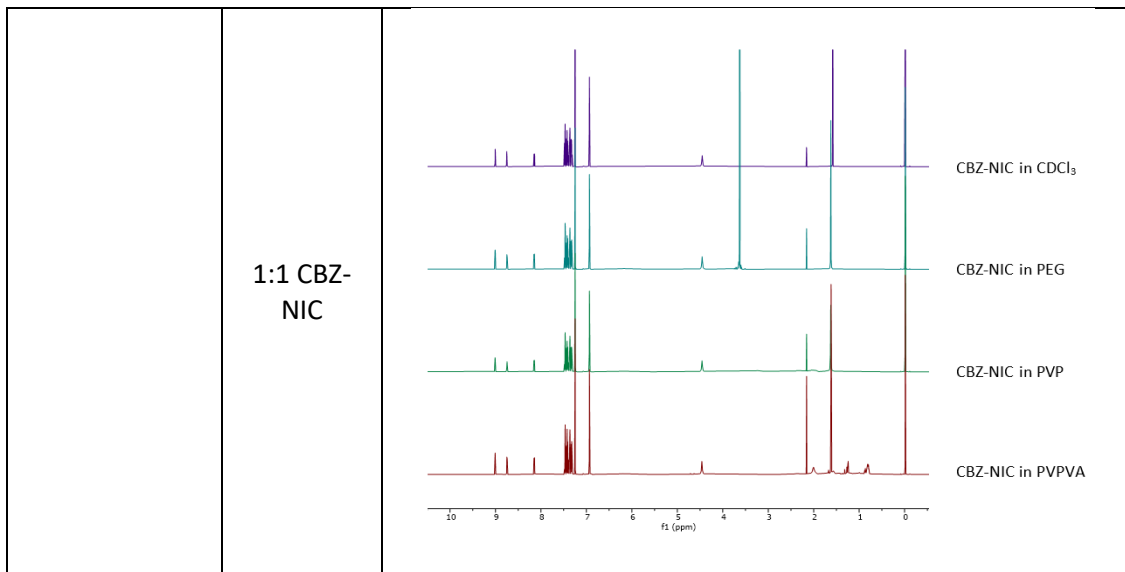


Table 4: NMR spectra of the polymer at 1 mg/ml.

	Polymer	NMR proton spectra
Singular components	PEG	
	PVP	
	PVPVA	

Table 6: Peak shift in the presence of 0.3mg/ml, 0.5mg/ml and 1mg/ml of PEG, PVP and PVP-VA polymer.

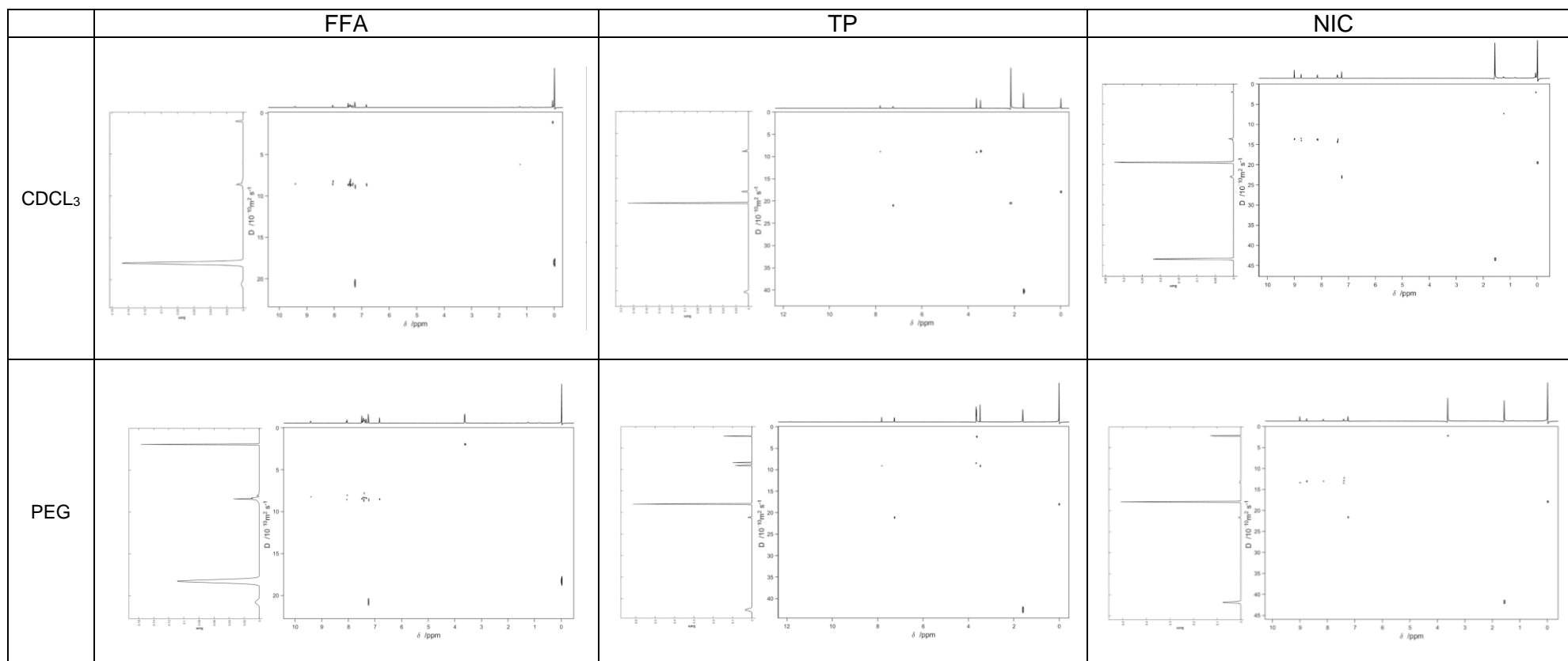
Compound		Characteristic peak	Peak shift			Difference of peak shift		
			PEG 0.3mg/ml	PVP 0.3mg/ml	PVPVA 0.3mg/ml	PEG 0.3mg/ml	PVP 0.3mg/ml	PVPVA 0.3mg/ml
-		-						
2mg/ml FFA		9.414	9.419	9.431	9.421	0.005	0.017	0.007
		8.053	8.053	8.05	8.051	0	-0.003	-0.002
1.28mg/ml TP		7.808	7.808	7.806	7.809	0	-0.002	0.001
		3.65	3.647	3.646	3.647	-0.003	-0.004	-0.003
		3.474	3.47	3.468	3.47	-0.004	-0.006	-0.004
0.86mg/ml NIC		9.006	9.007	9.007	9.007	0.001	0.001	0.001
		5.707	5.696	5.696	5.641	-0.011	-0.011	-0.066
FFA-TP	FFA	9.423	9.427	9.438	9.427	0.004	0.015	0.004
		8.072	8.071	8.069	8.071	-0.001	-0.003	-0.001
	TP	7.843	7.843	7.841	7.842	0	-0.002	-0.001
		3.658	3.657	3.656	3.657	-0.001	-0.002	-0.001
FFA-NIC	FFA	9.519	9.521	9.522	9.522	0.002	0.003	0.003
		8.781	8.78	8.779	8.781	-0.001	-0.002	0
	NIC	9.045	9.045	9.042	9.046	0	-0.003	0.001
		6.204	6.207	6.172	6.209	0.003	-0.032	0.005
2mg/ml CBZ		6.935	6.935	6.934	6.934	0	-0.001	-0.001
		4.417	4.417	4.419	4.419	0	0.002	0.002
1.03mg/ml NIC		9.005	9.007	9.006	9.005	0.002	0.001	0
		5.664	5.699	5.671	5.671	0.035	0.007	0.007
CBZ-NIC	CBZ	6.934	6.934	6.934	6.935	0	0	0.001
		4.443	4.443	4.444	4.427	0	0.001	-0.016
	NIC	9.001	9.002	9.002	9.003	0.001	0.001	0.002
		5.765	5.765	5.765	5.738	0	0	-0.027

Compound		Characteristic peak	Peak shift						Difference of peak shift					
			PEG		PVP		PVPVA		PEG		PVP		PVPVA	
			0.5mg/ml	1mg/ml	0.5mg/ml	1mg/ml	0.5mg/ml	1mg/ml	0.5mg/ml	1mg/ml	0.5mg/ml	1mg/ml	0.5mg/ml	1mg/ml
-		-												
2mg/ml FFA		9.425	9.431	9.434	9.456	9.483	9.45	9.462	0.006	0.009	0.031	0.058	0.025	0.037
		8.047	8.046	8.045	8.043	8.038	8.044	8.042	-0.001	-0.002	-0.004	-0.009	-0.003	-0.005
1.28mg/ml TP		7.809	7.815	7.819	7.813	7.813	7.815	7.816	0.006	0.01	0.004	0.004	0.006	0.007
		3.646	3.648	3.649	3.648	3.648	3.648	3.648	0.002	0.003	0.002	0.002	0.002	0.002
		3.468	3.471	3.473	3.471	3.47	3.471	3.472	0.003	0.005	0.003	0.002	0.003	0.004
0.86mg/ml NIC		9.006	9.007	9.008	9.008	9.009	9.008	9.008	0.001	0.002	0.002	0.003	0.002	0.002
		5.671	5.724	5.702	5.724	5.702	5.724	5.702	0.053	0.031	0.053	0.031	0.053	0.031
FFA-TP	FFA	9.423	9.429	9.434	9.448	9.471	9.448	9.455	0.006	0.011	0.025	0.048	0.025	0.032
		8.071	8.07	8.069	8.065	8.062	8.066	8.066	-0.001	-0.002	-0.006	-0.009	-0.005	-0.005
	TP	7.841	7.84	7.84	7.839	7.836	7.84	7.834	-0.001	-0.001	-0.002	-0.005	-0.001	-0.007
		3.657	3.656	3.655	3.656	3.654	3.656	3.655	-0.001	-0.002	-0.001	-0.003	-0.001	-0.002
FFA-NIC	FFA	9.551	9.558	9.563	9.571	9.573	9.569	9.573	0.007	0.012	0.02	0.022	0.018	0.022
		8.067	8.066	8.059	8.064	8.053	8.063	8.056	-0.001	-0.008	-0.003	-0.014	-0.004	-0.011
	NIC	9.038	9.039	9.038	9.038	9.037	9.039	9.038	0.001	0	0	-0.001	0.001	0
		6.161	6.169	6.151	6.164	6.151	6.167	6.143	0.008	-0.01	0.003	-0.01	0.006	-0.018
2mg/ml CBZ		6.935	6.935	6.934	6.934	6.933	6.934	6.934	0	-0.001	-0.001	-0.002	-0.001	-0.001
		4.394	4.394	4.397	4.394	4.4	4.394	4.398	0	0.003	0	0.006	0	0.004
1.03mg/ml NIC		9.007	9.008	9.008	9.009	9.01	9.009	9.009	0.001	0.001	0.002	0.003	0.002	0.002
		5.742	5.75	5.757	5.755	5.757	5.755	5.757	0.008	0.015	0.013	0.015	0.013	0.015
CBZ-NIC	CBZ	6.932	6.933	6.931	6.931	6.93	6.931	6.93	0.001	-0.001	-0.001	-0.002	-0.001	-0.002
		4.452	4.452	4.453	4.492	4.456	4.491	4.46	0	0.001	0.04	0.004	0.039	0.008

	NIC	9.002	9.003	9.007	9.003	9.008	9.004	9.006	0.001	0.005	0.001	0.006	0.002	0.004
		5.767	5.777	5.788	5.781	5.788	5.781	5.797	0.01	0.021	0.014	0.021	0.014	0.03

A6 DOSY Spectra

Table 1: 2.4mg/ml drug in the presence of 0.3mg/ml polymer



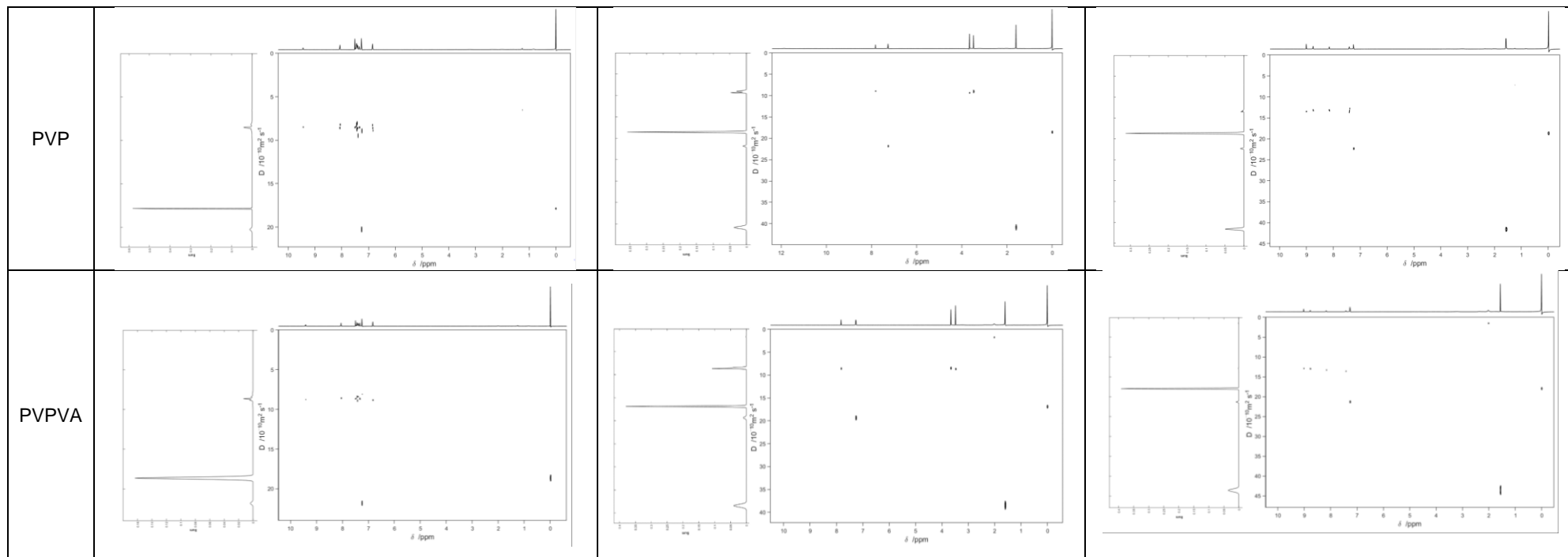
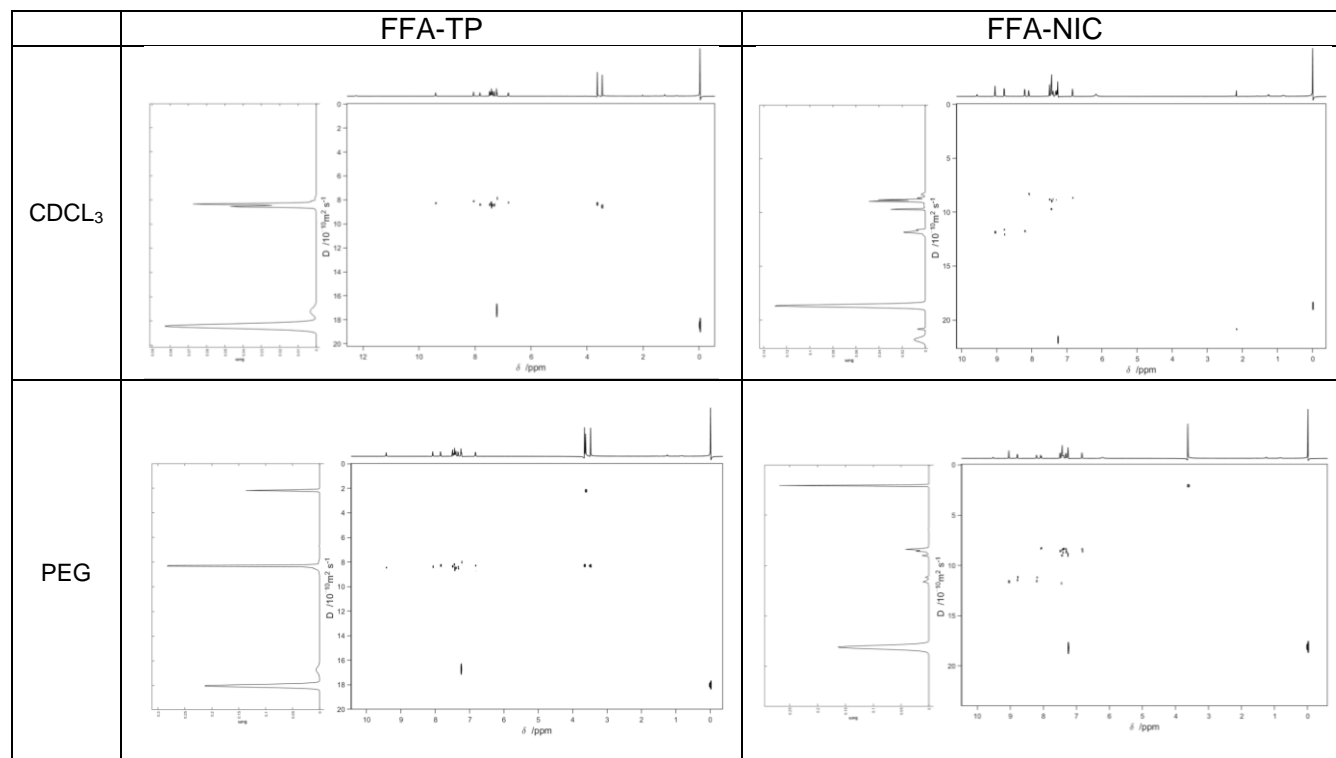


Table 2: 1:1 FFA-TP and 1:1 FFA-NIC CO in the presence of 0.3mg/ml polymer



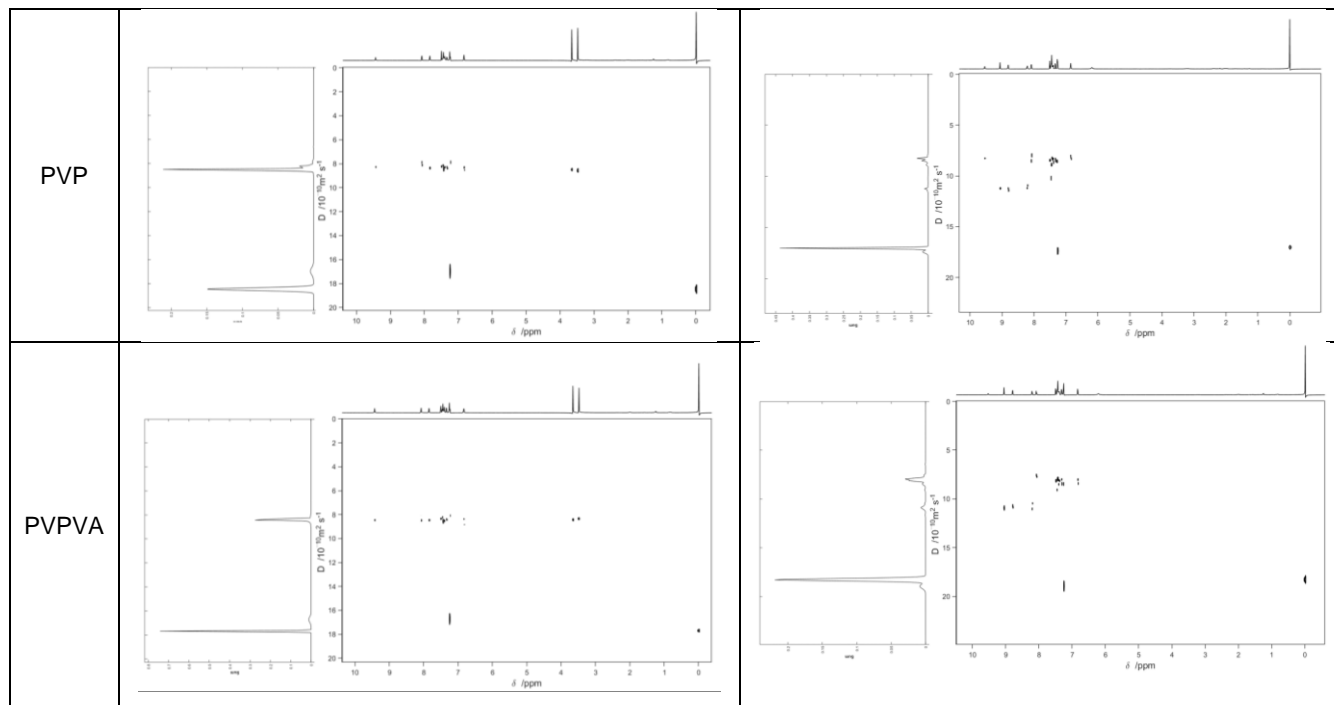
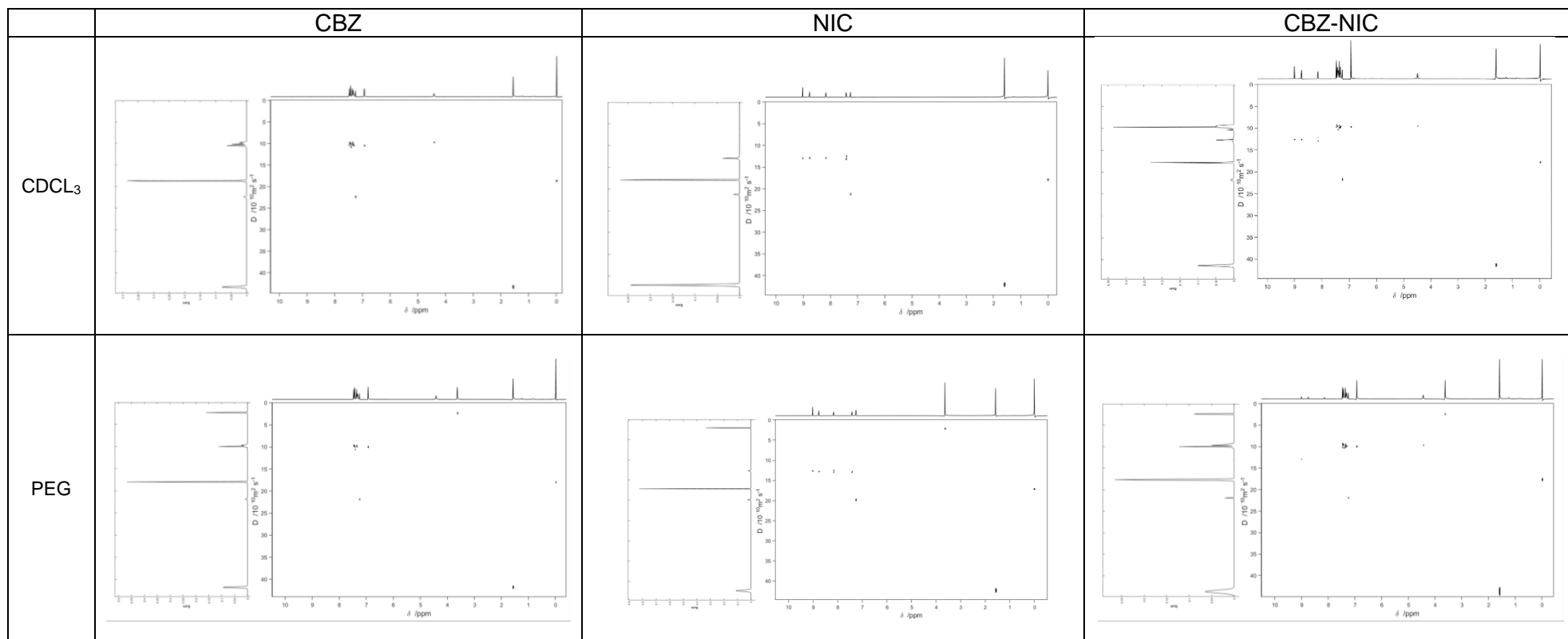


Table 3: 2.4mg/ml CBZ, NIC and 1:1 CBZ-NIC CO in 0.3mg/ml polymer



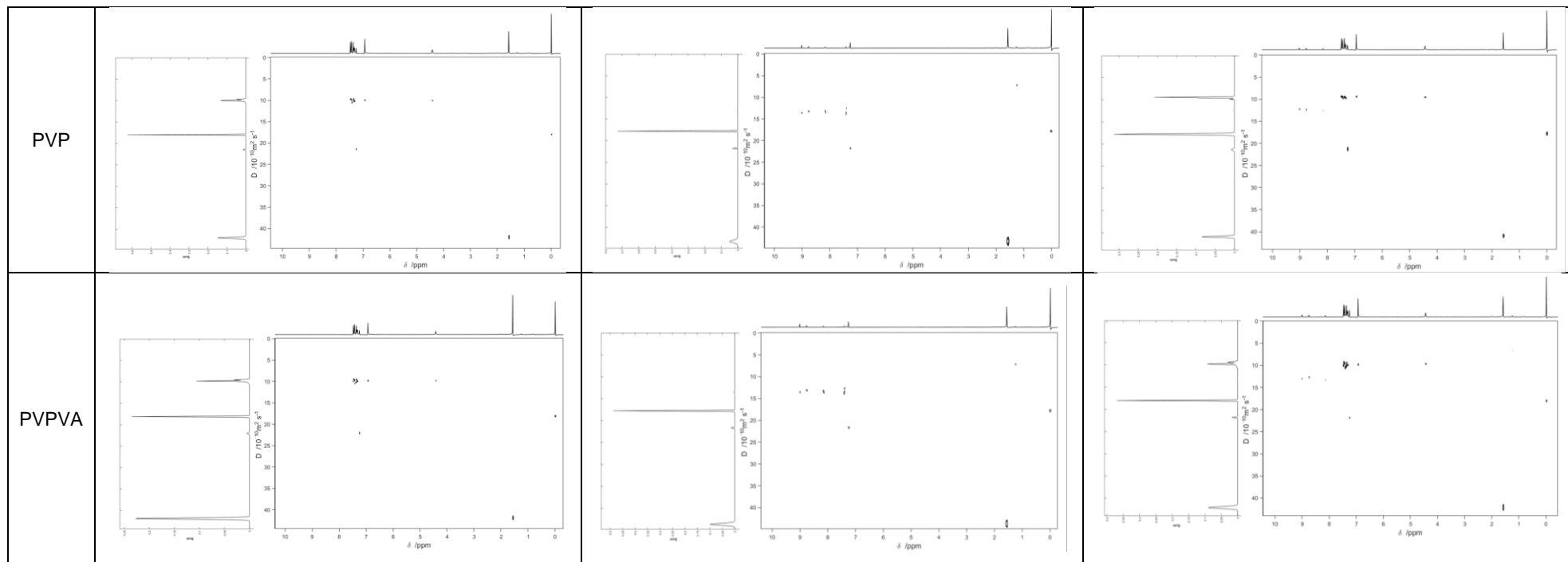
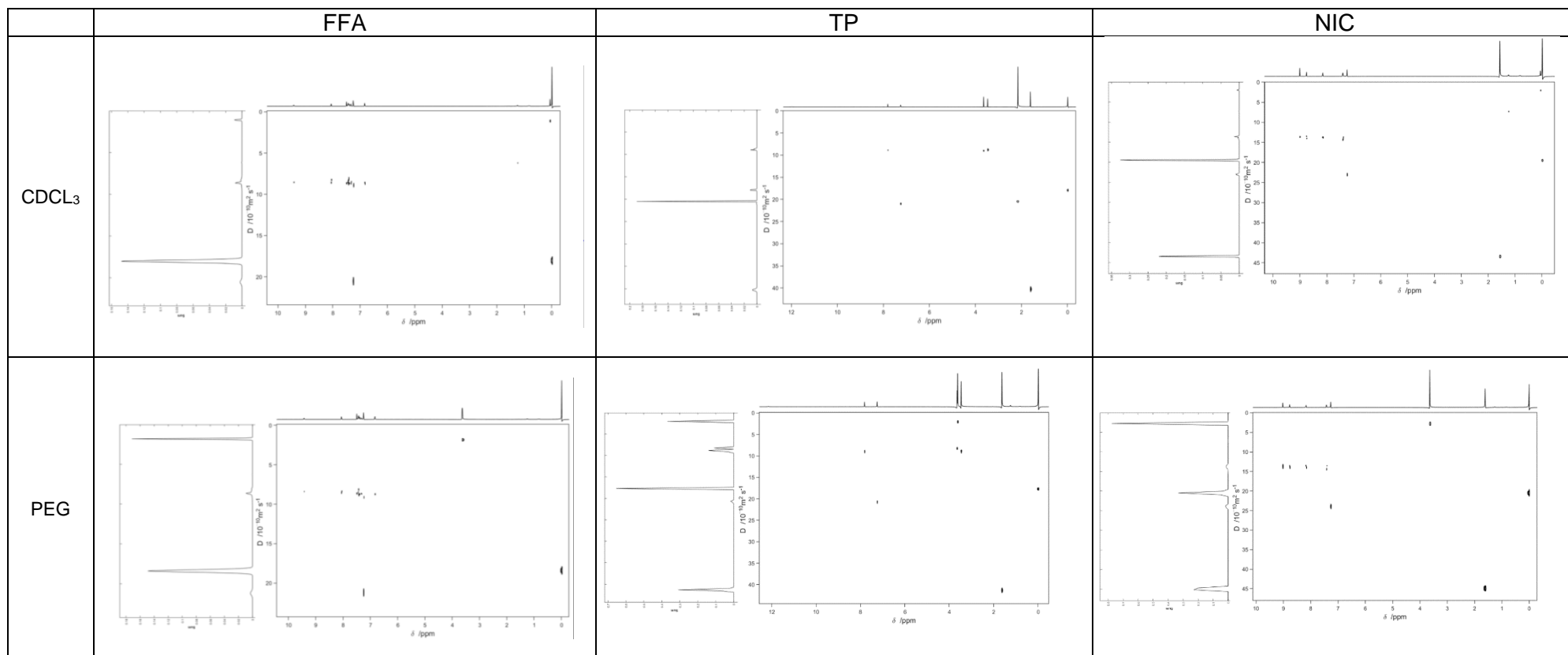


Table 4: FFA, TP and NIC with/without 0.5mg/ml polymers



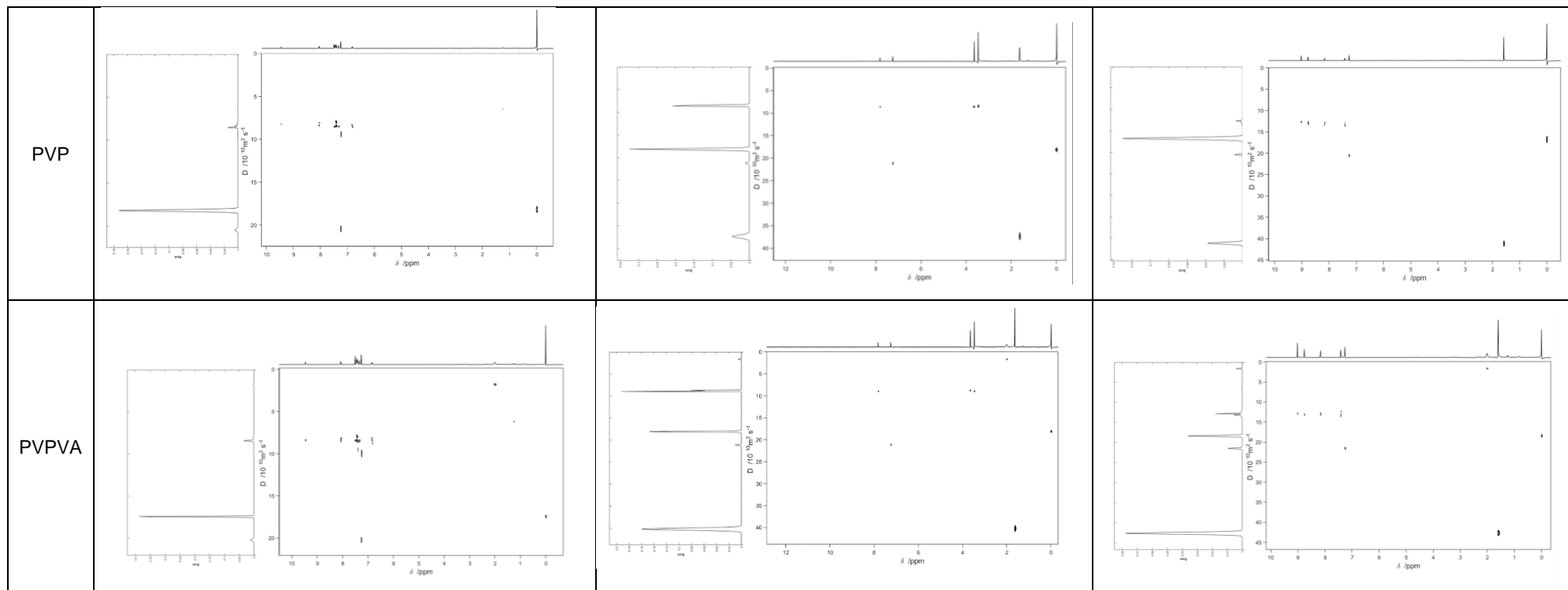
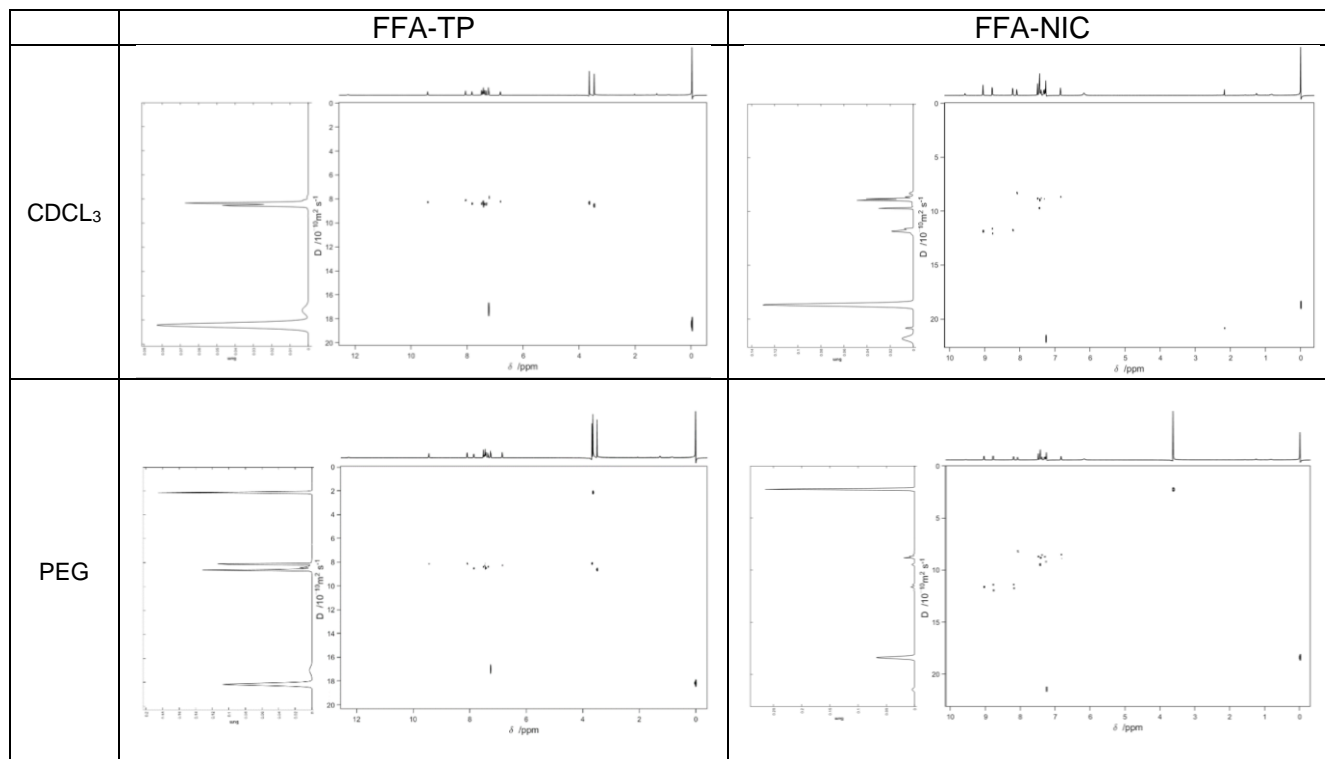


Table 5: 1:1 FFA-TP and 1:1 FFA-NIC with/without 0.5mg/ml polymers



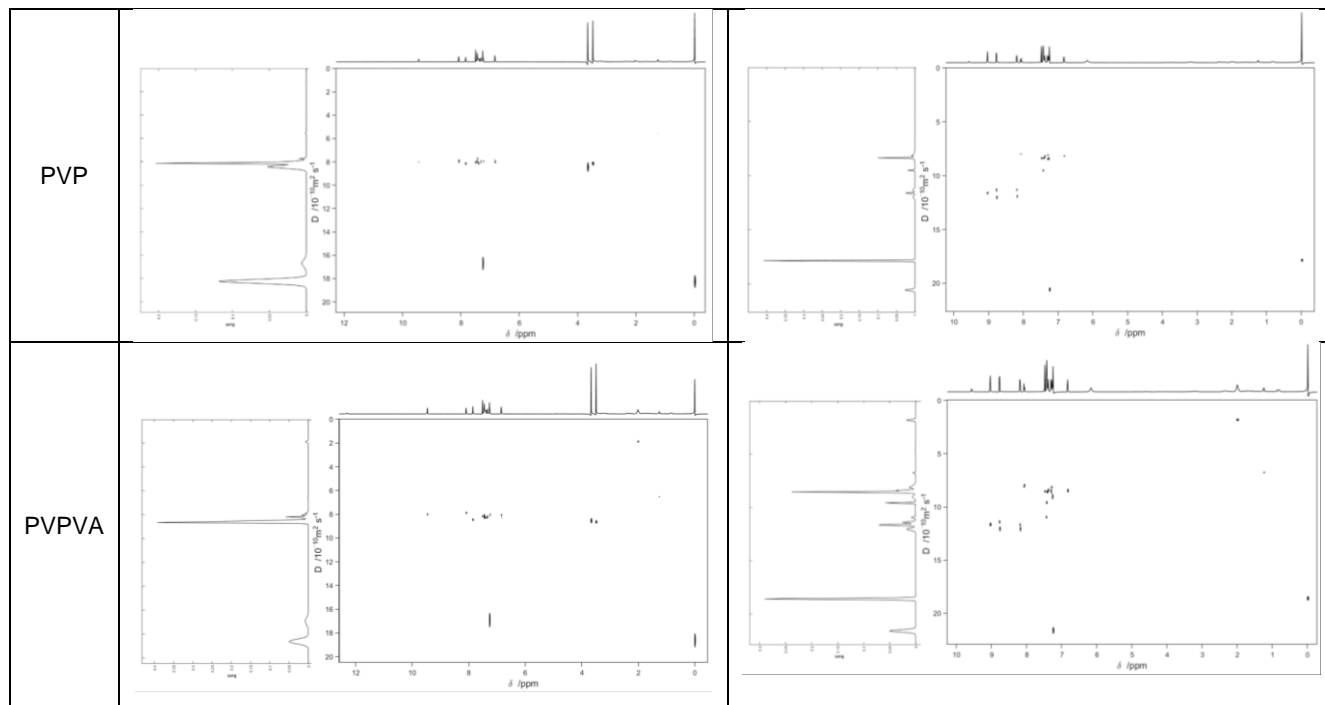
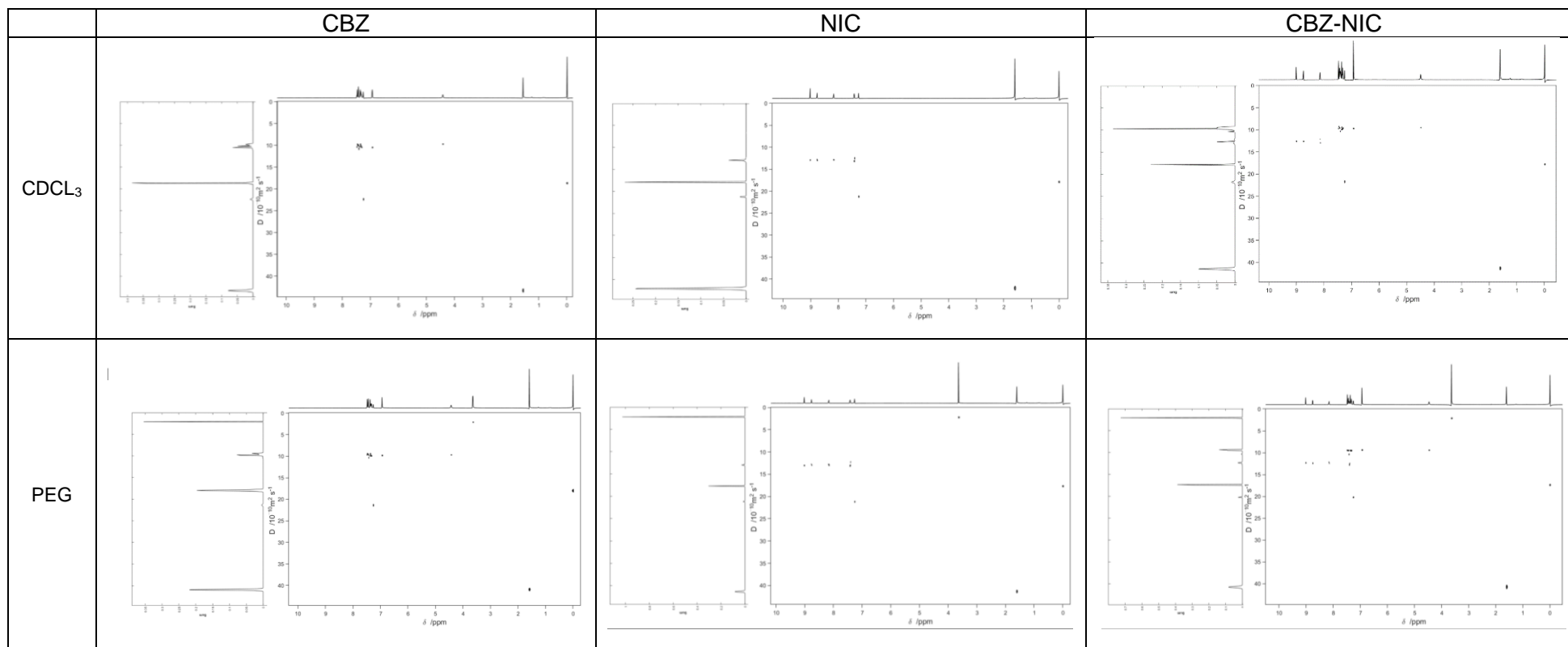


Table 6: CBZ, NIC and 1:1 CBZ-NIC with/without 0.5mg/ml polymers



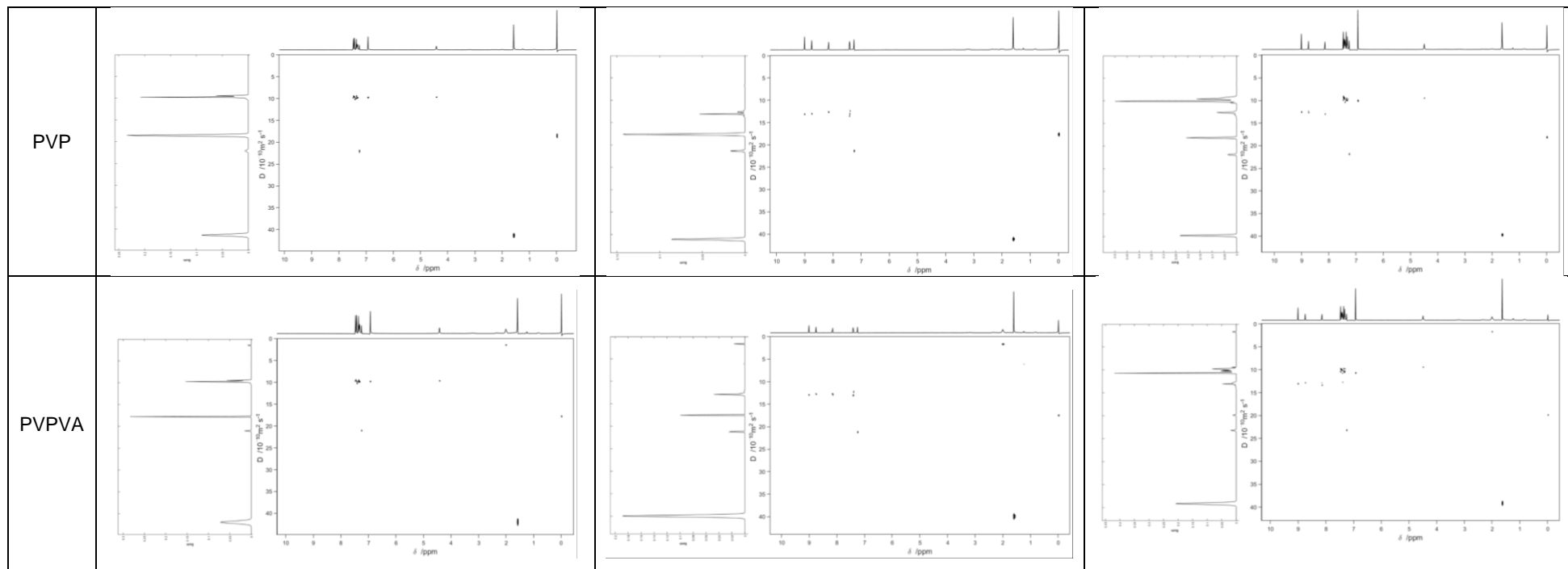
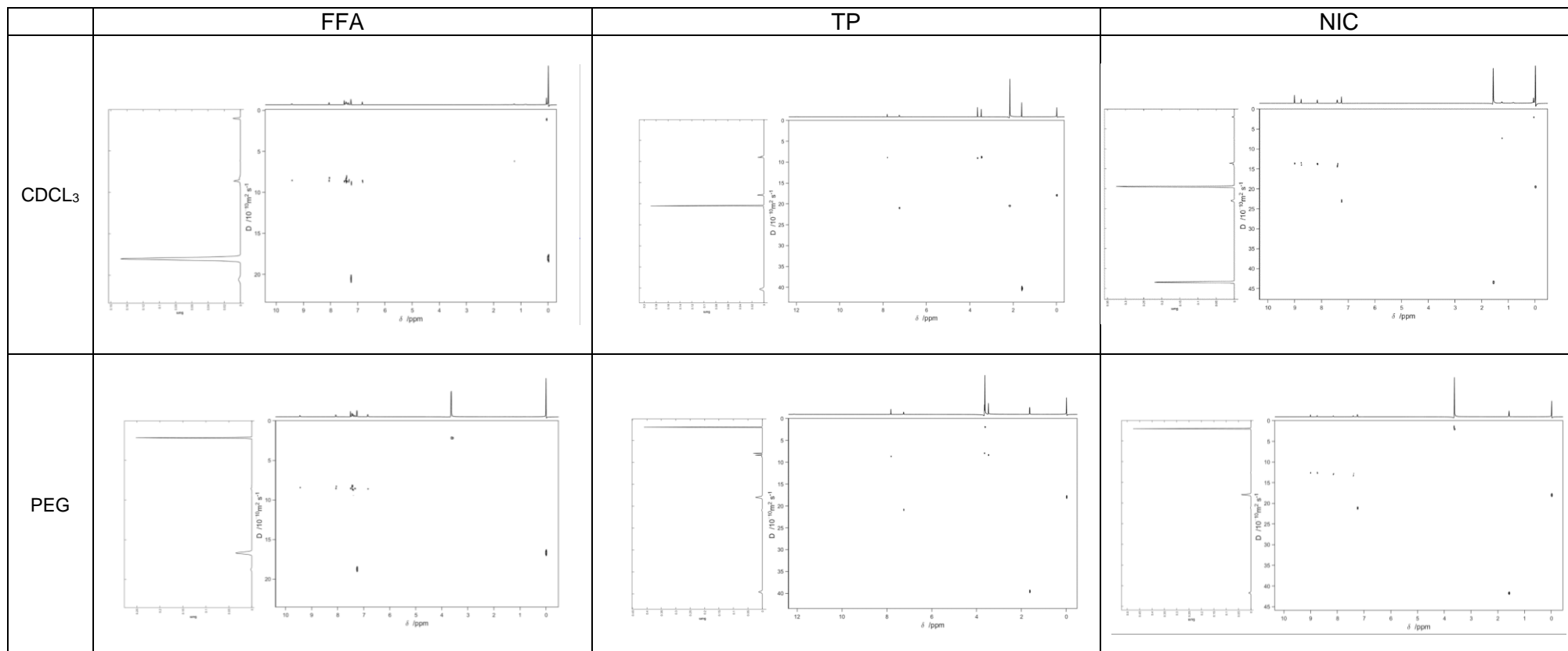


Table 7: FFA, TP and NIC with/without 1mg/ml polymers



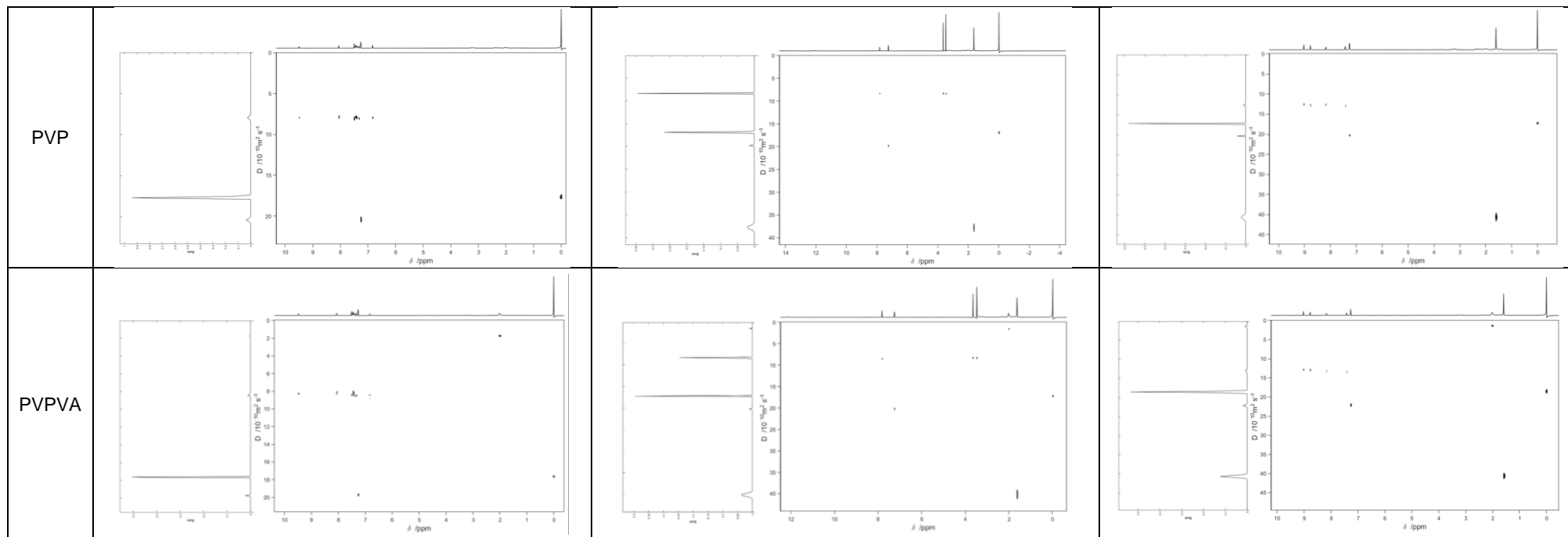
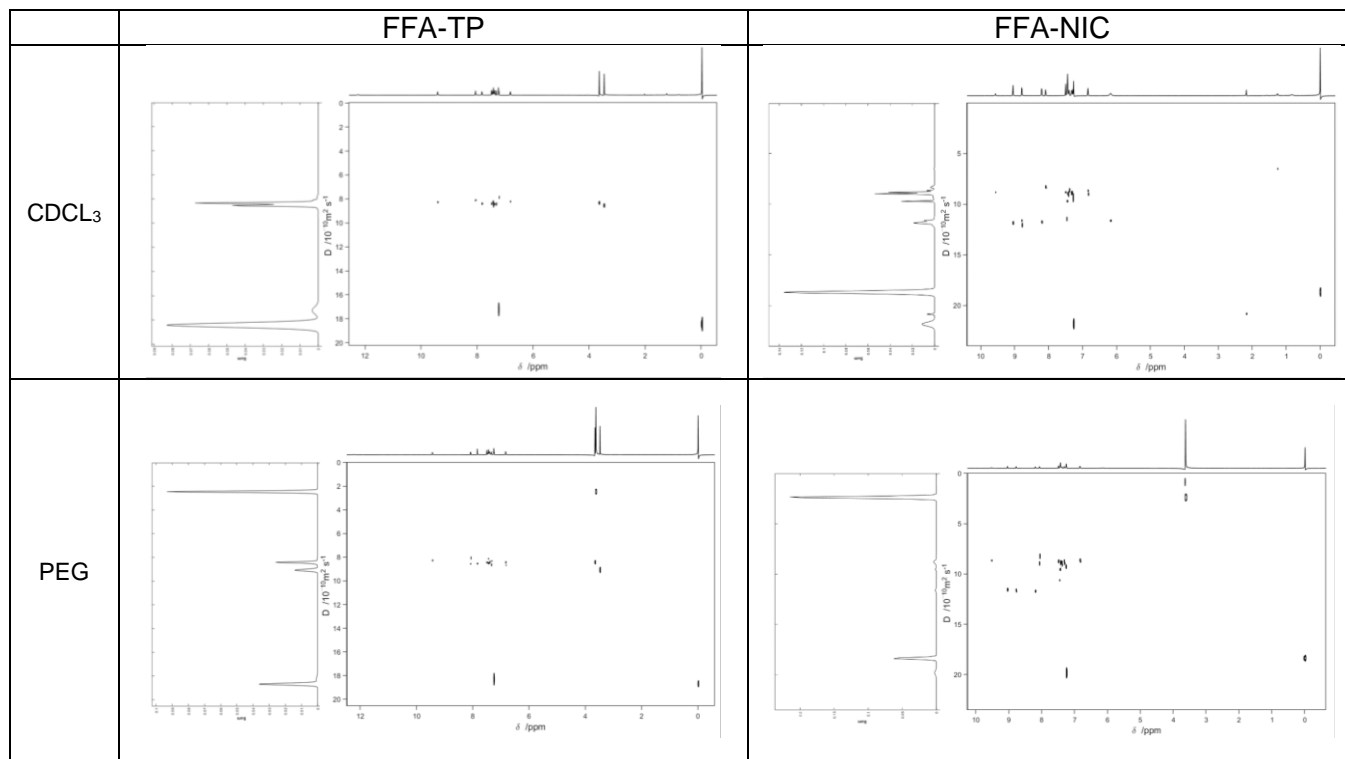


Table 8: 1:1 FFA-TP and 1:1 FFA-NIC with/without 1mg/ml polymers



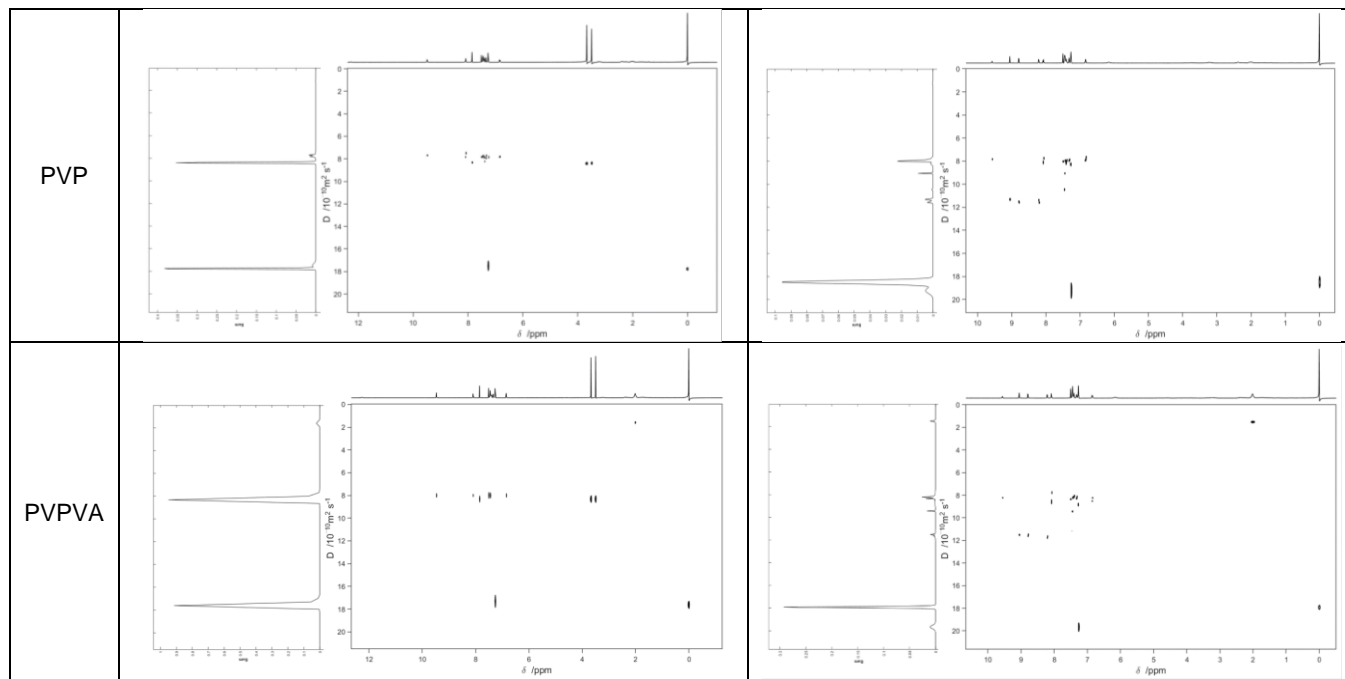
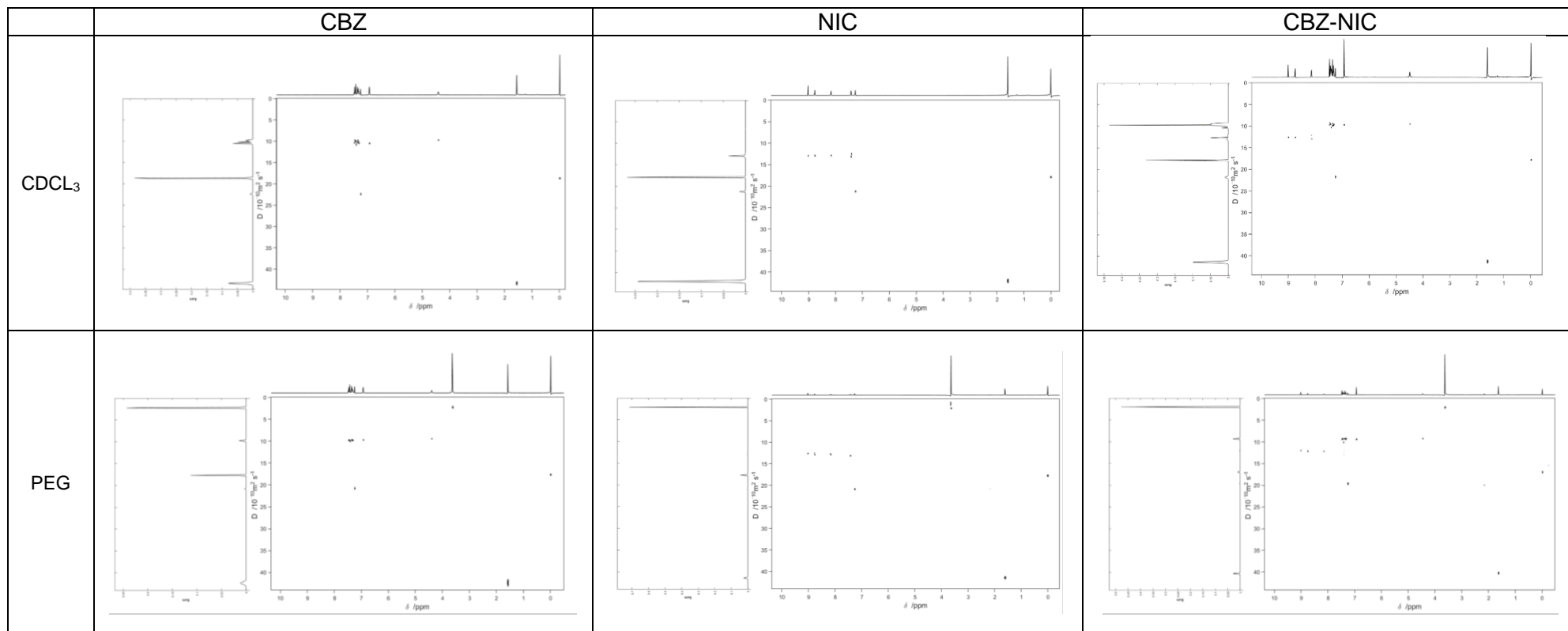


Table 9: CBZ, NIC and 1:1 CBZ-NIC with/without 1mg/ml polymers



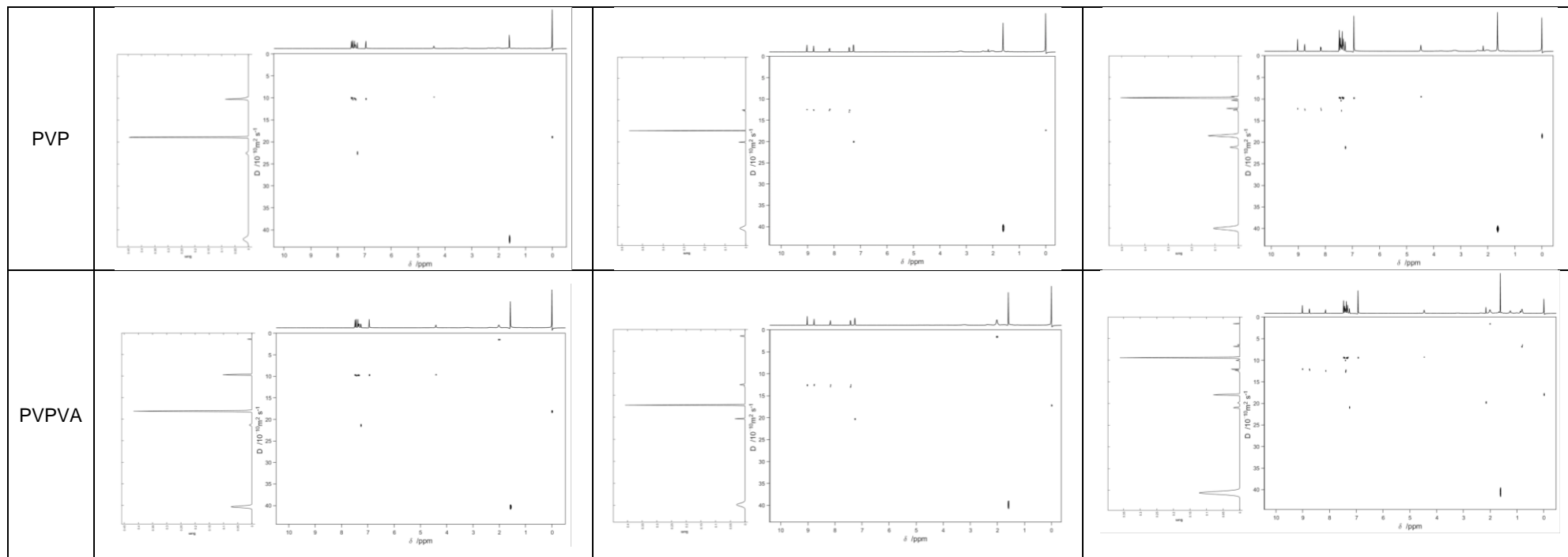
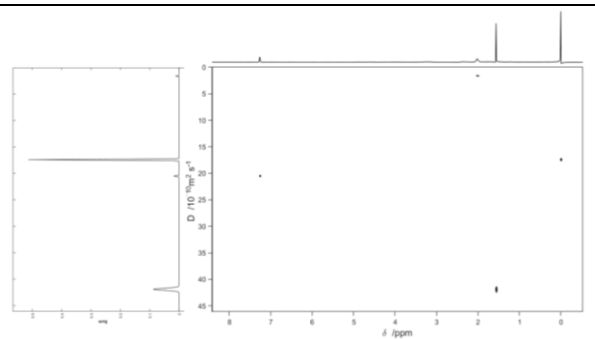
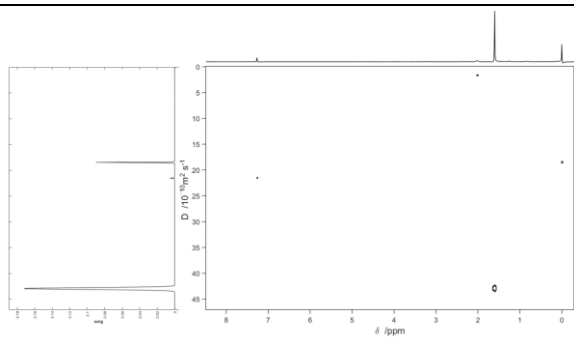


Table 10: 0.5mg/ml and 1mg/ml of polymers

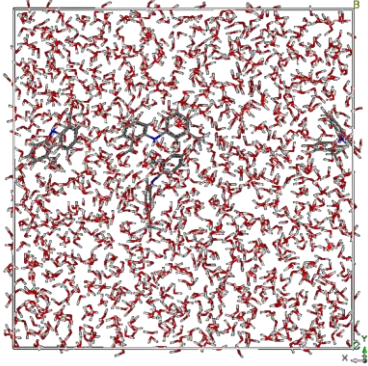
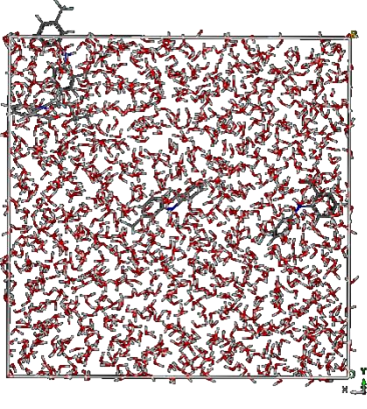
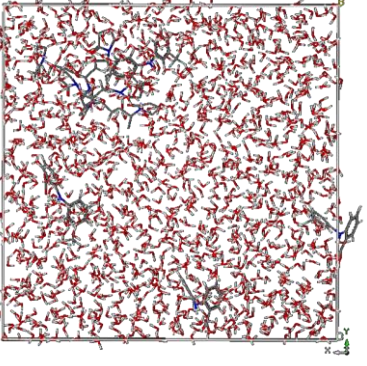
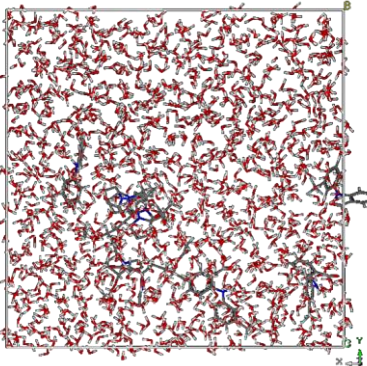
	0.5mg/ml	1mg/ml
PEG		
PVP		

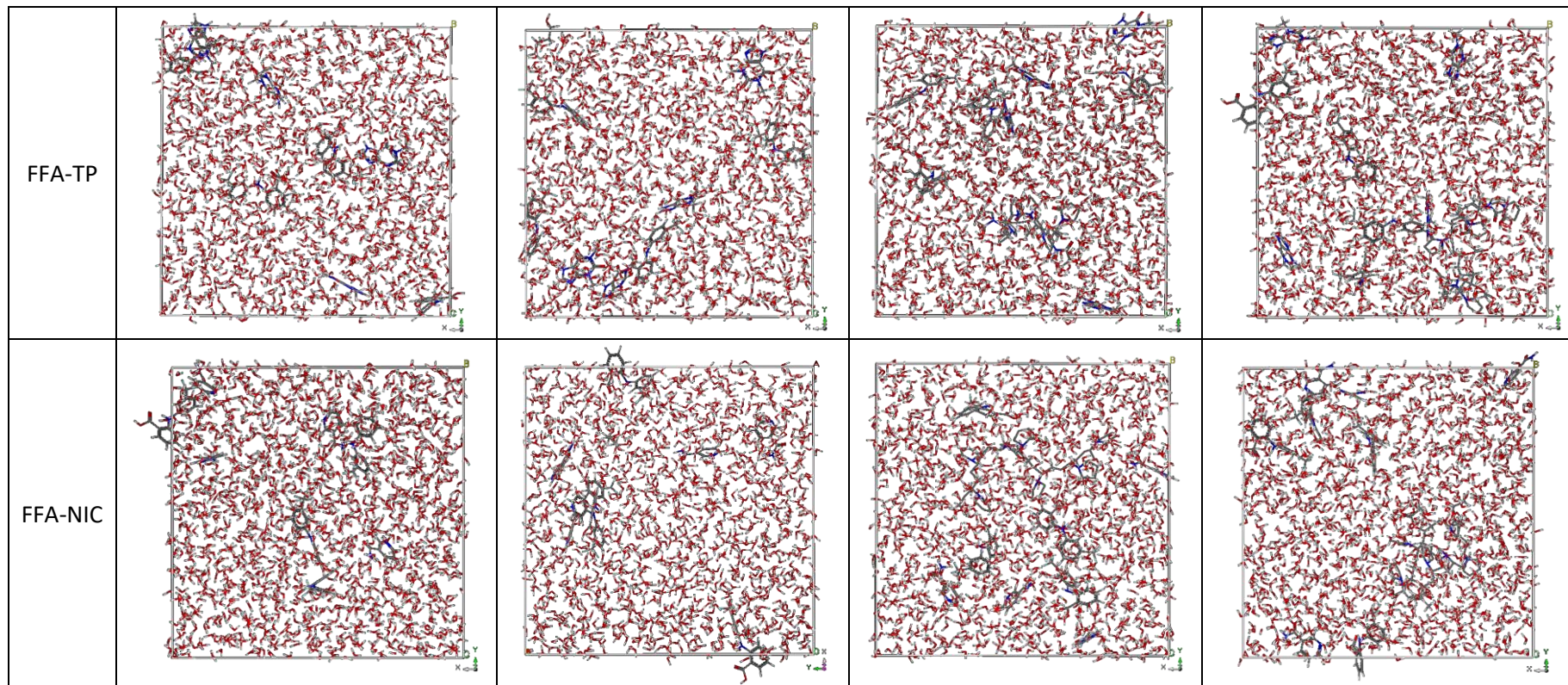
PVPVA



A7 Molecular dynamic simulations

Table 1: systems after GO containing API, various polymers and water molecules.

	No polymer	PEG	PVP	PVPVA
FFA				



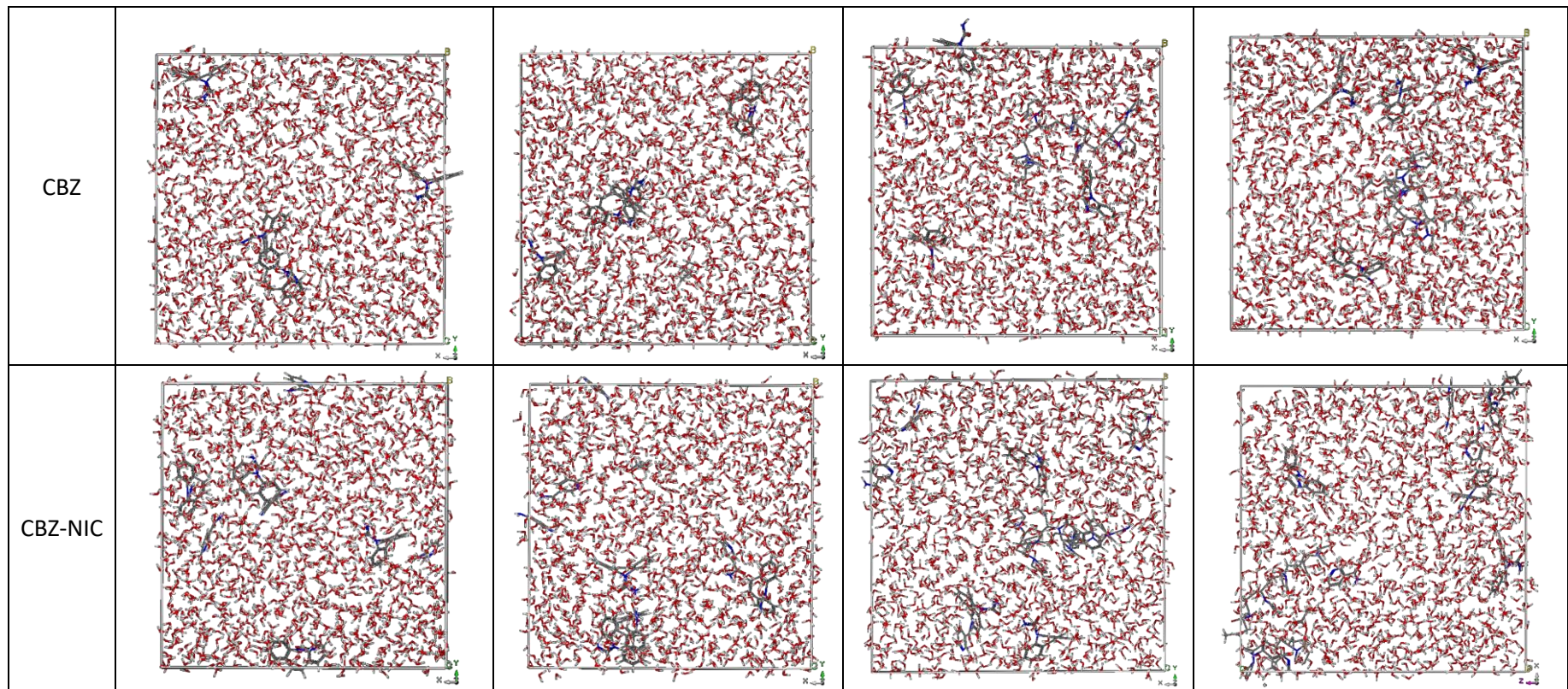
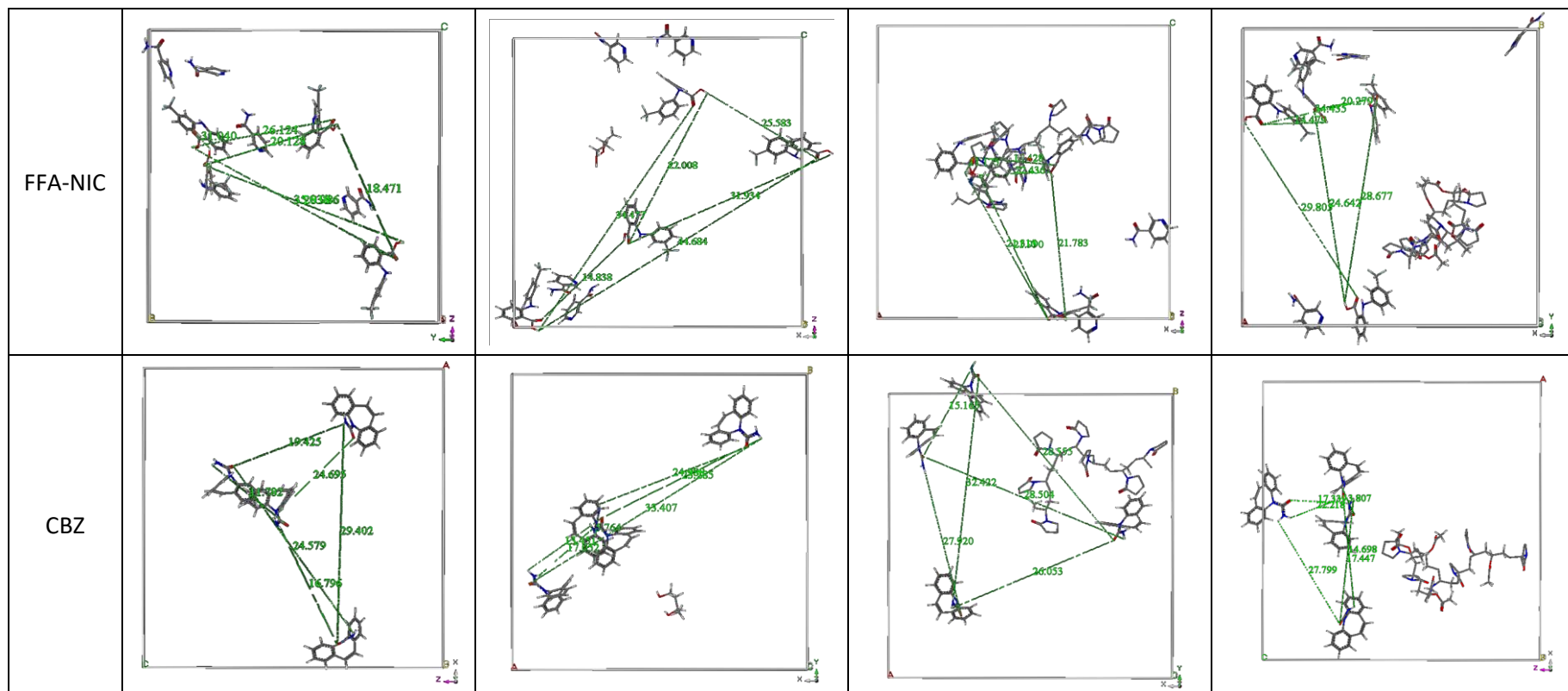


Table 2: Models used for length evolution and length distribution calculations

	No polymer	PEG	PVP	PVPVA
FFA				
FFA-TP				



CBZ-NIC

